Single Cell Force Spectroscopy for

Quantification of Cellular Adhesion on Surfaces

by

Wayne B Christenson

A Dissertation Presented in Partial Fulfillment
of the Requirements for the Degree
Doctor of Philosophy

Approved November 2016 by the
Graduate Supervisory Committee:

Robert Ros, Chair
Oliver Beckstein
Stuart Lindsay
Tatiana Ugarova

ARIZONA STATE UNIVERSITY

December 2016

ABSTRACT

Cell adhesion is an important aspect of many biological processes. The atomic force microscope (AFM) has made it possible to quantify the forces involved in cellular adhesion using a technique called single cell force spectroscopy (SCFS). AFM based SCFS offers versatile control over experimental conditions for probing directly the interaction between specific cell types and specific proteins, surfaces, or other cells. Transmembrane integrins are the primary proteins involved in cellular adhesion to the extra cellular matix (ECM). One of the chief integrins involved in the adhesion of leukocyte cells is $\alpha_M\beta_2$ (Mac-1). The experiments in this dissertation quantify the adhesion of Mac-1 expressing human embryonic kidney (HEK Mac-1), platelets, and neutrophils cells on substrates with different concentrations of fibrinogen and on fibrin gels and multi-layered fibrinogen coated fibrin gels. It was shown that multi-layered fibrinogen reduces the adhesion force of these cells considerably. A novel method was developed as part of this research combining total internal reflection microscopy (TIRFM) with SCFS allowing for optical microscopy of HEK Mac-1 cells interacting with bovine serum albumin (BSA) coated glass after interacting with multi-layered fibrinogen. HEK Mac-1 cells are able to remove fibrinogen molecules from the multi-layered fibrinogen matrix. An analysis methodology for quantifying the kinetic parameters of integrin-ligand interactions from SCFS experiments is proposed, and the kinetic parameters of the Mac-1 fibrinogen bond are quantified. Additional SCFS experiments quantify the adhesion of macrophages and HEK Mac-1 cells on functionalized glass surfaces and normal glass surfaces. Both cell types show highest adhesion on a novel functionalized glass surface that was prepared to induce macrophage

fusion. These experiments demonstrate the versatility of AFM based SCFS, and how it can be applied to address many questions in cellular biology offering quantitative insights.

To Hannah

ACKNOWLEDGMENTS

I have had the privilege of collaborating with some great people while doing the research for this dissertation at Arizona State University. The staff and faculty of the physics department have always been professional and courteous with me, and I am very grateful for the opportunity the physics department bestowed on me by accepting as a student. I owe Robert Ros debt of gratitude that can probably never be repayed, and I thank him for advising me, and guiding me with kindness and patience. I wish to thank all the students I worked with in Robert's lab – Patrick Bookjans, Nethmi Ariyasinghe, Alex Ward, Melanie Dannemeyer, Kiarash Rahmani Eliato, Jiawei Liu, Birgit Plochberger, and Charles Michael Gilbert. I want to especially thank Olaf Schulz as an important mentor to me early in my graduate studies, Jack Rory Staunton for helping me with MATLAB coding, and Bryant Doss for helping me to code and being a friend to me.

I want to thank Tatiana Ugarava for her guidance and support. Students from her lab have been important partners in my research as well. Also Valeryi Lishko, a senior researcher in Tatiana's lab, provided invaluable advice and ideas. I thank Hadil Owaynat for working with me. I thank Nataly Podolnikova for providing samples and her help. I am especially grateful to Ivan Yermolenko, who was a great mentor, and taught everything I know about AFMs. I am especially grateful to James "Bo" Faust as well, who has been a great friend, and offered encouragement when research seemed impossible.

I thank my graduate supervisory committee, Robert Ros, Oliver Beckstein, Stuart Lindsay, and Tatiana Ugarova, for their time and support during the completion of this dissertation.

I am grateful for and acknowledge funding from the U.S. Department of Education Graduate Assistance in Areas of National Need Fellowship (P200A090123, PI: Otto Sankey), summer research fellowships (2011, 2014), and teaching assistantships (2010, 2014, 2015, 2016) from the ASU Physics department. I am grateful for additional funding provided by a grant from the National Institute of Health (NIH R01HL107539, PI: Robert Ros and Tatiana Ugarova).

TABLE OF CONTENTS

Page

CHAPTER Page

LIST OF TABLES

Table Page

LIST OF FIGURES

Figure Page

Figure Page

LIST OF ABBREVIATIONS

AC ..... acid cleaned

AFM ..... atomic force microscope

BSA ..... bovine serum albumin

CLEM ..... correlated light and electron microscopy

ConA ..... Concanavalin A

dSTORM ..... direct stochastic optical reconstruction microscopy

ECM ..... extra cellular matrix

FA ..... focal adhesion

FAC ..... focal adhesion complex

FAK ..... focal adhesion kinase

FD ..... fluorodish

Fg ..... fibrinogen

Fn ..... fibrin

HBSS ..... hanks balanced salt solution

HEK ..... human embryonic kidney

ICAM-1 ..... intercellular adhesion molecule 1

mAb ..... mono-clonal anti-body

MPRF ..... most probable rupture force

MGC ..... multinucleated giant cell

P ..... paraffin

PC ..... plasma cleaned

PET ..... polyethylene terephthalate

PPACK ..... D-phenylalanyl-Lprolyl-L-arginine chloromethyl ketone

PTFE ..... polytetrafluoroethylene

SCFS ..... single cell force spectroscopy

SEM ..... scanning electron microscopy

SMFS ..... single molecule force spectroscopy

TIRFM ..... total internal reflection fluorescent microscopy

PBS ..... phosphate buffered saline

1. Introduction

The word “cells” was coined by Robert Hooke in his book *Micrographia* or *Some Physiological Descriptions of Minute Bodies Made by Magnifying Glasses with Observations and Inquiries Thereupon* published in January of 1665 as one of the first major publications of the Royal Society. Hooke observed dozens of forms of life under his microscope, but when he observed a slice of a “good clear piece of Cork” he noticed irregular pores that constituted the body of the cork. He called these pores cells because they reminded him of honeycomb. Later, Antonie van Leeuwenhook contributed more observations regarding single celled organisms and the nature of many animal tissues with his uniquely powerful microscopes for the time. In the 1800s it was proposed that all life was made out of some combination of cells.

While Robert Hooke was making his important observations on the microscopic world, he was also discovering a very fundamental law in the field of mechanics. In 1678 he published the solution to an anagram he had made as “Ut tensio, sic vis” meaning “As the extension, so the force.” This is what we now call Hooke’s Law, and is typically expressed in the formula

$$F = kx \tag{1}$$

where F is the force needed to compress or extend a spring by the distance x. k then is a material property of the spring called the spring constant. This law is at the foundation of being able to quantify the adhesion forces of cells to substrates in this dissertation as the operating principle of force spectroscopy, the basic law that is used in all AFM experiments, and the mathematical basis for elasticity models of materials. In *Micrographia*, Hooke expressed curiosity about whether or not there were yet smaller

units of matter that connected cells together, and allowed nutrients to pass between cells. He said that perhaps someday "some diligent Observer, if help'd with better *Microscopes*, may in time detect" the small machines of nature that connect cells. This dissertation is the results of a diligent observer using better microscopes to probe the mechanics of the interconnecting molecules between cells and their environment.

Recent studies have been focusing on quantifying and modeling both the complex interplay between a cell and its environment and the internal dynamic processes within the interior of the cell [1]. This is a challenging prospect because of the non-equilibrium nature of biological systems [2]. Tools that have become established methods for understanding material science and fundamental physics phenomena are now being put to use to tackle these fundamental biological problems in order to form a more complete understanding of the basic processes of life. One tool that has been increasing the insight into biological processes is the AFM. With it's abilities to image topography [3], measure the mechanical stiffness and viscocity of biomaterials [4], quantify the adhesion of biomolocules [5], and manipulate the microenvironment of cells [6] the AFM is providing insights into fundamental issues of cell biology.

In this dissertation I present techniques for using the AFM in order to address some basic biological principles about cells and their interaction with their environment. A review of the basic biological systems studied will be given in §2 as well as a review of the AFM and various techniques used to investigate those systems.

§3, §4, §5, and §6 are different studies of how the extracellular protein, fibrinogen, is able to act as an anti-adhesive agent for biomaterials and thrombi. §3 studies directly the adhesion of cells to certain biomaterials coated with different

concentrations of fibrinogen. §4 describes a novel method for combining total internal reflection fluorescent microscopy with AFM SCFS to determine the extensibility of a fibrinogen matrix, and a cell's ability to remove fibrinogen molecules from the matrix. §5 gives detailed analysis of data from AFM SCFS experiments of cells on different concentrations of fibrinogen in attempt to provide a framework for uncovering single molecule data from SCFS experiments. §6 is a study measuring the adhesion of single platelets and neutrophils to fibrin gels with and without fibrinogen coating to understand the basic processes of thrombus formation during vascular wound healing. In §7 a novel glass technology is proposed which promotes the fusion of macrophages. SCFS of macrophage cells and HEK Mac-1 cells on the glass correlates adhesion with the fusion process. The appendix to this dissertation includes a published study using AFM microrheology experiments quantifying the elastic modulus of different hydrogel based biomaterials.

2. Background

2.1 Biological Background

2.1.1 Cells

Cells are the smallest self-reproducing unit of life, and they contain all the genetic codes for a living organism. They are broadly categorized into two basic types: prokaryotic cells and eukaryotic cells. Prokaryotic cells are organisms lacking any major organelles usually consisting only of a single cell. There are two domains of prokaryotic cells: Achaea and Bacteria. The focus of this work is on eukaryotic cells, which are cells with distinct organelles, especially a nucleus containing the cell's nuclear DNA.

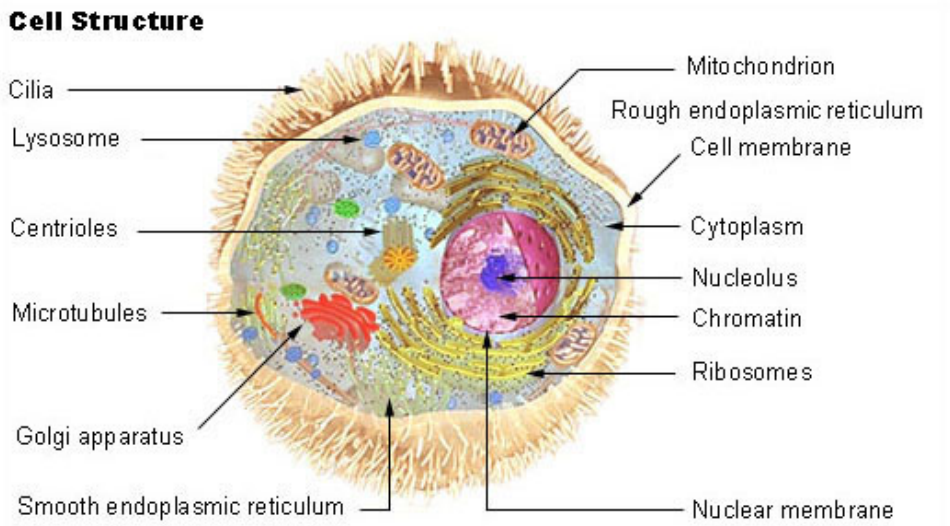

Figure 2.1 Illustration of a cell from Wikimedia commons [7]

Cells are able to respond to stimuli from their environment, and adjust their structure accordingly. In mammalian cells, the integrity of the cell's structure and shape is primarily determined by the cell cytoskeleton; a network of actin filaments, intermediate filaments, and microtubules. The greatest contributors to the mechanical

strength of a mammalian cell are the actin network, often referred to as the actin cortex, and the cell nucleus. The actin cortex of the cell is connected to the extracellular matrix (ECM) via integrins that pass through the cell membrane [8]. The secretion of extracellular molecules into the space surrounding a cell creates the ECM. These molecules form different types of material, which provide structural and biochemical support for the surrounding cells. Examples of ECM in animals include basement membranes, gels of polysaccharides and fibrous proteins such as collagen, and bone minerals [8]. Proteins on the cell membrane, such as cadherins, connect cells to each other providing communication between cells, and forming tissues. The interplay between the cell cytoskeleton, the plasma membrane, transmembrane integrins, and the ECM is complex, and vital to cellular processes that regulate a cell's function in its environment. This dissertation provides experimental procedures, results, and insights into specific systems involved in this process.

2.1.2 The Plasma Membrane

The outside layer of the cell is called the plasma membrane. It is a lipid bilayer approximately 6nm thick, and decorated with various surface proteins, transmembrane proteins, and polysaccharides. The phospholipids that constitute the lipid membrane have polar head groups with hydrophobic tails. There are various models that describe the plasma membrane, but the dominant model for the past 40 years has been the fluid mosaic model first proposed in 1972 by Singer and Nicolson [9]. The fluid mosaic model posits that the lipid bilayer of cell membranes can be considered a two dimensional fluid, and that proteins and carbohydrates are arranged randomly over a long range (> 200 nm).

Proteins and lipids in the membrane undergo translational diffusion at rates determined by the viscosity of the lipids.

While the basic idea of the fluid mosaic model, that of a two dimensional fluid, is still useful, today, many corrections to the model have needed to be made to account for various experimental results [10]. There appears to be some restrictions to the diffusion of integral proteins within the lipid membrane [11]. Some ideas put forward to explain the restriction in lateral diffusion sometimes observed include lipid rafts, ordered protein complexes, and cytoskeletal fences [12].

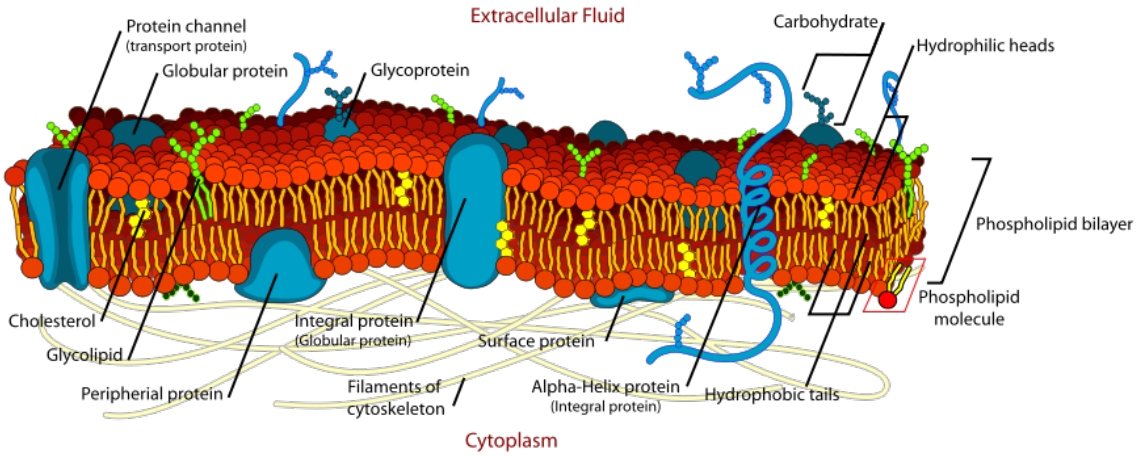

Figure 2.2 Illustration of cellular membrane based on the FMM from Wikimedia commons [13]

It is through the plasma membrane that cells communicate and sense their environment. There are several ways in which cells are able to communicate with their environment. This communication or signaling takes place via transmembrane protein receptors throughout the cell membrane. There are several varieties of signal proteins, such as ion channel receptors, enzyme receptors, G protein-coupled receptors, and

adhesion proteins [8]. They interact with extracellular molecules such as hormones, neurotransmitters, cytokines, growth factors, cell adhesion molecules, or nutrients [8]. This dissertation focuses on a type of adhesion protein known as integrins. The fluid nature of the cell membrane allows for cell adhesion proteins to cluster into focal adhesion complexes (FAC) that are critical anchor points for the cell cytoskeleton. These FAC allow for information from the ECM to be transmitted into the cell. The formations of FAC are the primary drivers of cell motility [14].

2.1.3 Adhesion Proteins

Cellular adhesion molecules (CAMs) are grouped into 4 families of proteins: Immunoglobulin superfamily, integrins, cadherins, and selectins. They are involved in several cell processes such as cell migration, cell differentiation, embryogenisis, cancer metastasis, cell growth, and also cell signaling [15].

Integrins are transmembrane protein heterodimers consisting of an α and β subunit. Each subunit has a large extracellular domain, a single spanning trasmembrane domain, and a short cytoplasmic domain (Figure 2.3). Integrins mediate cell-cell, cell-ECM, and cell pathogen interactions. They are critical for the immune system in leukocyte trafficking, migration, and phagocytosis [16]. Integrins are also vital for signal transduction from the ECM to the cell, and have been shown to be mechanosensors of the extracellular environment [17]. Signaling through integrins occurs bidirectionally. When intracellular proteins bind to the short cytoplasmic tails of integrins it induces an opening up of the ligand binding site in the extracellular domain in a process known as inside-out signaling. Similarly, ligand binding is capable of transducing signals from the extracellular matrix to the cytoplasm of the cell in a process known as outside-in

signaling [18]. This signaling in both directions serves to integrate the extracellular and intracellular environments, hence the name 'integrins,' by linking extracellular ligands to cytoskeletal components and signaling molecules inside the cell. Activation of integrins is associated with a number signaling molecules that serve to form a focal adhesion complex that can drive cell motility, cell morphology, and deformation of the ECM. Further review of integrins role in the formation of focal adhesions and consequently cell signaling and motility can be found in §2.1.6.

This dissertation focuses on one type of integrin important to the immune system, the $\alpha_M\beta_2$ integrin that is found exclusively on leukocytes in mammals.

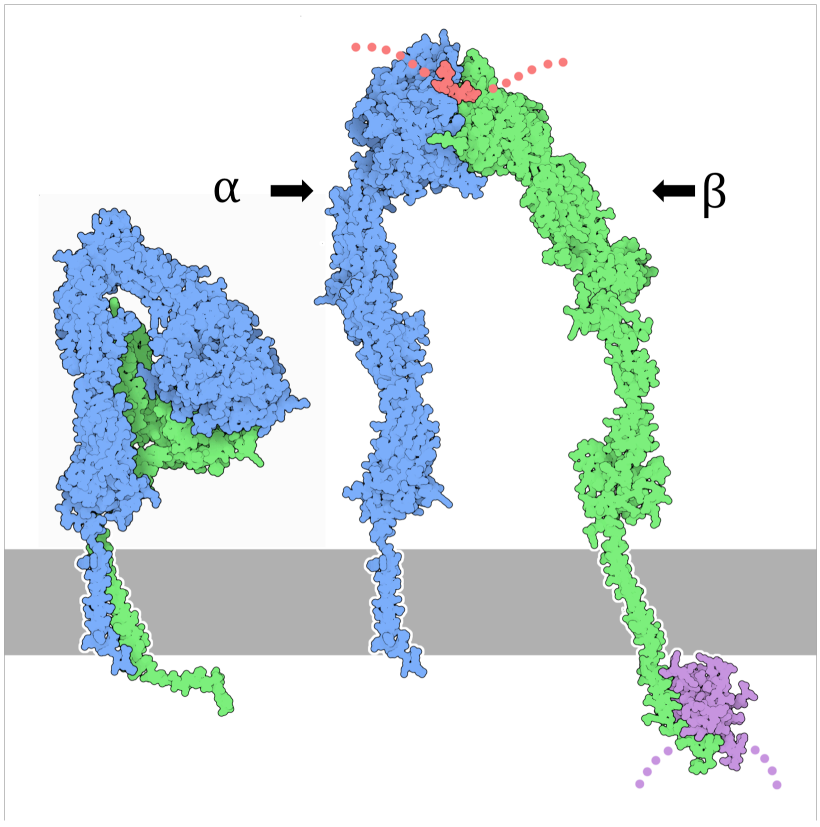

Figure 2.3 An illustration of a typical integrin from crystallography data. Image from Protein Public Data Base's "Molecule of the Month" series [19].

2.1.4 $\alpha_M\beta_2$ Integrins

$\alpha_M\beta_2$ (Mac-1) Integrins regulate important functions including adhesion, migration, proteolysis, phagocytosis, oxidative burst, and signaling [20-22]. Mac-1 is an important integrin that makes recruitment of leukocytes to vascular damage sites possible, and, in turn contributes to inflammation and the progression of atherosclerosis [23]. This integrin also plays an important role in host defense, and can cause rejection of transplants [22]. Mac-1 is also well known to be the most promiscuous in terms of its capacity to recognize multiple ligands of the β_2 subfamily of integrins [24]. The I-domain of the α sub-unit acts as the primary ligand recognition site for Mac-1 integrins [25]. Fibrinogen is one of the many known ligands capable of binding to Mac-1.

2.1.5 Fibrinogen

Fibrinogen is the third most abundant protein in human blood. It is a 340 kDa glycoprotein with a symmetrical dimeric structure consisting of two sets of three polypeptide chains: Aα (610 residues), Bβ (461 residues) and γ (411residues). It is normally found at a concentration of 2-4 mg/ml in circulation. Fibrinogen is the precursor to fibrin, which is the essential protein in blood coagulation during wound healing [26]. A thorough review of fibrinogen structure, and the process of forming fibrin networks from fibrinogen has been given by Doolittle [27]. The αC domain of fibrinogen is critical for the formation of the fibrin mesh that leads to blood clotting [28]. Although fibrin is the well known protein involved in platelet activation during thrombus formation, it has been shown that fibrinogen coated surfaces can lead to platelet activation and leukocyte

adhesion via outside-in signaling as well [29].

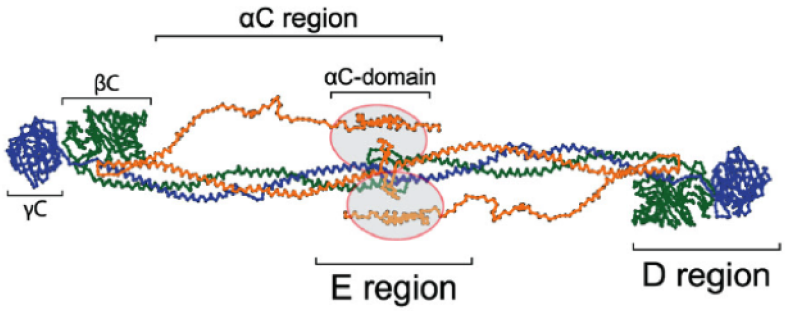

Figure 2.4 An Illustration of the fibrinogen protein based on its crystal structure [30].

Because of its high concentration in the blood and its known ability to support integrin-mediated adhesion of platelets and leukocytes, fibrinogen absorption has been studied extensively to understand the process of thrombus formation, inflammation, and vascular graft failure [28, 31, 32]. Complications in the formation of thrombus during wound healing can lead to unwanted blood clots. Because of fibrinogen's involvement in thrombus formation, it has been investigated seriously as a primary factor in cardiovascular diseases [32].

Recently it has been shown that fibrinogen is only highly adhesive when it is at low surface density on various substrates [29, 33]. High concentrations of fibrinogen leads to the creation of non-adhesive surfaces [34]. Fibrinogen has been shown to form a multi-layered matrix on mica surfaces, and it was shown that the formation of this multilayer is due to the disassociation of αC chains from the central E domain of the fibrinogen molecule upon absorption to the surface [35]. These free αC chains are then able to bind with the E domain, or some other portion of the fibrinogen molecule, in the

next higher layer. Yermolenko et. al. were able to show that this fibrinogen matrix consists of 7-8 molecular layers of fibrinogen with an average matrix height of 7.5 ± 0.6 nm [35]. It has been suggested that this non-adhesive feature of high concentrations of fibrinogen on the vascular surface is the final step of hemostasis, critical for complete wound healing, and is in fact necessary to stop uncontrolled thrombus formation [33]. The mechanism behind the non-adhesive property of multilayerd fibrinogen is poorly understood, and is one of the central topics of this dissertation.

2.1.6 Signal Transduction

Activation of Mac-1 integrins initiates several intracellular signaling events that regulate many responses in leukocytes such as adhesion, migration, apoptosis, and aggregation [21, 24]. Mac-1 integrins binding to immobilized ligands leads to the formation of intracellelular structures such as focal complexes and focal adhesions [22, 36-38]. The primary anchors for cell locomotion in 2D are focal adhesions [14]. FAs contain a plethora of cytoplasmic signaling and structural proteins including talin, paxilin, vinculin, filamin, and α-actinin that all begin to be activated when integrins bind to ligands, and begin clustering into large supramolecular complexes. The molecular structure of focal adhesions has been reviewed by Jokusch et al. [39]. The focal adhesions are spear like projections up to 10 μm long and 0.5 μm wide. The cytoplasmic face of the focal adhesions contain microbundles of actin filaments connected to integrin molecules via talin vinculin, alpha-actaninin, or paxillin.

Assembly and disassembly of focal adhesions is controlled by focal adhesion kinase, a type of tyrosine kinase that regulates Rho-family GTPases [40]. The interplay and dynamics of focal adhesion formation is a complex process, and it is known that

GTPases act as a molecular "switch" that controls the formation and disassembly of actin cytoskeletal structures within the cell [40]. Experiments have also shown that FA sites are able to grow linearly in response to mechanical tension maintaining an intracellular stress of 5.5 nN/μm^2 on micropatterned substrates [41]. This mechanically induced activation is thought to be one way mechanical signals are transduced into chemical signals within the cell leading to regulation of cell function and gene expression [42].

The activation of GTPases, and subsequent actin polymerization or disassembly is one method of 2D locomotion [8]. Another method is the generation of contractile force by myosin II on actin filaments bound to FACs. Figure 2.5 shows frames from a live fluorescent video of an Alexa-647 actin labeled fibroblast cell contracting. Focal adhesions on the leading edge of the cell anchor the cell in place while focal adhesions in the tail disassemble. Myosin II causes the cell to contract, and a new leading edge of the cell will polymerize.

Notably, FAC have mostly been observed in 2D cell culture, and not in 3D cellular environments [15]. Interest in the role of FA associated proteins in 3D environments has developed a lot of excitement because FA associated proteins, such as focal adhesion kinase (FAK), are expressed at elevated levels in malignant cancers [43]. However, the research in this dissertation deals mainly with the response of leukocytes to planar environments. It has been proposed that formation of FAs on 2D surfaces is in response to an apparent wound environment [14].

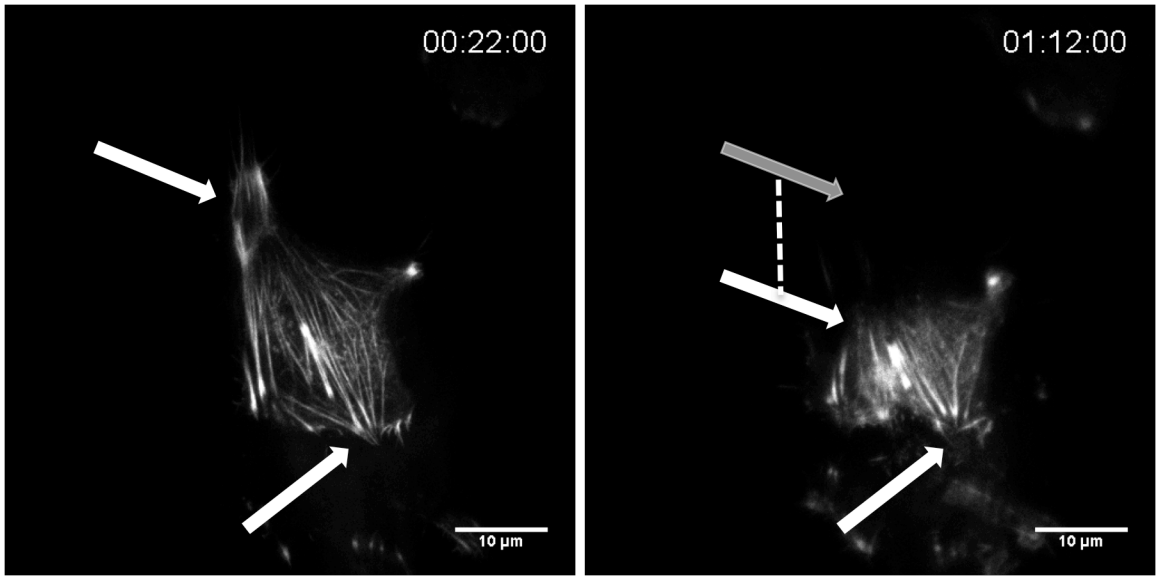

Figure 2.5 An example of cell contractility. The fluorescently labeled actin cytoskeleton has formed stress fibers that span the cell. The actin filaments are anchored in focal adhesion sites in the lower part of the cell. Focal adhesion in the upper tail of the cell are disassembled, and myosin II proteins contract the cell toward the anchored portion.

2.2 Single Cell Force Spectroscopy

2.2.1 AFM Based SCFS

Cell adhesion is a vital regulator of several biological processes in multi-cellular organisms such as embryonic development [44], blood cell interactions with vascular walls [45], mechanosenitivity [46], and mechanochemical processes [47].

Several different methods including: AFM, magnetic tweezers, optical tweezers, micropipettes, and a biomembrane force probe can be used for measuring the adhesion of a cell to another cell or a cell to a substrate. A review of the advantages and disadvantages of various SCFS techniques was given by Taubenberger et al. [48]. Table 1 shows the major points from the review. These techniques all measure the detachment

force of a probe that has been in contact with a cell. Often times a cell itself will be used as a probe to identify detachment forces from various substrates. Of all these techniques, AFM based SCFS provides for measurement with the largest range of forces (10 pN to >1000 nN).

Table 2.1 Comparing SCFS methods [48]

SCFS Method	Measurement Range	Pro	Contra
AFM-SCFS	10 pN to >100 nN	• High force resolution • Good Control of contact conditions • Large range of applicable forces • Commercially available	• Time and cost intensive
Magnetic tweezers	10 – 200 pN	• Combination with optics • High force resolution	• Restricted to low detachment forces
Optical tweezers	0.1 – 100 pN	High force resolution	• Difficult experimental setup • Restricted to low detachment forces
Micropipettes	> 1 nN		• Low force resolution • Cell morphology changes by aspiration
Biomembrane force probe	0.1 – 1 nN	• High force resolution • Good temporal control	• Cell morphology changes by aspiration

Optical and magnetic tweezers are capable of providing better force sensitivity, however they are limited to measuring weak adhesion forces that occur in short contact times. For the purpose of measuring the forces of adhesion involved with a whole cell, an AFM based approach seems the most advantageous. AFMs have been used extensively to conduct single molecule force spectroscopy experiments that have explored the folding, conformational entropy, mobility, assembly, and functionalities of purified biomolecules [5, 49-51], These SMFS experiments have helped to substantiate models of the dynamics of molecular adhesion bonds; most notably the model put forth by Bell, Evans, and Ritchie [52] that will be discussed in more depth in §2.2.5.

Researchers would like to be able to measure the biomolecular machinery of cells within their native cellular environments and verify whether the models of molecular adhesion put forth to explain the adhesion of purified biomolecules hold true when those biomolecules are in the cell membrane. Dufrene et al. have proposed that there are five challenges to bringing SMFS into living cells [2]. These challenges are: 1. Defining and overcoming the limitations of current tools. 2. Establishing standards and improving data quality. 3. Developing ways to treat and interpret complex data. 4. Improving data statistics and analysis. 5. Sensing multiple parameters simultaneously. These challenges deal directly with probing molecular machinery inside a living cell. Many of these challenges are overcome in SCFS for probing the molecular machinery of biomolecules on the surface of the cell, or that transverse the cell membrane, e.g. integrins. §6 details my attempt at providing better data quality, interpreting complex data, and improving data statistics and analysis for understanding the Mac-1 fibrinogen interaction.

2.2.2 AFM Description and Instrumentation

The atomic force microscope was developed in 1986 by Binnig, Quate, and Gerber [53], and was based on the previous invention of the scanning tunneling microscope(STM) [54] invented in 1981 for which Binnig and Rohrer received the Nobel prize. The AFM was developed in order to measure topographical features at the atomic scale of non-conductive materials that could not be imaged by the STM, which operated on the basis of conduction. In the decades since its invention, the AFM has developed several technological improvements for ease of use and versatility.

There are three main components of any AFM instrument: a cantilever best suited for the experiment in question, a piezoelectric scanning apparatus (either via the AFM head or sample stage), and a detection system for monitoring the bending of the cantilever. Originally, the detection system was a STM atop the AFM cantilever, but most modern AFM instruments today use an optical lever type detection system with a photodiode [55]. For this method, a laser is focused onto and reflected off the back side of the cantilever and onto a photodiode. The photodiode monitors the deflection of the cantilever as it scans over the sample in a raster-like manner.

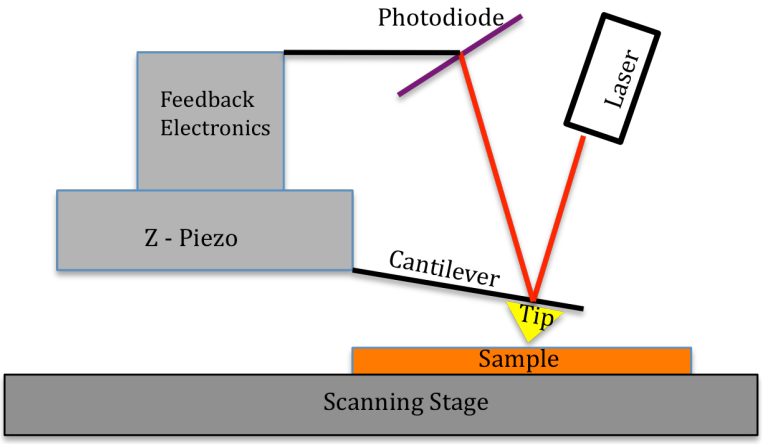

Figure 2.6 A sketch of a basic AFM set up.

The deflection of the cantilever detected by the photodiode is fed into a feedback system, which controls the z-position of the piezoelectric scanner. This system works to minimize the difference between a user defined set-point and the deflection signal monitored by the photodiode by adjusting the z-position of piezoelectric scanner after receiving information from the photodiode. This effectively keeps the distance between the tip and the sample constant, and is known as "constant force mode." The z-position of the scanner is recorded as the sample is scanned and used to build up a topographical map of the surface. Alternatively, the z-position of the cantilever can be held constant, and the deflection of the cantilever can be monitored without a feedback loop to adjust the height of the cantilever. This technique builds an image from the deflection of the cantilever, and is called "constant height mode." Another imaging mode is known as "AC mode" or "tapping mode." In AC mode, the cantilever is oscillated near the resonant frequency. Forces near the sample surface, such as van der Waals forces, can attract or repel the cantilever, decreasing or increasing the resonance frequency of the cantilever. A feedback loop allows the AFM to keep the oscillation amplitude or frequency constant, and this

keeps distance between the tip and the sample constant while the sample is scanned [56]. One of the advantages of using AC mode is that it decreases the likely hood of damaging the AFM tip. AC mode also ensures less interference from lateral forces, and minimizes the effect of strong surface forces such as capillary forces. This is the primary method that is used to generate topography images with the AFM in ambient conditions, and helps to protect soft biological samples from damage.

While making topographical images of surfaces on the nanoscale has proven to be an incredibly useful application of the AFM, it is not the only experimental technique that can be employed with the instrument. The major use of an AFM in this dissertation is for single cell force spectroscopy (SCFS) experiments. §2.2.5 - §2.2.7 will give the background for SCFS and SMFS experiments. Besides imaging, SCFS, and SMFS experiments, the AFM can be used for nanoindentation experiments or microrheology experiments for determining mechanical characteristics of materials.

2.2.3 Cantilever Functionalization and Calibration

AFM cantilevers today can be manufactured into a plethora of geometries from very sharp tips on the order of < 5 nm radius of curvature to relatively large beads (> 10 μm diameter) attached to the end of the cantilever. The tip geometry is an important parameter when performing microrheology to determine the elastic modulus of materials. Because of manufacturers ability to precisely control the geometry of tips, careful consideration should be made in deciding which type of probe would be suitable for a given application. Different mathematical models are used for different tip geometries [57], but these models are all based on modified Hertzian mechanics [58]. The mechanics for determining the Young's modulus of materials will be explained more in §2.2.3.

Another crucial parameter of AFM cantilevers is the spring constant or force constant. When measuring the elastic modulus of the sample or the adhesion to the sample it is assumed that the cantilever behaves as a Hookean spring and follows the form:

$$F = kd \tag{2.1}$$

where F is the force felt by the cantilever, k is the spring constant, and d is the cantilever deflection distance. Determining k is not a trivial matter when it comes to AFM cantilevers, and there are multiple methods to determine the spring constant.

One widely used method for determining k is the thermal tuning method [59, 60]. This method is based on the equipartition theorem:

$$\frac{1}{2}k\langle z^2\rangle = \frac{1}{2}k_B T \tag{2.2}$$

where k_B is Boltzmann's constant, T is temperature, and $\langle z^2 \rangle$ is the mean square deflection of the cantilever caused by thermal vibrations. In order to perform this method, cantilever oscillations caused by Brownian motion are monitored to determine the power spectrum. By fitting a Lorentzian to the power spectrum one is able to calculate $\langle z^2 \rangle$ if the optical lever sensitivity is known [60]. Determining the optical lever sensitivity is done by indenting the probe tip onto a rigid surface to generate a z-piezo versus photo-diode voltage curve, and then taking the slope of a linear fit of the data to be the inverses of the optical lever sensitivity. Several factors in this method including the nature of laser spot used in the optical lever system in relation to the size of the cantilever, and assumptions in the mathematical modeling causes a ~15% systematic error for cantilever spring constant [61].

Another method for determining the spring constant of rectangular cantilevers is the Sader method [62]. The Sader method uses the equation:

$$k = \frac{\pi}{16}\rho w^2 l Q \omega^2{}_R \Gamma''\left(\omega_R\right) \tag{2.3}$$

in order to determine the spring constant. The parameters *w* and *l* are the width and length of the cantilever respectively, and are usually provided by the manufacturer with very high precision. *Q* and ω_R are the quality factor and radial resonant frequency determined by fitting the resonance curve of the cantilever in air with a Lorenzian. $\Gamma''(\omega_R)$ is the imaginary part of the hydrodynamic function evaluated at the resonant frequency in a medium of density ρ. Although, this is the equation for a rectangular cantilever, the Sader method has been developed for other cantilever shapes as well [63].

Determining the spring constants of cantilevers is one of the greatest sources of uncertainty in force spectroscopy measurements, and is therefore an active area of research in the field of AFM. All cantilever calibrations in this work have been done using the thermal tuning method.

Cantilevers involved in SCFS experiments need to be functionalized in order to have cells bind to the cantilever. This is done by decorating the cantilever with some kind of ligand that a cell has a strong affinity for. These can be proteins specific to a cell type, or a protein that is known to bind universally to cells such as fibronectin, collagen, or some kind of lectin. The experiments in this dissertation use the lectin Concavilin A (ConA) which is known to bind to many sugars, glycoproteins, and glycolipids found on the membrane of cells [64]. The details of the ConA functionalization procedure will be

given for each experiment. It is assumed that decorating the cantilevers with various proteins or organic molecules has negligible effect on the physical properties of the cantilever [65].

2.2.4 Force-Distance Curves

Once the spring constant of an AFM cantilever is known, it can be used to measure the stiffness and adhesion to different materials. Figure 2.7 details the procedure of generating a force distance curve via an AFM. Because the spring constant of the cantilever is known, the deflection data read out by the photodiode can be converted into a force measurement. Data from the indentation portion of the force-distance curve (III in Figure 2.7) can be fit using the different models to obtain the elastic modulus or Young's modulus of the material. Lee, Lindsay, and Lees demonstrated the use of an AFM to measure the elasticity of biomaterials in 1992 using a model known as the Sneddon model [66, 67]. The type of model used to determine the Young's modulus of the material depends on the geometry of the indenter or AFM tip. Data from the retraction portion of the force-distance curve (IV & V in Figure 2.7) can also be modeled using worm-like chain model or the freely jointed chain model [5, 68, 69]. In this dissertation, the retraction portion of force-distance curves will be analyzed for adhesion forces.

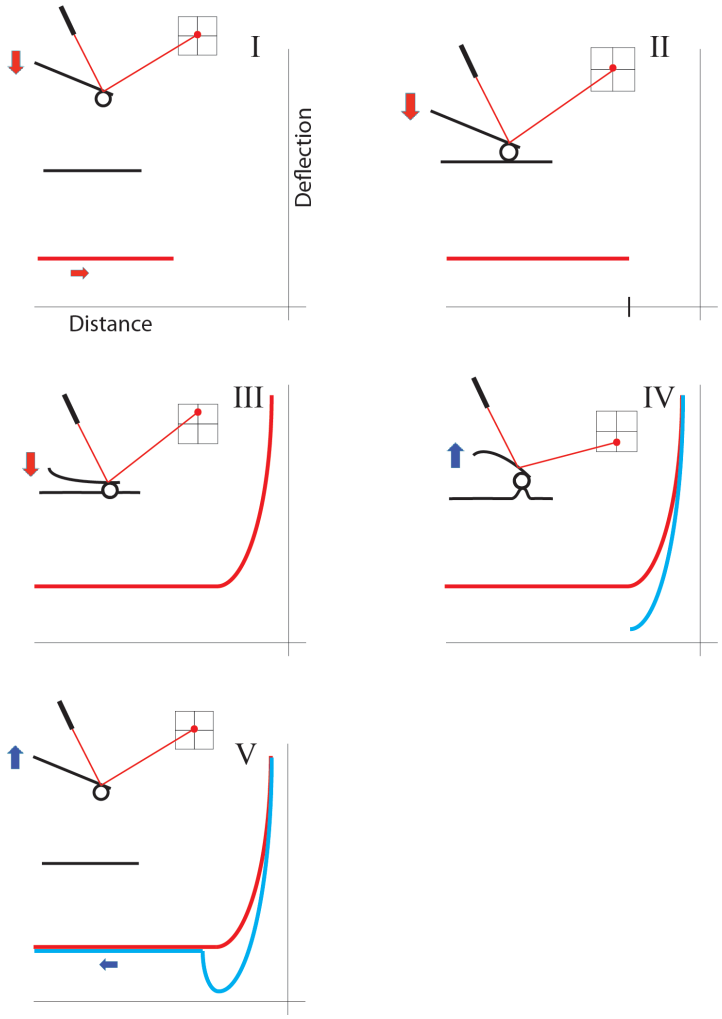

Figure 2.7 An illustration of a typical force curve cycle. I) the AFM cantilever approaches the surface. II) the cantilever comes in contact with the surface. III) the probe indents a defined distance into the surface or until the deflection reaches a defined set point. IV) the probe is withdrawn from the surface. The probe can adhere to the substrate causing a change in the deflection until the probe reaches some maximum adhesion point. V) the probe is completely withdrawn from the surface.

The papers given in the appendix contains some experimental results characterizing the ECM using the Briscoe model of contact mechanics. A brief explanation will be given of the Briscoe model, and how to apply it to AFM force-distance curves to determine the elastic modulus of materials, but the bulk of this

dissertation will deal with analyzing the adhesion data obtained from force distance curves. Models like the worm-like chain model offer insight into the persistence length of biopolymers such as DNA, but this dissertation deals mostly with the interaction of integrins with ligands, and so a review of the thermodynamically driven model for single molecule bond ruptures put forth by Ritchie and Evans will be given. A model proposed by Dudko et al. will also be reviewed, which deals with the same thermodynamics the Ritchie and Evans use, but makes no assumptions on the underlying energy landscape of the integrin ligand bond.

2.2.5 AFM Microrheology

The foundation for contact mechanics was laid by Hertz in 1882 to understand the stress response of optics lenses [58]. Since that time many models have been proposed to explain how materials will deform based on different indenter geometries. This is assuming that the indenter elastic modulus is much greater than that of the material. There are other assumptions that must be made for Hertzian contact mechanics and including: strains are within the elastic limit, the materials are homogenous, the material is an infinite half space, and the surfaces are frictionless and nonadhesive. For biological soft matter materials almost all of the assumptions are not valid. For a spherical indenter, the Hertz model gives the relation of indentation depth to a given applied force as:

$$F = \frac{4}{3}\frac{E}{\left(1-\upsilon^2\right)}\sqrt{R\delta^3} \tag{2.4}$$

where F is the applied force, E is the elastic modulus, υ is the Poisson ratio of the material (a typical assumption for the Poisson ratio of biomaterials is 0.5), R is the radius of the spherical indenter, and δ is the indentation depth.

A critical parameter of Hertzian contact mechanics is the contact area between the indenter and the sample. In AFM microrheology, this is a difficult parameter to account for, and it is known that if the sample is noticeably adhesive, then the contact area can change dramatically, and cause significant errors in the Hertzian model of contact mechanics [70-72]. There have been some models to account for adhesive materials such as the Johnson-Kendall-Roberts model, best suited for soft materials using a relatively large radius indenter [70, 73], and the Derjaguin-Muller-Toporov model, best suited hard materials with a relatively small radius indenter [71, 73]. A more precise parameter for determining when to use the JKR model or the DMT model is known as the Tabor coefficient, and is given by:

$$\mu \approx \left[\frac{R(\Delta\gamma)^2}{E^{*2} z_0^3} \right]^{1/3} \tag{2.5}$$

Where R is the indenter radius, $\Delta\gamma$ is the work of adhesion , E^* is the effective elastic modulus, and z_0 is the equilibrium separation between the two contact surfaces. These parameters are not easy to determine *a priori* of any knowledge of the material because it depends on surface forces, surface roughness, and the mechanical properties of the materials involved [74]. For large values of μ, the JKR model is best suited, and the DMT model is more appropriate for small values of μ.

Despite the flawed assumptions in Hertzian mechanics, it is still used as the foundational model for the determination of elastic modulus of biomaterials today [75].

For the results in the appendix of this dissertation, the indenter geometry of a conical large radius AFM tip is approximated to that of a parabola that transitions to a cone at some given point. Briscoe derived a model for this type of tip [57], but it does not present the relationship between applied force and indentation depth in a simple closed manner. Rather, a solution for the contact area and indentation depth must be solved numerically before the elastic modulus can be determined.

A piecewise depth-dependent linearized regression method for determining the Young's modulus for small segments of the indentation portion of the force-distance curve was developed by Guo and Akhremitchev [76]. This method was applied by Fuhrmann et al. for determining the Young's modulus of cells [77]. This method works by considering the change in force with respect to indentation depth:

$$\Delta F(\delta) = \frac{E}{\left(1-\upsilon^2\right)}\Delta\lambda(\delta) \tag{2.6}$$

where the function λ describes the contact area between the indenter and material, and is based on the geometry of the indenter. λ is an exact power law function for a parabolic and conical indenters, but for other geometries, such as a sphere-cone, must be approximated as a power law function for small piecewise portions of data [76, 77]:

$$\Delta\lambda(\delta) \rightarrow A\Delta\delta^B \tag{2.7}$$

After determining the exponent in the power law, the force can be linearized by

$$\Delta F^{1/B}(\delta) = \left[\frac{EA}{\left(1-\upsilon^2\right)}\right]^{1/B}\Delta\delta \tag{2.8}$$

Finding the slope of F with respect to δ will produce a constant value

$$\frac{\Delta F^{1/B}(\delta)}{\Delta\delta} = \left[\frac{EA}{\left(1-\upsilon^2\right)}\right]^{1/B} = C \tag{2.9}$$

The Young's modulus of a small piecewise segment of indentation data can then be approximated as

$$E = \frac{C^B\left(1-\upsilon^2\right)}{A} \tag{2.10}$$

2.2.6 Statistical Modeling of Adhesion Data

Analyzing the indentation portion of a force-distance curve determines the elastic modulus of a material, however a force-distance curve can also provide adhesion data of the material. In this dissertation, the primary adhesion data will be from SCFS experiments attempting to elucidate information regarding the binding force of integrin-ligand bonds. These bonds disassociate under an externally applied force provided by the AFM cantilever. Rather than these bonds reaching some elastic limit, and breaking under mechanical failure, these disassociations are driven by thermal fluctuations according to classical rate theory [78].

The bonds between cell receptors and ligands can be described by classical reaction rate theory where a ligand L and a receptor R have their interactions governed by:

$$[L]+[R] \underset{k_{off}^0}{\overset{k_{on}^0}{\rightleftharpoons}} [L\cdot R] \tag{2.11}$$

where the brackets represent perspective concentrations of the free ligands L and receptors R as well as their associated product L·R. The disassociation constant K_D is the ratio of reactants to products:

$$\frac{[L][R]}{[L\cdot R]} = \frac{k_{off}^0}{k_{on}^0} = K_D \tag{2.12}$$

The free reaction enthalpy is given by the Gibbs free enthalpy at the end and initial state under constant temperature and pressure:

$$\Delta G = \Delta H - T\Delta S = G_2 - G_1 \tag{2.13}$$

where ΔH is the reaction enthalpy and ΔS is the entropy change of the system. Using the free standard enthalpy ΔG^0 equation (2.13) becomes:

$$\Delta G = \Delta G^0 - RT\ln K_D \tag{2.14}$$

where R is the molecular gas constant. The reaction enthalpy ΔG equals 0 in thermal equilibrium, and this then gives the standard free enthalpy of the disassociation process:

$$\Delta G^0 = RT\ln K_D \tag{2.15}$$

Arrhenious discovered the off-rate for a given potential barrier $\Delta G^{\neq}$ to be:

$$k_{off} \sim \exp\left[\frac{-\Delta G^{\neq}}{k_B T}\right] \tag{2.16}$$

where k_B is Boltzmann's constant and T the temperature. Models for understanding how the off-rate of ligands and receptors change under application of an external force in SMFS experiments were developed by Bell, Evans, and Ritchie [52, 79].

2.2.7 Ligand – Receptor Interactions Under an Applied Force

Bell proposed that disassociations under an externally applied force, f, occur as a result of an increase in the bond off-rate caused by application of mechanical energy to the bond according to the equation

$$k_{off}(f) = k_{off}^{0} \exp\left[\left(x_{\beta} f\right)/k_B T\right] \tag{2.17}$$

where k_{off}^{0} is the off-rate of the bond at $f = 0$, f is the applied force, and x_{β} is reaction length or disassociation length [79]. For a dynamic external force such as an increasing force applied by an AFM, the reaction kinetics are approximated as:

$$\frac{dp(t)}{dt} = -k_{off}\left(f(t)\right)p(t) \tag{2.18}$$

p(t) is the survival probability of the bond. Evans and Ritchie propose that *f(t)* incorporates the elastic mechanics of all components involved in the separation and depends on their total extension s = vt:

$$F(s) = F(v \cdot t) = f(t) \tag{2.19}$$

Evans and Ritchie also define a parameter known as the loading-rate *r* which is a combination of the effective spring constant κ_{eff} and the retraction velocity v such that

$$f(t) = \kappa_{eff} v \cdot t = r \cdot t \tag{2.20}$$

The formal solution of (2.18) gives the survival probability of a bond under an applied force:

$$p_v(f) = \exp\left\{-\frac{1}{v}\int_{f_{\min}}^{f} df' \frac{k_{off}(f')}{F'\left(F^{-1}(f')\right)}\right\} \tag{2.21}$$

where $p_v(f)=p(t)$ and $p(t=0)=p_v(f=f_{min})=1$. The variable f_{min} represents a minimum threshold where disassociation forces are indistinguishable from thermal fluctuations. The integral in (2.21) is possible under the assumption that x_β is constant and $f(t)=r\cdot t$:

$$p_v(f) = \exp\left\{-\frac{k_{off}}{v\kappa_{eff}} \frac{\exp\left(\frac{x_\beta f}{k_B T}\right) - \exp\left(\frac{x_\beta f_{\min}}{k_B T}\right)}{\frac{x_\beta}{k_B T}}\right\} \tag{2.22}$$

A most probable rupture force (MPRF) $\hat{F}$ can then be determined for a given loading rate using the maximum of the distribution $-dp_v(f)/df$ with (2.17) for the off rate. This gives:

$$\hat{F} = \frac{k_B T}{x_\beta} \ln\left(\frac{x_\beta r}{k_{off}^0 k_B T}\right) \tag{2.23}$$

the standard Bell, Evans, and Ritchie model, or simply Bell model [52]. The common approach to fitting data with the Bell model is to find the slope of the retraction portion of the force-distance curve data just before a rupture to determine r and subsequently $F(s)$. By plotting most probable rupture forces semi logarithmically versus loading rates, x_β

can be determined from the slope of a linear fit of the data, as well as a value for the off-rate from extrapolation the regression line to $\hat{F} = 0$.

Notable discrepancies have been observed between this standard theory and experimental SMFS data [80-82]. Some extensions of the Bell model have been proposed based on the assumption that x_β and k_{off}^0 are not constant, but follow some statistical distribution [82, 83]. Also, an approach by Ros et. al has been proposed to fit data preceding a rupture event with a second degree polynomial rather than a linear fit to determine *F(s)* and the subsequent loading rate. This method does not have a known solution for the integral in (2.12), but does provide for more accurate estimates for loading rates [82].

The critical assumption of the Evans and Ritchie model is that the off rate of single molecule bonds follows the Bell model in (2.17). This model assumes that the bond has a single potential energy well with some barrier with height ΔG_β that lowers linearly when an external force is applied to the bond. It is possible that the receptor - ligand interaction has more than one barrier [84], or the height does not respond linearly to an applied force [83]. In these cases, Dudko et al. derived an alternative approach for determining the most probable rupture force and kinetic parameters of receptor – ligand bonds [85, 86].

2.2.8 Dudko Method

Rather than assume a receptor – ligand bond follows the Bell model, and without the assumption of (2.20) that the loading rate is independent of force, Dudko et al. give

the solution of (2.18) using the probability distributions of rupture forces F which are related to the lifetimes by $p(F)dF = -p'(t)dt$ yielding

$$p(F) = \frac{k(F)}{\dot{F}(F)} \exp\left(-\int_0^F \left[\frac{k(f)}{\dot{F}(f)} \right] df \right) \tag{2.24}$$

Using $\tau(F) = 1/k(F)$, (2.24) can be readily inverted to solve for bond lifetimes in terms of rupture force distributions and loading rates:

$$\tau(F) = \int_F^\infty \frac{p(f)}{\left[\dot{F}(F) p(F) \right]} df \tag{2.25}$$

From this equation one can obtain an approximate relationship between the lifetime at a force equal to the mean rupture force and the variance of the rupture force distribution by setting F = <F> and approximating $p(F)$ by a normalized Gaussian distribution. Making these assumptions (2.25) gives [86]:

$$\tau(\langle F \rangle) \approx \frac{\left[\frac{\pi}{2} \left(\langle F^2 \rangle - \langle F \rangle^2 \right) \right]^{1/2}}{\dot{F}(\langle F \rangle)} \tag{2.26}$$

This formalism makes it possible to use loading rates that are dependent on the force itself, such as the worm-like chain model[86]. However, despite this advantage, the Dudko model relies on the assumption that the rupture force distributions for a given force and loading rate follow a normal distribution. The validity of this assumption is not thoroughly verified. Dudko suggested that an alternative relationship for bond lifetimes can be given by:

$$\tau\left(\langle F\rangle\right) \approx \frac{\frac{3}{4}\delta F}{\dot{F}\left(\langle F\rangle\right)} \tag{2.27}$$

where δF is the interquartile range of the rupture force distributions for a given loading rate. Indeed, Dudko suggests (2.27) actually provides a more robust approximation for the lifetimes of receptor – ligand bonds under an applied force.

This formalism suggests a simple approach for analyzing single receptor – ligand bonds. Using the rupture force histograms for a given range of loading rates, one can solve for $\tau(<F>)$. Dudko, Hummer, and Szabo showed that for several simple one-dimensional free-energy profiles, the lifetime $\tau(F)$ calculated from Kramers theory can be written as [78]

$$\tau(F) = \tau_0\left(1 - \frac{\nu F x_\beta}{\Delta G_\beta}\right)^{1-1/\nu} \exp\left[-\beta\Delta G_\beta\left(1 - \left(\frac{1-\nu F x_\beta}{\Delta G_\beta}\right)^{1/\nu}\right)\right] \tag{2.28}$$

This equation introduces a new parameter ν, which is a scaling factor that specifies the nature of the underlying free-energy profile [85]: $\nu = 1/2$ corresponds to a harmonic barrier with a cusp-like well; $\nu = 2/3$ corresponds to a potential that contains linear and cubic terms. This equation simplifies down to Bell's formula for the bond lifetime when $\nu = 1$. ΔG_β, x_β, and τ_0 are then fitting parameters for a plot of the $\tau(<F>)$ and the loading rate data. While this method holds the advantage of generality, the introduction of extra fitting parameters makes it difficult to determine the validity of results from experimental methods.

Both the Evans and Ritchie method and the Dudko method for SMFS analysis are used in §6 in an attempt to get receptor-ligand kinetics from SCFS experiments.

3. Fibrinogen Matrix Deposited on the Surface of Biomaterials Acts as a Natural Anti-Adhesive Coating

3.1 Acknowledgments

This chapter is a reprint of the paper; “Fibrinogen matrix deposited on the surface of biomaterials acts as a natural anti-adhesive coating,” by Roman Saroafiullin, Wayne Christenson, Hadil Owaynat, Ivan Yermolenko, Marsil K. Kadirov, Robert Ros, and Tatiana Ugarova published in *Biomaterials* volume 67 (2015) pp. 151-159. Tatiana Ugarova and Robert Ros were responsible for experiment design. Roman Saroafiullin, Hadil Owaynat, and myself were equally contributing first authors. I specifically handled analysis of the SCFS data as well as conducting the SCFS experiments. Roman Saroafiullin conducted the AFM tip adhesion experiments and analysis with help from Ivan Yermolenko. Hadil Owaynat conducted and analyzed the adhesion assay experiments with help from Marsil Kadirov. This work was supported by NIH grant HL107539 awarded to Tatiana P. Ugarova and Robert Ros. April Boone of Bard Peripheral Vascular Inc. provided ePTFE samples.

3.2 Abstract

Adsorption of fibrinogen on the luminal surface of biomaterials is a critical early event during the interaction of blood with implanted vascular graft prostheses which determines their thrombogenicity. We have recently identified a nanoscale process by which fibrinogen modifies the adhesive properties of various surfaces for platelets and leukocytes. In particular, adsorption of fibrinogen at low density promotes cell adhesion while its adsorption at high density results in the formation of an extensible multilayer

matrix, which dramatically reduces cell adhesion. It remains unknown whether deposition of fibrinogen on the surface of vascular graft materials produces this anti-adhesive effect. Using atomic force spectroscopy, single cell force spectroscopy, and standard adhesion assays with platelets and leukocytes, we have characterized the adhesive and physical properties of the contemporary biomaterials, before and after coating with fibrinogen. We found that uncoated PET, PTFE and ePTFE exhibited high adhesion forces developed between the AFM tip or cells and the surfaces. Adsorption of fibrinogen at the increasing concentrations progressively reduced adhesion forces, and at ≥2 mg/ml all surfaces were virtually nonadhesive. Standard adhesion assays performed with platelets and leukocytes confirmed this dependence. These results provide a better understanding of the molecular events underlying thrombogenicity of vascular grafts.

3.3 Introduction

It is widely recognized that after implantation, prosthetic vascular grafts spontaneously acquire a layer of adsorbed plasma proteins. Among them, fibrinogen has received the most attention because of its high concentration in the circulation (2-3 mg/ml), quick adsorption on various surfaces, and ability to support integrin-mediated adhesion of platelets and leukocytes. Since one of the primary graft failures is adhesion-dependent platelet activation and thrombus formation, fibrinogen is generally viewed as a culprit. Consequently, considerable research effort has been made to create nonfouling materials that resist protein adsorption and platelet adhesion (Reviewed in Refs. [87-89]). In addition, innumerable in vitro studies have focused on the mechanisms of fibrinogen adsorption in an attempt to understand its thrombogenic potential [[90-96] and references therein]. Paradoxically, other studies have focused on the design of anti-thrombogenic

vascular grafts utilizing fibrin(ogen)-coated surfaces with apparently beneficial results in animal studies and in humans [97-100].

Intact fibrinogen deposited on various surfaces is indeed adhesive for platelets and leukocytes, but only when adsorbed at certain concentrations and, especially, when cell adhesion is tested in buffers without fibrinogen [33, 101-104]. Furthermore, fibrin, a clotting product of fibrinogen, mediates strong adhesion of blood cells suspended in protein-free buffers [104-108]. From these in vitro observations, it is expected that fibrinogen, which is deposited early after vascular graft implantation, should support rapid accumulation of platelets. Likewise, fibrin, which is eventually formed and remains on the surface of grafts implanted in humans over the years, should promote platelet deposition and activation. This, in turn, would be expected to result in the continuous thrombus propagation and vascular occlusion. However, the flow surface of vascular grafts is highly thrombogenic only during the early postoperative period [109-111]. Subsequently, graft maturation results in a nonthrombogenic surface [111-113], which sustains its characteristic acellular appearance over the decades in spite of the presence of the stable fibrin lining [114-117]. These observations suggest the existence of natural anti-adhesive mechanisms operating on the flow surface of mature vascular graft prostheses that prevent the accumulation of blood cells. The crucial question as to why platelets adhere to fibrinogen deposited on the surface of vascular grafts early after implantation but not attach to the, likewise, highly adhesive fibrin present on mature grafts remains open.

In recent reports we described a new nanoscale phenomenon whereby adsorption of fibrinogen on various surfaces, including fibrin clots, dramatically reduces cell adhesion. In particular, we showed that the ability of fibrinogen to support cell adhesion strikingly depends on its coating concentration. Counterintuitively, while low-density fibrinogen is highly adhesive for platelets and leukocytes, its adsorption at the increasing concentrations reduces cell adhesion under both static and flow conditions [29, 33]. This effect is specific for fibrinogen since no other plasma proteins exhibit this unusual behavior [33]. The underlying mechanism by which fibrinogen renders surfaces nonadhesive is its surface-induced unfolding and self-assembly leading to the formation of a nanoscale (~10 nm) multilayer matrix [29, 34]. The fibrinogen matrix is extensible and characterized by weak adhesion forces, which makes it incapable of transducing strong mechanical forces via cellular integrins, resulting in weak intracellular signaling and infirm cell adhesion [29, 34, 35]. In contrast, fibrinogen deposited at low concentrations produces a single molecular layer in which molecules are directly attached to the surface. The monolayer is characterized by high adhesion forces that transduce strong outside-in signaling in platelets leading to firm adhesion [29]. It remains unknown whether this behavior is observed when fibrinogen is adsorbed on the surface of vascular graft materials.

In this study, employing atomic force microscopy (AFM)-based force spectroscopy, single cell force spectroscopy (SCFS) and standard adhesion assays with platelets and leukocytes, we examined the adhesive and physical properties of two materials, PTFE (polytetrafluoroethylene) and PET (polyethylene terephthalate) used for the production of contemporary vascular grafts, before and after adsorption of fibrinogen.

We show that in spite of the high adhesion forces exhibited by uncoated biomaterials and when coated with low fibrinogen concentrations, adsorption of fibrinogen at higher concentrations renders the surfaces virtually nonadhesive for platelets and leukocytes.

3.4 Methods

3.4.1 Materials

Human fibrinogen depleted of fibronectin and plasminogen was obtained from Enzyme Research Laboratories (South Bend, IN). Fibrinogen was treated with iodoacetamide to inactivate the residual Factor XIII and then dialyzed against phosphate buffered saline (PBS). Fibrinogen was labeled with 125-Iodine using IODOGEN (Thermo Scientific Pierce Protein Research Products, Rockford, IL), dialyzed against PBS and stored at 20 °C. The concentration of fibrinogen was determined by spectrophotometry at 280 nm using the extinction coefficient 1.51 at 1 mg/ml. Polyclonal antibodies against human fibrinopepetide A was obtained from Assypro (St. Charles, MO). Calcein AM was purchased from Molecular Probes (Life Technologies, Grand Island, NY). The following biomaterials were used in this study: 1) Mylar™, a non-crystalline form of polyethylene terephthalate (PET) purchased as films (type A, 0.127-mm thick) from Cadillac Plastic and Chemical (Birmingham, MI); 2) polytetrafluoroethylene (PTFE) was obtained as a 0.0508-mm sheet from Professional Plastics (Fullerton, CA); and 3) Impra® ePTFE (expanded PTFE; internodal distance 30 μm) vascular graft was obtained from Bard Peripheral Vascular Inc. (Tempe, AZ) in the form of vascular graft tubing with a diameter of 7 mm.

3.4.2 Cells

Human embryonic kidney 293 cells stably expressing leukocyte integrin Mac-1 (HEK-Mac-1) have been described previously [118, 119]. The cells were maintained in RPMI-1640 medium containing 10% fetal bovine serum, 100 IU/ml penicillin and 100 mg/ml streptomycin. Before each experiment, cells were detached from the flasks using the cell dissociation buffer (Cellgro, Mediatech Inc., Manassas, Virginia), washed twice in Hank's Balanced Salt solution (HBSS) containing Ca^{2+} and Mg^{2+} and resuspended in HBSS + 0.1% BSA. U937 monocytic cells were obtained from the American Tissue Culture Collection and cultured in RPMI 1640 supplemented with 10% fetal bovine serum. Human platelets were isolated as described previously [120]. Briefly, platelets were collected from fresh aspirinfree human blood in the presence of 2.8 mM prostaglandin E1, and isolated by differential centrifugation followed by gel filtration on Sepharose 2B in divalent cation-free Tyrode's buffer (pH 7.2) containing 0.1% bovine serum albumin (BSA) and 0.1% glucose. The present work was approved by the Institutional Review Board of Arizona State University.

3.4.3 Surface Preparation for AFM and SCFS

The PET and PTFE sheets were cut into small squares and rinsed with methanol, ethanol, and deionized water. The ePTFE samples were prepared from the vascular graft tubing by cutting squares of the same size. The samples for AFM and SCFS were cut into 6 x 6 mm squares and prepared by adsorption of different concentrations of fibrinogen (0.05-20 mg/ml) in PBS onto the biomaterial surfaces for 3 h at 37 °C.

3.4.4 Atomic Force Microscopy-Based Force Spectroscopy

Force-distance measurements on fibrinogen coated substrates of biomaterials were performed in PBS at 37 °C using an MFP-3D atomic force microscope (Asylum Research, Santa Barbara, CA) as described [34, 35]. Silicon nitride probes (MLCT, Veeco Probes, Camarillo, CA) with nominal spring constants in the range of 10-15 pN/nm were used. Cantilevers were plasma-cleaned in oxygen plasma for 40 s before use. The surfaces coated with different concentrations of fibrinogen were probed using a force trigger of 600 pN and an approach and retract speed of 2 μm/s. Force-distance curves were acquired in 64 x 64 arrays of 5 x 5 mm^2 areas. For each concentration of fibrinogen three arrays at different areas on the surface were probed (12288 force-distances per coating concentration). Spring constants for each cantilever were determined using built-in Thermal method. Each curve was analyzed by a custom program written in IGOR Pro 6 (Wavemetrics, Lake Oswego, OR), which calculates adhesion forces. To obtain mean values of these parameters, the data were fitted using log-normal distributions.

3.4.5 Single Cell Force Spectroscopy

Cantilevers for SCFS measurements were prepared as previously described [34]. Briefly, tipless cantilevers with nominal springconstants of 0.035 N/m (HYDRA6R-200NG-TL, AppNano, Santa Clara, CA) were functionalized with (3-aminopropyl) triethoxysilane (APTES). After washing, the cantilevers were incubated in 1.25 mM Bis (ssulfosucccinimidil) suberate (BS3 ; Sigma) solution for 30 min at 22 °C and then placed into 0.5 mg/ml concanavalin A (Sigma) solution for 30 min at 22 °C. Cantilevers

were then rinsed with PBS and stored in 1 M NaCl at 4 °C. SCFS measurements were performed in HBSS with 0.1% BSA at 37 °C. Integrin Mac-1- expressing HEK293 cells were pipetted into the custom-made AFM chamber and a single cell was instantly picked up from the glass surface by pressing on a cell with a cantilever using a contact force of 500-2000 pN for 5-30 s. After that, the cell was lifted from the surface, allowed to attach firmly to the cantilever for 5-10 min and then lowered onto the fibrinogen coated biomaterial. The biomaterials coated with different concentrations of fibrinogen were probed using a 1 nN force trigger, an approach and retract speed of 2 μm/s, and a 120 s dwell time on the surface. After the trigger force was reached, the z position was kept constant. After each force measurement, a cell was allowed to recover for at least 5 min before the next cycle. As monitored optically, the cells always detached from the fibrinogen substrate but not from the cantilever during pulling. Cell detachment was indicated by the superposition of trace and retrace baselines over the pulling range (25-35 μm).

3.4.6 Confocal Microscopy

ePTFE was coated with fibrinogen (20 mg/ml) and incubated with calcein-labeled platelets for 30 min at 37 °C. The samples were stained with anti-fibrinogen mAb FPA followed by Alexa 647- conjugated goat anti-mouse secondary antibody. Confocal images were taken using a confocal microscope (Leica TSC SP5, Buffalo Grove, IL) at excitation wavelengths of 488 (green: platelets) and 647 (red: fibrinogen).

3.4.7 Scanning Electron Microscopy

PET, PTFE, and ePTFE samples were precoated by a standard sputtering technique with AuePd alloy. Samples were observed using a JEOL JSM6300 (Tokyo, Japan) scanning electron microscope. In selected experiments, PET was coated with different concentrations of fibrinogen on which platelets (1 x 10^7 /mL) were allowed to adhere. After 30 min incubation at 37 °C, samples were washed, fixed with 2% gluteraldehyde, and post-fixed with 1% osmium tetroxide (OsO4) in 1x PBS (pH 7.4) for 1 h each at 22 °C. Samples were dehydrated and then dried through the critical point drying of CO_2, mounted onto aluminum stubs, and sputter coated with palladium-gold (approximately 5 nm) in a sealed vacuum. The samples were observed using a JEOL JSM6300 microscope.

3.4.8 Standard Cell Adhesion Assays

The biomaterial surfaces were freshly cut into squares (9 x 9 mm), cleaned with methanol, ethanol and deionized water, and placed into 24-well plates. The biomaterials were incubated with different concentrations of fibrinogen for 3 h at 37 °C. 3 mL of calcein-labeled U937 cells (1 x 10^6 /mL) or calcein-labeled platelets (1 x 10^7 /mL) in Hanks' balanced salt solution (HBSS) or Tyrode's buffer, respectively, containing 0.1% BSA were added to the surfaces. After 30 min incubation at 37 °C, the non-adherent cells were removed by dipping the surfaces into PBS. Photographs of five random fields for each surface were taken with the 20x and 40x objectives of a Leica DM4000B microscope (Leica Microsystems, Buffalo Grove, IL), and the number of adherent cells was counted. In selected experiments, adherent U937 cells were fixed with 4% paraformaldehyde for 15 min, permeabilized with 0.1% Triton X- 100 for 5 min, then

washed with PBS and incubated with Alexa Fluor 546 phalloidin to stain for the actin cytoskeleton.

3.4.9 Statistical Analyses

Statistical significance of differences between mean values for various conditions has been assessed using a Student's t-test, with $p < 0.05$ considered as statistically significant. For SCFS, statistical significance between median values for different samples was evaluated using a Manne Whitney U test, with $p < 0.05$ considered as statistically significant.

3.5 Results and Discussion

3.5.1 Characterization of Selected Biomaterials by Scanning Electron Microscopy

To assess how fibrinogen might modify the adhesive properties of biomaterials, we have selected two commonly used materials: polyethylene terephthalate (PET or Dacron) and polytetrafluoroethylene (PTFE). Since an uneven surface of woven or knitted Dacron used in commercial grafts may complicate the AFM-based force spectroscopy analyses, we have used smooth flat sheets made of solid PET which mimics the chemical and mechanical properties of the vascular graft material [121]. Likewise, the flat sheets made of PTFE were shown to imitate the chemical properties of ePTFE used for the production of vascular tubes having a complex three-dimensional structure [121]. Scanning electron microscopy of the test materials showed the differences in the surface architecture of PET and PTFE (Fig. 3.1). The figure also shows the typical structure of ePTFE with irregular-shaped flat islands (known as “nodes”) and a dense meshwork of fine fibers stretching between the nodes.

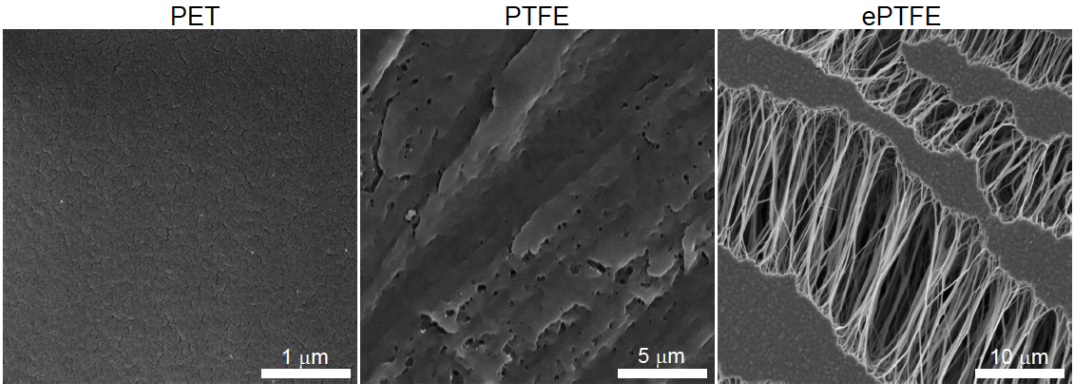

Figure 3.1 Scanning electron microscopy images of biomaterial surfaces . The PET, PTFE and ePTFE surfaces were prepared for SEM as described in materials and methods.

3.5.2 Adhesion Forces Developed by Uncoated and Fibrinogen-Coated Biomaterials Determined by Force Spectroscopy

Adhesion forces of the surfaces before and after adsorption of different concentrations of fibrinogen were probed using an unmodified AFM tip. The strongest adhesion forces were observed between the AFM tip and uncoated materials (Fig. 3.2A-C). Among the materials, both PET and PTFE displayed higher adhesion forces (~1100 pN) compared to ePTFE (~600 pN). Because of the complex architecture, the adhesion forces on ePTFE were measured on the surface of nodes and found to be 596 ± 191 pN. The ~1.7-fold difference in adhesion forces between naked PTFE and ePTFE is not clear since both are made of chemically identical material, but potentially may arise from the ePTFE's modification during manufacturing. As expected, the increase in the fibrinogen coating concentrations resulted in the decrease of adhesion forces for all three materials. In agreement with previous data obtained on mica and glass [34], the steep decrease of

adhesion forces occurred in a very narrow range of fibrinogen coating concentrations (0-1 mg/ml for PTFE and ePTFE) and 0-2 mg/ml for PET. At the concentrations ≥1-2 mg/ml, the adhesion forces reduced by ~6-, 40- and 3-fold for PET, PTFE, and ePTFE, respectively, compared to uncoated surfaces. The subsequent increase in the concentration of fibrinogen up to 50-100 mg/ml did not produce an additional decrease in the adhesion forces for PTFE, although it further decreased adhesion forces for PET and ePTFE. These results indicate that regardless of the initial adhesiveness of uncoated surfaces, the deposition of fibrinogen results in a dramatic drop of adhesion forces making the surface of biomaterials virtually nonadhesive.

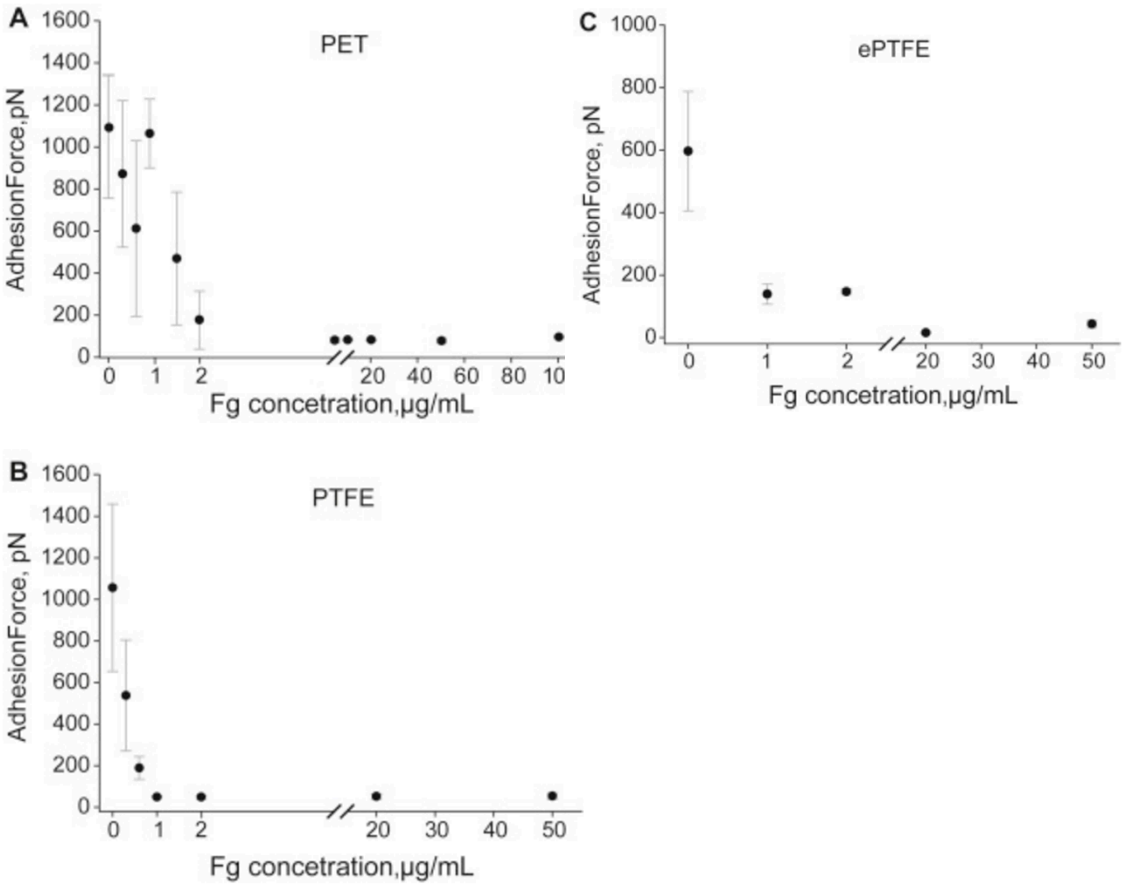

Figure 3.2 Force spectroscopy analyses of the surfaces prepared by adsorption of fibrinogen on biomaterials. Most probable adhesion forces between an unmodified AFM tip and fibrinogen coated biomaterials plotted as a function of the fibrinogen coating concentration adsorbed on PET (A), PTFE (B) and ePTFE (C). The data shown are the means ± SD from three to four experiments with 12288–16384 force-distance curves collected from the force maps for each concentration of fibrinogen. Fg, fibrinogen.

3.5.3 Adhesion of U937 Monocytic Cells and Platelets to Biomaterials Examined by Standard Adhesion Assays

We previously showed a parallelism between the adhesion forces probed by AFM-based force spectroscopy and cell adhesion tested in standard adhesion assays [29, 34, 35]. To examine whether adsorbed fibrinogen reduces integrin-mediated cell adhesion

on biomaterials, we performed adhesion assays with platelets isolated from blood and U937 monocytic cells, a model cell line commonly used in lieu of peripheral blood monocytes. The surfaces were coated with increasing concentrations of fibrinogen and calcein-labeled platelets or U937 cells were allowed to adhere for 30 min at 37 °C. As shown in Fig. 3.3A and B for U937 cells and in 3.3C and 3.3D for platelets, cell adhesion progressively declined as the coating concentration of fibrinogen adsorbed on the surface of PET increased. Furthermore, while U937 cells and platelets were spread on low-density fibrinogen (1.0 mg/ml), they remained round on surfaces coated with 20 mg/ml fibrinogen, underscoring a direct relationship between cell spreading and firm adhesion (Fig. 3.3B and D).

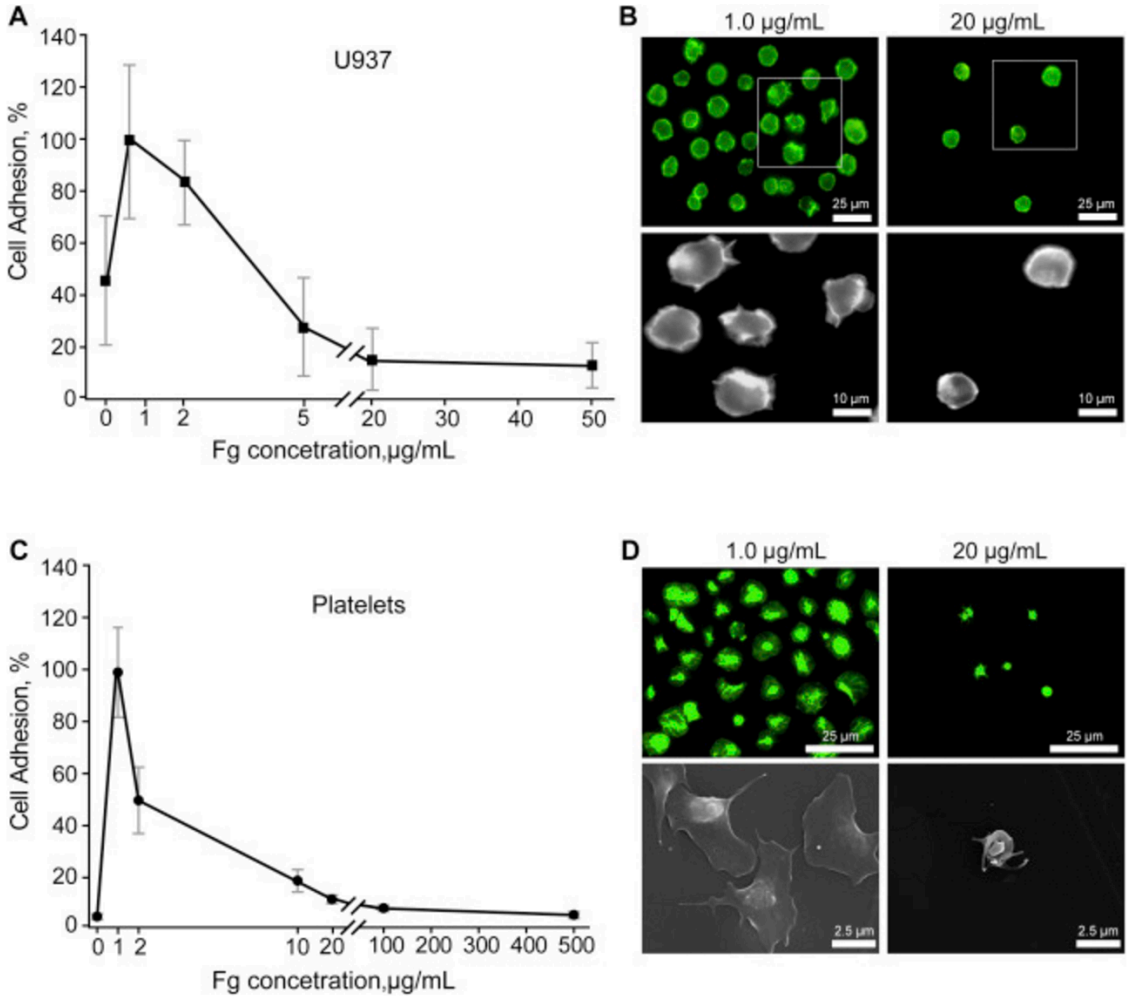

Figure 3.3 Adhesion of U937 monocytic cells and platelets to fibrinogen-coated PET. Different concentrations of fibrinogen were adsorbed on the surface of PET squares (9 × 9 mm) and calcein-labeled U937 cells (A) or platelets (C) were allowed to adhere for 30 min at 37 °C. Non-adherent cells were removed by washing, and adherent cells were quantified by taking pictures of five random fields with a 20x and 40x objectives. Three PET surfaces were prepared for each fibrinogen concentration. Adhesion is expressed as a percentage of maximal adhesion observed at 1 µg/ml. Data shown are means ± SD of three independent experiments with each cell type. (B) representative fluorescent images of U937 cells adherent to PET coated with 1 µg/ml (*left panels*) and 20 µg/ml (*right panels*) fibrinogen. Adherent U937 cells were fixed with 4% paraformaldehyde for 15 min, permeabilized with 0.1% Triton X-100 for 5 min, and then washed and incubated with Alexa Fluor 546 phalloidin to stain for the actin cytoskeleton. (D) representative fluorescent (*upper panels*) or scanning electron microscopy (*lower panels*) images of platelets adherent to PET coated with 1 µg/ml (*left panels*) and 20 µg/ml (*right panels*) fibrinogen.

Similar results were obtained using flat PTFE sheets (Fig. 3.4). The lack of correlation between the coating concentration of fibrinogen and cell adhesion was not due to the abnormal adsorptive capacity of PET and PTFE. Using 125I-labeled fibrinogen, we verified that deposition of protein on PET and PTFE followed a dose-dependent pattern. Notable, however, was the lack of clear saturation of fibrinogen adsorption, which was observed on other surfaces [33] and may be attributed to a continuing assembly of the multilayer. Adhesion assays with fibrinogen-coated ePTFE were hampered by a nonuniform nature of the surface. It was found that many platelets and U937 cells were mechanically trapped within the meshwork of fibers connecting the nodes. Nevertheless, the results revealed that only few platelets adhered to the flat nodes. Thus, consistent with previous findings, fibrinogen adsorbed on the surface of biomaterials at low concentrations supports cell adhesion while high concentrations render the surfaces nonadhesive.

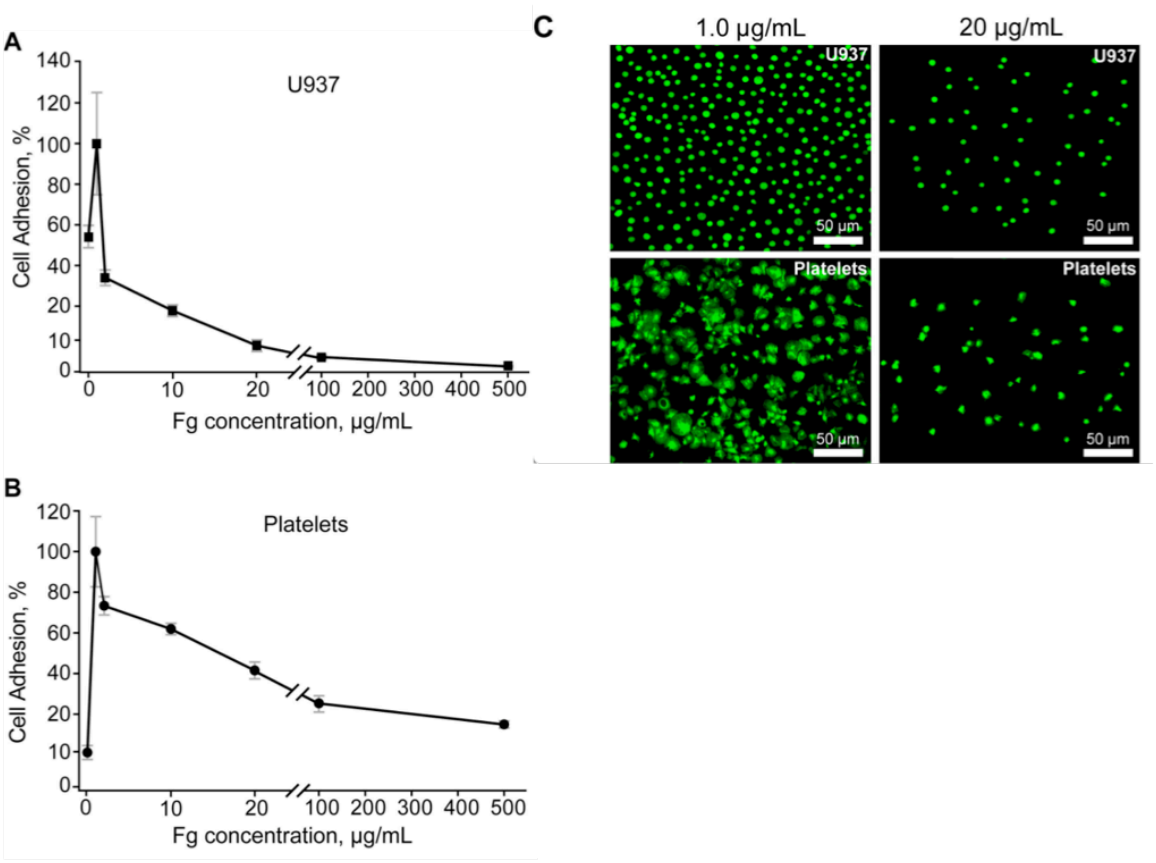

Figure 3.4 Cell adhesion to fibrinogen-coated PTFE. Calcein-labeled U937 cells (A) or platelets (B) were allowed to adhere for 30 min at 37 °C to PTFE squares (9 × 9 mm) coated with different concentrations of fibrinogen. Non-adherent cells were removed by washing and the number of adherent cells was quantified by taking pictures of five random fields, per each concentration of fibrinogen, with a 20x and 40x objectives. Cell adhesion is expressed as a percentage of maximal adhesion observed at 1 µg/ml. Data shown are means ± SD of three independent experiments with each cell type. (C) representative fluorescent images of U937 cells (*upper panel*) or platelets (*lower panel*) adherent to PTFE coated with 1 µg/ml (*left panel*) and 20 µg/ml (*right panel*) fibrinogen.

3.5.4 Single Cell Force Spectroscopy

Although standard adhesion assays provide useful insights into the capacity of various substrates to support cell attachment, these analyses are largely qualitative. Therefore, we obtained quantitative data by measuring the maximal adhesion forces developed between cells and coated biomaterials using SCFS. In these analyses we used

HEK293 cells stably expressing leukocyte integrin Mac-1 ($\alpha_M\beta_2$). This cell line was previously employed to characterize integrin Mac-1-dependent adhesion and to measure adhesion forces between cells and fibrinogen-coated mica [34]. Single Mac- 1-HEK cells were attached to a Con A-functionalized cantilever, and then each cell was brought into contact with uncoated or fibrinogen-coated PET and PTFE surfaces (Fig. 3.5A). Cells were pressed onto each surface with a force of 1 nN for 120 s and then withdrawn with a constant speed of 2 μm/s. The maximal adhesion forces were determined from force-distance retraction curves (Fig. 3.5B). Fig. 3.5C and D show box plots for the maximal forces required for cell detachment from uncoated PET and PTFE, respectively, and coated with low and high concentrations of fibrinogen. For uncoated PET, the median force was 773 pN. The 25th percentile was 487 pN, and the 75th percentile was 1001 pN (Fig. 3.5C). Adsorption of low concentrations of fibrinogen (0.3-0.6 mg/ml) did not alter significantly the median adhesion forces. However, when the coating concentration of fibrinogen increased to 20 mg/ml the median maximal force decreased to 138 pN with the 25th percentile at 93 pN and the 75th percentile at 262 pN, a ~6-fold decline compared to uncoated PET and PET coated with 0.3-0.6 mg/ml fibrinogen (Fig. 3.5C). The median adhesion force for cell adhesion to uncoated PTFE was smaller (417 pN) than those determined on uncoated PET surfaces (Fig. 3.5D) and did not change when PTFE was coated with 0.6 mg/ml fibrinogen. However, coating PTFE with 20 mg/ml fibrinogen resulted in a ~5-fold drop in the median adhesion force (84 pN). The direct measurement of adhesion forces between cellular integrins and fibrinogen substrates is in agreement with the data obtained using the AFM tip, thus, corroborating the idea that deposition of fibrinogen on the surface of biomaterials strongly decreases their adhesiveness for cells.

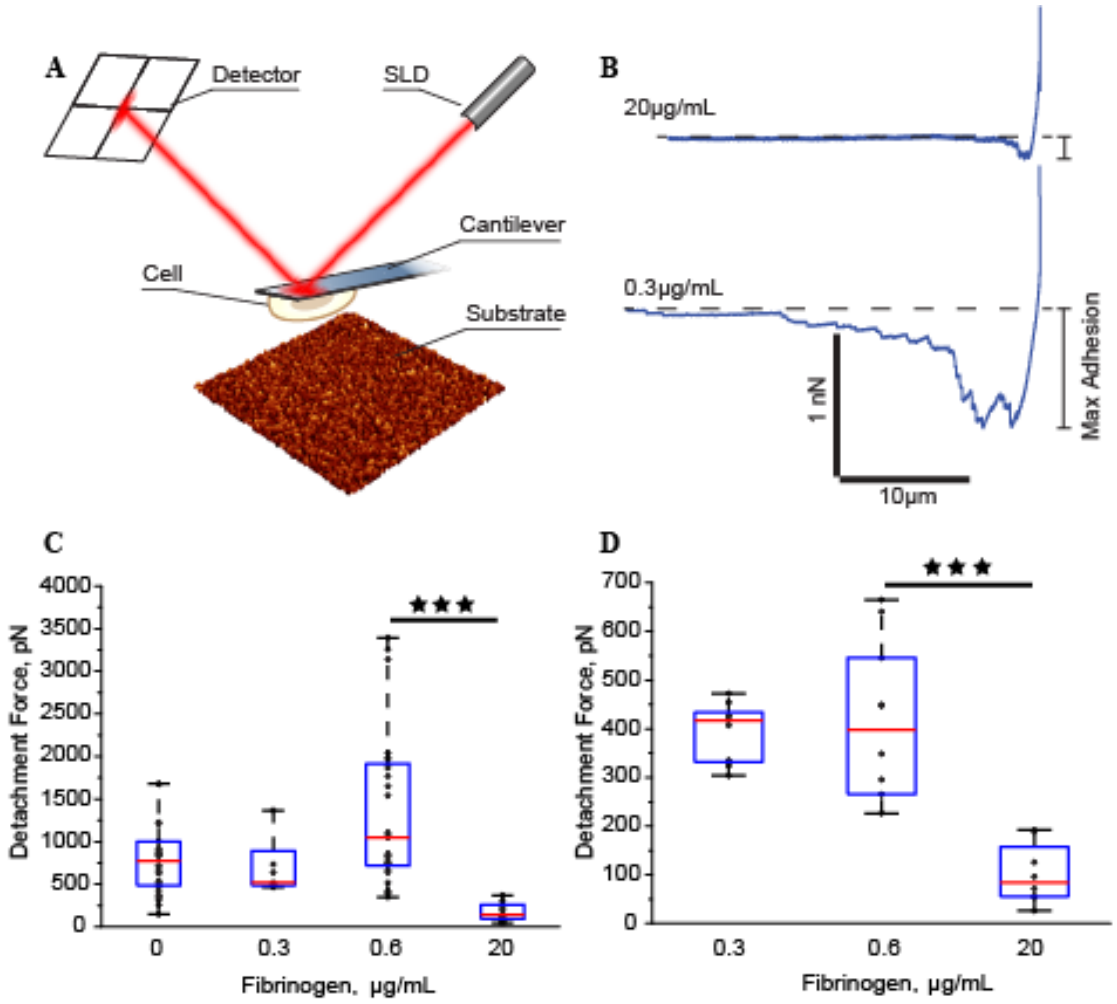

Figure 3.5 Cell adhesion to fibrinogen substrates formed on the surface of PET and PTFE measured by SCFS. (A) schematic representation of a cell attached to the cantilever during its approach to the fibrinogen matrix. (B) representative force-distance curves for the Mac-1-HEK cells brought into contact with fibrinogen adsorbed on PET at 0.3 and 20 µg/ml. Cells were pressed onto each surface with a force of 1 nN for 120 s and then withdrawn with a constant speed of 2 µm/s (C) maximal adhesion forces for cell adhesion to untreated PET, and PET coated with 0.3 µg/ml (2 cells, 9 curves), 0.6 µg/ml (8 cells, 30 curves) and 20 µg/ml (3 cells, 22 curves) fibrinogen solutions. (D) maximal adhesion forces for cell adhesion to untreated PTFE, and PTFE coated with 0.6 µg/ml (6 cells, 29 curves) and 20 µg/ml (4 cells, 28 curves) fibrinogen solutions. Adhesion forces are shown as the median (red lines) of each data set, and the top and bottom of the box represent the 75th and 25th percentile. ***, $p < 0.001$.

3.5.5 Discussion

In the present study, we examined how adsorption of fibrinogen on the surface of two materials, PET and PTFE, used for the production of commercial vascular graft modifies their physical and adhesive properties. The principal finding of this work is that fibrinogen adsorbed at low concentrations (≤ 2 mg/ml) supports platelet and leukocyte adhesion, while adsorbed at higher concentrations fibrinogen makes the surfaces virtually nonadhesive. Furthermore, cell adhesion precipitously drops in a very narrow range of fibrinogen coating concentrations. These data are in agreement with previous observations obtained on other surfaces, including mica, glass, plastic and fibrin clots [29, 33, 35]. Furthermore, examination of adhesive properties of fibrinogen-coated PET and PTFE using AFM force spectroscopy and SCFS is consistent with the data collected on other surfaces, i.e., adsorption of fibrinogen at increasing concentrations reduces the adhesion forces developed between the unmodified AFM tip or a cell and fibrinogen substrates. These findings indicate that adsorption of fibrinogen on biomaterials modify their physical and adhesive properties in a way similar to that observed on other surfaces, underscoring the generality of the fibrinogen-dependent anti-adhesive mechanism.

In previous studies we revealed the molecular basis for the differential cellular responses to low- and high-density fibrinogen adsorbed on various surfaces. In particular, we showed that adsorption of fibrinogen at low concentrations results in the formation of a molecular monolayer in which single molecules are directly attached to the surface [34]. As the fibrinogen concentration increases, the molecules self-assemble through the interaction between their aC domains [35] which results in the formation of the multilayer matrix with a thickness of ~10 nm consisting of 7-8 molecular layers packed

in the horizontal orientation [34, 35]. The monolayer and multilayer exhibit different adhesion forces when probed by AFM-based force spectroscopy and SCFS. The monolayer is highly adhesive for cells and develops high adhesion forces with the AFM tip. The greater cell adhesion observed on the monolayer arises as response to the resistance derived from the hard surfaces to which fibrinogen molecules are attached firmly. Thus, this substrate may not yield when cellular integrins or the AFM tip pull on it. Conversely, the multilayered fibrinogen matrix is characterized by weak adhesion forces and is incapable to support firm cell adhesion. The origin of the nonadhesive properties of the multilayer lies in its extensibility resulting from the separation of the molecular layers held by noncovalent interactions between the long flexible αC regions of fibrinogen [35]. The multilayer is incapable of transducing strong mechanical forces via integrin receptors; hence, when platelet integrins pull on the multilayer matrix it yields to the pulling force resulting in weak intracellular signaling, cell spreading, and adhesion [29]. The inability of platelets or leukocytes to firmly adhere and consolidate their grip on the extensible matrix leads to their detachment under flow. In spite of its nanoscale nature, the fibrinogen matrix has potent antiadhesive properties and is capable of repelling cells, even when only 2-3 layers of the fibrinogen molecules have been assembled [34].

One additional mechanism that may contribute to the nonadhesive properties of the fibrinogen matrix is the weaker association between fibrinogen molecules in the superficial layers of the matrix compared with that in the deeper layers. Such reduced stability would allow integrins to pull fibrinogen molecules out of the matrix with forces comparable to or smaller than required for breaking integrin-fibrinogen bonds. Indeed,

using a method based on a combination of total internal reflection fluorescence microscopy and atomic force microscopy-based single-cell force spectroscopy, we have recently shown that HEK293 cells expressing leukocyte integrin Mac-1 have the capability to pull fibrinogen molecules from the fibrinogen matrix [122]. However, further studies are needed to determine the capacity of platelets and leukocytes to pull fibrinogen molecules from the matrix.

Analyses of adhesion forces developed between uncoated biomaterials and the AFM tip showed a range of 600-1000 pN. These adhesion forces are similar to those detected on glass but in sharp contrast to uncoated mica which displays very low forces (~25 pN) [29]. However, even though the adhesion forces determined on uncoated surfaces differ, adsorption of fibrinogen at low concentrations (monolayer) on all surfaces supports high adhesion forces and then, as the concentration of fibrinogen increases, invariably initiates a sharp decline of adhesion forces. At >2 mg/ml fibrinogen, all surfaces, including biomaterials (Fig. 3.2), are characterized by very low forces. Thus, regardless of the type of the material, fibrinogen modifies surfaces rendering them nonadhesive. A comparable pattern was detected when adhesion forces were measured by SCFS using integrin Mac-1-expressing HEK293 cells (Fig. 3.5). In particular, SCFS showed high adhesion forces for uncoated biomaterials (~770 pN and 420 pN for PET and PTFE), which decreased by 6 and 5 fold respectively, when the coating concentration of fibrinogen increased. As in the force spectroscopy experiments, the difference in adhesion forces observed in SCFS appears to be due to differences in the chemical bond composition of the PET and PTFE surfaces [121]. At variance with biomaterials, adhesion forces probed by SCFS on uncoated mica were low (~100 pN) and adsorption

of low-density fibrinogen first increased them to ~1.7 nN. Nonetheless, adhesion forces dropped to ~200 pN when mica was coated with ≥2 mg/ml fibrinogen [34]. While the above discussion emphasizes the diversity of adhesion forces detected on uncoated materials and after their modification by low concentrations of fibrinogen, which may tentatively be linked to the chemistry of the surfaces [121] and their ability to induce unfolding of fibrinogen, deposition of high-density fibrinogen consistently creates a nonadhesive surface.

The lack of correlation between the amount of adsorbed fibrinogen and platelet adhesion has been previously reported for a broad range of surface chemistries [95] and when fibrinogen was adsorbed from plasma on hydrophobic surfaces [91-93]. The interpretation of this discordance has traditionally been linked to the alterations of fibrinogen conformation and/or availability of integrin-binding sites [90, 93, 95]. However, even though fibrinogen is known to unfold on various surfaces exposing cryptic binding sites for platelets and leukocytes [120, 123], the accessibility of these sequences for platelet integrin $\alpha_{IIb}\beta_3$ and leukocyte integrin Mac-1 does not depend on the coating concentration of fibrinogen [29]. On the contrary, the contact of fibrinogen with various surfaces induces unfolding of the αC regions which then participate in the formation of the extensible multilayer [35]. The formation of this nonadhesive multilayer, the existence of which has not been discovered until very recently, is a primary mechanism regulating mechanosensing by blood cells of and their adhesion to the fibrinogen-coated surfaces.

Based on the unique pattern of platelet and leukocyte adhesion to fibrinogen-coated surfaces, it is reasonable to suggest that fibrinogen deposition on the surface of vascular grafts should differently impact their adhesive properties immediately after implantation and after graft maturation. Accordingly, as soon as the first molecules of fibrinogen contact and adsorb on the surface, they will apparently create a monolayer, which mediates firm platelet adhesion. As adsorption of fibrinogen continues, the surface of grafts may potentially be coated with the fibrinogen multilayer which is not capable of supporting firm cell adhesion, and from which platelets and leukocytes would be washed away by flow. Therefore, the adhesive capacity of implanted vascular grafts after their initial contact with blood may be strongly affected by the rate of fibrinogen adsorption. It is possible that if fibrinogen is deposited quickly, and consequently the nonadhesive fibrinogen multilayer is formed rapidly, few platelets would be attracted to such surfaces. Furthermore, the surface chemistry that promotes efficient selfassembly of the fibrinogen multilayer may decrease initial thrombogenicity. Speculatively, surfaces pre-coated with the fibrinogen matrix before implantation may be even less adhesive than the naked polymers. In contrast to this idea, which seems counter-intuitive, much of the effort in biomaterials research over the past four decades has been directed toward the development of materials that do not react with platelets and fibrinogen [87]. However, even though success in reducing platelet adhesion to virgin biomaterials can be achieved, it will not necessarily lead to the reduced platelet adhesion after implantation since initial contact of the fibrinogen molecules with vascular grafts will inevitably create an adhesive monolayer. In this regard, our data show that although uncoated PET is poorly adhesive for platelets and leukocytes, adsorption of very low concentrations of fibrinogen supports

strong cell adhesion (Fig. 3.3). It is only after the fibrinogen multilayer matrix has been formed (>10 mg/ml) that platelet adhesion is strongly reduced.

Although the formation of the nonadhesive multilayer is a natural progression of fibrinogen adsorption, this process is unlikely to be realized in the circulation. Even before the multilayer is formed, the initial formation of the fibrinogen monolayer, which invariably supports rapid platelet adhesion, should lead to their activation, resulting in thrombin generation and fibrin formation. Indeed, numerous studies demonstrated that very soon after implantation, a thrombotic material consisting of fibrin, platelets and leukocytes is deposited on the inner surface of the prostheses (Reviewed in Ref. [124]). While some variability in the extent and timing of thrombus formation has been noted, the reaction itself does not depend on the type of biomaterial and was observed on both implanted PET and ePTFE grafts. During the first few days after implantation, the thrombus is stabilized and over the subsequent weeks to many years, its thickness stays constant. The outermost layer of stabilized thrombi in contact with blood has often been described as loosely packed or compacted fibrin having a smooth, glistening and transparent appearance. The presence of fibrin on the flow surface of vascular grafts has been known for five decades since De Bakey et al. described the fibrin lining on Dacron grafts recovered from patients following implant periods up to 7 years [114]. Numerous studies subsequently confirmed this finding [114-117, 125, 126]. Furthermore, it has been repeatedly emphasized that the fibrin matrix, especially in the middle regions of grafts, lacks all forms of cellular coverage [124]. Discussion of the acellular appearance of the inner fibrin capsule of grafts implanted in humans has traditionally focused on the conspicuous lack of endothelial cells, which signifies the inability to achieve complete

healing. Perhaps even a more prominent feature of mature grafts is the almost complete absence of adherent platelets or leukocytes, i.e., the nonthrombogenic nature of the fibrin lining. The lack of endothelial cells and platelets on the surface of fibrin lining may have the same underlying mechanisms; however, the origin of this phenomenon has not been addressed. One reason for the lack of interest in this problem in the field might have been the good overall performance of large-diameter prostheses. In this regard, some studies concluded that the ultimate development of the endothelial lining, a feature of complete healing, is nonessential since vascular grafts remained patent and functional for many years [125, 127].

We and other groups have shown that pure fibrin, which is a highly adhesive substrate for platelets and leukocytes, loses its capacity to support cell adhesion in the presence of soluble fibrinogen or after coating of fibrin clots with fibrinogen [29, 33, 127]. The mechanism by which fibrinogen neutralizes the adhesion promoting capacity of fibrin is evidently the deposition of the nonadhesive fibrinogen multilayer on its surface. Thrombus formation on the surface of vascular grafts immediately after implantation seems to closely recapitulate the events occurring on damaged areas of natural blood vessels: i.e., initial platelet adhesion followed by their activation and platelet aggregation. The formation of the platelet plug is spatially coordinated with the activation of the blood coagulation system leading to thrombin generation and the formation of fibrin, which is deposited over the platelet plug. Similar to fibrin lining of vascular grafts, many studies of experimental thrombosis have found no platelets on the surface of thrombus-associated fibrin [107, 128]. Since thrombi in the circulation are continuously exposed to high (2-3 mg/mL) concentrations of fibrinogen, the nonadhesive fibrinogen matrix appears to

assemble on the surface of fibrin developed around stabilized thrombi, thereby preventing platelet adhesion. Indeed, our recent examination of the spatial distribution of fibrin and fibrinogen on the surface of stabilized thrombi generated in flowing blood showed the presence of intact fibrinogen on the surface of the fibrin cap (manuscript submitted). These data imply that the formation of a nonadhesive fibrinogen layer on top of fibrin prevents thrombus propagation and, thus, represents a final step of hemostasis. These findings also suggest that the lining on the surface of mature vascular grafts may, in fact, not be pure fibrin, but a fibrinogen layer which acts as a natural anti-adhesive coat. This would explain the lack of platelets and other cells on the surface of mature vascular grafts. Thus, similar to normal hemostasis, implantation of vascular grafts appears to evoke the normal protective reaction of host to injury. However, in contrast to hemostatic thrombi that occasionally form on the surface of locally damaged endothelium in the circulation and eventually heal, prosthetic vascular grafts are "frozen" in the state of persistent healing for years. At present, the mechanisms that maintain the nonadhesive state of fibrin lining on the surface of vascular grafts for extended periods of time remain to be elucidated.

3.6 Conclusion

The results of the present study show that adsorption of fibrinogen on the surface of PET and PTFE, the synthetic materials used for manufacturing of contemporary vascular grafts, modifies their adhesive properties in a way described previously for other hard surfaces. In particular, while fibrinogen deposited at very low concentrations creates a substrate highly adhesive for platelets and leukocytes, adsorption of fibrinogen at the increasing concentrations results in the formation of the non-adhesive matrix. The non-

adhesive properties of the high density fibrinogen matrix are derived from its multilayer organization and extensibility which, in turn, results in the inability to transduce strong mechanical forces through cellular integrins, a requirement for the firm cell adhesion. Thus, the findings indicate that adsorption of fibrinogen on biomaterials supports the generality of the fibrinogen-dependent antiadhesive mechanism. The formation of the nonadhesive fibrinogen multilayer, the structure still poorly appreciated in the biomaterials field, may explain previous observations of a poor correlation between the amount of adsorbed fibrinogen and platelet adhesion [92, 93, 95]. Further elucidation of the molecular details of this process should assist in better understanding of hemocompatibility of existing and new biomaterials.

4. Combined Single Cell AFM Manipulation and TIRFM for Probing the Molecular Stability of Multilayer Fibrinogen Matrices

4.1 Acknowledgments

This chapter is a reprint of the paper "Combined single cell AFM manipulation and TIRFM for probing the molecular stability of multilayer fibrinogen matrices," by Wayne Christenson, Ivan Yermolenko, Birgit Plochberger, Fernanda Camacho-Alanis, Alexandra Ros, Tatiana Ugarova, and Robert Ros published in *Ultramicroscopy* volume 136 (2014) pp. 211-215. I conducted all the experiments in the paper and analyzed the data with help from Ivan Yermolenko. Birgit Plochberger built the TIRFM apparatus for the study. Fernanda Camacho-Alanis provided the stamp molds necessary for the microfluidic device used for protein patterning. Experiments were conceived by Robert Ros with help from Tatiana Ugarova and Alexandra Ros.

4.2 Abstract

Adsorption of fibrinogen on various surfaces produces a nanoscale multilayer matrix, which strongly reduces the adhesion of platelets and leukocytes with implications for hemostasis and blood compatibility of biomaterials. The nonadhesive properties of fibrinogen matrices are based on their extensibility, ensuing the inability to transduce strong mechanical forces via cellular integrins and resulting in weak intracellular signaling. In addition, reduced cell adhesion may arise from the weaker associations between fibrinogen molecules in the superficial layers of the matrix. Such reduced stability would allow integrins to pull fibrinogen molecules out of the matrix with comparable or smaller forces than required to break integrin-fibrinogen bonds. To

examine this possibility, we developed a method based on the combination of total internal reflection fluorescence microscopy, single cell manipulation with an atomic force microscope and microcontact printing to study the transfer of fibrinogen molecules out of a matrix onto cells. We calculated the average fluorescence intensities per pixel for wild-type HEK 293 (HEK WT) and HEK 293 cells expressing leukocyte integrin Mac-1 (HEK Mac-1) before and after contact with multilayered matrices of fluorescently labeled fibrinogen. For contact times of 500 seconds, HEK Mac-1 cells show a median increase of 57% of the fluorescence intensity compared to 6% for HEK WT cells. The results suggest that the integrin Mac-1-fibrinogen interactions are stronger than the intermolecular fibrinogen interactions in the superficial layer of the matrix. The low mechanical stability of the multilayer fibrinogen surface may contribute to the reduced cell adhesive properties of fibrinogen-coated substrates. We anticipate that the described method can be applied to various cell types to examine their integrin-mediated adhesion to the extracellular matrices with a variable protein composition.

4.3 Introduction

Fibrinogen is a multifunctional plasma protein, which plays a central role in hemostasis and wound healing. During blood vessel injury, fibrinogen is converted to a fibrin clot, which seals the breach and prevents blood loss. Fibrinogen also contains binding sites for integrin receptors on platelets and leukocytes. Consequently, in addition to acting as a mechanical scaffold of clots, fibrin(ogen) can serve as an adhesive substrate for blood cells. Beside its role in hemostasis, fibrinogen deposition on implanted biomaterials may affect their biocompatibility by promoting the adhesion of platelets and leukocytes, which, as generally believed, can trigger unwanted processes such as

thrombosis and inflammation. We have recently identified a previously unrecognized fibrinogen-dependent mechanism that controls adhesion of blood cells [33, 34, 129, 130]. Specifically, we have found that the ability of fibrinogen to support cell adhesion strikingly depends on its coating concentration: while low-density fibrinogen is deposited in a (sub)-monolayer form which is highly adhesive for platelets and leukocytes, its adsorption on various surfaces at high concentrations results in the formation of multilayered matrix incapable of supporting integrin-mediated cell adhesion. In the multilayer, fibrinogen molecules interact with each other through their flexible αC regions [129]. The conversion of a highly adhesive, low-density fibrinogen monolayer to the nonadhesive fibrinogen multilayer occurs within a very narrow range of fibrinogen coating concentrations [33, 34, 129, 130]. A molecular basis for the nonadhesive properties of the fibrinogen matrices is their extensibility, ensuing the inability to transduce strong mechanical forces via cellular integrins and resulting in weak intracellular signaling. Reduced cell adhesion may also arise from the weaker associations between fibrinogen molecules in the superficial layers of the matrix leading to reduced stability. The latter would allow integrins to extract fibrinogen molecules from the matrix with comparable or smaller forces than necessary to break integrin-fibrinogen bonds.

Atomic force microscopy (AFM) [131], primarily known as a high resolution imaging technique, can be utilized for precise force measurements with pN resolution [132-137]. In single cell force spectroscopy (SCFS) [34, 65, 138-147], AFM is applied to manipulate single living cells and quantify interaction forces between the cells and substrates or other cells. For this technique, a single cell is attached to a tipless AFM

cantilever, brought into contact with the surface or another cell, and retracted while the acting force is monitored. AFM can be combined with various optical microscopy techniques like widefield optical epifluorescence and differential interference contrast microscopy [148], total internal reflection fluorescence microscopy (TIRFM) [149-151], two-photon microscopy [152], confocal fluorescence microscopy [153-155], fluorescence lifetime imaging microscopy [154-156], and optical superresolution microscopy techniques [157].

In this paper, we describe a novel method based on the combination of single cell manipulation by an AFM, TIRFM and microcontact printing [158] (Fig. 4.1a) to study the stability of multilayer fibrinogen matrices and address a question whether weak intermolecular forces in the matrix can play an additional role in the low adhesive properties of such surfaces.

4.4 Methods

4.4.1. Combined AFM-TIRFM Setup

A MFP-3D AFM (Asylum Research) placed on an inverted microscope (IX71, Olympus) was used in combination with a custom setup for objective-type TIRFM. This setup is part of a combined AFM-confocal fluorescence lifetime microscope [154, 155, 159]. We used a 100x oil immersion objective with a NA of 1.45 (Olympus) and a 640 nm diode laser (LDH-D-C-640, PicoQuant). The total internal reflection angle was aligned manually. The laser was pulsed at 10 Hz during image sequencing. Image sequences were recorded using an EMCCD camera (Ixon+ DU897, Andor) with 132 ms per frame. The image sequences were analyzed using ImageJ [160]. The average pixel

intensity was determined from measuring the intensity of all pixels within a 15 μm diameter circle surrounding the location of the cell.

4.4.2. Cantilever Preparation

The cantilevers were prepared as described in [34]. Briefly, tipless silicon nitride cantilevers (HYDRA, AppNano, Santa Clara, CA) were plasma-cleaned at 29.6W, 400 mTorr in O_2 gas using a plasma cleaner (PDC-001, Harrick Plasma, Ithaca, NY). Cantilevers were incubated in 2 mM (3-Aminopropyl)triethoxysilane (APTES, Sigma) in chloroform solution. After 40 min at 22 °C, the cantilevers were rinsed with chloroform, followed by ethanol and deionized water. Deionized water was supplied from a Milli-Q synthesis purification unit (Millipore). Cantilevers were incubated in 1.25 mM Bis(sulfosuccinimidyl) suberate sodium salt (BS^3, Sigma) solution for 30 min and then placed into 0.5 mg/ml concanavalin A (Sigma) solution for 30 min at 22 °C. Cantilevers were then rinsed with phosphate buffered saline (PBS) and stored in 1 M NaCl at 4 °C.

4.3.3 Sample Preparation

Human fibrinogen was obtained from Enzyme Research Laboratories (South Bend, IN). Fibrinogen was labeled with Alexa647 (Invitrogen) fluorescent dye according to the manufacturers specifications with an average final 1:1 degree of labeling according to the Invitrogen protocol. Aliquots of labeled protein were stored at -20°C. Glass bottom petri dishes (Fluorodish FD-5040, World Precision Instruments) were patterned using microcontact printing where a PDMS stamp was placed on the glass surface creating a temporary microfluidic network [161]. The inverted microstructure was created on a Si wafer via photolithography as previously reported [162, 163]. Briefly, a Si wafer was spin-coated with the negative photoresist SU-8, UV-exposed through a chrome on soda-

lime photomask (Photosciences), and developed in a developer bath. This structure served as the master wafer for elastomer molding. The latter step was performed by casting PDMS on the master wafer and curing for 4 h at 65°C. Subsequently, the structured PDMS slab was peeled off from the wafer. In total, 100 µL of 100 µg/mL fibrinogen solution was drawn into the microfluidic network via vacuum and allowed to incubate for 1 hour. Excess fibrinogen was removed by flowing 300 µL of PBS through the temporary microfluidic network. Upon removal of the stamp, 2 mL of PBS containing 1% bovine serum albumin (BSA) was allowed to incubate on the surface. BSA was selected as a commonly used nonadhesive substrate for integrin-bearing cells. The BSA solution was rinsed away and replaced with Hank's balanced salt solution (HBSS) containing Ca^{2+} and Mg^{2+} and 0.1% BSA.

4.4.4 Cell Culture

Human embryonic kidney 293 cells (HEK 293) stably expressing leukocyte integrin $\alpha_M\beta_2$ (aka Mac-1) have been described previously [164, 165]. The $\alpha_M\beta_2$-expressing HEK 293 cells (HEK Mac-1) and their wild-type counterparts (HEK WT) were maintained in Dulbecco's Modified Eagle's medium (DMEM) cell growth media with 10% FBS, 100 IU/mL penicillin, and 100 µg/mL streptomycin at 37°C. Prior to experiments, cells were detached from the flask with cell dissociation buffer (Cellgro, Mediatech Inc., Manassas, VA), washed in HBSS, and suspended in HBSS with 0.1% BSA.

4.5 Results and Discussion

4.5.1 Fibrinogen Protein Patterning

For our experiments, glass surfaces were functionalized with human fibrinogen labeled with Alexa 647 and BSA in a defined pattern using a temporary microfluidic network (MFN) in which the fibrinogen solution was drawn into at 100 mg/ml, a concentration known to produce nonadhesive multilayer matrices [34, 130]. Upon removal of the stamp, the remaining surface was coated with BSA to prevent nonspecific binding of cells. This process generates well-defined micrometer fibrinogen/BSA patterned surfaces. Fig. 4.1b shows a fluorescence microscopy image of such a patterned surface. The brighter stripes are areas covered with the labeled fibrinogen, while in the dark stripes the glass surface is covered with unlabeled BSA. The PDMS stamp was designed to create 20 stripes, each 100 μm wide, of labeled fibrinogen with a section of contrasting BSA 100 μm wide between each stripe.

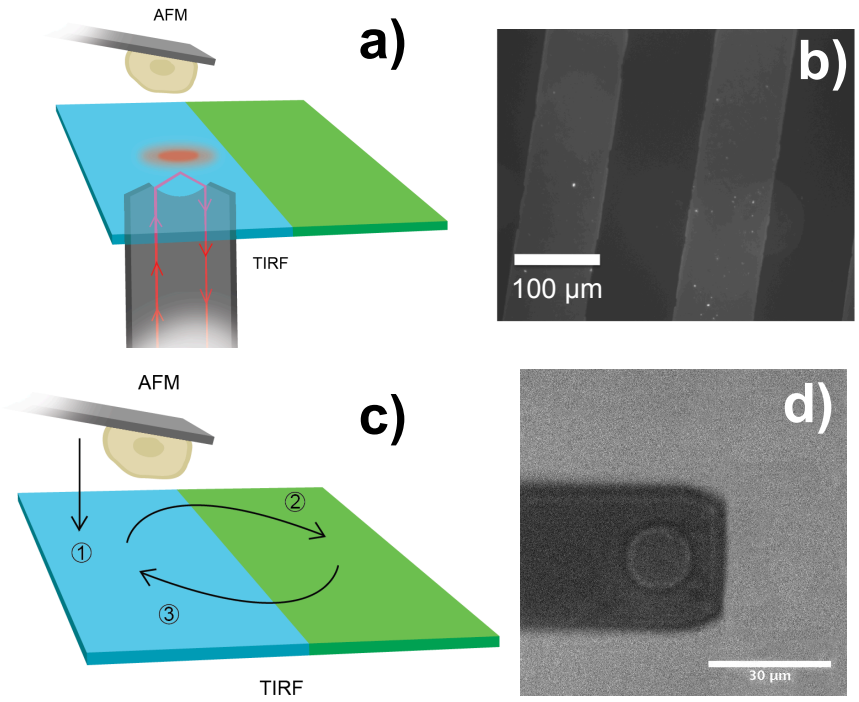

Figure 4.1 a) Illustration of the experimental set up. A living cell is attached to a tipless AFM cantilever and imaged using TIRFM. The surface contains separated regions with multilayer fibrinogen matrices and BSA. b) Fluorescence microscopy image of a micro patterned surface. Alexa647 labeled fibrinogen stripes are patterned onto the surface with contrasting unlabeled BSA stripes using microcontact printing methods. c) Schematic of experimental procedure. A cell is lowered to a surface area covered with unlabeled BSA and imaged with TIRFM (1), the cell is then moved to a surface covered with labeled fibrinogen, and allowed to adhere for 500 s (2), the cell is then transferred back to the unlabeled region, and the fluorescence intensity is measured with TIRFM again (3). d) Bright field microscopy image of a cell attached to a tipless AFM cantilever.

This patterned surface was used for single cell measurements. A typical measurement sequence is shown in Fig. 4.1c. First, HEK 293 Mac-1 cells stably expressing the leukocyte integrin $\alpha_M\beta_2$ or HEK 293 WT cells as control were pipetted onto the surface and maintained at 37 °C in HBSS. Then a single cell on the BSA coated region of the surface was selected and picked up by pressing the concanavalin A functionalized AFM cantilever with a contact force of ~500 pN for ~5 to 30 s on the cell.

After the retraction of the cantilever, the cell was allowed to firmly attach to the cantilever. Since this cell was not in contact with an adhesive substrate this assured that no integrin-mediated outside-in signaling occurred. Fig. 4.1d shows a bright field microscopy image of a single cell attached to an AFM cantilever.

Next, to reduce background we photo-bleached an area in the BSA region using a 640 nm diode laser with maximum intensity for 10 s. On this spot, the previously selected cell was pressed down with a contact force of 500 pN and the fluorescence signal of the cell was imaged in the TIRFM mode for 10 s with a 10 times attenuated laser intensity. The fluorescence intensity recorded in this step is used as reference intensity. The cell was then lifted from the BSA coated substrate and transferred to a fibrinogen region on the sample surface and pressed down with a contact force of 500 pN remaining on the surface for 500 s. Finally, the cell was lifted again, and moved back to the BSA region.

4.5.2 Force-Curve Measurements

Fig. 4.2 shows the retracting parts of force-distance curves of HEK Mac-1 and HEK WT cells after the contact with the fibrinogen multilayer matrices. The observed adhesion forces of both cell types are in good agreement with our previous study [34]. Fig. 4.2a shows the force-distance curve of a HEK Mac-1 cell with an adhesion force of about 360 pN, while the control measurement with the HEK WT cells shows a lower adhesion force of about 90 pN (Fig. 4.2b). In our previous study [34], we systematically quantified the adhesion forces of the two cell types under a variation of conditions and substrates. For HEK Mac-1 cells on multilayer matrices (coating concentrations of 2 and 20 μg/mL) we found adhesion forces of 200 – 400 pN for contact times between 10 – 120 s.

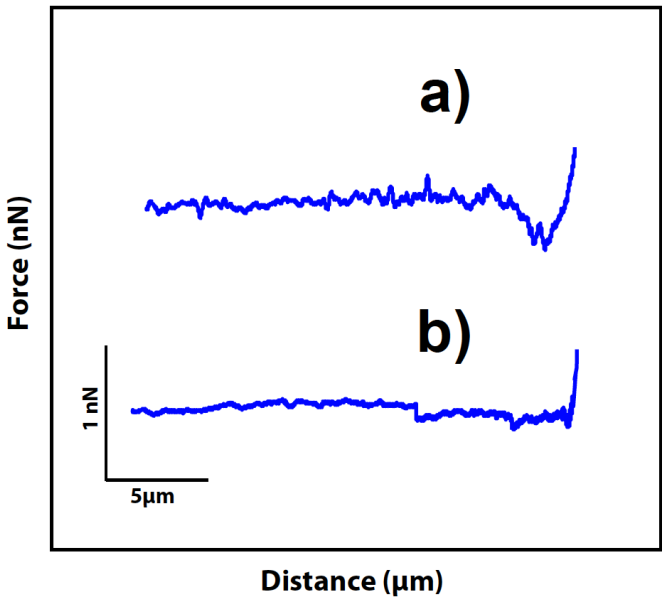

Figure 4.2 Retraction part of force-distance curves after the cell was in contact with the fibrinogen surface. In a) a HEK Mac-1 cell is attached to the AFM cantilever, and in b) a HEK WT cell.

Before the cell was lowered to the BSA region with the same contact force, the area below the cell was photo-bleached for 10 s with maximum laser intensity. The time between when the cell was lifted from the fibrinogen and then lowered onto the BSA after photo-bleaching was less than 60 s.

4.5.3 Fluorescent Measurements Before and After Contact with Labeled Fibrinogen

Fig. 4.3a shows a TIRFM image of a HEK Mac-1 cell before the contact with a fibrinogen matrix. A low fluorescence background at the position of the cell is visible. After the contact, the fluorescence intensity is increased, indicating that fluorescently labeled fibrinogen molecules were removed from the fibrinogen matrix and attached to the cell (Fig. 4.3b). As control, the same experimental procedure was performed with HEK WT cells. In Fig. 4.3c and d, TIRFM images of a HEK WT cell before and after the

contact with the fibrinogen matrix are shown. Here, the fluorescence intensity in both images is very similar indicating no significant transfer of fluorescently labeled fibrinogen molecules.

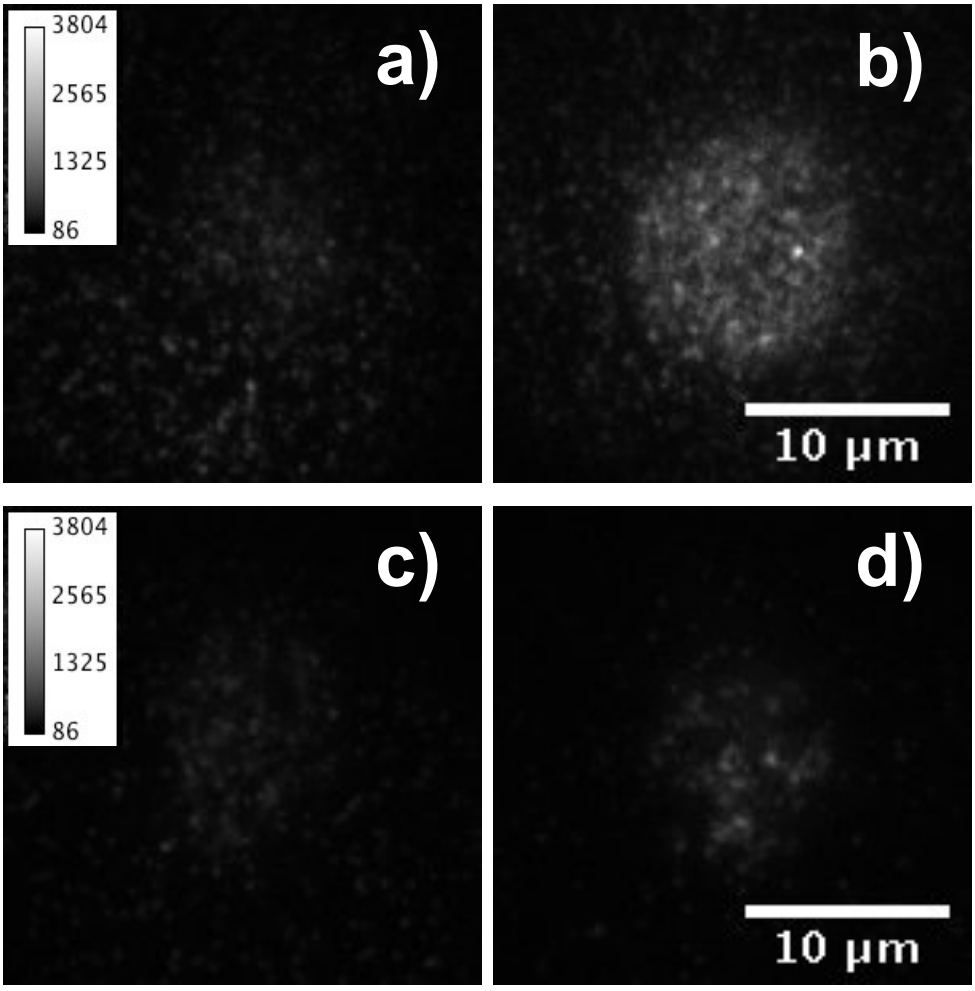

Figure 4.3 TIRFM images of cells before (a and c) and after (b and d) contact with a matrix of fluorescently labeled fibrinogen. In (a) and (b) HEK Mac-1 cell, and in (c) and (d) HEK WT cells are shown. The HEK Mac-1 cell shows a considerable increase in fluorescence intensity after contact with a fibrinogen coated surface.

4.5.4 Quantification of Fluorescent Measurements

For quantification, we calculated the average fluorescence intensities per pixel for 14 HEK Mac-1 and 18 HEK WT cells before and after the contact with multilayered

matrices. The first image captured during image sequencing was used for quantification of average fluorescent intensities per pixel before and after contact with fibrinogen. The fluorescent intensity of all pixels within a 15μm diameter circle surrounding the cell was averaged. Fig. 4.4 shows box plots for the relative increase in the average fluorescence intensity per pixel before and after the contact of the cells with the matrices. For the HEK Mac-1 cells, the median of the relative increase is 57%, the 25th percentile is 14%, and the 75th percentile is 93%. For HEK WT cells, the median is 6%, 25th percentile is 2%, and 75th percentile was 19%. The results suggest that integrin $\alpha_M\beta_2$ - fibrinogen interactions are stronger than the intermolecular fibrinogen interactions in the superficial layer of the matrix. The low mechanical stability of the multilayer fibrinogen surface may contribute to the reduced cell adhesive properties of fibrinogen-coated substrates.

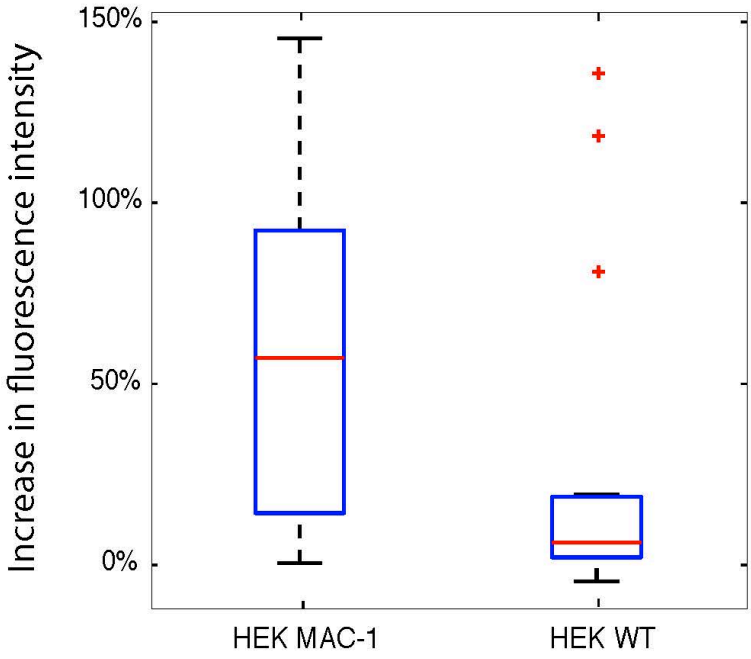

Figure 4.4 Box plot of the relative increase in average fluorescent intensity per pixel of 14 HEK Mac-1 cells and 18 HEK WT cells. The red line represents the median of the data set, and the top and bottom of the box represent the 75th and 25th percentile. For the HEK Mac-1 cells the median is 56.8%, the 25th percentile is 14.2%, and the 75th percentile is 92.6%. For HEK WT cells the median is 6.1%, 25th percentile is 2.0%, and 75th percentile is 18.8%.

4.6 Conclusion

We developed a sensitive single cell method to study the transfer of molecules from a surface to a cell during the detachment process. We found that $\alpha_M\beta_2$ integrins are able to pull fibrinogen molecules out of multilayered matrices. The interaction forces between fibrinogen molecules in multilayer matrices are smaller or comparable with integrin-fibrinogen interactions suggesting a low mechanical stability of the matrices. This indicates that together with the well accepted increased extensibility of the fibrinogen multilayer the low stability of its surface plays a role in the reduced cell

adhesive properties of the fibrinogen matrices. We anticipate that the method described in this paper can be applied to other cell types to examine their integrin-mediated adhesion to extracellular matrices with a variable protein composition. Further, our approach may be used advantageously in defining the activation state of the cell before the experiment and precisely controlling activation times, which is of general interest for all single cell force spectroscopy experiments.

5. Quantifying Discrete Single Molecular Events in Cellular Adhesion Experiments

5.1 Acknowledgments

This chapter is analysis of data gathered by Ivan Yermolenko from SCFS experiments. I analyzed all the data from the experiments, and wrote the algorithms for isolating and analyzing single molecule events. Experiments were designed by Tatiana Ugarova and Robert Ros, who also provided consultation.

5.2 Abstract

Single Cell Force Spectroscopy (SCFS) can be used to measure the maximum adhesion force between cells and a surface, but determining the nature of discrete interactions within SCFS data can be challenging. The $\alpha_M\beta_2$-fibrinogen bond plays an important role in the adhesion of monocytes to synthetic materials implanted in the human body. The adhesion of monocytes leads to complications that can be detrimental to the function of the implanted material. We present a method for quantifying specific $\alpha_M\beta_2$ integrin and fibrinogen interactions on living cells using atomic force microscopy (AFM) based SCFS experiments. SCFS data from HEK 293 cells expressing $\alpha_M\beta_2$ leukocyte integrin (HEK Mac-1) and wild-type HEK 293 (HEK WT) cells on surfaces coated with fibrinogen were analyzed to identify specific "rupture events." High force load ruptures (> 250 pN/s) imply a connection of the integrin with the underlying actin cortex of the cell, while low force load (< 250 pN/s) ruptures result from the formation of a membrane tether. For highly adhesive fibrinogen surfaces, we found 40% of all rupture events to have a high force load for HEK Mac-1 cells compared to only 11% of rupture events having a high force load for HEK WT data of the same surface. The high force

load events in the HEK Mac-1 data showed a most probable rupture force of 48 pN, whereas the most probable rupture force of the HEK WT high force load events was 32 pN. After adding monoclonal antibody directed against the α_M subunit of the integrin, HEK Mac-1 cells showed similar rupture force values to that of the HEK WT. This analysis demonstrates the ability to quantify specific integrin-ligand interactions within SCFS data. Additionaly the kinetic parameters of k_{off}^{0} and x_β were for Mac-1:fibrinogen were quantified. k_{off}^{0} was between 0.01 and 0.2 s^{-1}, and x_β was between 0.51 and 0.95 nm.

5.3 Introduction

The $\alpha_M\beta_2$ (CD11b/CD18, Mac-1) integrin has been shown to be a key integrin in mediating leukocyte migration and adhesion [20, 22, 166]. Mac-1 plays a critical role in the immune response both in leukocyte recruitment and leukocyte cytotoxic functions [167]. Leukocyte recruitment driven by Mac-1 has also been shown to be necessary for neointimal thickening after vascular injury [23]. Although Mac-1 is capable of binding with a variety of ligands including iC3b and ICAM-1 [24, 25, 119], its interaction with fibrinogen has been shown to play a critical role in the host inflammatory response [33, 168].

Fibrinogen circulates in the blood at a high concentration (2-3 mg/ml), and plays a primary role in wound healing and thrombus formation [26, 28]. Recently, it has been shown that despite its involvement in leukocyte recruitment during inflammation, fibrinogen can also act as an anti-adhesive and anti-inflammatory agent [33, 169]. We have previously demonstrated that the adhesiveness of fibrinogen toward Mac-1 expressing cells is concentration dependent for several biomaterial surfaces [34, 170].

Mac-1 is unable to bind with soluble fibrinogen, and only binds to immobilized fibrinogen [168]. Because of this fact, little attention has been paid to the kinetics of Mac-1:fibrinogen bonds despite it's importance in several immune responses. We have proposed that the anti-adhesive effect of high concentrations of immobilized fibrinogen is due to the extensibility of the multi-layered fibrinogen matrix that is formed [35]. Previously, we demonstrated that Mac-1 expressing HEK-293 cells (HEK Mac-1) were able to remove fibrinogen molecules from this extensible fibrinogen matrix [122]. In this study, we set out to quantify the binding forces involved between membrane bound Mac-1 integrins and fibrinogen using detailed statistical analysis of SCFS data, and to estimate kinetic parameters of the bond formation.

SCFS is a powerful tool for analyzing the adhesion of cells to surfaces and to other cells [44, 49, 171]. Atomic force microscopy (AFM) based SCFS provides several advantages compared to other force spectroscopy methods including high force resolution (~10 pN), large range of forces (10 pN to >100 nN), and excellent control of contact conditions [48]. Determining the individual molecular forces involved between specific ligand-receptor interactions while in their native cellular environment should is possible with SCFS through appropriate control experiments and detailed data analysis [172]. While much research has been done with isolated biomolecules using single molecule force spectroscopy (SMFS) [5, 52, 82, 86, 173], quantifying the forces of biomolecules within a living cell membrane remains challenging because of the complex interactions involved in a cellular environment [2, 174]. One major challenge is linking discrete events within SCFS data with specific biomolocules because of all the possible interactions that could be occurring between a cell and a surface of interest.

For this analysis, we use a classification of rupture events similar to classification schemes others have proposed [171, 172, 175, 176]. That is a classification of events based on the slope, or loading rate, leading up to the point of rupture in the force-distance curve generated by a SCFS experiment. Notably, a high loading rate prior to the point of rupture imply binding of integrins that are anchored in the cell cytoskeleton, whereas a low loading rate implies a bond to cell receptors coupled only to the cell membrane [174, 176]. Here we analyze the rupture force of high loading rate events based on a threshold determined from 2D histograms of the data in order to determine the most probable rupture force of Mac-1 integrins with fibrinogen for a given range of loading rates. We then apply the theoretical models for dynamic single molecule force spectroscopy (SMFS) established by Bell, Evans, and Ritchie [52, 79] as well as a method proposed by Dudko et al. [85], as outlined in §2.2.7 and §2.2.8 to the high loading rate data in order to determine kinetic parameters of Mac-1:fibrinogen bonds.

5.4 Methods

5.4.1 Surface Preparation

Fibrinogen coated surfaces were prepared as has been described previously [34]. Briefly, freshly cleaved mica squares (8 x 8 mm^2) were incubated in the various concentrations of fibrinogen (Enzyme Research Laboratories, South Bend, IN) in phosphate buffered saline (PBS) for 3 hours. Previous work has established the absorption kinetics of radiolabeled fibrinogen on mica surfaces in various solution concentrations of fibrinogen (0.25 – 3 μg/mL), showing that fibrinogen absorption reaches a maximum surface concentration for a specific solution concentration after 3 hours [34].

5.4.2 Cell Culture

Human embryonic kidney 293 cells (HEK 293) were incubated in RPMI – 1640 medium containing 10% fetal bovine serum, 100 IU/ml penicillin, and 100 μg/mL streptomycin. Two types of HEK 293 cells were used in experiments. One cell line stably expressing $\alpha_M\beta_2$ (HEK Mac-1) which have been previously described [118, 119] and the wild-type HEK 293 cell line (HEK-WT). Cells were detached from flasks before experiments using cell dissociation buffer (Cellgor, Mediatech Inc., Manassas, VA). Cells were then doubly washed in Hank's balanced salt solution (HBSS) containing Ca^{2+} and Mg^{2+}, and resuspended in HBSS + 0.1% BSA. For one set of control experiments HEK Mac-1 cells were incubated with monoclonal antibody (mAb) 44a as previously described [34].

5.4.3 AFM Cantilever Preparation

Tipless silicon nitride cantilevers (HYDRA, App-Nano, Santa Clara, CA) were prepared according to our previously established method [34]. Cantilevers were plasma-cleaned in O_2 gas using a plasma cleaner (PDC-001, Harrick Plasma, Ithaca, NY). Cantilevers were then incubated in 0.04 mM APTES ((3-amino-propyl)triethoxysilane) in chloroform solution for 40 min. After rinsing the cantilevers with chloroform, then ethonal, and then Millipore-quality water, the cantilevers were incubated in 1.25 mM bis(sulfosuccinimidyl)suberate sodium salt (BS^3, Sigma) solution for 30 min followed by 30 min of incubation in a 0.5 mg/mL concanavalin A (Sigma) solution. All incubation

steps were at 22º C. Concanavalin A binds to cells through cell-surface carbohydrates with much greater strength than other receptor-ligand interactions [1]. Cantilevers were stored in 1 M NaCl at 4º C.

5.4.4 Single Cell Force Spectroscopy

Cantilever spring constants and optical lever sensitivity were calibrated prior to each experiment using a built in thermal noise method on the MFP-3D AFM (Asylum Research, Santa Barbara, CA). The spring constant for cantilevers were near the manufacturers nominal spring constant of 0.035 N/m. Force-distance measurements were performed using the MFP-3D. The MFP-3D is part of a combined optical set-up on top of an inverted microscope (IX71, Olympus). This set-up allows for the monitoring of cells during cell capture, and during force-distance measurements. Cells in HBSS supplemented with 0.1% BSA were pipetted into a custom-made AFM chamber kept at 37º C. Immediately after pipetting the cells, the AFM cantilever was manually aligned above the cell, and then brought into contact with the cell using a contact force of 500-2000 pN for 5-30 s. The cell was then lifted from the surface, and allowed to firmly attach to the cantilever for 5 min. Force-distance measurements were then taken on the different fibrinogen coated surfaces using the cell as a probe. Each force-distance measurement was performed using an approach and retract velocity of 2000 nm/s and a trigger force of 1 nN. Cells dwelled on the surface for 0.01 – 150 s. Z-position was held constant during the dwell time. After each force-distance measurement the cell was allowed to recover for 2 min before the next cycle. Cells were able to undergo 3 – 8 force measurements before the cell lost all adhesive properties. 5 – 19 cells were used on each surface type.

5.4.5 Data Analysis

Force-distance curves were all processed to correct virtual deflection and cantilever bending using a linear fit of the detached baseline as is typical in SCFS experiments [172]. Discrete rupture events were identified manually. Each rupture event was characterized by 3 parameters: the distance from the beginning of the force-distance curve to the point of rupture, the magnitude of the rupture force determined by the size of the step, and the loading rate preceding the rupture. A manually selected amount of data between 10 nm and 200 nm preceding a rupture was selected for a linear fit to determine the loading rate ($\Delta F/\Delta t$). 2D histograms were created to visualize populations of rupture events with a given loading rate versus the distance of the rupture occurrence similar to other analysis methods [176]. Force rupture distributions were fit with a kernel density function in MATLAB to determine the most probable rupture force [177]. High loading rate events were binned according to the natural log of their loading rates. The mean rupture force, and most probable rupture force was determined for each bin in order to use the Bell-Evans method and Dudko method for determining single bond kinetics for Mac-1:fibrinogen.

5.5 Results and Discussions

5.5.1 Single Cell Force Spectroscopy

SCFS measurements of HEK Mac-1 cells on mica surfaces with low concentrations of fibrinogen (0.6 μg/ml) and mica surfaces with high concentrations of fibrinogen (20 μg/ml) were taken along with SCFS measurements of HEK WT cells and HEK Mac-1 cells pre-incubated with anti-α_M mAb 44a on surfaces of low concentration fibrinogen. Representative retraction curves for each experimental condition are shown in

Fig. 5.1. It has been shown previously that mica incubated in 0.6 μg/ml fibrinogen solution produces a mica surface with a sub-monolayer of fibrinogen molecules that is maximally adhesive for HEK Mac-1 cells [34]. In the same study, it was shown that mica incubated in 20 μg/ml fibrinogen produced a multi-layered fibrinogen matrix that was anti-adhesive. SCFS generates force-distance curves that record the force acted upon the AFM cantilever during the approach and retraction of the cell.

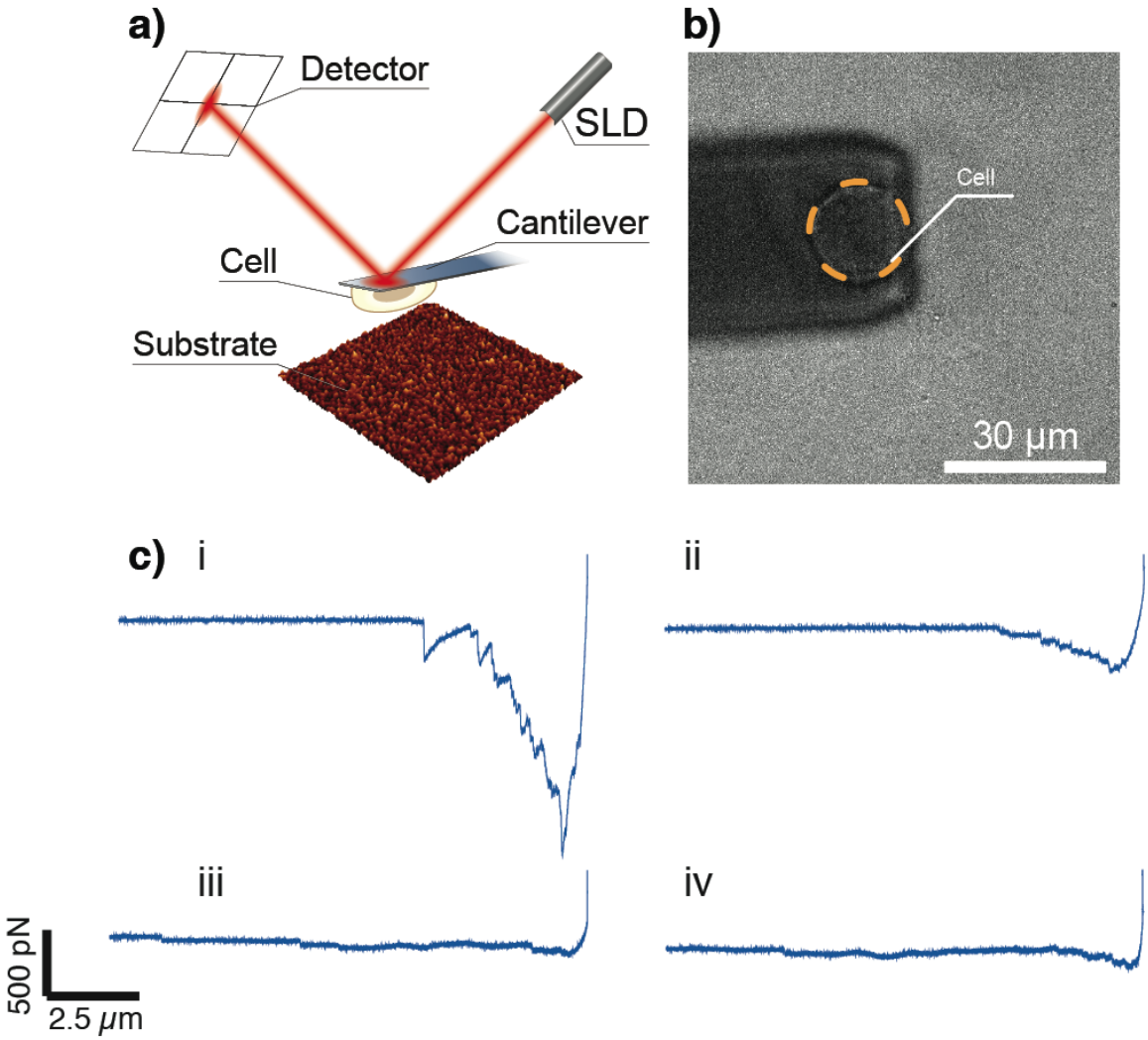

Figure 5.1 a) Schematic of a single cell force spectroscopy experiment. A living cell attached to a tipless AFM cantilever is lowered to a fibrinogen-coated surface with 1nN of force. The cell is removed at 2µm/s, and a force v. distance curve is generated. b) A bright field image of a HEK cell attached to a tipless cantilever. c) Representative curves for each experimental condition. i) HEK Mac-1 on 0.6 µg/ml fibrinogen coated mica. ii) HEK Mac-1 on 20 µg/ml fibrinogen coated mica. iii) mAb blocked HEK Mac-1 on 0.6 µg/ml fibrinogen coated mica. iv) HEK WT on 0.6 µg/ml fibrinogen coated mica.

5.5.2 Classifying Discrete Steps in Force-Distance Curves

The primary information from the retraction portion of a force-distance curve is the maximum adhesion of the cell to a surface, which is the minimum value of the

retraction curve [44, 65]. While this provides valuable insight into the mechanics of whole cell adhesion, it says little about the molecular mechanics involved with cellular adhesion. Force-distance curves do contain relevant information to the molecular processes involved in adhesion [45], but being able to retrieve specific receptor-ligand interactions requires rigorous control experiments as well as detailed statistical analysis. We characterized discrete step-like events, or rupture events, from our 4 experimental conditions with 3 parameters outlined in Fig. 5.2: the distance from the start of the retraction curve to the base of the rupture event, the magnitude of the rupture event (the size of the step), and the loading rate. The discrete step-like events shown in Fig. 5.2 correspond with ruptures between individual molecular bonds or clusters of individual bonds [176]. Correlating individual rupture events with specific integrin-ligand interactions requires rigorous controls to verify the specificity of the interaction [171]. Rupture events can be broadly categorized into two classes as shown in Fig. 5.2.

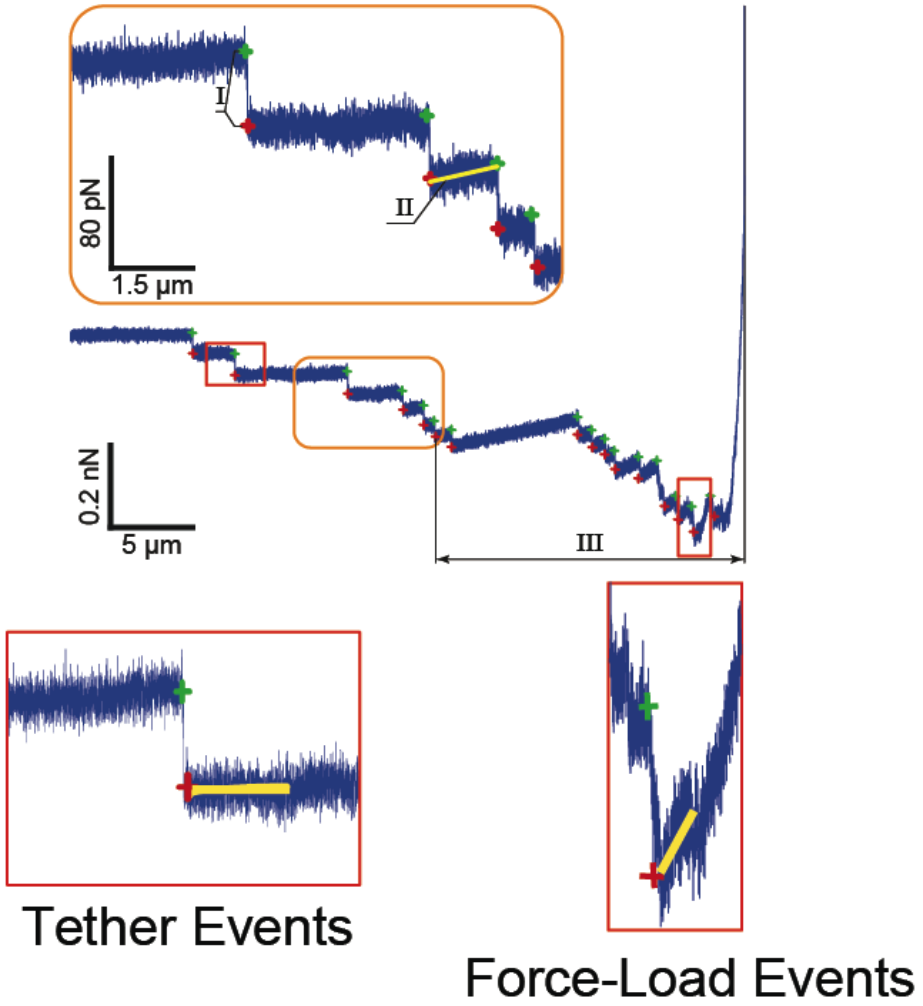

Figure 5.2 An example force v. distance retraction curve of a single HEK Mac-1 cell after contact with a fibrinogen coated substrate. Data is generated from right to left as the cell is separated from the surface. Rupture events were identified according to the described algorithm and confirmed by inspection. Three parameters were measured for each rupture event. I. The magnitude of the rupture force. II. A linear fit of data before the rupture event. The slope of this fit is the loading rate. III. The distance from the beginning of the curve to the rupture, which can be converted into a lifetime of the bond given the constant retraction speed.

5.5.3 Tether Events

Tether events have a slope < 250 pN/s leading up to the rupture event. These tether events represent membrane receptors bound to the surface that are not linked to the

cellular cytoskeleton. The surface bound receptors anchor the plasma membrane to the surface while the cell is retracted off the surface. Because the membrane acts as a two dimensional fluid, long nanotubes are formed from the anchor point to the body of the cell until the bond forming that anchor disassociates stochastically [47, 174, 175, 178]. These membrane tethers act as a natural force clamp for the bond acting as anchor, and the force acting on the bond depends on the cantilever retraction velocity [174, 178]. In these experiments, a constant retraction velocity of 2 μm/s was used, and the tether events for all experimental conditions showed a practically equivalent probability distribution with a most probable rupture force of ~30 pN (Fig. 5.3). This rupture force is less than the typical force required to pull membrane proteins from a lipid bilayer (~100-150 pN) [178]. While this rupture force contains information characteristic of the cell membrane, it is unable to distinguish useful information regarding the specific molecular bonds that anchor the membrane tethers.

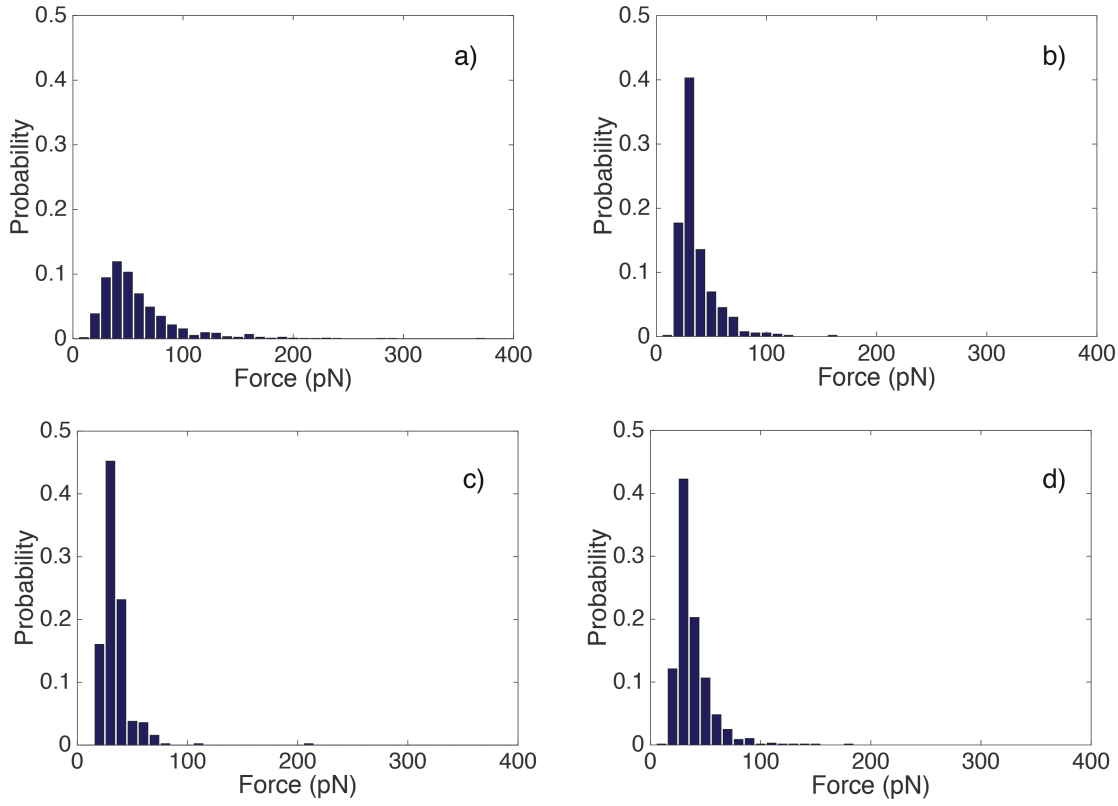

Figure 5.3 Probability distributions of tether events. Rupture forces for class 1 events have a most probable rupture force of ~30 pN for all conditions. Each distribution is normalized over all events for a given experimental condition. a) HEK Mac-1 on 0.6 µg/ml fibrinogen coated mica. b) HEK Mac-1 on 20 µg/ml fibrinogen coated mica. c) mAb blocked HEK Mac-1 on 0.6 µg/ml fibrinogen coated mica. d) HEK WT on 0.6 µg/ml fibrinogen coated mica.

The distance from the beginning of the retraction curve to the point of rupture for tether events represent the bond lifetime for the bond anchoring the membrane tethers. The lifetime distributions for any specific bond follow an exponential decay. The lifetime distributions for the tether events for the experimental conditions in this study fit an exponential decay with an R^2 value of 0.91, 0.90, 0.84, and 0.81 for a, b, c, and d of Fig. 5.4 respectively. Each condition has a different mean lifetime representing the different molecular interactions for each condition (Fig. 5.4).

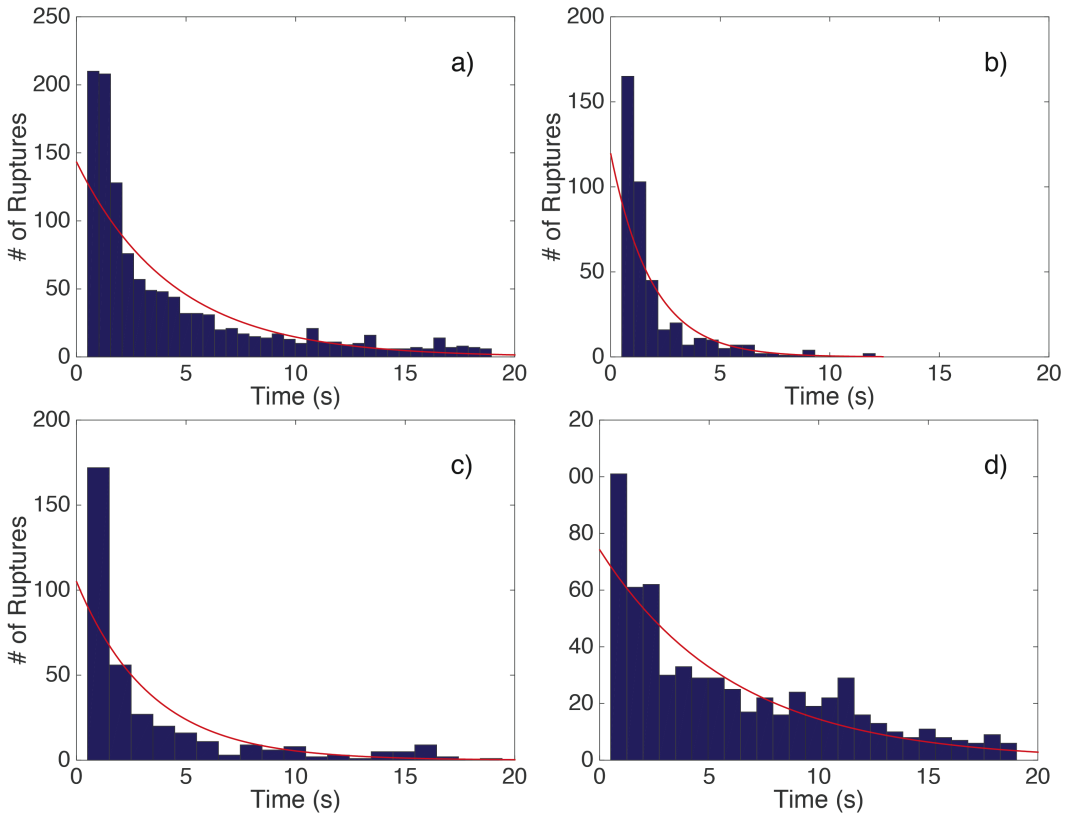

Figure 5.4 Lifetime of tether events for each condition. a) HEK Mac-1 on 0.6 µg/ml fibrinogen coated mica. b) HEK Mac-1 on 20 µg/ml fibrinogen coated mica. c) mAb blocked HEK Mac-1 on 0.6 µg/ml fibrinogen coated mica. d) HEK WT on 0.6 µg/ml fibrinogen coated mica. τ = 4.4 s, 1.9 s, 3.4 s, and 6.1s for a, b, c, and d respectively.

5.5.4 Force-Load Events

Force-load events show a slope in the data before the event. The slope of the data in the force distance curve leading up to a rupture corresponds to the loading-rate in single molecule force spectroscopy (SMFS) experiments. We analyzed all individual rupture events from all SCFS experiments in order to categorize them according to this classification system. Tether events can be seen to occur along nearly the entire length of the retraction portion of the force distance curves for each experimental condition, whereas force-load events were clustered near the first 5 µm of the curves.

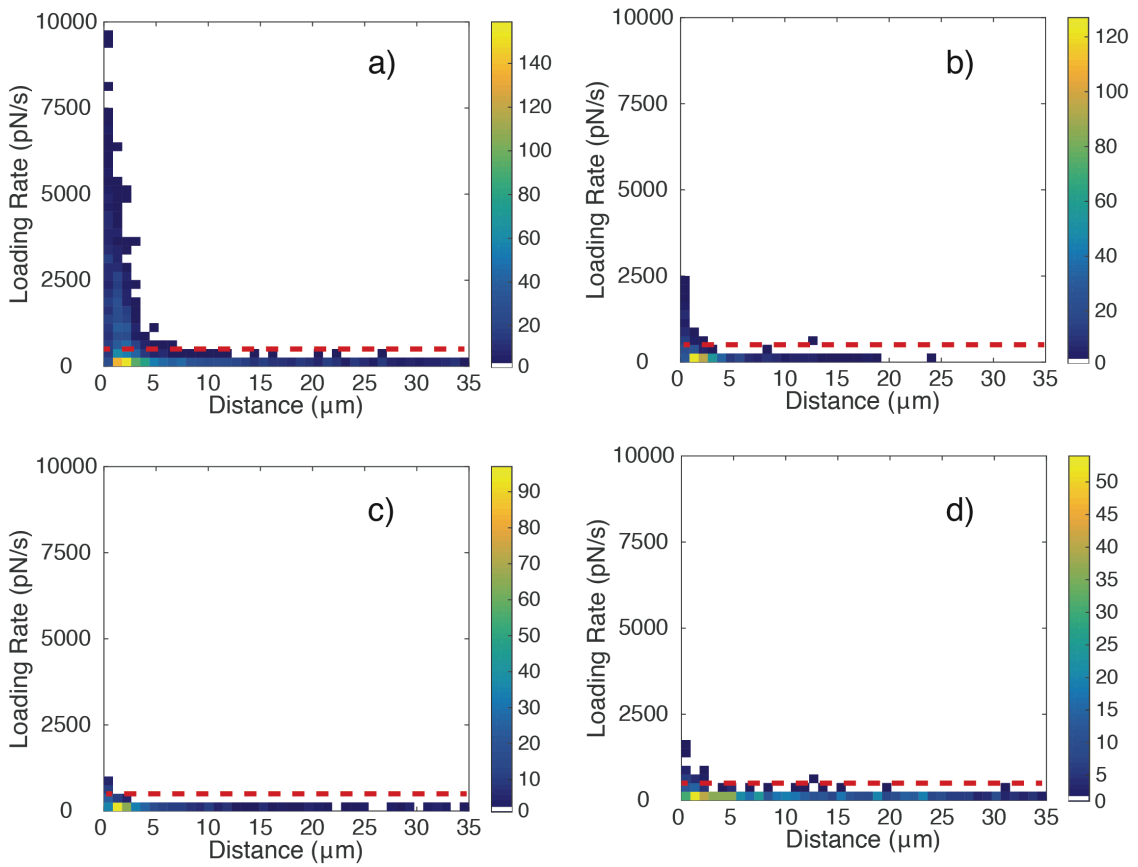

Figure 5.5 2D histograms of loading rate v. distance from the force curve analysis of 4 different SCFS experiments: a) HEK Mac-1 cells on 0.6 µg/ml fibrinogen, b) HEK Mac-1 cells on 20 µg/ml fibrinogen, c) antibody blocked HEK Mac-1 cells on 0.6 µg/ml fibrinogen, and d) HEK WT cells on 0.6 µg/ml fibrinogen. Events are classified into two types based on the loading rate preceding the rupture. Tether events have loading rates less than 250 pN/s, and force-load events have loading rates greater than 250 pN/s.

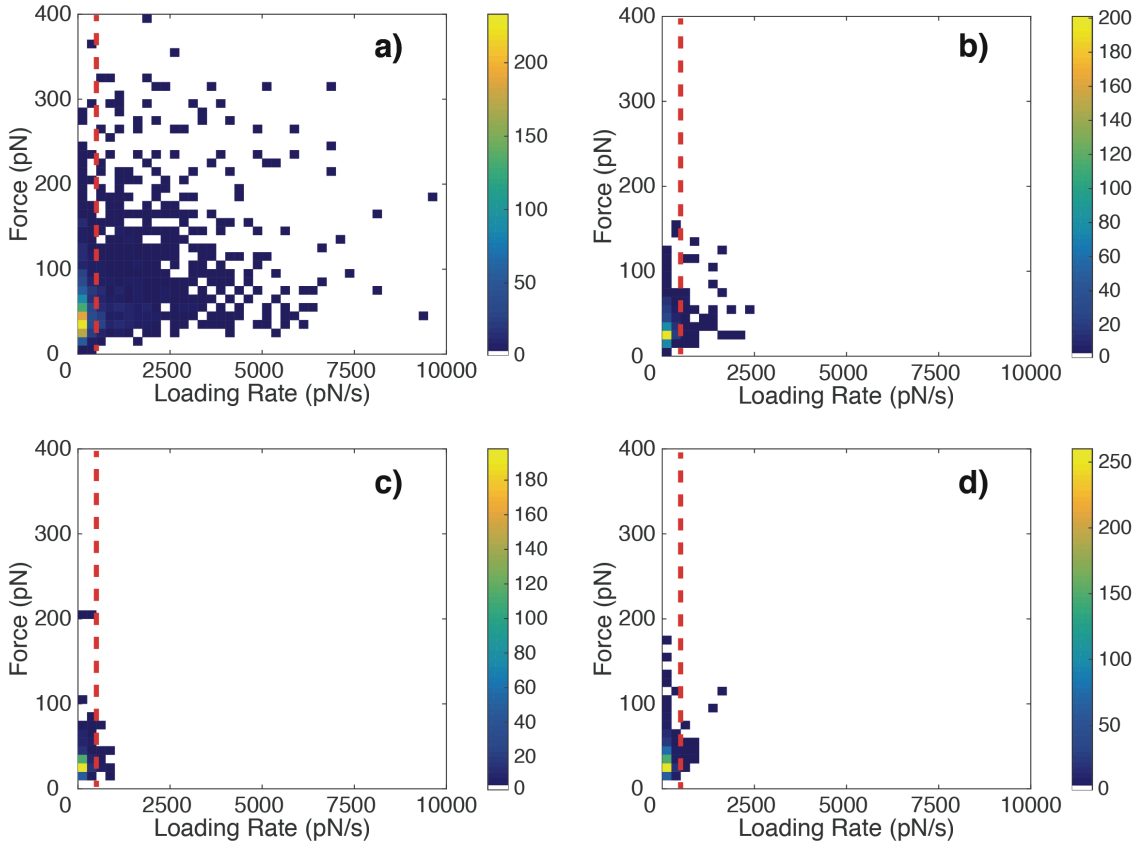

Figure 5.6 2D histograms of force v. loading rate for each experimental condition. a) HEK Mac-1 cells on 0.6 µg/ml fibrinogen, b) HEK Mac-1 cells on 20 µg/ml fibrinogen, c) antibody blocked HEK Mac-1 cells on 0.6 µg/ml fibrinogen, and d) WT HEK cells on 0.6 µg/ml fibrinogen. The force-load events in a) show a possible trend of increasing rupture force with increasing loading rate.

The 2D histograms in Fig. 5.5 and 5.6 show that HEK Mac-1 cells on 0.6 µg/ml fibrinogen have a large population of events with a loading rate greater than 250 pN/s. The noise in force measurements for these experiments was ~25 pN, and since we took a linear fit of data up to 200 nm preceding a rupture (with a retraction velocity of 2 µm/s, 200 nm represents 0.1 s), any loading rate less than 250 pN/s is indistinguishable from noise, and classified as a tether event. After categorizing rupture events based on their loading rate, it was found that force-load events (loading rate > 250 pN/s) comprise 40% of all ruptures for HEK Mac-1 cells on low fibrinogen concentration mica surfaces.

Force-load events accounted for 11% of all events for HEK Mac-1 cells on 20 μg/ml fibrinogen, 4% of all events for HEK WT cells on 0.6 μg/ml fibrinogen, and 6% of α_M blocked HEK Mac-1 cells on 0.6 μg/ml fibrinogen. Fig. 5.7 shows the rupture force probability distribution of force-load events for each condition normalized over all possible events for each condition. The most probable rupture force (MPRF) for force-load events in HEK Mac-1 on 0.6 μg/ml fibrinogen experiments was between 39 and 56 pN. The distributions force-load event forces for the control conditions all have MPRF within the range of 27 – 36 pN. This range of rupture forces could correspond to some interactions unaffiliated with the Mac-1:fibrinogen system. Table 5.1 contains the analysis for both classes of events for all experimental conditions. Since retraction speed was constant throughout all experiments, and cantilever spring constant was equivalent, the large population of high loading rate events in the experiments involving HEK Mac-1 cells on 0.6 μg/ml fibrinogen surfaces correspond to specific Mac-1:fibrinogen bonds.

Table 5.1 Statistics for the rupture events for each experimental condition. MPRF is most probable rupture force.

	Tether Events					Force-Load Events				
Experiment Condition	% Pop.	MPRF (pN)	Mean (pN)	Med. (pN)	St. Dev. (pN)	% Pop.	MPRF (pN)	Mean (pN)	Med. (pN)	St. Dev. (pN)
HEK Mac-1 on 0.6µg/ml fibrinogen	60	36	57	45	70	**40**	48	116	71	179
HEK Mac-1 on 20µg/ml fibrinogen	89	24	32	27	17	11	32	51	43	29
HEK Mac-1 mAb on 0.6µg/ml fibrinogen	94	25	30	28	14	6	27	42	30	37
HEK WT on 0.6µg/ml fibrinogen	96	27	34	30	17	4	36	43	42	22

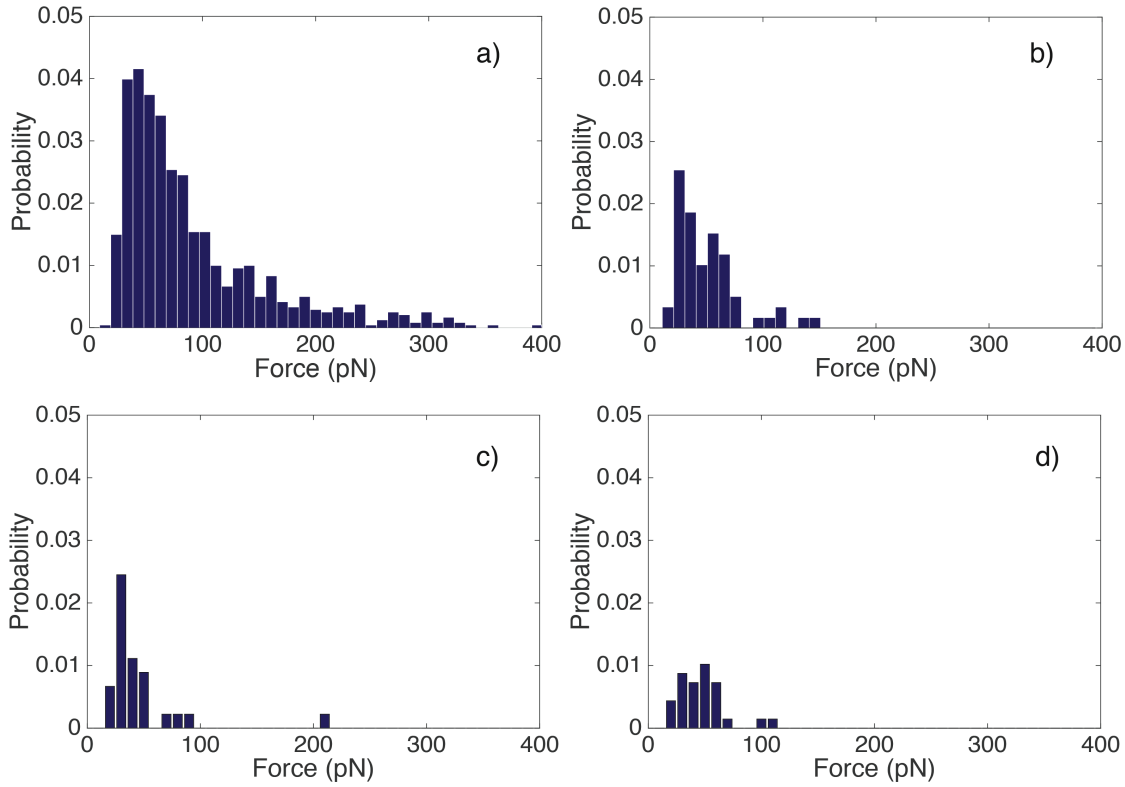

Figure 5.7 Probability distributions of force-load events for the different experimental conditions. a) HEK Mac-1 cells on 0.6 µg/ml fibrinogen, b) HEK Mac-1 cells on 20 µg/ml fibrinogen, c) antibody blocked HEK Mac-1 cells on 0.6 µg/ml fibrinogen, and d) WT HEK cells on 0.6 µg/ml fibrinogen.

5.5.5 Most Probable Rupture Force of Mac-1:Fibrinogen Bond

Fig. 5.8 shows the rupture force distribution for force-load events fitted with a kernel density fit in order to determine the most probable rupture force. A kernel density fit is currently considered the most appropriate fit for rupture force distributions [177, 179]. It is tempting to fit these distributions with multiple Gaussians, where each peak represents some multiple of the most probable rupture force of a single bond, however it has been shown that the rupture force of multiple bonds does not simply scale with the number of bonds involved [84]. Fitting the rupture force distributions with multiple Gaussians leaves gaps where expected peaks should be. While Fig. 5.6 shows the most

probable rupture force according to a kernel density fit of all force-load events for HEK Mac-1 on 0.6 µg/ml fibrinogen, Fig. 5.3 and 5.4 show that these force-load events cover a wide range of loading rates (250 – 6,500 pN/s). According to the standard Bell, Evans, and Ritchie model, the most probable rupture force should depend on the natural log of the bond loading rate and the kinetics of the molecular bond.

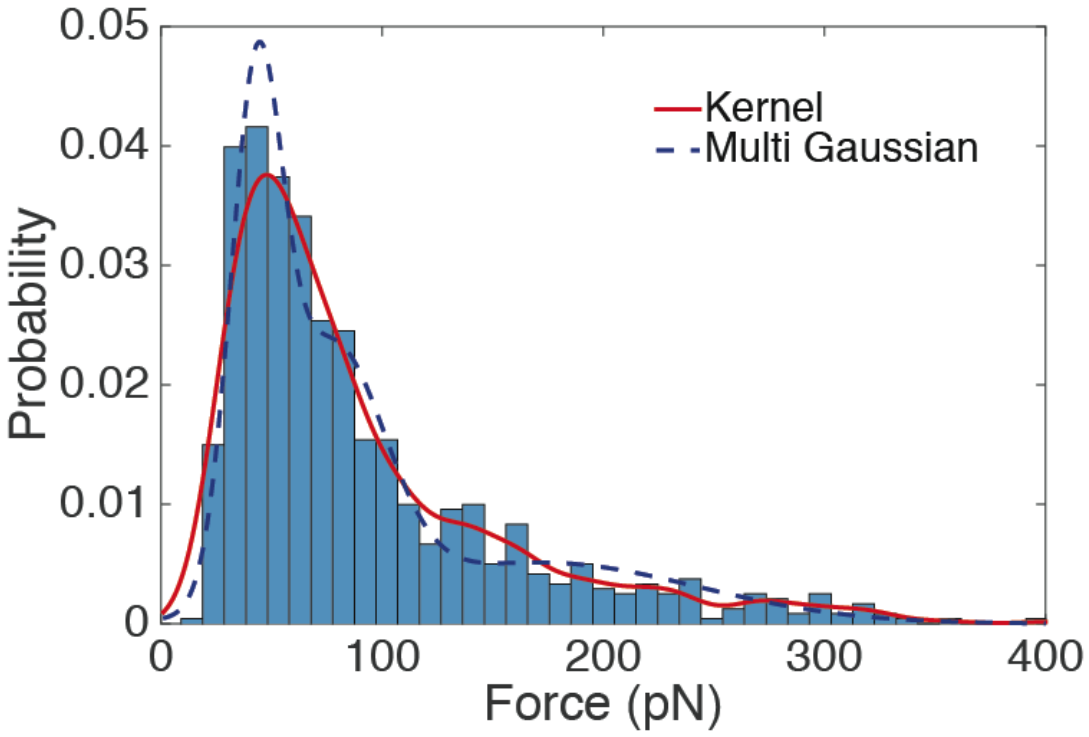

Figure 5.8 HEK Mac-1 on 0.6 µg/ml fibrinogen force-load events with different fitting parameters. Kernel fit gives most probable rupture force of 48 pN. Fitting distribution with 3 gaussians gives peaks at 43 pN, 77 pN and 172 pN. Fitting with 2 gaussians gives peaks at 56 pN and 154 pN (not shown).

5.5.6 Single Molecule Force Spectroscopy Theory

The background for SMFS theory was presented in §2.2.7 and §2.2.8. According to the standard Bell, Evans, and Ritchie model, the most probable rupture force has a linear relationship with the natural log of the loading rate according to

$$\hat{F} = \frac{k_B T}{x_\beta} \ln\left(\frac{x_\beta r}{k_{off}^0 k_B T}\right) \tag{1}$$

where r is the loading rate, k_B is Boltzmann's constant, T is the absolute temperature, k^0_{off} is the zero force off rate of the bond, and x_β is the disassociation length. k^0_{off} and x_β are kinetic parameters of the bond that can be determined by a linear fit of MPRF versus ln(r) data (Fig. 5.9a).

Dudko et al. describe the lifetime of bonds calculated from Kramers theory as

$$\tau(F) = \tau_0\left(1 - \frac{\nu F x_\beta}{\Delta G_\beta}\right)^{1-1/\nu} \exp\left[-\frac{\Delta G_\beta}{k_B T}\left(1 - \left(\frac{1-\nu F x_\beta}{\Delta G_\beta}\right)^{1/\nu}\right)\right] \tag{2}$$

which introduces a scaling factor ν that represents the underlying energy landscape of the bond and ΔG_β the apparent free energy of activation in the absence of an external force. We approximate $\nu = 1$ for this analysis because $\nu = 1$ provided the most stable fit of the data to (2), $\nu = 1$ corresponds to a single harmonic well. When $\nu = 1$, (2) simplifies to a linear relationship between the natural log of the bond lifetime and the mean rupture force in which k^0_{off} and x_β are fitting parameters ($1/\tau_0 = k^0_{off}$). The bond lifetime for a

given mean rupture force $\tau(F)$ can be found by approximating the force distribution for a given range of loading rates as a Gaussian, or by using ¾ of the interquartile range of the force distribution as outlined in §2.2.7. Fig. 5.9b shows the linear fit of the bond lifetime versus mean rupture force data.

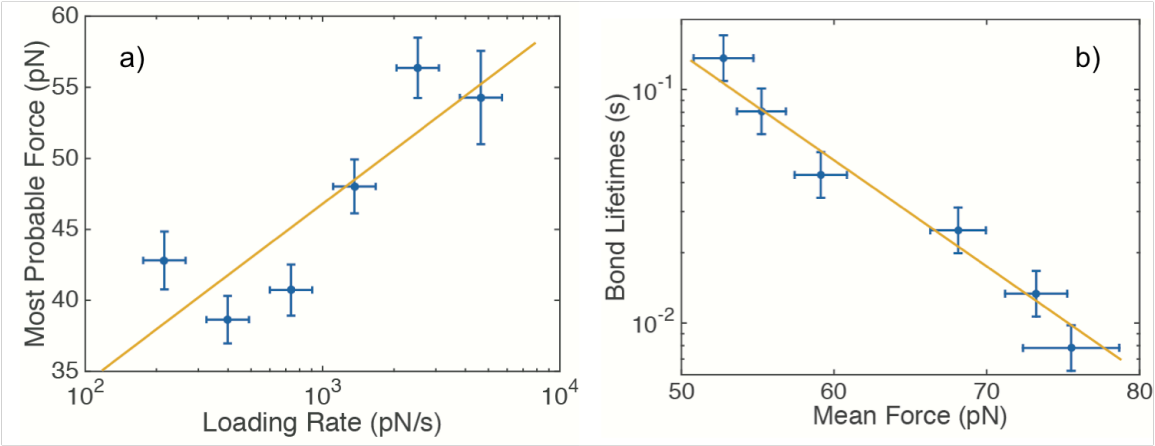

Figure 5.9 Two different methods for determing k^0_{off} and x_β. a) is the classic Bell-Evans method where the most probable rupture force is plotted against the logarithm of the loading rate. b) is based on the Dudko method using the interquartile range of the the force histograms to determine bond lifetimes.

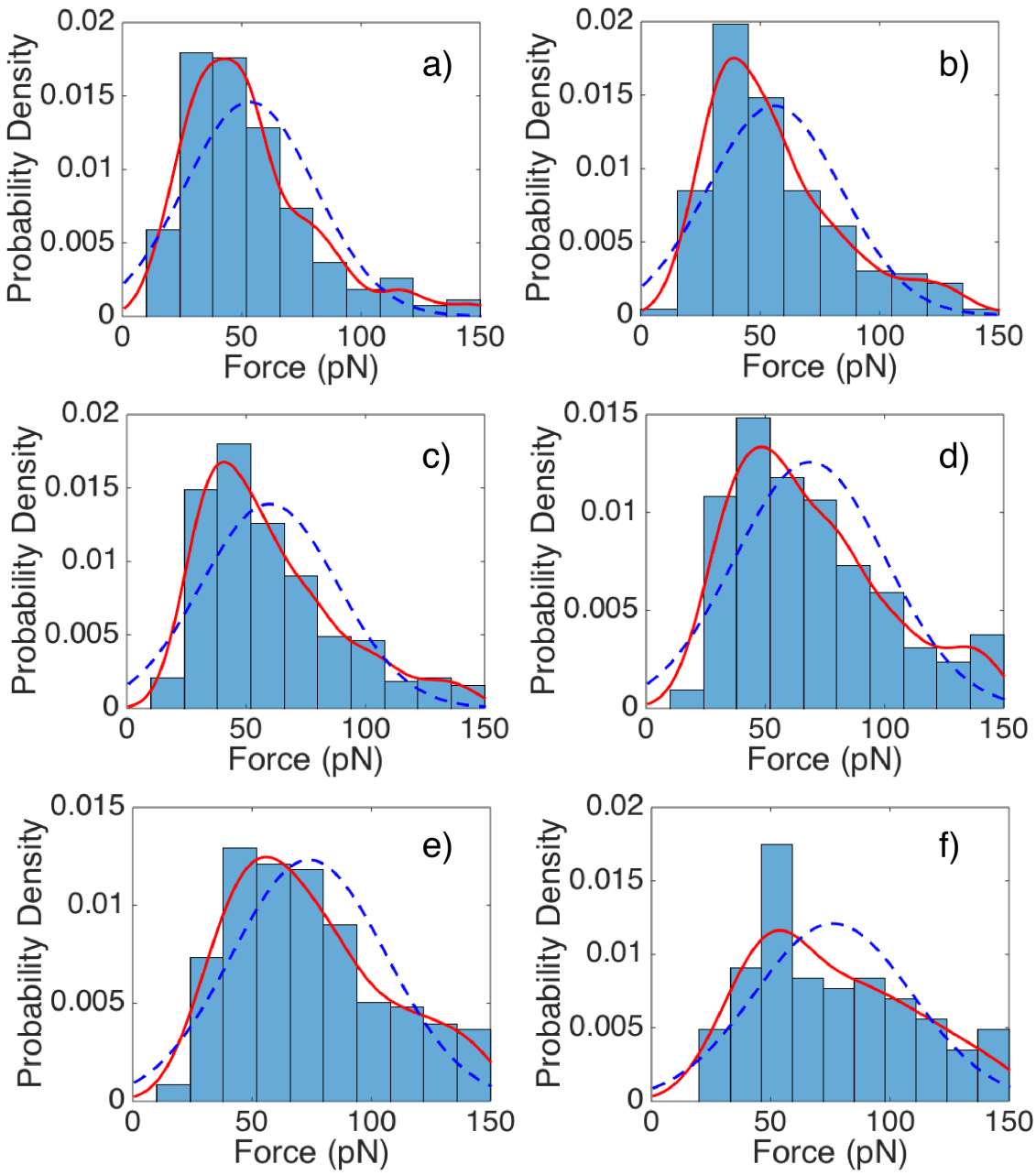

Figure 5.10 Rupture force distributions for each bin used to create 5.9. Red solid line is a Kernel density fit giving the most probable rupture force, and the blue dotted line is a Gaussian fit giving the mean rupture force. Each distribution corresponds to a different range of loading rates: a) is 200 pN/s – 300 pN/s, b) is 300 pN/s – 500 pN/s, c) is 500 pN/s – 900 pN/s, d) is 900 pN/s – 1700 pN/s, e) is 1700 pN/s – 3300 pN/s, and f) is 3300 pN/s – 6500 pN/s.

Dudko's method allows for the possibility of loading rates that are dependent on the applied force whereas the Bell-Evans requires the loading rate to be independent of the applied force. Because retraction velocity was held constant, the wide distribution in loading rates of force-load events for HEK Mac-1 on 0.6 μg/ml fibrinogen (see Fig. 5.5) is either due to a force dependent loading rate or variation in the effective spring constant of the system. We have approximated the loading rate using the slope of a linear fit preceding the rupture event as other researchers have done [175, 176]. It is known that integrins play a primary role in the formation of focal adhesions, and that focal adhesion sites will actively grow in response to force to maintain a constant stress on the focal adhesion site, and this response begins in a matter of seconds [41]. Mac-1 integrins are known to play an important role in FAs [37, 38], and whether this active recruitment of additional integrins to the focal adhesion site effects the loading rate of a specific integrin bond remains to be seen.

5.5.7 Determining the Kinetics of Mac-1:Fibrinogen Bonds

There may be several intermediate states of Mac-1 activation when bonded to immobilized fibrinogen. A previous study [122] has shown that Mac-1 integrins will bind to fibrinogen molecules on surfaces of high concentrations of fibrinogen (> 2 μg/ml), but because of the extensibility of the multilayered fibrinogen matrix that forms from sufficiently high concentrations of fibrinogen, Mac-1 was unable to generate any tensile force. Without the tensile force from the Mac-1:fibrinogen bond, the Mac-1 integrins appeared to be unable to anchor into the cell cytoskeleton, and Mac-1:fibrinogen pairs were able to diffuse on the cell membrane. The state of the Mac-1 connection to the cellular cytoskeleton no doubt influences the loading rate on the Mac-1:fibrinogen bond

when acted upon by an external applied force. Despite the complexities involved with the loading rate of single Mac-1:fibrinogen bonds in living cells, we can still make a general approximation for the kinetic parameters from the Bell model using either the Evans-Ritchie method or the Dudko method.

Table 5.2 shows the estimates for the kinetic parameters using both the Evans-Ritchie model and the Dudko method. We estimate a disassociation length between 0.51 and 0.95 nm, and an off rate ~0.02 s^{-1}. The off rate has a very wide deviation, however, as it is the most sensitive parameter in these fitting methods. While estimates for these parameters for Mac-1:fibrinogen bonds can not be found in the literature, there are several estimates for other integrins known to bind with fibrinogen, as well as Mac-1 bonds with other ligands. In an experiment with fibrinogen attached to an AFM tip, Carvalho et al. measured the interaction between platelets and fibrinogen, and determined k^0_{off} and x_β to be 0.034 s^{-1} and 0.1 nm respectively [180]. $\alpha_{IIb}\beta_3$ is the major integrin on platelets that binds with fibrinogen. Several other studies using various methods give a range of values between 0.052 and 2.42 s^{-1} for k^0_{off} of $\alpha_{IIb}\beta_3$:fibrinogen bonds, and a range between 0.01 and 0.8 nm for x_β of $\alpha_{IIb}\beta_3$:fibrinogen bonds [173, 181-183]. Yang et al. determined k^0_{off} and x_β between Mac-1 and intercellular adhesion molecule 1 (ICAM-1) via SMFS to be 0.49 ± 0.23 s^{-1} and 0.18 ± 0.01 nm respectively [184]. Several other studies of the same bond using other methods give a range of values between 0.12 and 1.3 s^{-1} for k^0_{off} and 0.053 and 0.23 nm for x_β [185-189]. x_β is dependent on the loading rate of the bond, and will vary accordingly. Each of these studies uses a different

methodology for dynamically extending these molecular bonds, and so direct comparisons of x_β are questionable. Because soluble fibrinogen not known to interact with Mac-1, there have been no quantifications of Mac-1:fibrinogen bond kinetics. The values found for the kinetic parameters for Mac-1:fibrinogen bonds in this study fall within the range of data for Mac-1 interactions with other ligands, and fibrinogen interactions with other receptors.

Table 5.2 Estimates for kinetic parameters x_β and k^0_{off} based on the Bell-Evans method and Dudko methods.

Fitting Method	x_β (nm)	k^0_{off} (s^{-1})
Evans-Ritchie	0.95±0.39	0.01±0.20
Dudko (mean)	0.55±0.08	0.01±0.23
Dudko (interquartile range)	0.51±0.06	0.02±0.23

5.5.8 Verifying Mac-1:Fibrinogen Bond Specificity

As another control to verify whether the high loading rate ruptures were indeed indicative of Mac-1-fibrinogen bond disassociations, we fluorescently labeled fibrinogen proteins and incubated them on glass at very low concentrations. At sufficiently low concentrations (0.01 μg/ml), single fibrinogen molecules were well dispersed and spaced further than the diffraction limit for single molecules. Total internal reflection fluorescence microscopy (TIRFM) images can then be made of the surface, and individual fibrinogen molecules could be counted with the particle analysis tool in

ImageJ after the image has been binarized. Fig. 5.11 shows a representative before and after binarized image of the fluorescent fibrinogen molecules. Fibrinogen molecules were counted in the region of contact between HEK Mac-1 cells and the surface before and after the cells were pressed on the surface. There was no significant difference in the number of fibrinogen molecules after a HEK Mac-1 cell made contact with the surface despite the typical occurrence of high loading rate rupture events in the force distance curves. This indicates that the high loading rate ruptures are not the result of pulling fibrinogen molecules off the surface. The results here are in agreement with a study by Gergely et al. that showed the unbinding of fibrinogen from a silica based surface required 180 – 1000 pN for loading rates comparable to those in this study [190].

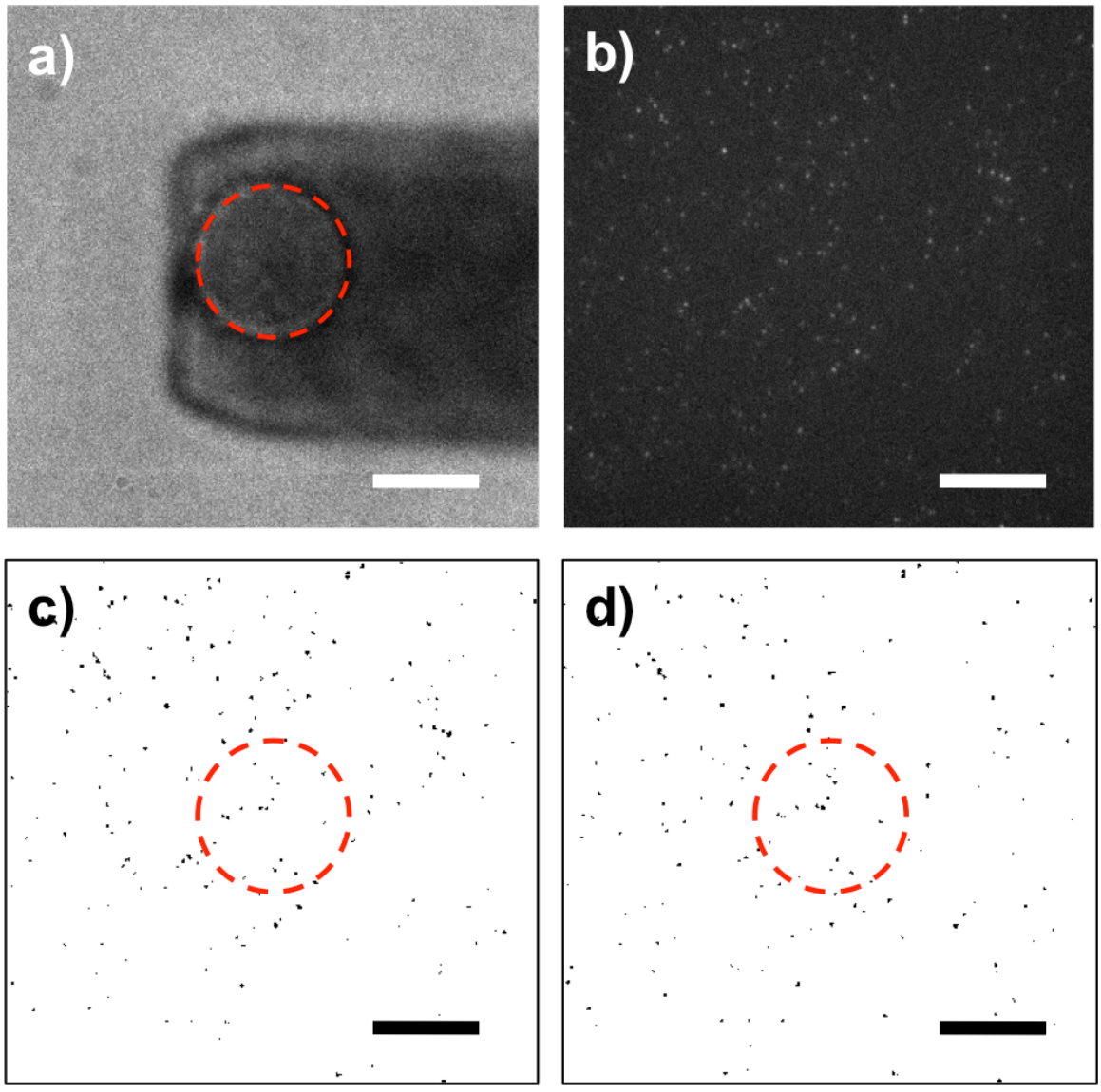

Figure 5.9 SCFS performed on a sub-monolayer of Alexa647 fluorescently labeled fibrinogen. A bright filed image of the cell (a) was used to determine the position of the cell. Particle analysis of binary images of the surface before cell contact (c) and after cell contact (d) was used to determine if a significant number of fibrinogen molecules were removed from the surface by the cell. Scale bars are 10 μm.

5.6 Conclusions

There are many types of interactions that can take place in a SCFS experiment. We have shown through rigorous control experiments and data analysis, populations of

specific molecular bond interactions can be isolated. I estimated the kinetic parameters of these specific molecular bonds, namely the Mac-1:fibrinogen bond using a linear fit of data preceding a force-load event to determine the loading rate of the bond. This linear fit showed a range of loading rates from force-load events from 250 pN/s to 6500 pN/s despite a constant retraction velocity of 2 μm/s. The cause of this large range of loading rates remains to be seen.

We were also able to quantify the unbinding force of specific Mac-1:fibrinogen bonds while the Mac-1 integrin was in its native membrane environment. The MPRF of Mac-1:fibrinogen bonds at a retraction velocities of 2 μm/s was 48 pN in these experiments. This methodology can be used to determine MPRF of other native cellular adhesion proteins at different retraction velocities in order to determine more accurate binding kinetics for proteins in their native cellular membrane environment.

6 Quantifying Adhesion of Platelets and Neutrophils to Fibrin Gels

6.1 Acknowledgments

This chapter examines the adhesion of human platelets and neutrophils to fibrin gels with various concentrations of fibrinogen. I conducted the SCFS experiments, and analyzed the data. Hadil Owaynat and Valeryi Lishko prepared fibrin gels for experiments. Nataly Podolnikova isolated platelets and neutrophils, and prepared thrombus samples. Tatiana Ugarova and Robert Ros designed experiments.

6.2 Abstract

Platelet adhesion is the first step of hemostasis and thrombi formation. Thrombi formation has been demonstrated to end with a fibrin cap on the surface of the thrombi. Platelets and leukocytes are known to adhere to fibrin *in vitro*, however fibrin capped thrombi *in vivo* show little or no accumulation of additional platelets. We previously demonstrated that intact fibrinogen adsorbed on the surface of fibrin capped thrombi acts as a natural anti-adhesive coating stabilizing the thombi. Using fibrin gels as a model of this fibrin cap, we quantify the adhesion of platelets and neutrophils to fibrin using AFM based SCFS, and quantify the anti-adhesive effect of multi-layered fibrinogen on the fibrin gels. Platelet adhesion on fibrin gels was 6 ± 2 nN, and addition of multi-layered fibrinogen reduced adhesion to 3 ± 2 nN. Neutrophil adhesion on fibrin gels was 1.0 ± 0.6 nN, and was reduced to 0.2 ± 0.2 nN after multi-layered fibrinogen was applied to the fibrin gel. We verified that multilayered fibrinogen acts as a natural ant-adhesive mechanism for thrombi by quantifying the adhesion of microbeads to thrombi formed *in*

situ. Microbeads adhered to fibrin gels with 1.5 ± 0.4 nN, and 0.19 ± 0.08 nN to fibrinogen coated thrombi.

6.3 Introduction

Platelets play a central role in blood vessel injury repair by initiating hemostasis and thrombosis after adhesion to altered endothelial cells or exposed ECM substrates [191-193]. This initial adhesion is also a critical step in inflammatory [194], and immunopathogenic responses [195]. After intial adhesion, platelets recruit additional platelets and leukocytes to the site of injury beginning the formation of a hemostatic plug [193]. The formation of arterial thrombi follows a similar process as that of hemostatic plugs [196] resulting in a mass of platelets supported by a fibrin mesh. Recently, it has been shown that *in vivo* formed thrombi are capped by a layer of polymerized fibrin free of platelet aggregation [197, 198]. *In vitro* experiments have demonstrated polymerized fibrin is highly adhesive to platelets [29, 199, 200]. We have proposed that a multi-layered fibrinogen matrix as a cap of the fibrin gel is responsible the discrepancy between *in vivo* observations and *in vitro* experiments [33, 34, 170, 201].

It has previously been shown that intact fibrinogen on the surface of fibrin-rich thrombi generated from flowing blood does indeed act as an anti-adhesive agent for platelets [202]. In this study, using fibrin gels as a model of fibrin-rich thrombi [203], we quantify the adhesion of platelets and neutrophils to fibrin gels and fibrinogen coated fibrin gels using AFM based SCFS. Additionally we quantify the adhesion of glass microbeads to fibrin gels and fibrinogen coated fibrin gels as well as the adhesion of microbeads to fibrinogen coated thrombi using AFM based force spectroscopy.

AFM based SCFS is a valuable tool for quantifying integrin mediated adhesion of cells on surfaces [48, 170], as shown in §3, §4, and §5. AFM based SCFS has been used recently to quantify the adhesion of red blood cells to subendothelial matrix laminin [45], and to quantify contractile force of activated platelets on fibrinogen [204]. Nguyen et al. quantified the rupture forces of platelets from collagen, poly-l-lysene (PLL), and fibronectin, as well as the rupture force of platelets from other platelets [205]. One aspect of SCFS with platelets, that is not addressed in Nguyen et al.'s study, is that the size of platelets (1-2 μm in diameter) makes it difficult to exclude direct cantilever interactions with the surface. We address this issue by adhering the platelets to the apex of a 5 μm diameter glass microbead that has been attached to the end of a tipless AFM cantilever. This method has been used by Beaussart et al. for SCFS experiments of microbial cells that are on the same size scale as platelets [206].

6.4 Methods

6.4.1 Materials

Human thrombin and fibrinogen, depleted of fibronectin and plasminogen, were obtained from Enzyme Research Laboratories (South Bend, IN). mAb 7E3 was a gift from Dr. B. Coller. D-phenylalanyl-Lprolyl-L-arginine chloromethyl ketone (PPACK) was from Haematologic Technologies Inc. (Essex Junction, VT). Platelets and neutrophils were collected from fresh aspirin free human blood in the presence of 2.8 μM prostaglandin E_1 and isolated by differential centrifugation. Platelets were labeled with CellMask^{TM} (Thermo Fisher, MA) deep red plasma membrane stain for 30 min, and then washed and suspended in Tyrode's solution.

6.4.2 Fibrin Gel Preparation

Fibrin gels were formed in by mixing 100 μL aliquots of 1.5 mg/mL fibrinogen in HBSS with thrombin (0.15 unit/mL), pipetting the solution on 35 mm dishes (FluoroDish; World Precision Instruments, Sarasota, FL), and incubating for 2 h at 37 º C. After polymerization, the thrombin activity was quenched by addition of PPACK. For fibrin gel + fibrinogen experiments, the fibrin gels were incubated with 1.5 mg/mL of soluble fibrinogen for 30 min at 37 º C. Gels were then rinsed and kept hydrated in HBSS buffer.

6.4.3 Thrombi Preparation

Glass coverslips (22 × 22 mm) were plasma cleaned and incubated with a solution of rat tail collagen type I (BD Biosciences, Bedford, MA) at 3.5 mg/mL. Glass coverslips were placed in a parallel plate flow chamber (flow path of 4 mm width, 16 mm length and 0.13 mm height), and the chamber was assembled for perfusion studies. Blood for perfusions was treated with 6 μM argatroban. Blood was then drawn for 15 min through the chamber by a Harvard Apparatus pump producing estimated shear rate of1500 s−1. 100 μM PPACK was then perfused over the formed thrombi at 300–1500 s−1 for 15 min to inactivate thrombin generated on the surface of thrombi, and 1.5 mg/ml fibrinogen was then perfused over the formed thrombi.

6.4.4 AFM Cantilever Preparation

Tipless silicon nitride cantilevers (HYDRA, App-Nano, Santa Clara, CA) were prepared according to our previously established method [34]. For platelet SCFS experiments, a 5 μm diameter glass bead was glued to the end of the cantilever.

Cantilevers were plasma-cleaned in O_2 gas using a plasma cleaner (PDC-001, Harrick Plasma, Ithaca, NY). Beadless cantilevers were then incubated in 0.04 mM APTES ((3-amino-propyl)triethoxysilane) in chloroform solution for 40 min. Cantilevers with beads were incubated in 2 mM APTES in ethanol. After rinsing the cantilevers with chloroform, then ethanol, and then Millipore-quality water, the cantilevers were incubated in 1.25 mM bis(sulfosuccinimidyl)suberate sodium salt (BS^3, Sigma) solution for 30 min followed by 30 min of incubation in a 0.5 mg/mL concanavalin A (Sigma) solution. All incubation steps were at 22º C. Cantilevers were stored in 1 M NaCl at 4º C.

6.4.5 Adhesion Experiments

Cantilever spring constants and optical lever sensitivity were calibrated prior to each experiment using a built in thermal noise method on the MFP-3D AFM (Asylum Research, Santa Barbara, CA). The spring constant for cantilevers were near the manufacturers nominal spring constant of 0.035 N/m. Force-distance measurements were performed using the MFP-3D. The MFP-3D is part of a combined optical set-up on top of an inverted microscope (IX71, Olympus). This set-up allows for the monitoring of platelets during capture, and during force-distance measurements. Platelets were fluorescently labeled and illuminated with a 640 nm diode laser (LDH-D-C-640, PicoQuant) to make them easier to identify and capture. The cantilever was manually lowered onto platelets, and positioned so that the platelet would adhere to the apex of the microbead just before the platelet made contact with the surface. Platelets were then lifted away from the surface, and allowed 1 min to adhere to the bead. Beadless cantilevers were used to manually capture neutrophil cells as has been described in previous SCFS experiments [170]. Immediately after pipetting the cells, the AFM cantilever was

manually aligned above the cell, and then brought into contact with the cell for 5-30 s. The cell was then lifted from the surface, and allowed to firmly attach to the cantilever for 2 min.

For the fibrin gel and thrombi adhesion measurements, an uncoated 5μm diameter microbead attached to a tipless cantilever was used to generate adhesion maps of the surface. 100 force curves over a 90 μm^2 area were generated for adhesion maps on fibrin gels. Adhesion maps on thrombi were made of the 90 μm^2 area encompassing the body of the thrombus using 900 force curves, and the 45 μm^2 area encompassing the tail of the thrombus using 450 force curves. Each force-distance measurement for all experiments was performed using an approach and retract velocity of 2000 nm/s and a trigger force of 2 nN. Cells and platelets dwelled on the surface for < 1 s – 15 s. Z-position was held constant during the dwell time. All experiments were done at 37º C.

6.4.6 Data Analysis

All force curves were analyzed using a custom algorithm in MATLAB, which adjusted the baseline deflection of all curves, and extracted the minimum force value of the force-distance curve as the maximum adhesion value. For the thrombi and fibrin gel adhesion measurements, this process was automated. Only force distance curves that corresponded to a location on the adhesion map of thrombi above a height of 10 μm were considered on the body or the tail of the thrombi. The force-distance curves for the platelet and neutrophil SCFS experiments were expected manually. Statistal analysis was done with Wilcoxon rank sum test in MATLAB.

6.5 Results

6.5.1 Quantifying Adhesion of Microbead on Fibrin Gel

In previous studies, fibrin gel has been used as a material that is more representative of physiological conditions than materials such as glass, plastic, or mica used for typical adhesion assays [29, 33, 203]. It was shown that fibrinogen coated fibrin gels inhibits the spreading of platelets [29], and the mechanism for this inhibition was hypothesized to be a result of an extensible fibrinogen matrix that is unable to offer resistance to cytoskeleton pulling. We quantified the adhesion of glass microbeads to fibrin gels and fibrin gels coated with 1.5 mg/ml fibrinogen. The bead on fibrin gel showed a maximum adhesion of 1.5 ± 0.4 nN, while fibrin gel coated with 1.5 mg/ml fibrinogen showed a maximum adhesion of 0.3 ± 0.3 nN (Fig. 6.1c). A trigger force of 2 nN was used to indent the fibrin gels. This trigger force resulted in an indentation depth of between 50 nm and 300 nm. The adhesion measurements in this experiment provide further evidence for the anti-adhesive effect of multi-layered fibrinogen.

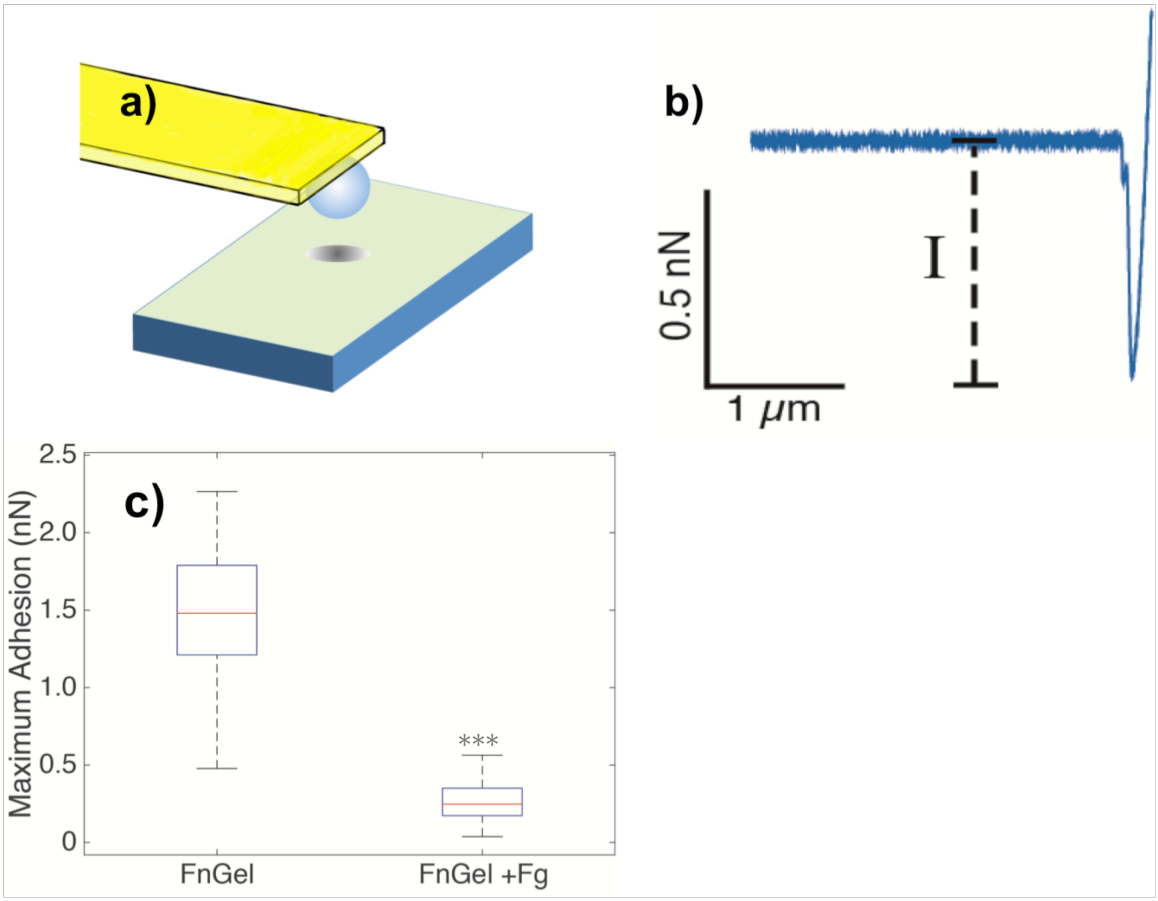

Figure 6.1. a) schematic of a 5 µm diameter microbead attached to a tipless AFM cantilever for adhesion measurements on fibrin gels. b) typical retraction portion of a force-extension curve from an adhesion measurement. The maximum adhesion is shown by I. c) experimental results of AFM based adhesion measurements of 5 µm diameter beads on fibrin gel with and without a coating of fibrinogen. 100 force curves in a 90 x 90 µm area of the fibrin gel for each condition were acquired. The maximum adhesion on uncoated fibrin gel was 1.5 ± 0.4 nN, and 0.3 ± 0.3 nN on fibrin gel coated with 1.5 mg/ml fibrinogen. ***$p<0.001$ determined by Wilcoxon rank-sum test.

6.5.2 SCFS of Platelets on Fibrin Gels

The size of platelets (1-2 µm diameter) presents a challenge for SCFS experiments. If a tipless cantilever is used, then it becomes impossible to ensure that there are no cantilever interactions with the surface, which result in false adhesion values. To avoid this complication, and to be certain we were only measuring the adhesion of the

platelet to the gel, we followed a technique proposed by Beaussart et al. for SCFS of microbial cells [206]. We attached a 5 μm diameter glass bead to the end of a tipless cantilever, and then adhered platelets to the apex of the glass bead as shown in Fig. 6.2a and 6.2b. Platelet force-distance curves were generated with short (<1)s surface dwell times, and 15 s dwell times (Fig. 6.2c) with a 2 nN trigger force. Platelet activation occurs very quickly after contact with fibrinogen [207], and these experiments demonstrate that the anti-adhesive effect of multi-layered fibrinogen persists even after possible platelet activation.

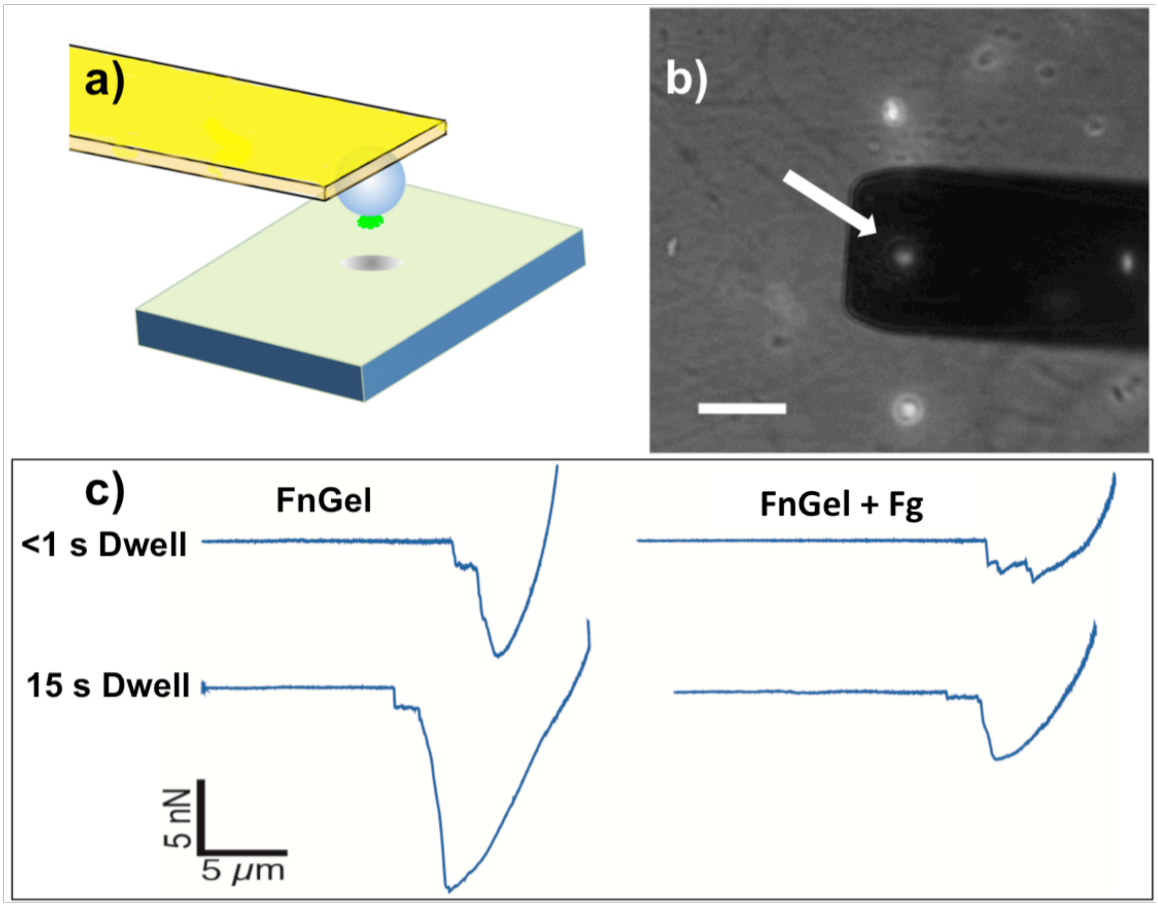

Figure 6.2. a) schematic of the platelet adhesion experiment. b) combined bright field and fluorescent microsopy image of fluorescently labeled platelet attached to the glass microbead. Adhering the platelet to the apex of the microbead is necessary to insure that the cantilever does not come in contact with the surface, and that only the adhesion of the platelet to the surface is measured. Scale bar is 15 µm. c) representative force-extension curves of platelets on uncoated fibrin gels for <1 s and 15 s dwell times respectively as well as representative curves on fibrinogen coated gels.

We quantified the adhesion of platelets on fibrin gels. Platelets with <1 s dwell time on fibrin gel showed a maximum adhesion of 6 ± 2 nN, and 12 ± 3 nN for 15 s dwell time. A coating of 1.5 µg/ml fibrinogen reduced adhesion by ~50% (3 ± 2 nN for <1 s dwell and 5 ± 3 nN for 15 s dwell). Platelets incubated with a mAb acting on the $\alpha_{IIb}\beta_3$ integrin showed similar results to the platelets on the fibrinogen coated fibrin gel. This indicates that the multi-layered fibrinogen is preventing $\alpha_{IIb}\beta_3$ signalling.

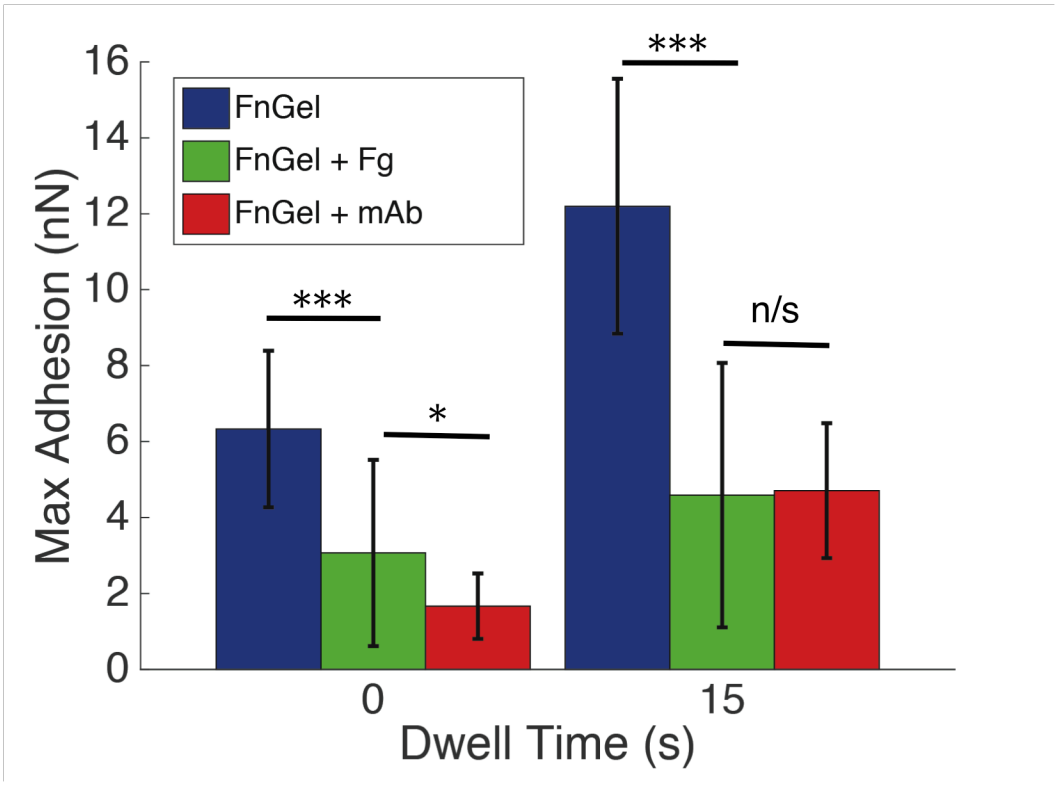

Figure 6.3. The results of platelet adhesion measurements on uncoated fibrin gel (blue), fibrin gel coated with 1.5 mg/ml fibrinogen (green), and platelets blocked with mAb on uncoated fibrin gel (red). 15 platelets were measured on uncoated fibrin gel. 11 platelets were measured on fibrinogen coated fibrin gel. 11 platelets being blocked with mAb were measured on uncoated fibrin gel. Each platelet generated ~5 force-curves. Platelets on uncoated fibrin gel had a maximum adhesion value of 6 ± 2 nN for <1 s dwell and 12 ± 3 nN for 15 s dwell. Platelets on fibrinogen coated fibrin gel had maximum adhesion value of 3 ± 2 nN for <1 s dwell and 5 ± 3 nN for 15 s dwell. mAb blocked platelets on uncoated fibrin gel had a maximum adhesion value of 2 ± 1 nN for <1 s dwell and 5 ± 2 nN for 15 s dwell. *$p<0.05$ and ***$p<0.001$ according to Wilcoxon rank-sum test.

6.5.3 SCFS of Neutrophils on Fibrin Gels

Neutrophil cells are some of the first responders to infection or vascular damage [21, 23]. They are highly motile, and depend on Mac-1 integrins for adhesion and migration [118, 208]. Mac-1:fibrinogen bonds were extensively studied in §6. We quantified the adhesion of neutrophil cells on fibrin gels and fibrinogen coated fibrin gels. Results showed a maximum adhesion of 1.0 ± 0.6 nN for short dwell times and 3 ± 2 nN

for 15 s dwell time on fibrin gels (Fig 6.4b). 1.5 µg/ml fibrinogen coated fibrin gels reduce neutrophil adhesion almost entirely with a maximum adhesion of 0.2 ± 0.2 nN for short dwell times and 0.7 ± 0.7 nN for 15 s dwell (Fig 6.4b). These findings are consistent with a previous study on the anti-adhesive effect of fibrinogen on fibrin gels for neutrophils [33].

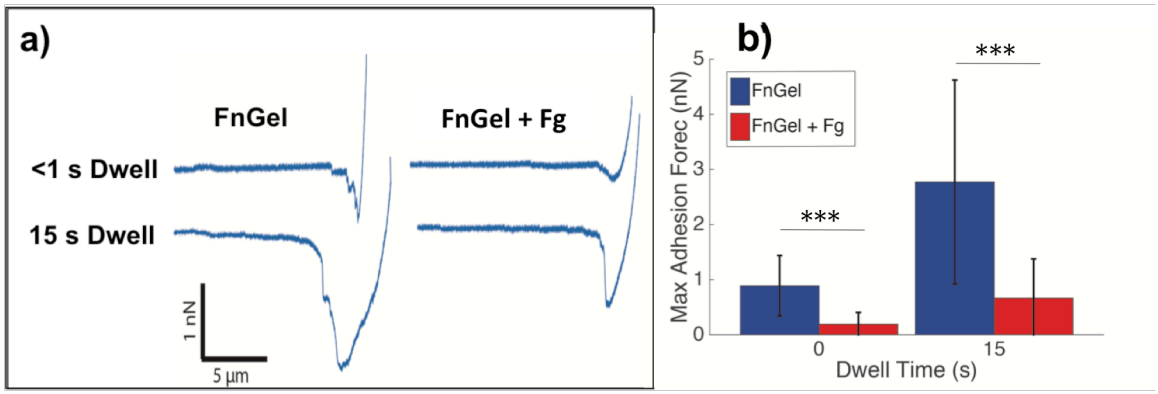

Figure 6.4. a) example retraction portions of force-extension curves from neutrophil adhesion experiments. b) results of neutrophil adhesion experiments on fibrin gel with and without 1.5 mg/ml fibrinogen coating. 12 neutrophils were measured for each surface type, and ~ 6 force-curves were generated per cell. Maximum adhesion was 1.0 ± 0.6 nN and 3 ± 2 nN on uncoated fibrin gel for <1 s dwell and 15 s dwell respectively. On fibrinogen coated fibrin gel, maximum adhesion was 0.2 ± 0.2 nN and 0.7 ± 0.7 nN for <1 s dwell and 15 s dwell respectively. ***p<0.001 according to Wilcoxon rank-sum test.

6.5.4 Quantifying Adhesion of Microbeads to Thrombi

Fibrin gels were used in this study because it has been recently shown that a fibrin shell forms on the surface of thrombi near the end of thrombi formation, and is critical to the stability of the thrombus [197, 198, 202]. While fibrin supports strong integrin-mediated adhesion of platelets *in vitro* [29, 199, 200] fibrin capped thrombi *in vivo* do not show an accumulation of platelets [197, 198]. Previously it was shown that thrombi coated with fibrinogen have an anti-adhesive effect on platelets [202]. In this study, we quantified that anti-adhesive effect by measuring the adhesion of a glass microbead to

fibrinogen coated thrombi with AFM based force spectroscopy. In the previous study, fluorescently labeled fibrinogen was used, and imaging revealed that the fibrinogen settles onto thrombi in a punctate manner [202]. We generated force-distance curves over the characteristic thrombi globules referred to as the thrombus "body," and over the long fibrin "tails" protruding from the thrombus body (Fig. 6.5a). Here we show that the main body of a thrombus is less adhesive (0.19 ± 0.08 nN) than the tail of a thrombus (0.6 ± 0.4 nN, Fig. 6.5c). Despite the difference in adhesion from different parts of the thrombus, both parts of the thrombus were significantly ($p<0.001$) less adhesive then fibrin gel (1.5 nN ± 0.4 nN, Fig. 6.1c). The difference in adhesion between thrombus bodies and tails is likely due to the punctate manner of fibrinogen adsorption, with the thrombus body creating disruptive flow conditions preventing full fibrinogen adsorption on the tails.

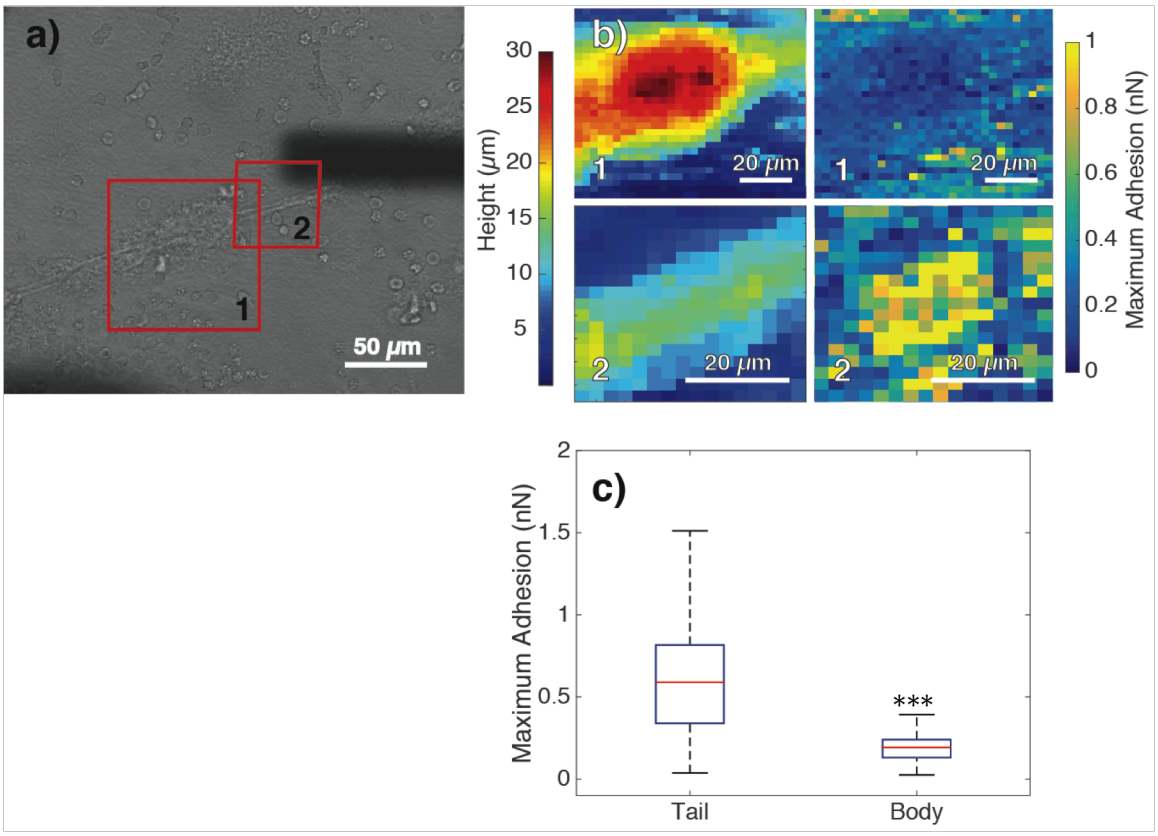

Figure 6.5 a) brightfield image of thrombi. b) height maps and adhesion maps of the inset on a thrombus body and tail in a). c) boxplot of data from adhesion maps of 2 different thrombus bodies and 2 different thrombus tails. Pixel sizes in the height and adhesion maps are 9 μm^2. For each map, the adhesion data for c are taken from pixels corresponding to pixels from the height map above a height threshold of 10 μm to ensure only measurments on the thrombus are taken. Thrombus body mean maximum adhesion value was 0.19 ± 0.08 nN and thrombus tail mean maximum adhesion value was 0.6 ± 0.4 nN. ***$p<0.001$ according to Wilcoxon rank-sum test.

6.6 Discussion

We quantified the adhesion force of platelets and neutrophils on fibrin gel and fibrinogen coated gel. The fibrinogen coated gel decreased adhesion forces by ~50%. Platelets and neutrophils that were allowed to dwell on the fibrin gel surfaces had their maximum adehsion values significantly ($p<0.001$) double. On fibrinogen coated fibrin gels, although the mean maximum adhesion value doubled for the platelets, Wilcoxon rank-sum test showed no significant difference in data populations. Platelets on

fibrinogen coated fibrin gels showed a larger range of maximum adhesion values. This suggests that some activation and spreading is occurring in platelets, and although maximum adhesion increases on multilayered fibrinogen over time, it is still ~50% less than platelets on fibrin gels over the same amount of time.

Interestingly, platelets showed higher absolute adhesion forces on the fibrin gels than neutrophils (Figs. 6.3 and 6.4a) despite the smaller surface area that platelets present on the fibrin gel. This could be due to the higher elastic modulus of platelets as opposed to neutrophils [209]. A high density of cytoskeletal filaments may be able to generate contractile forces on a shorter time scale in platelets as compared to neutrophils. Indeed, Lam et al. demonstrated that platelets are capable contractile forces of up to 72 nN, and this contraction happens nearly instantaneously upon contact with a fibrinogen surface in SCFS experiments [204]. In Lam et al.'s study, platelet adhesion to fibrinogen surfaces was quantified, and they found that the maximum adhesion for platelets after adhering to the fibrinogen surface for 15 min was 69.0 ± 12.7 nN [204]. The surface concentration of fibrinogen in Lam et al.'s study was not determined, but they incubated a glass surface for 30 min in a solution of 20 μg/ml fibrinogen. We previously showed that mica incubated in a solution of 20 μg/ml fibrinogen for 3 hours produced a multilayerd fibrinogen surface [35], so 30 min may have not been enough time to form multilayered anti-adhesive surface. Surface plasmon resonance from a previous study [33] demonstrated that the amount of time for a surface to adsorb a maximum fibrinogen saturation was concentration dependent, and that a concentration of 20 μg/ml would take considerably longer than 10 min to form a multi-layered fibrinogen matrix in flow conditions. In this study, we incubated fibrin gels with a solution of 1.5 mg/ml

fibrinogen, which is closer to physiological conditions (2-3 mg/ml), and a high enough concentration to form multilayered fibrinogen on fibrin gels as was determined from a previous study [35].

Another recent study by Nguyen et al. quantified the maximum adhesion force of platelets to collagen, fibronectin, and PLL using SCFS [205]. They showed maximum adhesion values of ~1.4 nN for collagen, ~2.2 nN for fibrinectin, and 2.7 nN for PLL. While platelets are known to adhere to collagen [210], we demonstrate that platelets adhere with a higher force to fibrin (6 ± 2 nN, Fig. 6.3). However, Nruyen et al.'s study used retraction velocities of 15 μm/s [205], while we used a retraction velocity of 2 μm/s. It has been shown that rupture force of integrin-ligand bonds is dependent on retraction velocities [52, 65, 174], because higher velocities should cause higher adhesion values, we are confident that platelets have a higher affinity for fibrin than collagen.

Our adhesion experiments of glass microbeads on fibrin gels and on fibrinogen coated thrombi showed that the multilayered fibrinogen acts as an anti-adhesive agent for non-biological elements as well. Maximum adhesion on fibrin gels was 1.5 ± 0.4 nN compared to 0.19 ± 0.08 nN on thrombi bodies coated with fibrinogen. This suggests that the multilayered fibrinogen formed on thrombi could act as an anti-adhesive barrier due to the mechanical nature of the fibrinogen matrix itself. Microbeads on thrombi tails showed higher maximum adhesion forces than on thrombi bodies at 0.6 ± 0.4 nN. This is monst likely due to the punctate nature of fibrinogen adsorption caused by turbulence in the flow of solution of in situ thrombus formation [202].

In conclusion, our results contribute to a growing body of evidence that multilayered fibrinogen acts as a safeguard to prevent cascading platelet adhesion [29, 33, 122, 170, 201]. It is clear that the effect of adsorbed fibrinogen on thrombi needs to be taken into consideration for any studies on the interaction of platelets and leukocytes with thrombi. The quantification of the adhesion of platelets to fibrin provides a fuller picture for understanding thrombus formation.

7. Direct Visualization of Multinucleated Giant Cell Formation

7.1 Acknowledgments

This chapter is a reprint of a paper submitted to the journal *Biomaterials* by James J. Faust, Wayne Christenson, Kyle Doudrick, Robert Ros, and Tatiana P. Ugarova called "Direct visualization of multinucleated giant cell formation." I worked closely with James Faust to develop a new type of glass surface, which enables the visualization of multinucleated giant cell formation for the first time. James discovered the breakthrough that made this surface possible, and designed the experiments for the paper. I carried out experiments, and characterized the surface using AFM topography, advancing water contact angle, and SCFS measurements to determine the surfaces adhesiveness for live cells. Kyle Doudrick conducted mass spectrometry experiments to determine the molecular make-up of the surface chemistry. Tatiana Ugarova and Robert Ros provided consultation on experimental design, and direction for the study.

7.2 Abstract

Macrophage fusion resulting in the formation of multinucleated giant cells (MGCs) occurs in a variety of chronic inflammatory diseases. Despite the long-standing premise that fusion of mononucleated macrophages results in the formation of MGCs, to date, no published study has shown fusion in context with living specimens. This is a consequence of the fact that optical-quality glass, which is required for the majority of live imaging techniques, does not promote macrophage fusion. In this study, we serendipitously identified a highly fusogenic glass surface and discovered that the capacity to promote fusion was due to oleamide contamination. When adsorbed on glass,

oleamide and other molecules that contain long-chain hydrocarbons promote high levels of macrophage fusion. Micropatterned glass further increased fusion and enabled a remarkable degree of spatiotemporal control of MGC formation. Using these surfaces, we reveal the kinetics and morphological aspects that govern in vitro MGC formation.

7.3 Introduction

Multinucleated giant cells (MGCs), derived from fusion of mononucleated macrophages, accompany a number of pathological states in the body, including granulomatous infections, the foreign body reaction to implanted biomaterials, atherosclerosis, cancer and others [211-213]. In order for macrophages to fuse, monocytes recruited from peripheral blood to sites of inflammation differentiate into macrophages that subsequently fuse as inflammation progresses to the chronic state. The T helper 2 cytokine interleukin-4 (IL-4) promotes macrophages fusion in vivo [214] and when applied in cell culture can be used to study monocyte/macrophage fusion [215]. Although this in vitro cell system has proven invaluable to our understanding of the molecular mediators that orchestrate macrophage fusion, there is a surprising paucity of data regarding the morphological changes that macrophages undergo during fusion as well as the cellular mechanisms that govern this process. In fact, despite several long-standing predictions that purportedly account for the mechanisms of macrophage fusion no published study to date has shown the formation of a MGC in context with living specimens.

This deficiency is primary due to the fact that most high resolution techniques in optical microscopy require glass as substrate. However, glass surfaces are known to

support very low levels of macrophage fusion in the presence of IL-4 despite robust adhesion [216]. When macrophage fusion does occur on glass, it is impossible to predict where and at what time macrophages will fuse, since the field of view decreases with increased magnification. Consequently, if the goal is to observe macrophage fusion with living specimens then low magnification objectives and long imaging durations are necessary in order to capture rare fusion events. On the other hand, plastic surfaces (e.g. Permanox) are known to support macrophage fusion in the presence of IL-4 [217], and currently serve as the gold standard for in vitro analysis of MGC formation [218]. However, the problem with most plastic substrates is that changes in refractive index lead to chromatic aberration, which is accentuated by substrate thickness. Further, birefringent properties of most plastic substrates make techniques that exploit polarity of light impossible. Further, plastic is not compatible with the use of high numerical aperture (N.A.) objectives. Consequently, if Permanox plastic is used, the only technique that can be successfully employed is low-resolution phase-contrast and only when long working distance or low magnification objectives are used. These barriers have restricted studies to fixed specimens and have thwarted our ability to utilize the large number of imaging techniques that rely on optical-quality glass for image formation.

Here we describe fabrication of optical-quality glass surfaces that exploit adsorption of molecules containing long hydrocarbon chains. Glass surfaces adsorbed with these substances promote extraordinary rates of macrophage fusion and adhesion, which is mediated in part by Mac-1 integrin ($\alpha_M\beta_2$, CD11b/CD18, CR3). Micropatterning glass with the aforementioned substances leads to a further increase in macrophage fusion and enables a high degree of spatiotemporal control over the formation of MGCs. For the

first time, we utilize living specimens to reveal the sequence of events that result in MGC formation via macrophage fusion. We show that MGC formation is a non-linear process that requires a lag-phase and involves three types of fusion events. Moreover, macrophage fusion occurs between intercellular margins, but not through the previously proposed "cellocytosis" mechanism. We anticipate that the spatiotemporal control afforded by this surface may expedite fundamental studies related to the mechanism of macrophage fusion.

7.4 Materials and Methods

7.4.1 Mice

C57BL/6J and Mac-$1^{-/-}$ (B6.129S4-*Itgam*^{tm1Myd}/J) mice were obtained from The Jackson Laboratory (Bar Harbor, ME). LifeAct mice [219] were a generous gift from Dr. Janice K. Burkhardt and used with permission from Dr. Roland Wedlich-Söldner. Mac-$1^{-/-}$ mice were housed in sterile cages. All mice were given *ad libitum* access to food and water and colonies were maintained at a constant temperature of 22 °C on a 12 hr light/dark cycle. All procedures were performed in accordance with the animal protocols approved by the Institutional Animal Care and Use Committee at the Arizona State University and the Mayo Clinic Arizona.

7.4.2 Macrophage Isolation and Cell Culture

Macrophages were isolated the peritoneum 72 hr after injection of a 0.5 mL sterile 4% solution of Brewer's thioglycollate (Sigma Aldrich, St. Louis, MO). Mice were humanely sacrificed according protocols approved by Mayo Clinic, Arizona and ASU Animal Care and Use Committees. Immediately following euthanasia, 5 mL of an ice-

cold solution of phosphate-buffered saline (PBS, pH 7.4) supplemented with 5 mM EDTA was injected aseptically into the peritoneum, the lavage containing cells was collected, and the cells were counted with a Neubauer hemocytometer. Low passage number (≤ 10) HEK293 cells stably expressing human integrin Mac-1 and wild-type HEK293 cells were previously described [119]. The cells were cultured in the complete DMEM:F12 medium and detached from the culture dish by incubation in Cellstripper™ (Cellgro, Manassas, VA). The cells were washed and then resuspended in the complete DMEM:F12 medium.

7.4.3 IL-4-Induced Macrophage Fusion

Peritoneal cleavage cells were applied to various surfaces at a concentration of $5x10^6$ cells/mL and incubated in 5% CO_2 at 37 °C for 30 min. Nonadherent cells were removed and adherent macrophages were washed 3-5 times with Hank's Balanced Salt Solution (HBSS; Cellgro, Manassas, VA) containing 0.1% bovine serum albumin (BSA) and allowed to incubate in the complete DMEM:F12 (Cellgro, Manassas, VA) medium supplemented with 10% fetal bovine serum (FBS, Atlanta Biological, Atlanta, GA) and 100 I.U./mL penicillin, 100 µg/mL streptomycin (Cellgro, Manassas, VA). After 2 hr, the medium was removed and fresh medium supplemented with 10 ng/mL of interleukin-4 (IL-4; Genscript, Piscataway, NJ) was applied to the culture to induce fusion. In this study, the application of IL-4 is considered t=0. At the respective time points, cultures of fusing macrophages were washed 2 times with PBS and incubated with ice-cold methanol for 2 min. The fixed cultures were placed in an oven at 60 °C until dried. Wright's stain (Sigma Aldrich, St. Louis, MO) was applied for 8 minutes, the stain was removed and substituted with fresh buffered Wright's stain (pH 6.5) for an additional 8 minutes. The

cover glass was placed under running deionized water to remove unbound stain and dried in an oven at 60 °C. The cover glass was mounted in Permount™ (Thermo Fischer Scientific, Waltham, MA), the mountant was air dry, and the specimens were imaged with bright field optics. The extent of MGCs formation was evaluated by determining the fusion index. The fusion index is defined as the number of nuclei present in fused macrophages divided by the total number of nuclei in both fused and non-fused macrophages. Three to 5 bright field images collected at 20x objective magnification were analyzed per specimen.

7.4.4 Adhesion Assays

Cell adhesion was determined by plating 2.5 x 10^5 cells in 35 mm dishes (FluoroDish; World Precision Instruments, Sarasota, FL). Care was taken to ensure that cells spread evenly across the entire surface area of the dish for each experimental condition. After 25 min at 37 °C in 5% CO_2, cell images were captured before washing in order to standardize the number of cells in the field of view. Three phase contrast images (20x objective magnification) corresponding to the center of the dish, the edge of the dish and the center-edge midpoint were collected for each sample. At 30 min, the specimens were washed gently 3 times with HBSS supplemented with 0.1% BSA and 3 images were collected as described above. Adhesion was calculated by dividing the average number of adherent cells after washing by the average number of total cells added before washing. For inhibition experiments, Mac-1-HEK293 cells were mixed with function blocking mAb 44a against the α_M integrin subunit (10 μg/ml per 10^6 cells) or an isotype IgG1 control for 15 min at 22 °C.

7.4.5 Surface Characterization

Nanotopography of each surface was resolved using an atomic force microscope (AFM; Nanosurf, Woburn, MA). Scans (10 x 10 μm) were acquired in tapping mode with conical silicon AFM probes (Nanoscience, Phoenix, AZ). The nominal tip radius was 8 nm, and nominal resonant frequency was 300 kHz. Imaging was conducted in air at 22 °C. Surface roughness was calculated using Gwyddion 2.45 software and represents an average of 3-5 randomly selected scans from at least 2 different preparations. Water contact angle was determined using an EasyDrop goniometer (Krüss, Matthews, NC). Water droplets (4 μL) were deposited on the sample surfaces, and their profiles were captured and analyzed for contact angle by the Drop Shape Analysis software (Krüss, Hamburg, Germany). 10 droplets were measured per each surface from at least 3 separate experiments.

7.4.6 Liquid Chromatography/Mass Spectrometry

The composition of mixtures eluted from the FD dishes was determined by mass spectrometry. The LC/MS instrument consisted of a Dionex Ultimate 3000 Rapid Separation UPLC system equipped with a Dionex Ultimate 3000 autosampler and a Dionex Ultimate 3000 photodiode array detector coupled with a Bruker MicrOTOF-Q II quadrupole time-of-flight hybrid mass spectrometer using Hystar 3.2 software. The Bruker electrospray ionization source was operated in the positive ion mode with the following parameters: end plate offset voltage = –500 V, capillary voltage = 2000 V, and nitrogen as both a nebulizer (4 bar) and dry gas (7.0 L/min flow rate at 180 ºC temperature). Mass spectra were accumulated over the mass range 50-3000 Da at an acquisition rate of 5,000 per second. Separations were performed on a Dionex Acclaim

RSLC 120 C18 2.2 um 120 Å 2.1 x 100 mm column. The mobile phase (A = 0.1% formic acid in water; B = 0.1% formic acid in acetonitrile) gradient consisted of elution at 0.4 mL/min with 90% A/10% B for 2 min, followed by a 14-min linear gradient to 100% B, hold at 100% B for two minutes, then return to initial conditions for 2 minutes.

7.4.7 Single Cell Force Spectroscopy

Tipless silicon nitride cantilevers (HYDRA, AppNano, Santa Clara, CA) were prepared as described previously[119]. Briefly, cantilevers were plasma-cleaned at 29.6W, 400 mTorr in O_2 gas using a plasma cleaner (PDC-001, Harrick Plasma, Ithaca, NY). Tips were functionalized by incubation in 2 mM (3-Aminopropyl) triethoxysilane (APTES, Sigma) in chloroform solution followed by changes of ethanol and then deionized water. Cantilevers were incubated in 1.25 mM Bis(sulfosuccinimidyl) suberate sodium salt (BS^3, Sigma Aldrich, St. Louis, MO) solution for 30 min and then placed into 0.5 mg/ml concanavalin A (Sigma) solution for 30 min at 22 °C. Cantilevers were then rinsed with PBS and stored in 1 M NaCl at 4 °C. Functionalized cantilevers were used in a MFP-3D AFM (Asylum Research) placed on an inverted microscope (IX71, Olympus). Cantilevers were brought into contact with target cells manually, and withdrawn from the surface. Cells were allowed to firmly attach for 1 minute. SCFS measurements were conducted at 37° C in HBSS with 0.1% BSA as described previously [34]. Force curves were recorded on different spots of the surface with a 2 nN trigger force and a 120 s dwell time. Approach and retraction speeds were 2 μm/s. Three-five force curves were generated for each cell and 6-12 cells were used for each condition.

7.4.8 Surface Fabrication

To prepare acid clean glass (AC), high stringency cover glass (Carolina Biological, Burlington, NC) was washed 3 times in hydrochloric acid, washed 10 times in copious volumes of nanopure water, washed 3 times in anhydrous acetone, washed an additional 10 times in nanopure water and stored in pure ethyl alcohol until use. Each washing step was 30 min and included either sonication or agitation. Plasma cleaned surfaces (PC) were prepared by exposure glass to vacuum gas plasma (Harricks, Ithaca, NY) for 60 s. PC preparations were stored in a vacuum desiccator until use.

Oleamide (Sigma) was dissolved in isopropyl alcohol at a concentration of 1 mg/mL and used immediately thereafter. The solution was adsorbed to AC glass for 30 s, the excess solution was decanted, and the glass was allowed to air dry. DMSO-free paraffin wax (Sigma) and tocopherol-free petrolatum (Sigma) were solubilized in toluene at 1 mg/mL and 10 mg/mL, respectively. Cover glass was paraffinized by application of each solution for 30 s. Excess solution was removed and the surfaces were allowed to dry for a minimum of 12 hr. Prior to use, modified surfaces were polished by three strokes in x- and y-axis directions using a lint-free cloth. The surfaces were sterilized by UV irradiation for 15-30 minutes and washed aseptically with sterile water. In preliminary experiments, the lowest concentrations of paraffin, oleamide, and petrolatum that made AC glass fusogenic were determined.

7.4.9 Surface Micropatterning

In order to create a micropattern, a finder grid (Electron Microscopy Sciences, Hatfield, PA) was dipped in a 1 mg/mL solution of paraffin in toluene, excess liquid was removed with Whatman no. 1 filter paper, and the finder grid was placed in the center of

the AC cover glass. The cover glass was allowed to air dry and then cleaned by vacuum gas plasma to remove paraffin between grid bars. The mask was carefully removed with Dumont no. 5 forceps (Electron Microscopy Sciences, Hatfield, PA) which left a pattern on the glass surface. Macrophage fusion was induced by IL-4 as described above.

7.4.10 Videomicroscopy

Micropatterned surfaces were fabricated as described above. Macrophages were applied to the glass and fusion was induced as described in the text above. The dish was transferred from the incubator to a stage-top incubation unit that was calibrated to consistently maintain a humified atmosphere of 5% CO_2 in air at 37 °C. Phase contrast images (20x objective magnification) were collected every 30 seconds with an Evos FL Auto microscope (Thermo Scientific, Waltham, MA) and transferred to ImageJ to create videos.

7.4.11 Correlated Light and Scanning Electron Microscopy (CLEM)

CLEM was conducted as previously described [220], albeit with minor modification. Macrophages expressing eGFP- or mRFP-LifeAct were mixed in equal number and applied to paraffin micropatterned surfaces. Twelve hours after the application of IL-4 the specimens were fixed with 2% formaldehyde for 30 minutes. The specimens were washed 3 times for 10 minutes each and incubated with Hoechst 33342 as described by the manufacturer. Images were collected with a 20x (0.7 N.A.) objective via a Leica SP5 laser scanning confocal microscope and subsequently fixed with 2% glutaraldehyde prepared in 100 mM cacodylate buffer (pH 7.2). The specimens were washed with copious volumes of cacodylate and post-fixed with 1% OsO_4 for 45 min.

After washing with water, the specimens were dehydrated through a graded series of ethanol. The specimen was dried through the CO_2 critical point and sputtered with Pt/Au. Images were collected on a JOEL JSM 6300 scanning electron microscope.

7.4.12 Direct Stochastic Optical Reconstruction Microscopy (dSTORM)

Fusing macrophages were detergent extracted with a solution containing 0.1% Triton X-100, 100 mM KCl, 5 mM $MgCl_2$, 2 mM EGTA, 20 mM HEPES, pH 6.8 for 1 min at room temperature. Macrophages were fixed in 2% formaldehyde made in 100 mM PBS (pH 7.2) for 15 min. The samples were washed 3 times for 15 min with PBS supplemented with 1% BSA (PBS-BSA) and incubated with a mouse anti-vinculin mAb (V9264, Sigma) at 4 °C overnight with gentle agitation. Antibody dilution buffer contains 100 mM KCl, 5 mM $MgCl_2$, 2 mM EGTA, 0.01% Tween-20, 1% non-fat milk, 20 mM HEPES (pH 6.8). The specimens were washed 3 times for 15 min with PBS-BSA followed by an Alexa-657-conjugated secondary antibody (Thermo Fischer Scientific, Waltham, MA) at 4 °C overnight. The samples were washed with PBS and imaged immediately thereafter. Vectashield diluted in Tris-glycerol, was used in combination with c.a. 12 mw laser excitation to achieve spatially separated single-molecule emitters. Emitters were collected in TIRF optics with a 100x 1.4 N.A. objective and recorded with an Andor EMCCD operating in kinetic mode. Single-molecule localizations were reconstructed in RapidSTORM as described elsewhere [221].

7.4.13 Statistics

Unless stated otherwise, results from three independent experiments are shown as mean ± standard deviation (S.D.). Differences were determined by analysis of variance

(ANOVA) followed by Tukey's or Dunn's post-test using GraphPad InStat software. Data were considered significantly different if post-tests indicated that $p < 0.05$.

7.5 Results and Discussion

7.5.1 FluoroDish™ Glass Surfaces Promote Macrophage Fusion

While performing direct stochastic optical reconstruction microscopy (dSTORM) for an independent investigation we observed serendipitously efficient IL-4-induced macrophage fusion on the FluoroDish™ (FD) glass surface (Figure 7.1A). The high level of macrophage fusion observed on this surface was surprising since clean glass surfaces are known to promote modest levels of fusion, even in the presence of robust adhesion [216, 222]. Indeed, 24 hr after the application of IL-4 there appeared very few MGCs on acid cleaned glass surfaces (AC) or FD surfaces treated with vacuum gas plasma (FD+PC), whereas a large number of MGCs decorated the FD surface (Figure 7.1A). Analysis of the fusion index confirmed this observation and demonstrated a significant increase in macrophage fusion when utilizing the FD (36 ± 13%), but neither AC (10 ± 7%) nor FD+PC (9 ± 3%) as substrates (Figure 7.1B). The low level of fusion observed after treating the FD surface with vacuum gas plasma indicated that it lost the capacity to promote macrophage fusion. It further suggested that the physico-chemical properties of the FD+PC surface were altered and/or an unknown contaminant present on the FD surface was removed by vacuum gas plasma.

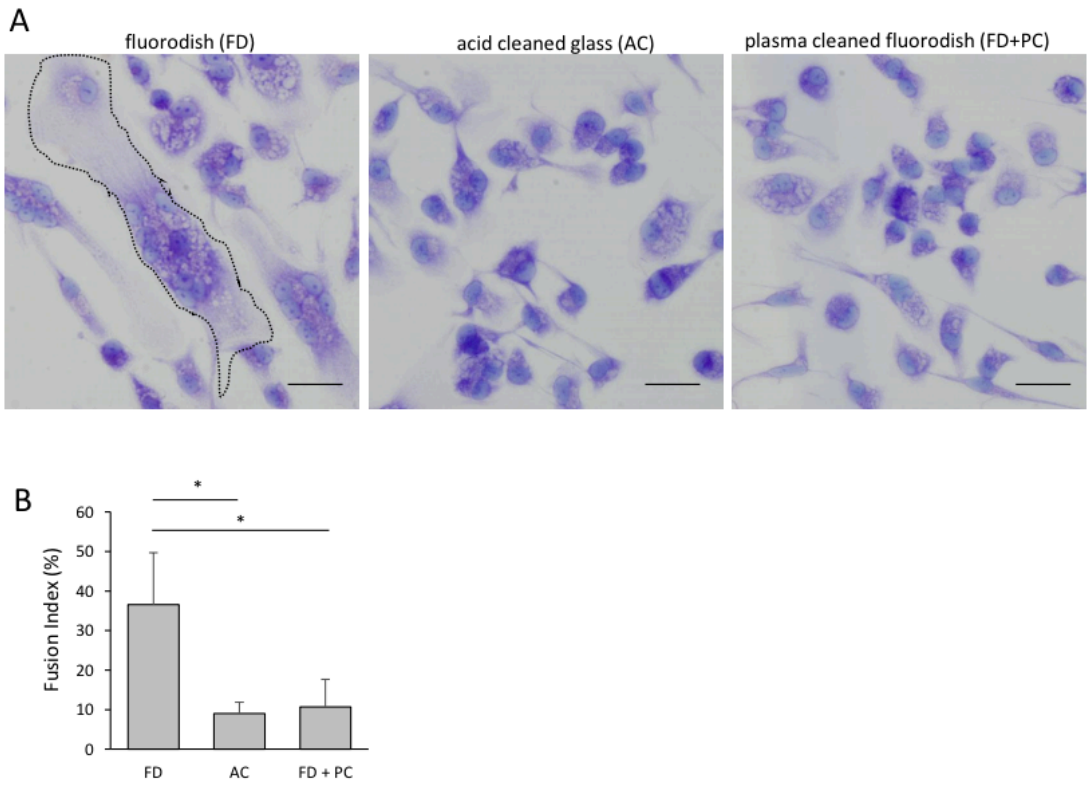

Figure 7.1 (A) Analysis of macrophages plated on three different surfaces 24 h after the application of IL-4. Macrophages were stained with Wright's stain. Outlined in black is a MGC formed on the FD surface. The scale bar is 50 μm. (B) Quantification of the fusion index. The histogram indicates that the FD surface, but not AC or FD + PC, supports a high degree of macrophage fusion. Results shown are means ± S.D. from three independent experiments each with three to five bright field images analyzed. **$p<0.1$ as determined by ANOVA. The scale bars in the lower right of each corner are 50 μm.

7.5.2 Characterization of FD, AC and FD+PC Surfaces

Interfacial processes driven by the physico-chemical properties of the material are known to be important modulators of macrophage fusion [211, 223, 224]. In order to gain insight into the characteristics of the surface that might promote macrophage fusion, we employed atomic force microscopy (AFM) to directly visualize surface features. FD surfaces appeared heterogeneous and contained large and small globules (Figure 7.2A).

In addition, there appeared patches of material raised from the surface (Figure 7.2A). In stark contrast, AC glass appeared uniform with very few surface features (Figure 7.2A). FD+PC surfaces contained a heterogeneous variety of surface globules (Figure 7.2A). Additional AFM analysis demonstrated that FD surfaces had a surface roughness (Ra) of 1.9 ± 0.7 nm, which was significantly greater than both AC glass (0.2 ± 0.02 nm) and FD + PC (1.3 ± 0.5 nm) surfaces (Figure 7.2B). Advancing water contact angles indicated that the FD surface was hydrophobic ($\theta = 92° \pm 2.5$) whereas AC glass and FD+PC surfaces were relatively hydrophilic at 23° ± 1.8 and 13° ± 9.2, respectively (Figure 7.2C).

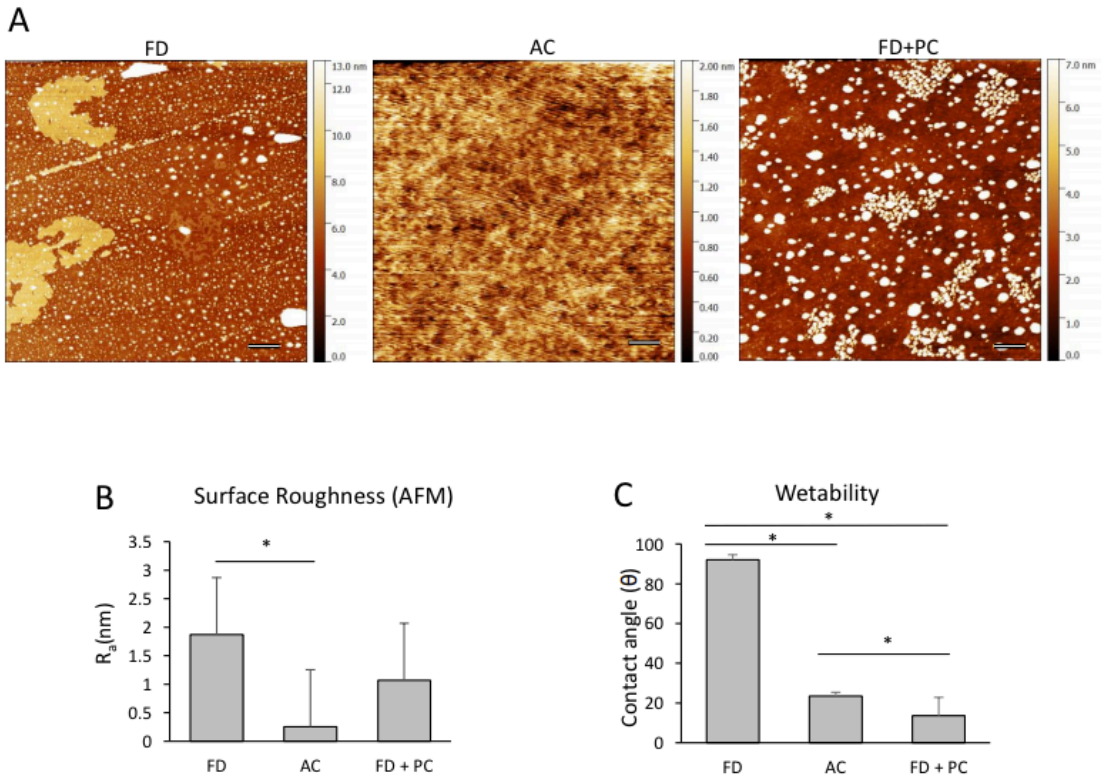

Figure 7.2 (A) AFM images show surface topography of the FD, AC and FD+PC surfaces. The z-scale is shown on the right side of each micrograph. (B) The surface roughness was measured from AFM scans (10x10 µm). (C) Advancing water contact angle analysis indicates the relative wettability of each surface. *p<0.05; **p<0.01. The scale bars in the lower right corner of the image correspond to 500 nm.

7.5.3 Cell Adhesion to the FD Surface is Mediated by Mac-1 Integrin

Before macrophages can fuse they must first adhere to the substrate [218]. Adhesion is mediated in part by integrins and in particular Mac-1 integrin is capable of mediating leukocyte adhesion to multiple ligands [119, 225]. In order to examine the possibility that Mac-1 might be involved in adhesion, macrophages isolated from the inflamed peritoneum of wild-type and Mac-$1^{-/-}$ mice were applied to FD and FD+PC surfaces and adhesion was assessed. Figure 7.3A and 7.3B show that macrophages adhered to both surfaces with no significant difference observed between wild-type and

Mac-1-deficient cells. However, inspection of phase contrast micrographs indicated that wild-type, but not Mac-1-deficient macrophages spread on the FD surface (Figure 7.3A). Quantitative analyses confirmed a significant increase in spreading (~3.5-fold) of wild-type compared to Mac-1-deficient macrophages on the FD surface (Figure 7.3C). Furthermore, although not significantly different, spreading of Mac-1-deficient macrophages on the FD+PC surface tended to decrease (Figure 7.3C). Single cell force spectroscopy (SCFS) demonstrated a significant decrease in the maximal adhesion force developed between Mac-1-deficient macrophages and the FD surface as compared to wild-types macrophages (3.0 ± 2.2 nN vs. 11.2 ± 6.7 nN; Figure 7.3D).

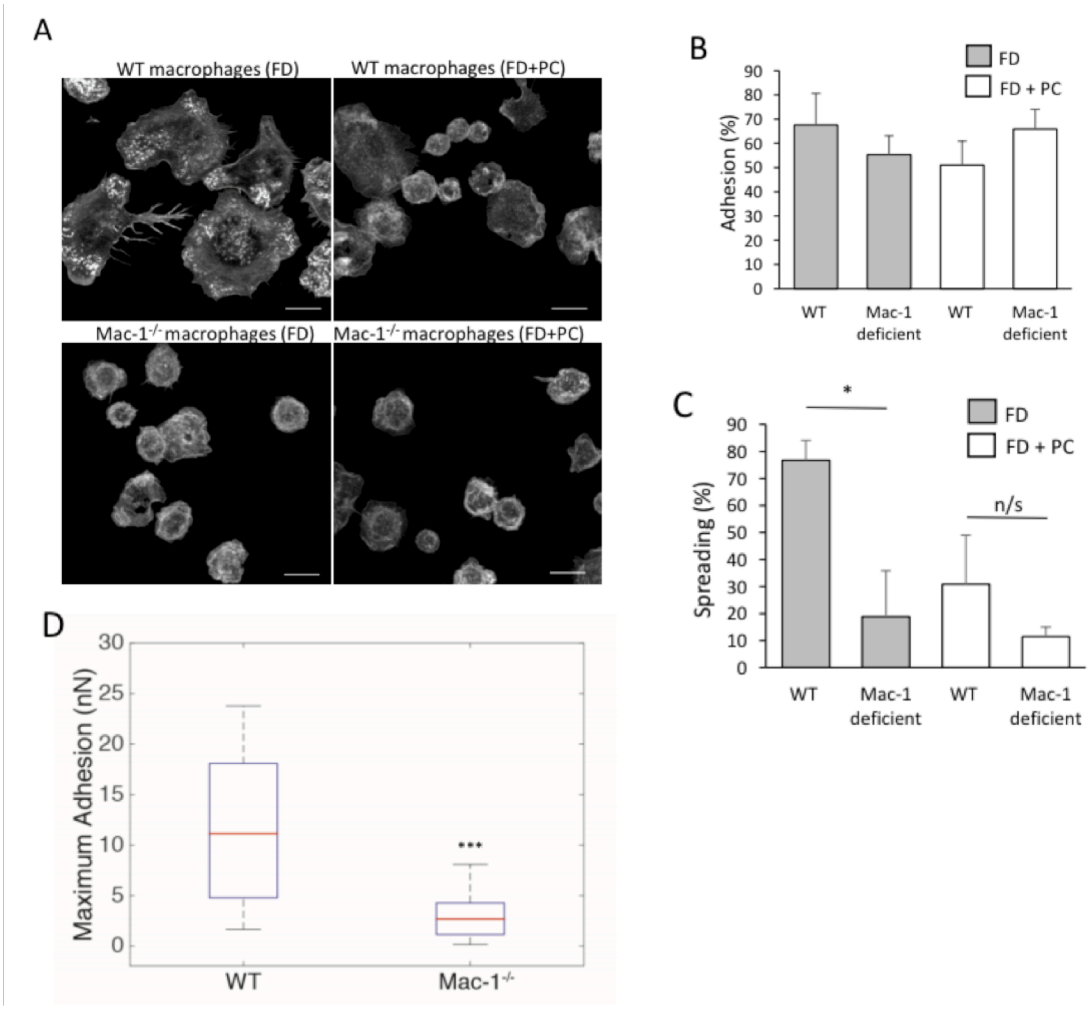

Figure 7.3 (A) Confocal micrographs of TG-elicited WT and Mac-1-deficient mouse macrophages applied for 30 min on the FD and FD + PC surfaces. Representative images are shown. (B) Quantification of adhesion of WT and Mac-1-deficient macrophages. (C) Quantification of spreading of WT and Mac-1-deficient macrophages. Results shown in (B) and (C) are means ± S.D. from 9 images with ~200-400 cells per image from three independent experiments. *$p<0.05$ as determined by ANOVA. (D) Quantification by single cell force spectroscopy of adhesion forces developed between WT and Mac-1-deficient macrophages and the FD surfaces. The median maximum adhesion force value is shown in red and significance was determined from Wilcoxon rank sum test. ***$p<0.001$. Scale bars, 50 μm.

Macrophages are known to contain a variety of adhesion molecules, which makes the cell system complex. In order to substantiate the ability of Mac-1 to support cell adhesion to the FD surface, we employed a model system based on HEK293 cells

genetically engineered to express Mac-1 (Mac-1-HEK293). Figure 7.4A and 7.4B show that wild-type HEK293 cells (WT) adhered poorly to the FD surface. However, application of Mac-1-HEK293 cells to the FD surface caused approximately a 4-fold increase in cell adhesion. The specificity of the interaction between Mac-1 and the FD surface was further assessed through the use of the function blocking mAb 44a, directed against the αM integrin subunit. Incubation of Mac-1-HEK293 cells with mAb 44a significantly decreased adhesion, whereas the IgG control did not (Figure 7.4B). No significant difference in adhesion was observed when HEK293 and Mac-1-HEK293 cells were plated on the FD+PC surface (Figure 7.4B). Consistent with the lack of involvement of Mac-1 in adhesion to the FD+PC surface, mAb 44a had no effect on adhesion of Mac-1-HEK293 cells (Figure 7.4B), suggesting that other structures supported adhesion. SCFS experiments demonstrated that the maximum adhesion force of Mac-1-HEK293 cells to the FD surface was ~2-fold higher than the WT counterpart (1.7 ± 1.0 vs. 0.64 ± 0.35 nN; Figure 7.4C). Together, these data indicate that Mac-1 contributes to adhesion and spreading to the FD surface.

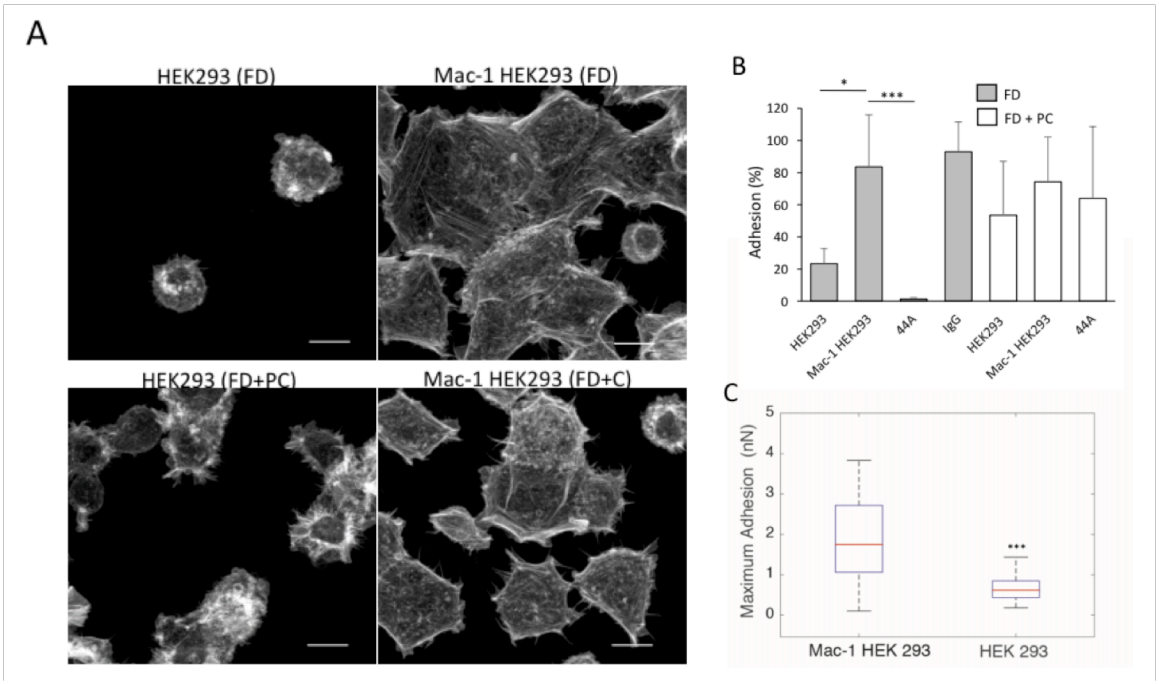

Figure 7.4 (A) Confocal micrographs of Mac-1- HEK293 and WT HEK293 cells adhered to the FD and FD + PC surfaces. Representative images are shown. (B) Quantification of adhesion of Mac-1-HEK293 and HEK293 cells to FD and FD+PC surfaces. Pre-incubation of Mac-1-HEK293 cells with function-blocking anti-Mac-1 mAb 44A abolished adhesion, whereas pre-incubation with IgG isotype control did not affect adhesion. Results shown are means ± S.D. 26 from 9 fields with ~200-310 cells per image from three independent experiments. *$p<0.05$; ***$p<0.001$ as determined by ANOVA. (C) Quantification by single cell force spectroscopy of adhesion forces developed between Mac-1-HEK293 and HEK293 cells and the FD surfaces. The median maximum adhesion force value is shown in red and significance was determined from Wilcoxon rank-sum test. ***$p<0.001$. The scale bars in the lower right corner of each micrograph are 50 μm.

7.5.4 Oleamide Contamination on the FD Surface Promotes Fusion

The dramatic decrease in macrophage fusion on the AC and FD+PC surfaces suggested that, in addition to different physico-chemical properties, a contaminant(s) present on the FD surface may contribute to the high fusion-promoting activity. To investigate this possibility, we sonicated the FD surface in isopropanol to remove the

potential contaminant(s) and found that the treated surfaces lost the ability to support macrophage fusion. Further, collecting isopropanol eluate from the FD surface and applying it back onto non-fusogenic AC glass restored macrophage fusion to a level comparable to that of intact FD surfaces (not shown). To identify a substance(s) responsible for the fusion-promoting activity, we analyzed the chemical composition of isopropanol eluate by liquid chromatography/mass spectrometry (LC/MS). The LC analysis revealed seven major peaks (Figure 7.5A), four of which corresponded to the solvent, isopropanol. MS analysis of the three LC peaks revealed triisopropanolamine (m/z 192.1481), oleamide (m/z 282.2756) and an unknown compound (m/z 387.1936) (Figure 7.5B). Since both triisopropanolamine and oleamide are used as agents in adhesive cures, we hypothesized that during the curing process of the adhesive that bonds the glass bottom of FluoroDish to the plastic walls, the cure vapors formed a thin layer on the glass surface.

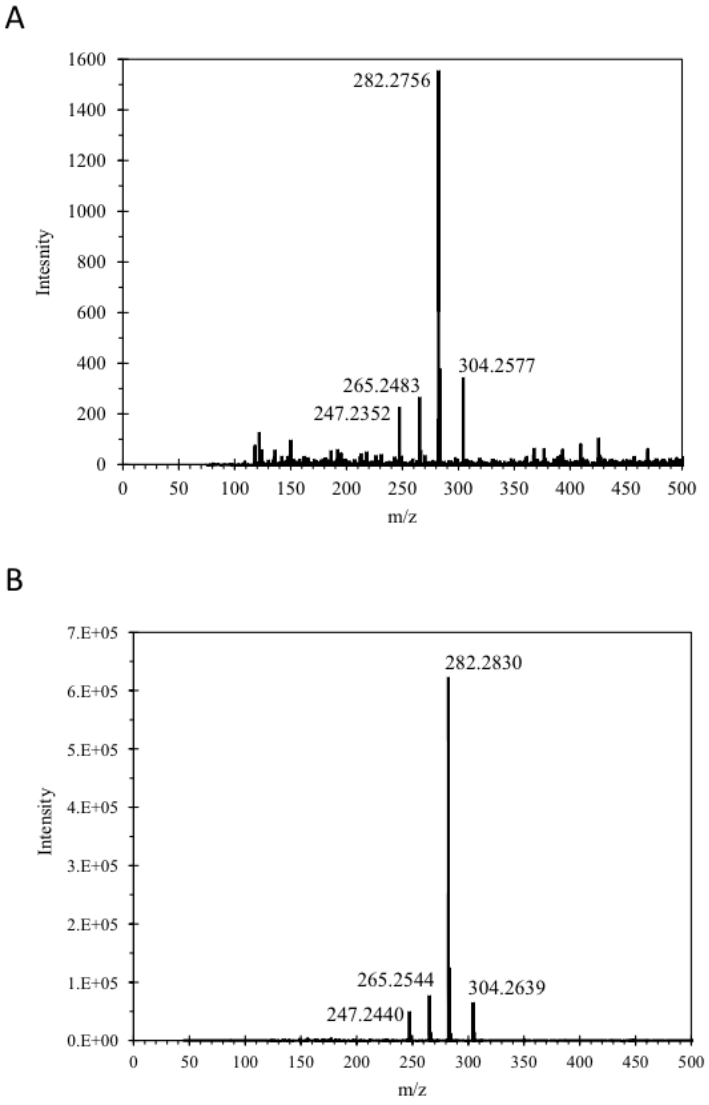

Figure 7.5 Mass spectra of (A) unknown peak from eluate and (B) oleamide standard. Both samples contain identical (within 0.01 m/z) peaks for oleamide and its derivatives.

When applied to AC glass, triisopropanolamine promoted neither adhesion nor fusion at any concentration tested (data not shown). However, when we applied oleamide to AC glass we observed high levels of macrophage fusion that qualitatively resembled the FD surface (Figure 7.6A). Moreover, the fusion index observed on oleamide-adsorbed and FD surfaces were similar (29 ± 8% vs. 27± 8%; Figure 7.6B). Oleamide is an amide

of oleic acid that contains a long-chain hydrocarbon (Figure 7.6A). We predicted that other molecules with similar hydrocarbon chains adsorbed to AC glass might also render AC glass fusogenic. To examine this possibility, we adsorbed paraffin wax and separately petrolatum, which both contain mixtures of hydrocarbon molecules, to AC glass. Figures 7.6A and 7.6B show that AC surfaces adsorbed with paraffin and petrolatum promoted effective macrophage fusion (Figure 7.6A) and quantitatively, paraffin significantly increased fusion compared to oleamide-adsorbed surfaces (46 ± 9% and 35 ± 6%, respectively; Figure 7.6B). No fusion was observed when AC glass was treated with toluene or isopropanol (Figure 7.6A and 7.6B). Under identical culture conditions, the level of macrophage fusion observed on paraffin-adsorbed glass was significantly greater than on Permanox (Figure 7.6B).

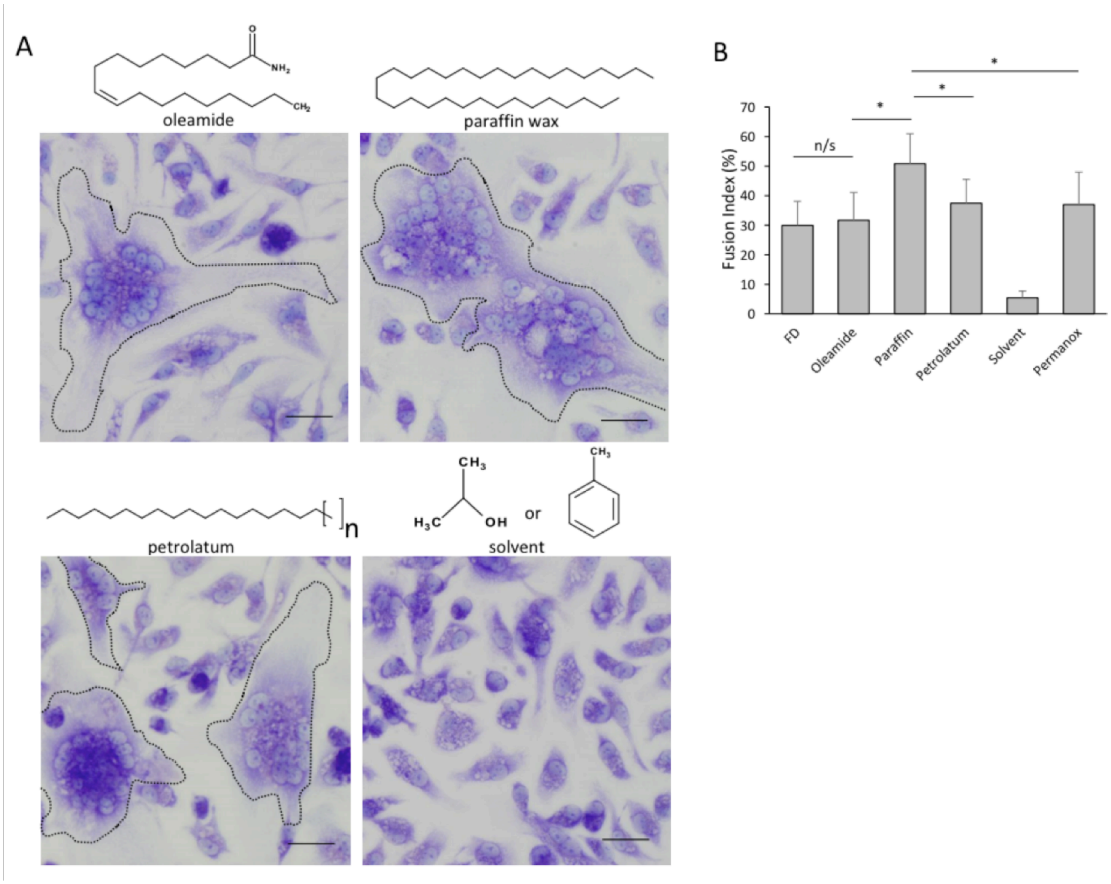

Figure 7.6 (A) Analyses of macrophages fusion on glass adsorbed with various long hydrocarbon chain molecules or exposed to solvent. Fusion of TG-elicited macrophages was induced by IL-4 for 24 hr. Cells were stained with Wright's stain. Selected MGCs are outlined in black. Glass treated with isopropanol or toluene does not promote macrophage fusion. The scale bar in each of the micrographs is shown in the lower right corner and represents 50 µm. Representative images are shown. (B) Quantification of fusion indexes for each surface. A fusion index on Permanox was determined under identical culture conditions. Results shown are means ± S.D from three independent experiments each with three to five bright field images analyzed. *$p<0.05$ as determined by ANOVA. The scale bars in the lower right corner of each micrograph are 50 µm.

7.5.5 Physical, Optical and Adhesive Properties of Paraffin-Adsorbed Surfaces

Having established that the surfaces adsorbed with hydrocarbon chain molecules exhibit high fusion-promoting capacity, we proceeded to investigate physical, adhesive and optical properties of the surface. Since surfaces adsorbed with paraffin promoted the

highest levels of macrophage fusion, we elected to utilize them to examine the surface topography, wettability and ability to support adhesion of Mac-1-HEK293 cells. Visualization of surface topography by AFM showed that paraffin-adsorbed glass (P surface) contained arrays of material that were raised from the surface by 10 nm (Figures 7.7A and 7.7B). However, despite the presence of these arrays, the P surface remained relatively flat (roughness 0.69 ± 0.15 nm; Figure 7.7A and 7.7B). Treatment of the P surfaces with vacuum gas plasma (P+PC) removed most, but not all, of the paraffin (Figure 7.7A) and slightly decreased surface roughness (0.52 ± 0.07 nm; Figure 7.7B). Advancing water contact angle indicated that adsorption of paraffin to AC glass strongly increased surface hydrophobicity of the P surface, whereas the P+PC surface was hydrophilic (Figure 7.7C).

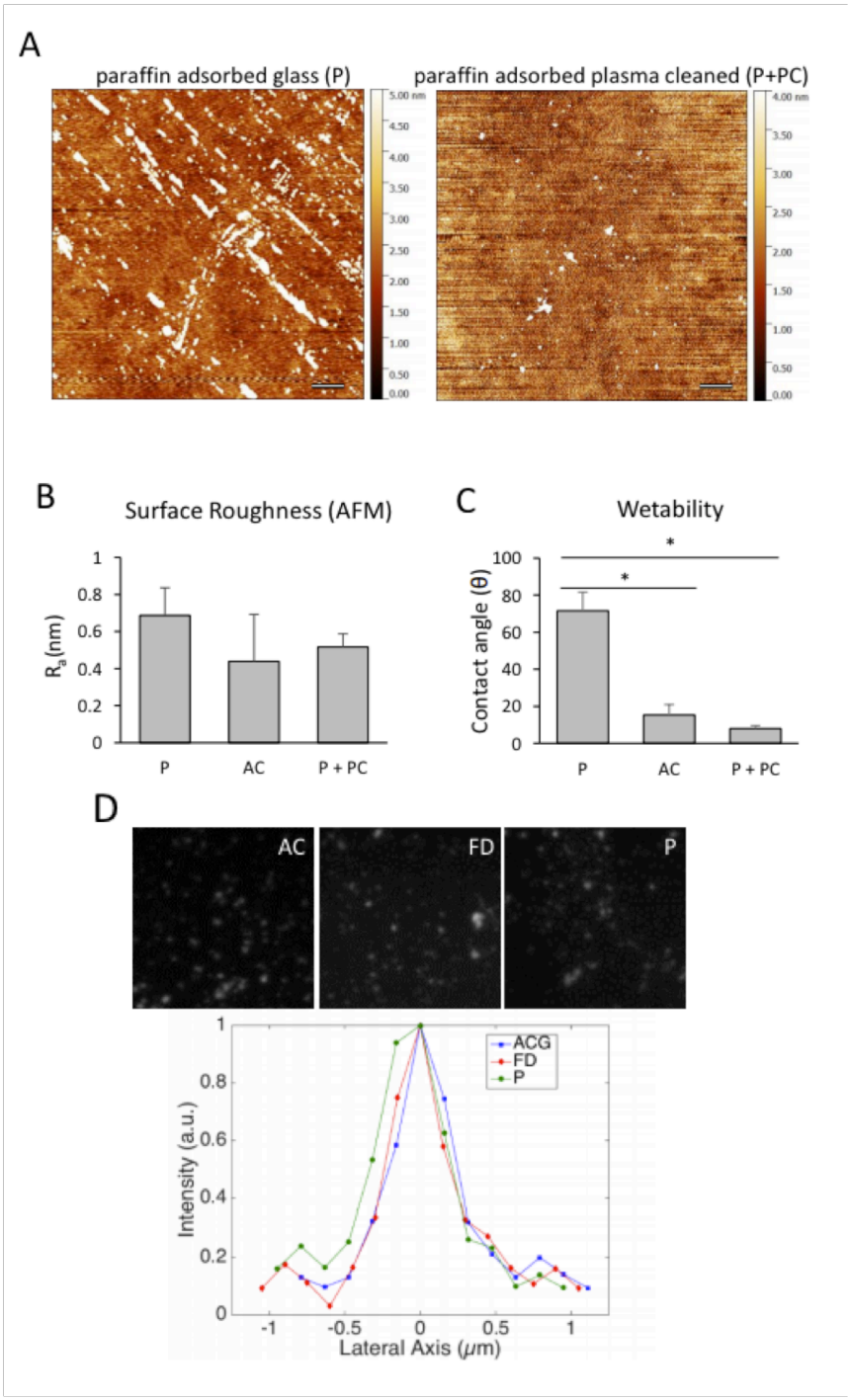

Figure 7.7 (A) AFM images of the nanotopography of paraffin-adsorbed and paraffin-adsorbed plasma cleaned surfaces. Scale bars are 500 nm. (B) Surface roughness as measured from 4-10 independent scans (10 x 10 μm). (C) Advancing water contact angle indicates that P surfaces are hydrophobic, whereas AC and P + PC surfaces are hydrophilic. (D) Representative intensity profiles for 100-nm TetraSpec beads on the AC, FD and P surfaces.

To examine the possibility that adsorption of paraffin influenced the optical properties of the P surfaces, we imaged 100 nm Tetraspec beads (488 nm excitation) with total internal reflection fluorescence (TIRF) microscopy. Qualitatively, the diameters of beads on the AC, FD and P surfaces did not appear to be different (Figure. 7.7D). Comparison of the lateral axis (i.e. bead diameters) showed that full width at half maximum obtained from line scans, which is a metric of the performance of the optical system, was 305 ± 28 nm, 313 ± 23 nm, and 308 ± 25 nm for the AC, FD and P surfaces, respectively. These data indicating that the P surface should be amenable to most imaging techniques, including single-molecule super resolution microscopy (Figure 7.8).

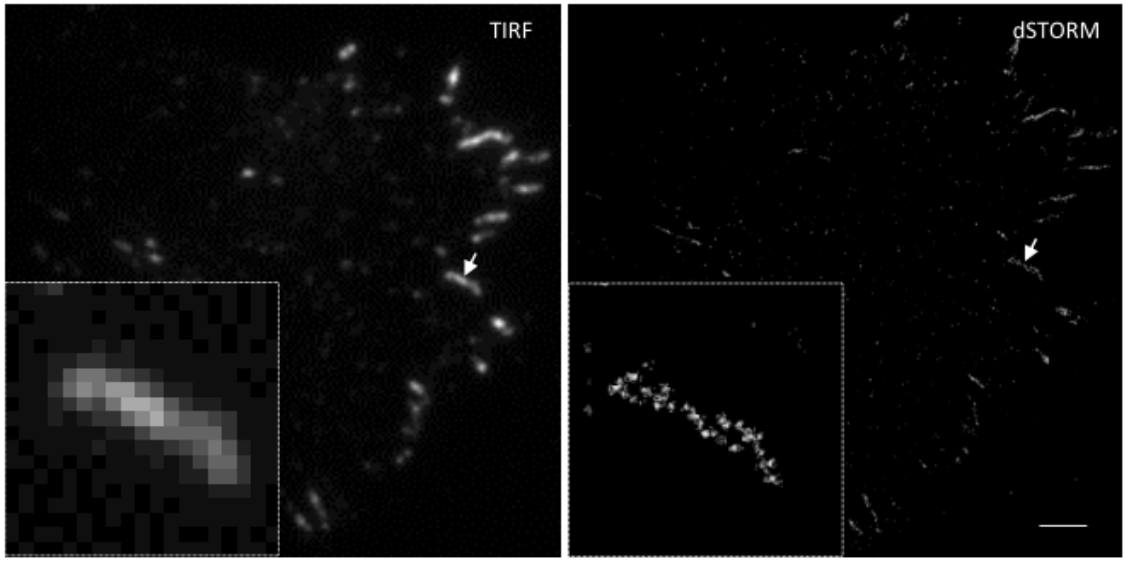

Figure 7.8 The P surface supports single-molecule super resolution microscopy (e.g. dSTORM). We observed a dramatic increase in image clarity compared to TIRF when localizations where reconstructed. The scale bar in the lower right corner is 2.5 μm.

The P surface was able to support strong adhesion of Mac-1-HEK293, but not WT HEK293 cells (Figures 7.9A and 7.9B). Similar to the FD surface, adhesion was solely dependent on Mac-1 integrin, since pre-incubation of Mac-1-HEK293 cells with mAb 44a, but not control IgG, completely inhibited adhesion (Figure 7.9B). Furthermore, consistent with a role for Mac-1 in cell adhesion, maximum adhesion force was ~3.5-fold greater for Mac-1-HEK293 compared to HEK293 cells (3.2 ± 1.3 vs. 1.4 ± 1.0 nN; Figure 7.9C). Two differences were identified between adhesion of Mac-1-HEK293 and HEK293 cells to the P- and FD surfaces. First, the maximal adhesion force required for detachment of Mac-1-HEK293 cells from the P-surface was ~2-fold greater than that from the FD surface (Figures 7.4B and 7.9B). Second, while both FD+PC and P+PC surfaces supported adhesion of wild-type HEK293 and Mac-1-HEK293 cells, mAb 44a inhibited adhesion to the P+PC, but not to FD+PC surface (Figures 7.4B and 7.9B).

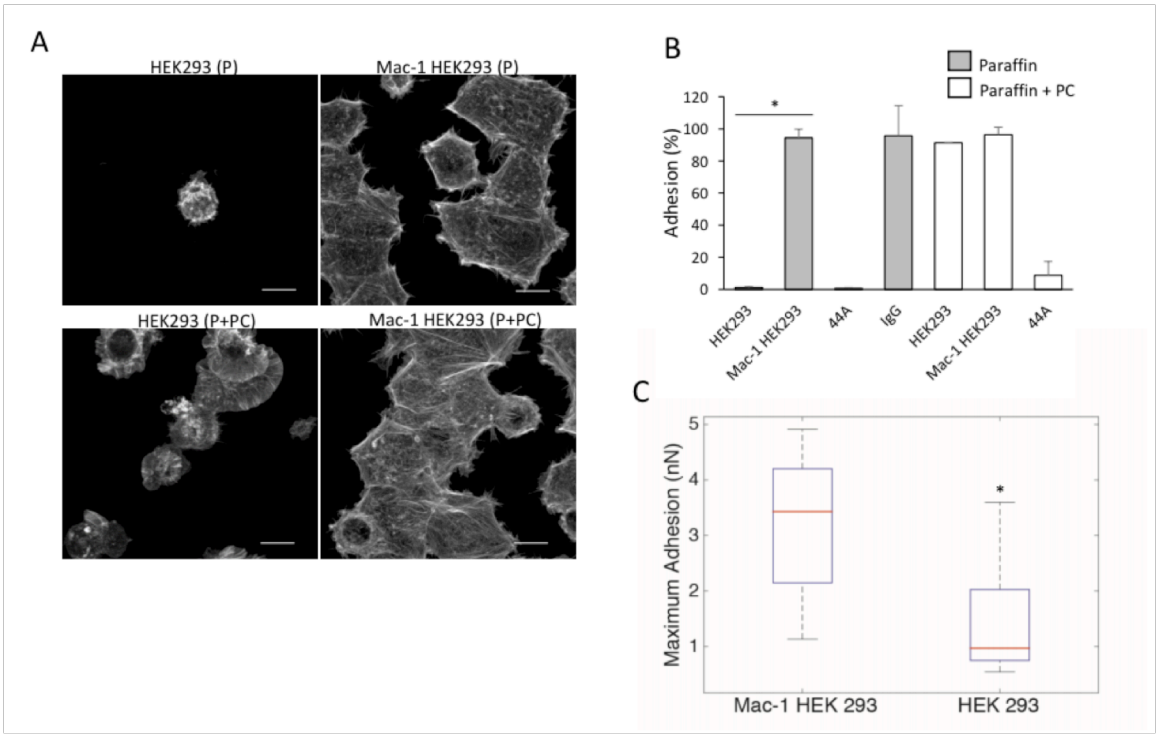

Figure 7.9 (A) Confocal micrographs illustrating the morphology and number of cells adhered after 30 minutes to the P and P+PC surfaces. Representative images are shown. (B) Quantification of adhesion of Mac-1-HEK293 and WT HEK293 cells to the P and P+PC surfaces. Pre-incubation of Mac-1-HEK293 cells with function-blocking anti-Mac-1 mAb 44A abolished adhesion to both P and P+PC surfaces, whereas pre-incubation with IgG isotype control did not affect adhesion. Results shown are means ± S.D. from 9 fields with ~160-430 cells per image from three independent experiments. *$p<0.05$ as determined by ANOVA. (C) Quantification by single cell force spectroscopy of adhesion forces developed between Mac-1-HEK293 and HEK293 cells and the P surfaces. Maximum adhesion was 3.2 ± 1.3 for Mac-1-HEK293 cells and 1.4 ± 1.0 nN for HEK293 cells. Significance was determined from Wilcoxon rank-sum test. *$p<0.05$. The scale bars in the lower right corner of each micrograph are 50 μm.

7.5.6 Micropatterned Paraffin Imparts Spatiotemporal Control over MGC Formation

For the first time, the P surface enabled us to visualize sequential fusion events that led to the formation of MGCs. However, increasing magnification limited the total field of view. This in turn, decreased the probability of observing MGC formation since macrophage fusion is a spatially stochastic process. Based on previous studies using

micropatterned plastic [226], we inferred that it might be possible to spatially confine the fusion process by micropatterning paraffin on optical-quality glass. Micropatterning paraffin in a grid-like pattern (Figure 7.10A) enabled us to obtain not only extraordinary rates of fusion (59 ± 10%) corresponding to an additional 10% increase in the fusion index compared to the P surface, but a high degree of spatial control over the formation of MGCs (Figure 7.10B). The grid system obtained by micropatterned paraffin (MP) enabled also visualization of mixed populations of macrophages expressing eGFP- and mRFP-LifeAct coupled with the ability to definitively show individual MGCs through SEM (Figure 7.10C).

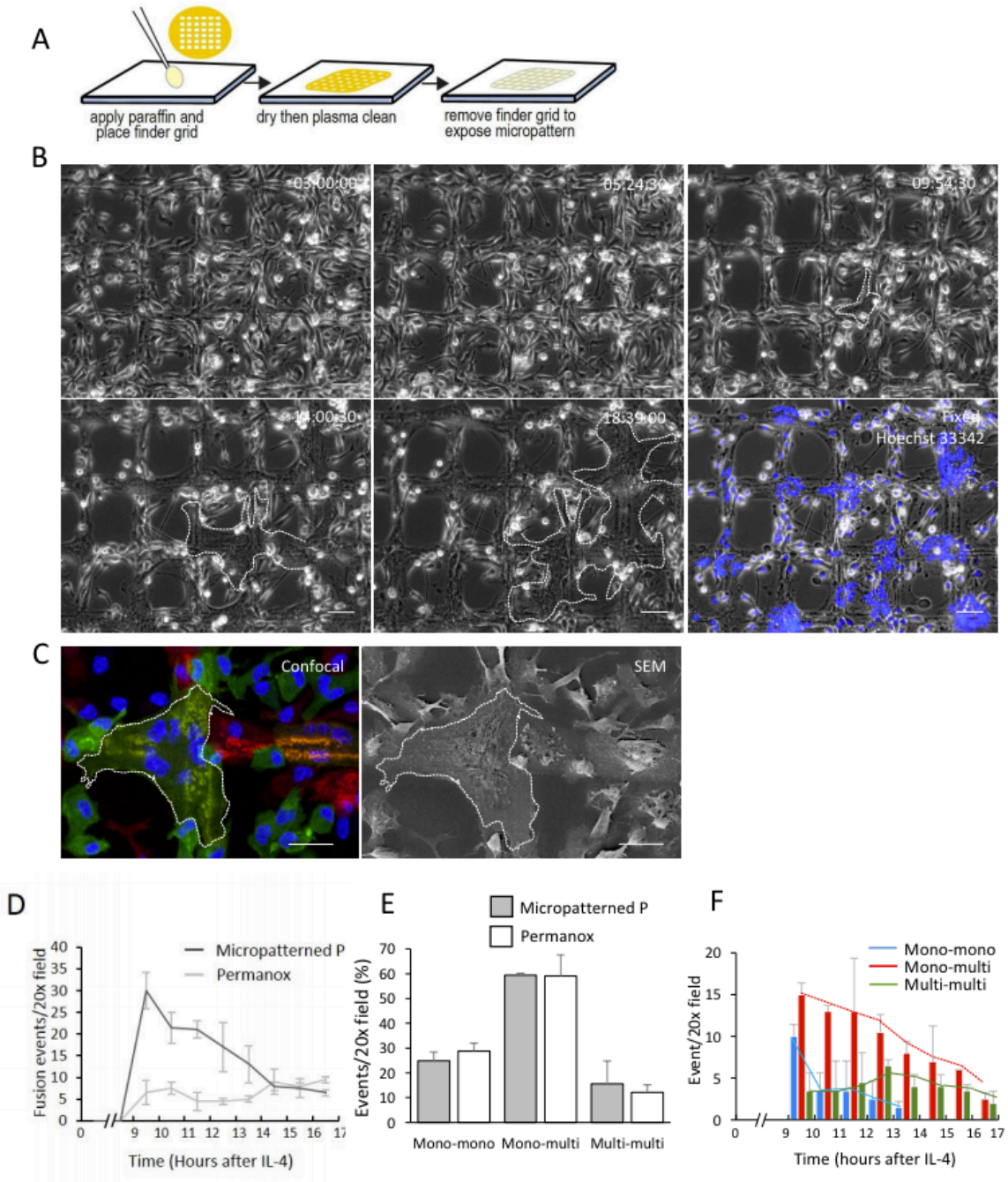

Figure 7.10 (A) Schematic of method used to create micropattered paraffin prints on glass. Five microliters of a 1 mg/mL solution of paraffin in toluene is dispensed onto the glass surface and a finder grid is placed on the drop. After the solution dries the cover glass is plasma cleaned and only surface covered by the print remains fusogenic. (B) Phase-contrast micrographs show the formation of MGCs on the print. Time (hours:min:sec) is shown in the top right corner of each micrograph. The scale bars are 50 μm. In the final still frame, blue corresponds to Hoechst 33342, which labels nuclei. (C) Correlated light and scanning electron microscopy views of a micropatterned P surface

show MGC formation from a mixture of eGFP- and mRFP-LifeAct cells. The scale bar corresponds to 25 μm. (D) Shown are the kinetics of fusion events on the micropatterned P and Permanox surfaces during 8 hr after the beginning of fusion (i.e. 9.5 hr 628 after the application of IL-4). Results shown are means ± S.D. from three independent experiments. (E) Quantification of the types of fusion events during MGC formation on the micropatterned P and Permanox surfaces during 8 hours after the onset of fusion. The data are expressed as percent of the total number of fusion events detected on each surface and are means ± S.D. from three experiments. (F) The kinetics of type 1, 2 and 3 fusion events on the micropatterned P surface during 8 hours after the onset of fusion at 9.5 hr. The data shown are means ± S.D. from three experiments. A 20x field corresponds to 570 x 295 μm.

The use of the MP surface enabled us to reveal the kinetics that govern the formation of MGCs (Figure 7.10D-F). Macrophage fusion began at 9.6 ± 0.8 hr after the application of IL-4, at which time a sudden burst of fusion was observed. The number of fusion events per hour within the 8 hour imaging window gradually decreased over time (Figure 7.10D). On average, we observed 125 ± 22 (n=3) fusion events from the onset of fusion over the next 8 hr of observation when sampled with 20x objective magnification (570 μm x 295 μm). After 24 hours in culture, 71 ± 17% of grid intersections contained MGCs. Since macrophage fusion and the formation of MGCs have never been observed, we refer to mononucleated macrophages that undergo fusion with one another as founders. The formation of MGCs followed three distinct patterns. During the initial phase, fusion occurred between founders and accounted for 25 ± 3% of total events (Figure 7.10E). We refer to these fusion events as type 1. Concurrent to type 1 fusion, mononucleated macrophages began to fuse with early multinucleated cells (type 2 fusion events) which accounted for 60 ± 1% of total events observed. Fusion between MGCs (type 3 events) accounted for 15 ± 9% of total events (Figure 7.10E). While type 1 fusion events ceased after the first 4 hours, type 2 fusion events continued through the entire period of

observation. The greatest number of type 2 events occurred during the first 4 hours (Figure 7.10F), after which time, type 2 of fusion began to decline. Although rare, type 3 fusion events between two multinucleated cells were observed shortly after the initiation of the fusion burst." The peak of type 3 fusion was observed at ~4 hour and then declined (Figure 7.10F).

We next investigated whether the pattern of macrophage fusion on the MP surface, as evidenced by the type of fusion events, was comparable to that induced on Permanox. Similar to the MP surface, fusion began 9.3 ± 0.3 hr after the application of IL-4. However, we observed markedly fewer total fusion events (58 ± 14, n=3) during the next 8 hours. Nevertheless, the relative ratio of the types of events on Permanox was similar (Figure 7.10E). In contrast to the MP surface, fusion on Permanox remained relatively constant over 8 hr observation period (Figure 7.10F). Together, these data suggest that the MP and Permanox surfaces support similar types of fusion events.

7.6 Discussion

In this study we engineered an optical-quality glass surface that enabled us to observe macrophage fusion leading to the formation of MGCs in vitro. To our knowledge, no previous study utilized live cell imaging techniques to visualize directly the process of MGC formation. This deficiency is attributed mainly to two facts. First, the most commonly used surfaces that promote macrophage fusion are plastic (e.g. Permanox, polysterene, etc.). However, plastic is not amenable to most live imaging techniques. Second, although optical-quality glass is required for microscopy, it supports very low levels of macrophage fusion [216]. This obstacle makes visualizing rare fusion events

nearly impossible. These limitations were overcome by engineering a glass surface that promotes high rates of macrophage fusion and at the same time enables the use of advanced live imaging techniques. We found that adsorption of oleamide, or other long hydrocarbon molecules, such as those present in paraffin or petrolatum, converted non-fusogenic glass into a fusogenic surface. Micropatterned glass surfaces further increased macrophage fusion and enabled a remarkable degree of spatiotemporal control over MGC formation.

Our fortuitous finding that the FluoroDish glass surface (FD) supported a high rate of macrophage fusion that was comparable to Permanox plastic led us to the discovery of oleamide contamination. The presence of oleamide contamination on the FD surface may not be surprising since oleamide is commonly used as an additive in the production of plasticware. Indeed, studies suggest that oleamide leaches from disposable plastic tubes exerting potent effects on protein activity [227]. However, the ability of oleamide to promote macrophage fusion has not been previously shown. We demonstrate that adsorption of oleamide onto clean glass increased fusion by ~6-fold. Similar to oleamide, which contains 18 carbon atoms, long (20-40 °C) hydrocarbon molecules present in paraffin and petrolatum were equally, if not more active. Characterization of the physico-chemical properties of the original FD and paraffin-adsorbed surfaces indicated that both surfaces are hydrophobic compared to clean glass (Figure 7.2C). In general, hydrophobic surfaces are known to promote macrophage fusion and have been reported in previous studies [211]. Surface roughness is also presumed to affect macrophage fusion [211]. Previous studies that investigated the effects of surface topology on macrophage fusion demonstrated that there was a 500 nm threshold for linear, parallel gratings of poly(ϵ-caprolactone), poly(lactic acid) and poly(dimethylsiloxane), below which macrophages did

not fuse (Chen et al., 2010). Our AFM imaging data revealed the existence of linear arrays of material on both the FD and paraffin-adsorbed surfaces (Figures 7.2A and 7.7A). However, the calculated roughness indicated that the surfaces were rather flat since adsorbed material was raised from the surface by ~10 nm or less. Furthermore, this study observed no clear connection between surface roughness and fusion. Although FD surface roughness was ~2.5-fold higher than paraffin- adsorbed surfaces, the latter was significantly more active. These data suggest that although surface roughness may be an important factor, surface chemistry or the pattern of adsorption of hydrocarbon molecules may be more critical parameters that affect fusion.

In adhesion assays, we found that on the FD and paraffin-adsorbed surfaces Mac-1 integrin supported adhesion of Mac-1-HEK293 cells. Furthermore, Mac-1 apparently mediated spreading since WT, but not Mac-1-deficient macrophages spread rapidly. Mac-1 is a multiligand receptor capable of binding numerous structurally and functionally unrelated molecules and is involved in numerous leukocyte activities, including adhesion, migration, phagocytosis and others [228]. Recently, we and others demonstrated that Mac-1 is essential also for macrophage fusion on Permanox [225, 229, 230]. Furthermore, spreading of Mac-1-deficient macrophages on Permanox, but not the integrin binding step was strongly reduced [225]. The latter observation is consistent with data obtained from macrophages plated on the FD surface (Figure 7.3C and 7.4C). The ability of Mac-1 to support adhesion to surface adsorbed with oleamide or other molecules containing long hydrocarbons suggests that Mac-1 may bind these molecules and thus directly links Mac-1-mediated recognition with fusion. The molecular basis for the interaction of Mac-1 with oleamide or other hydrocarbon chains is currently under investigation.

The capacity of paraffin-adsorbed glass to promote fusion and retain important optical properties necessary for imaging allowed us to derive insights into the kinetics and morphological features that govern MGC formation. It should be noted that although macrophage fusion on paraffin-adsorbed surfaces is efficient, fusion is spatially stochastic. The randomness associated with the location of fusion makes visualizing MGC formation with high magnification optics challenging. This barrier was mitigated by the use of a paraffin micropattern (MP), which localized fusion to defined regions. Using this cell system, we observed a "burst" in fusion that commenced ~9.5 hours after the application of IL-4. This finding suggests that a latent "priming" period is necessary to attain fusion competence. Based on 8 hours of continuous observation after the onset of the "burst" we were able to distinguish three distinct types of fusion events that account for MGC formation. Initially, fusion occurred between mononucleated macrophages (founder events, type 1), which appears to be a prerequisite for the formation of early multinucleated cells. Fusion of mononucleated macrophages with multinucleated cells is defined as type 2 fusion (Figure 7.10E). Type 2 fusion events were by far the most abundant event that led to MGC formation. Similar to type 1, type 3 fusion events were less frequent. It is interesting to note that macrophage fusion on Permanox, the most fusogenic plastic currently used in the field, was similar in the event type, but not magnitude, to that observed on the MP surface. This indicates that the underlying mechanism responsible for MGC formation on both of these surfaces is similar and underscores the possibility that type 2 fusion is the predominant mechanism of MGC formation. The fact that ~60 % of plated macrophages participated in fusion on MP surface after 24 hours in culture indicates that this subset acquired fusion-competence. Although the transcriptional program required for macrophage "priming"

leading to fusion competence is largely unknown, upregulation of several proteins has been detected [231]. The kinetics of fusion determined in the present study will be critical for future studies aimed at identifying key signaling, cytoskeletal and cell surface molecules involved in macrophage fusion.

Despite the long history of research on MGCs there have been no systematic studies to directly visualize fusion using living macrophages [211, 217, 224, 232]. Furthermore, no ultrastructural studies reported to date detected clear morphological features in fusing macrophages that could have provided clues as to how two external plasma membranes fuse [233-235]. Consequently, unlike phagocytosis which has been extensively characterized [236, 237], the cellular and molecular mechanisms involved in macrophage fusion remain poorly understood. Based on a limited number of electron microscopy data, a model has been proposed that macrophage fusion may involve the phenomenon referred to as "cellocytosis" [232]. According to this model, after attachment of one macrophage to the surface of another, the surface bound macrophage internalizes by sinking. During this process, the internalized cell is enveloped by two plasma membranes, one from the internalizer cell and one being its own plasma membrane. The two membranes then fuse and might be recycled to form the outer plasma membrane of MGC while the cytoplasm and organelles of both cells are integrated. Thus, the main feature of the proposed model is that two external membranes fuse after one cell has been internalized by other cell. In the present investigation, the fusion process appears to be phenotypically different than predicted by the "cellocytosis" model. Although we observed mononucleated macrophages shrouded by MGCs, out of >750 fusion events detected on the P and Permanox surfaces, we observed only two events that may be described as "cellocytosis." In these rare cases,

fusion occurred exclusively on ventral surfaces of the MGC. In the vast majority of events, fusion occurred between intercellular margins with obvious phase-dark protrusions emanating between cells. Thus, macrophage fusion on Permanox and the P surfaces in vitro with living specimens does not seems to support the "cellocytosis" model and suggests that the process involves other mechanisms. For example, the formation of a fusion pore between two cells, as proposed in other fusion systems may be a tenable model [238, 239]. We have observed also that macrophages were highly motile. This finding lends further support to a view that macrophage migration is essential for fusion [218]. Future analyses of the interface between live macrophages undergoing fusion using the method described in the present study as well advanced live imaging techniques may reveal specific morphological features that govern fusion between apposing membranes. This, in turn, may lead to a better understanding of the molecular players involved in this process.

8. Conclusions and Outlook

This dissertation has provided several experiments quantifying the adhesion of cells to various substrates using the AFM. In each chapter, SCFS was used to address interesting biological questions. §3 quantified the adhesion of Mac-1 expressing HEK cells on biomaterials with various concentrations of fibrinogen, demonstrating the anti-adhesive effect of fibrinogen at high surface densities. A novel method combining TIRFM imaging and SCFS was put forward in §4 that allowed for monitoring of Mac-1:fibrinogen binding during SCFS experiments. The analysis of specific integrin-ligand bonds from SCFS experiments was shown to be possible in §5, providing a way to quantify the kinetic parameters of integrin-ligand bonds in their native cell membrane environment. §6 the adhesion forces of platelets and neutrophils on fibrin gels were quantified providing insight into thrombus formation. Finally, in §7 the adhesion of macrophage cells was measured on a novel glass surface, which promoted macrophage fusion. Each of these SCFS experiments presents a unique understanding of the small machines of nature for the diligent observer.

The anti-adhesive effect of multi-layered fibrinogen on biomaterials needs to be considered when developing and evaluating any materials design for implantation that comes in contact with blood. While we evaluated HEK Mac-1 cells on fibrinogen coated biomaterials, our methodology can be used to test how other types of cells found in the blood may interact with biomaterials, and other proteins that may adhere to them [45]. This type of fundamental research could help in the design of biomaterials. Our methodology could also be applied to drug development testing the effect of new drugs on cell adhesion by performing SCFS experiments in the presence of clinical doses.

Combined TIRFM/SCFS experiments offer new insights into cellular interactions with surfaces. The set up we used need not be limited to only TIRFM, but other super resolution methods could potentially be used to evaluate biological parameters such as diffusion coefficients of integrin-ligand pairs or focal adhesion associated protein recruitment while acted upon by a tensil force [240]. The micropatterned surface used in the combined TIRFM/SCFS experiment can be used to offer definitive controls for SCFS experiments [241].

The analysis method for evaluating single molecule interactions from SCFS data proposed here is a first step toward learning the definitive kinetic parameters of integrin-ligand pairs in their physiological conditions. In future experiments, having a wider range of loading rates will provide a more robust data set for quantifying kinetic paramaters. In SMFS experiments varying the retraction velocity is a simple way to change the loading rates, but for SCFS experiments careful attention needs to be given to the effect different retraction velocities will have on the cell membrane and body. A wider range of loading rates will provide more accurate quantification for kinetic parameters, which is necessary in order to understanding the motility of leukocytes [208].

Being able to quantify the adhesion of platelets and neutrophils on fibrin gels provides insight into the stabilization of thrombus during hemostasis. A natural next study would be quantifying adhesion of platelets and neutrophils to thrombi formed *in situ*, and possibly to thrombi formed *in vivo*. Understanding the interaction of platelets with thrombi is critical for understanding possible treatments and symptoms of heart disease [196].

The macrophage inducing glass functionalization technology presented in this dissertation provides unprecedented insight into the formation of MGCs. It will no doubt lead to new discoveries about the macrophage foreign body response. Future SCFS experiments will help to evaluate the role of Mac-1 integrins in macrophage fusion, especially since the novel paraffin glass surface can be used in super resolution microscopy.

The development of these ideas and more is left to another diligent observer equipped with tools developed in this dissertation.

REFERENCES

1. Wojcikiewicz, E.P., X. Zhang, and V.T. Moy, *Force and compliance measurements on living cells using atomic force microscopy (AFM).* Biological Procedures Online, 2004. **6**(1): p. 1-9.

2. Dufrene, Y.F., et al., *Five challenges to bringing single-molecule force spectroscopy into living cells.* Nat Methods, 2011. **8**(2): p. 123-7.

3. Dufrene, Y.F., et al., *Direct probing of the surface ultrastructure and molecular interactions of dormant and germinating spores of Phanerochaete chryosporium.* Journal of Bacteriology, 1999. **181**(17): p. 5350-5354.

4. Rother, J., et al., *Atomic force microscopy-based microrheology reveals significant differences in the viscoelastic response between malign and benign cell lines.* Open Biol, 2014. **4**(5): p. 140046.

5. Zlatanova, J., S.M. Lindsay, and S.H. Leuba, *Single molecule force spectroscopy in biology using the atomic force microscope.* Progress in Biophysics & Molecular Biology, 2000. **74**: p. 37-61.

6. Shen, Y., et al., *Single cell adhesion force measurement for cell viability identification using an AFM cantilever-based micro putter.* Measurement Science and Technology, 2011. **22**(11): p. 115802.

7. Arcadian, *Cell Structure.* Wikimedia Commons, 2006.

8. Alberts, B. and e. al, Molecular Biology of the Cell (Garland Science), 2008.

9. Singer, S.J. and G.L. Nicolson, *The fluid mosaic model of the structure of cell membranes.* Science, 1972. **175**(4023): p. 720-731.

10. Fujiwara, T., et al., *Phospholipids undergo hop diffusion in compartmentalized cell membrane.* J Cell Biol, 2002. **157**(6): p. 1071-81.

11. Ritchie, K., et al., *Detection of non-Brownian diffusion in the cell membrane in single molecule tracking.* Biophys J, 2005. **88**(3): p. 2266-77.

12. Nicolson, G.L., *The Fluid-Mosaic Model of Membrane Structure: still relevant to understanding the structure, function and dynamics of biological membranes after more than 40 years.* Biochim Biophys Acta, 2014. **1838**(6): p. 1451-66.

13. Ruiz, M., *Cell membrane detailed diagram en.* Wikimedia Commons, 2007.

14. Burridge, K. and M. Chrzanowska-Wodnicka, *Focal adhesions, contractility, and signaling.* Annu. Rev. Cell Dev. Biol., 1996. **12**: p. 463-519.

15. Fraley, S.I., et al., *A distinctive role for focal adhesion proteins in three-dimensional cell motility.* Nat Cell Biol, 2010. **12**(6): p. 598-604.

16. Luo, B.-H., C.V. Carman, and T.A. Springer, *Structural Basis of Integrin Regulation and Signaling.* Annual Review Immunology, 2007. **25**: p. 619-647.

17. Katsumi, A., et al., *Integrins in mechanotransduction.* J Biol Chem, 2004. **279**(13): p. 12001-4.

18. Arnaout, M.A., S. Goodman, and J.-P. Xiong, *Structure and mechanics of integrin-based cell adhesion.* Current Opinions in Cell Biology, 2007. **19**(5): p. 495-507.

19. Goodsell, D., et al., *The RCSB PDB "Molecule of the Month": Inspiring a Molecular View of Biology.* PLoS Biol, 2015.

20. Lu, H., et al., *LFA-1 is sufficient in mediating neutrophil emigration in Mac-1-defecient mice.* Journal of Clinical Investigation, 1997. **99**(6): p. 1340-1350.

21. Coxon, A., et al., *A novel role for the beta2 integrin CD11b/CD18 in neutrophil apoptosis: a homeostatic mechanism in inflammation.* Immunity, 1996. **5**: p. 653-666.

22. Arnaout, M.A., *Structure and function of the leukocyte adhesion molecules CD11/CD18.* Blood, 1990. **75**(5): p. 1037-1050.

23. Simon, D.I., et al., *Decreased neointimal formation in Mac-1(-/-) mice reveals a role for inflammation in vascular repair after angioplasty.* J Clin Invest, 2000. **105**(3): p. 293-300.

24. Plow, E.F. and L. Zhang, *A MAC-1 attack: integrin function directly challenged in knockout mice.* Journal of Clinical Investigation, 1997. **99**(6): p. 1145-1146.

25. Diamond, M., et al., *The I domain is a major recognition site on the leukocyte integrin Mac-1 (CD11b/CD18) for four distinct adhesion ligands.* Journal of Cell Biology, 1993. **120**: p. 1031-1043.

26. Blombäck, B., et al., *A two-step fibrinogen-fibrin transition in blood coagulation.* Nature, 1978. **275**: p. 510-505.

27. Doolittle, R.F., *Fibrinogen and fibrin.* Annual Reviews Biochemistry, 1984. **53**: p. 195-229.

28. Gorkun, O.V., et al., *Role of the alphaC domains of fibrin in clot formation.* Biochemistry, 1994. **33**: p. 6986-6997.

29. Podolnikova, N.P., et al., *Control of integrin alphaIIb beta3 outside-in signaling and platelet adhesion by sensing the physical properties of fibrin(ogen) substrates.* Biochemistry, 2010. **49**(1): p. 68-77.

30. Kollman, J.M., et al., *Crystal structure of human fibrinogen.* Biochemistry, 2009. **48**(18): p. 3877-86.

31. Tang, L., et al., *Molecular determinants of acute inflammatory responses to biomaterials.* Journal of Clinical Investigation, 1996. **97**(5): p. 1329-1334.

32. Bots, M.L., et al., *Level of fibrinogen and risk of fatal and non-fatal stroke. Eurostroke: a collaborative study among research centres in Europe.* J ournal of Epidemiol Community Health, 2002. **56**: p. i14-i18.

33. Lishko, V.K., T. Burke, and T. Ugarova, *Antiadhesive effect of fibrinogen: a safeguard for thrombus stability.* Blood, 2007. **109**(4): p. 1541-9.

34. Yermolenko, I.S., et al., *Origin of the nonadhesive properties of fibrinogen matrices probed by force spectroscopy.* Langmuir, 2010. **26**(22): p. 17269-77.

35. Yermolenko, I.S., et al., *The assembly of nonadhesive fibrinogen matrices depends on the alphaC regions of the fibrinogen molecule.* J Biol Chem, 2012. **287**(50): p. 41979-90.

36. Shattil, S.J., C. Kim, and M.H. Ginsberg, *The final steps of integrin activation: the end game.* Nat Rev Mol Cell Biol, 2010. **11**(4): p. 288-300.

37. Tang, H., et al., *The Urokinase-type Plasminogen Activator Receptor Mediates Tyrosine Phosphorylation of Focal Adhesion Proteins and Activation of Mitogen-activated Protein Kinase in Cultured Endothelial Cells.* Journal of Biological Chemistry, 1998. **273**(29): p. 18268-18272.

38. Wei, Y., et al., *Regulation of integrin function by urokinase receptor.* Science, 1996. **273**: p. 1551.

39. Jokusch, B.M., et al., *The molecular architecture of focal adhesions.* Annu Rev Cell Dev Biol, 1995. **11**: p. 379-416.

40. Mitra, S.K., D.A. Hanson, and D.D. Schlaepfer, *Focal adhesion kinase: in command and control of cell motility.* Nat Rev Mol Cell Biol, 2005. **6**(1): p. 56-68.

41. Balaban, N.Q., et al., *Force and focal adhesion assembly: a close relationship studied using elastic micropatterned substrates.* Nature Cell Biology, 2001. **3**: p. 466-472.

42. Roca-Cusachs, P., T. Iskratsch, and M.P. Sheetz, *Finding the weakest link: exploring integrin-mediated mechanical molecular pathways.* J Cell Sci, 2012. **125**(Pt 13): p. 3025-38.

43. Cance, W.G., et al., *Immunohistochemical analyses of focal adhesion kinase expression in benign and malignant human breast and colon tissues: correlation with preinvasive and invasive phenotypes.* Clinical Cancer Research, 2000. **6**: p. 2417-2423.

44. Puech, P.H., et al., *Measuring cell adhesion forces of primary gastrulating cells from zebrafish using atomic force microscopy.* J Cell Sci, 2005. **118**(Pt 18): p. 4199-206.

45. Maciaszek, J.L., et al., *Single-cell force spectroscopy as a technique to quantify human red blood cell adhesion to subendothelial laminin.* J Biomech, 2014. **47**(16): p. 3855-61.

46. Bershadsky, A.D., N.Q. Balaban, and B. Geiger, *Adhesion-dependent cell mechanosensitivity.* Annu Rev Cell Dev Biol, 2003. **19**: p. 677-95.

47. Sheetz, M.P., *Cell control by membrane-cytoskeleton adhesion.* Nature Reviews Molecular Cell Biology, 2001. **2**: p. 392-396.

48. Taubenberger, A.V., D.W. Hutmacher, and D.J. Muller, *Single-cell force spectroscopy, an emerging tool to quantify cell adhesion to biomaterials.* Tissue Eng Part B Rev, 2014. **20**(1): p. 40-55.

49. Benoit, M., et al., *Discrete interactions in cell adhesion measured by single-molecule force spectroscopy.* Nature Cell Biology, 2000. **2**.

50. Merkel, R., et al., *Energy landscapes of receptor-ligand bonds explored with dynamic force spectroscopy.* Nature, 1999. **397**: p. 50-53.

51. Myong, S., et al., *Repetitive shuttling of a motor protein on DNA.* Nature, 2005. **437**(7063): p. 1321-5.

52. Evans, E. and K. Ritchie, *Dynamic strength of molecular adhesion bonds.* Biophysical Journal, 1997. **72**: p. 1541-1555.

53. Binnig, G., C.F. Quate, and C. Gerber, *Atomic force microscope.* Phys Rev Lett, 1986. **56**(9): p. 930-933.

54. Binnig, G., et al., *Surface Studies by Scanning Tunneling Microscopy.* Physical Review Letters, 1982. **49**(1): p. 57-61.

55. Alexander, S., et al., *An atomic-resolution atomic-force microscope implemented using an optical lever.* Journal of Applied Physics, 1989. **65**(1): p. 164.

56. García, R. and R. Pérez, *Dynamic atomic force microscopy methods.* Surface Science Reports, 2002. **47**: p. 197-301.

57. Briscoe, B.J., K.S. Sebastian, and M.J. Adams, *The effect of indenter geometry on the elastic response to indentation.* Journal of Physics D: Applied Physics, 1994. **27**(6): p. 1156-1162.

58. Hertz, H., *Über die Berührung fester elasticher Körper.* J. für die reine und Angew. Math., 1882. **171**: p. 156-171.

59. Butt, H.-J. and M. Jaschke, *Calculation of thermal noise in atomic force microscopy.* Nanotechnology, 1995. **6**: p. 1-7.

60. Hutter, J.L. and J. Bechhoefer, *Erratum: ''Calibration of atomic-force microscope tips'' [Rev. Sci. Instrum. 64, 1868 (1993)].* Review of Scientific Instruments, 1993. **64**(11): p. 3342.

61. te Riet, J., et al., *Interlaboratory round robin on cantilever calibration for AFM force spectroscopy.* Ultramicroscopy, 2011. **111**(12): p. 1659-69.

62. Sader, J.E., J.W.M. Chon, and P. Mulvaney, *Calibration of rectangular atomic force microscope cantilevers.* Review of Scientific Instruments, 1999. **70**(10): p. 3967-3969.

63. Stark, R.W., T. Drobek, and W.M. Heckl, *Thermomechanical noise of a free v-shaped cantilever for atomic-force microscopy.* Ultramicroscopy, 2001. **86**: p. 207-215.

64. Petris, S.d., *Concavalin A receptors, immunoglobulins and O antigen of the lymphocyte surface.* Journal of Cell Biology, 1975. **65**: p. 123-146.

65. Benoit, M. and H.E. Gaub, *Measuring Cell Adhesion Forces with the Atomic Force Microscope at the Molecular Level.* Cells Tissues Organs, 2002. **172**(3): p. 174-189.

66. Tao, N.J., S.M. Lindsay, and S. Lees, *Measuring the microelastic properties of biological material.* Biophysical Journal, 1992. **63**: p. 1165-1169.

67. Sneddon, I.N., *The relation between load and penetration in the axisymmetric Boussinesq problem for a punch of arbitrary profile.* Int. J. Engng Sci., 1965. **3**: p. 47-57.

68. Rief, M., et al., *Reversible unfolding of individual titin immunoglobulin domains by AFM.* Science, 1997. **276**(5315): p. 1109-1112.

69. Bouchiat, C., et al., *Estimating the persistence length of a worm-like chain molecule from force-extension measurements.* Biophysical Journal, 1999. **76**: p. 409-413.

70. Johnson, K.L., K. Kendall, and A.D. Roberts, *Surface energy and the contact of elastic solids.* Proc. of the R. Soc. of Lond., 1971. **324**: p. 301-313.

71. Derjaguin, B.V., V.M. Muller, and Y.P. Toporov, *Effect of contact deformations on the adhesion of particles.* Journal of Colloid and Interface Science, 1975. **53**(2): p. 314-326.

72. Ebenstein, D.M., *Nano-JKR force curve method overcomes challenges of surface detection and adhesion for nanoindentation of a compliant polymer in air and water.* Journal of Materials Research, 2011. **26**(08): p. 1026-1035.

73. Carrillo, F., et al., *Nanoindentation of polydimethylsiloxane elastomers: Effect of crosslinking, work of adhesion, and fluid environment on elastic modulus.* Journal of Materials Research, 2011. **20**(10): p. 2820-2830.

74. Tabor, D., *Surface forces and surface interactions.* Journal of Colloid and Interface Science, 1977. **58**(1): p. 2-13.

75. Lin, D.C. and F. Horkay, *Nanomechanics of polymer gels and biological tissues: A critical review of analytical approaches in the Hertzian regime and beyond.* Soft Matter, 2008. **4**(4): p. 669.

76. Guo, S. and B.B. Akhremitchev, *Packing density and structural heterogeneity of insulin amyloid fibrils measured by AFM nanoindentation.* Biomacromolecules, 2006. **7**: p. 1630-1636.

77. Fuhrmann, A., et al., *AFM stiffness nanotomography of normal, metaplastic and dysplastic human esophageal cells.* Phys Biol, 2011. **8**(1): p. 015007.

78. Kramers, H.A., *Brownian motion in a field of force and the diffusion model of chemical reactions.* Physica, 1940. **7**(4): p. 284-304.

79. Bell, G., *Models for the specific adhesion of cells to cells.* Science, 1978. **200**(4342): p. 618-627.

80. Evstigneev, M. and P. Reimann, *Dynamic force spectroscopy: optimized data analysis.* Physical Review E, 2003. **68**: p. 045103(R).

81. Raible, M., et al., *Theoretical analysis of dynamic force spectroscopy experiments on ligand-receptor complexes.* Biotechnology, 2004. **112**: p. 13-23.

82. Fuhrmann, A., et al., *Refined procedure of evaluating experimental single-molecule force spectroscopy data.* Phys Rev E Stat Nonlin Soft Matter Phys, 2008. **77**(3 Pt 1): p. 031912.

83. Getfert, S., M. Evstigneev, and P. Reimann, *Single-molecule force spectroscopy: Practical limitations beyond Bell's model.* Physica A: Statistical Mechanics and its Applications, 2009. **388**(7): p. 1120-1132.

84. Guo, S., et al., *Effects of multiple-bond ruptures on kinetic parameters extracted from force spectroscopy measurements: revisiting biotin-streptavidin interactions.* Biophys J, 2008. **95**(8): p. 3964-76.

85. Dudko, O.K., G. Hummer, and A. Szabo, *Intrinsic rates and activation free energies from single-molecule pulling experiments.* Phys Rev Lett, 2006. **96**(10): p. 108101.

86. Dudko, O.K., G. Hummer, and A. Szabo, *Theory, analysis, and interpretation of single-molecule force spectroscopy experiments.* PNAS, 2008. **105**(41): p. 15755-15760.

87. Jordan, S.W. and E.L. Chaikof, *Novel thromboresistant materials.* Journal of vascular surgery, 2007. **45**(6): p. A104-A115.

88. Yang, W., et al., *Pursuing "zero" protein adsorption of poly (carboxybetaine) from undiluted blood serum and plasma.* Langmuir, 2009. **25**(19): p. 11911-11916.

89. Pillai, S., et al., *Preventing protein adsorption from a range of surfaces using an aqueous fish protein extract.* Biomacromolecules, 2009. **10**(10): p. 2759-2766.

90. Lindon, J.N., et al., *Does the conformation of adsorbed fibrinogen dictate platelet interactions with artificial surfaces?* Blood, 1986. **68**(2): p. 355-362.

91. Tsai, W.B., J.M. Grunkemeier, and T.A. Horbett, *Human plasma fibrinogen adsorption and platelet adhesion to polystyrene.* Journal of biomedical materials research, 1999. **44**(2): p. 130-139.

92. Tsai, W.B., J.M. Grunkemeier, and T.A. Horbett, *Variations in the ability of adsorbed fibrinogen to mediate platelet adhesion to polystyrene-based materials: A multivariate statistical analysis of antibody binding to the platelet binding sites of fibrinogen.* Journal of Biomedical Materials Research Part A, 2003. **67**(4): p. 1255-1268.

93. Wu, Y., et al., *The role of adsorbed fibrinogen in platelet adhesion to polyurethane surfaces: a comparison of surface hydrophobicity, protein adsorption, monoclonal antibody binding, and platelet adhesion.* Journal of Biomedical Materials Research Part A, 2005. **74**(4): p. 722-738.

94. Xu, L.-C. and C.A. Siedlecki, *Atomic force microscopy studies of the initial interactions between fibrinogen and surfaces.* Langmuir, 2009. **25**(6): p. 3675-3681.

95. Sivaraman, B. and R.A. Latour, *The relationship between platelet adhesion on surfaces and the structure versus the amount of adsorbed fibrinogen.* Biomaterials, 2010. **31**(5): p. 832-839.

96. Szott, L.M. and T.A. Horbett, *Protein interactions with surfaces: cellular responses, complement activation, and newer methods.* Current opinion in chemical biology, 2011. **15**(5): p. 677-682.

97. Patel, M., et al., *Experimental evaluation of ten clinically used arterial prostheses.* Annals of vascular surgery, 1992. **6**(3): p. 244-251.

98. Gosselin, C., et al., *In vivo platelet deposition on polytetrafluoroethylene coated with fibrin glue containing fibroblast growth factor 1 and heparin in a canine model.* The American journal of surgery, 1995. **170**(2): p. 126-130.

99. Swartz, D.D., J.A. Russell, and S.T. Andreadis, *Engineering of fibrin-based functional and implantable small-diameter blood vessels.* American Journal of Physiology-Heart and Circulatory Physiology, 2005. **288**(3): p. H1451-H1460.

100. Hasegawa, T., et al., *Autologous fibrin-coated small-caliber vascular prostheses improve antithrombogenicity by reducing immunologic response.* The Journal of thoracic and cardiovascular surgery, 2007. **133**(5): p. 1268-1276. e1.

101. Coller, B.S., *Interaction of normal, thrombasthenic, and Bernard-Soulier platelets with immobilized fibrinogen: defective platelet-fibrinogen interaction in thrombasthenia.* Blood, 1980. **55**(2): p. 169-178.

102. Savage, B. and Z. Ruggeri, *Selective recognition of adhesive sites in surface-bound fibrinogen by glycoprotein IIb-IIIa on nonactivated platelets.* Journal of Biological Chemistry, 1991. **266**(17): p. 11227-11233.

103. Endenburg, S., et al., *Platelet adhesion to fibrin (ogen).* Blood coagulation & fibrinolysis, 1993. **4**(1): p. 139-142.

104. Endenburg, S.C., et al., *Plasma fibrinogen inhibits platelet adhesion in flowing blood to immobilized fibrinogen.* Arteriosclerosis, thrombosis, and vascular biology, 1996. **16**(5): p. 633-638.

105. Lishko, V.K., T. Burke, and T. Ugarova, *Antiadhesive effect of fibrinogen: a safeguard for thrombus stability.* Blood, 2007. **109**(4): p. 1541-1549.

106. Jen, C. and J. Lin, *Direct observation of platelet adhesion to fibrinogen-and fibrin-coated surfaces.* American Journal of Physiology-Heart and Circulatory Physiology, 1991. **261**(5): p. H1457-H1463.

107. van Ryn, J., et al., *Accumulation of radiolabelled platelets and fibrin on the carotid artery of rabbits after angioplasty: effects of heparin and dipyridamole.* Thrombosis and haemostasis, 2003. **90**(6): p. 1179-1186.

108. Podolnikova, N.P., et al., *Control of integrin αIIbβ3 outside-in signaling and platelet adhesion by sensing the physical properties of fibrin (ogen) substrates.* Biochemistry, 2009. **49**(1): p. 68-77.

109. Hamlin, G., et al., *Evaluation of the thrombogenic potential of three types of arterial graft studied in an artificial circulation.* British Journal of Surgery, 1978. **65**(4): p. 272-276.

110. Goldman, M., et al., *Femoropopliteal bypass grafts—an isotope technique allowing in vivo comparison of thrombogenicity.* British Journal of Surgery, 1982. **69**(7): p. 380-382.

111. Goldman, M., et al., *Platelet accumulation on mature Dacron grafts in man.* British Journal of Surgery, 1982. **69**(S6): p. S38-S40.

112. Harker, L.A., S.J. Slichter, and L.R. Sauvage, *Platelet consumption by arterial prostheses: the effects of endothelialization and pharmacologic inhibition of platelet function.* Annals of surgery, 1977. **186**(5): p. 594.

113. McCollum, C., et al., *Arterial graft maturation: the duration of thrombotic activity in Dacron aortobifemoral grafts measured by platelet and fibrinogen kinetics.* British Journal of Surgery, 1981. **68**(1): p. 61-64.

114. De BAKEY, M.E., et al., *The fate of Dacron vascular grafts.* Archives of Surgery, 1964. **89**(5): p. 755-782.

115. Szilagyi, D.E., et al., *Long-term behavior of a dacron arterial substitute: clinical, roentgenologic and histologic correlations.* Annals of surgery, 1965. **162**(3): p. 453.

116. Berger, K., et al., *Healing of arterial prostheses in man: its incompleteness.* Annals of surgery, 1972. **175**(1): p. 118.

117. Shi, Q., et al., *Endothelium on the flow surface of human aortic Dacron vascular grafts.* Journal of vascular surgery, 1997. **25**(4): p. 736-742.

118. Lishko, V.K., V.P. Yakubenko, and T.P. Ugarova, *The interplay between integrins alphaMBeta2 and alpha5beta1 during cell migraiton to fibronectin.* Experimental Cell Research, 2003. **283**: p. 116-126.

119. Yakubenko, V.P., et al., *A molecular basis for integrin alphaMbeta 2 ligand binding promiscuity.* J Biol Chem, 2002. **277**(50): p. 48635-42.

120. Ugarova, T.P., et al., *Conformational changes in fibrinogen elicited by its interaction with platelet membrane glycoprotein GPIIb-IIIa.* Journal of Biological Chemistry, 1993. **268**(28): p. 21080-21087.

121. Anamelechi, C.C., G.A. Truskey, and W.M. Reichert, *Mylar™ and Teflon-AF™ as cell culture substrates for studying endothelial cell adhesion.* Biomaterials, 2005. **26**(34): p. 6887-6896.

122. Christenson, W., et al., *Combined single cell AFM manipulation and TIRFM for probing the molecular stability of multilayer fibrinogen matrices.* Ultramicroscopy, 2014. **136**: p. 211-5.

123. Lishko, V.K., et al., *Regulated unmasking of the cryptic binding site for integrin αMβ2 in the γC-domain of fibrinogen.* Biochemistry, 2002. **41**(43): p. 12942-12951.

124. Zilla, P., D. Bezuidenhout, and P. Human, *Prosthetic vascular grafts: wrong models, wrong questions and no healing.* Biomaterials, 2007. **28**(34): p. 5009-5027.

125. Stewart, G.J., et al., *A scanning and transmission electron microscope study of the luminal coating on Dacron prostheses in the canine thoracic aorta.* The Journal of laboratory and clinical medicine, 1975. **85**(2): p. 208-226.

126. Guidoin, R., et al., *Polyester prostheses as substitutes in the thoracic aorta of dogs. I. Evaluation of commercial prostheses.* Journal of biomedical materials research, 1983. **17**(6): p. 1049-1077.

127. Lishko, V., et al., *Fibrinogen counteracts the antiadhesive effect of fibrin-bound plasminogen by preventing its activation by adherent U937 monocytic cells.* Journal of Thrombosis and Haemostasis, 2012. **10**(6): p. 1081-1090.

128. Kinlough-Rathbone, R.L., M.A. Packham, and J.F. Mustard, *Vessel injury, platelet adherence, and platelet survival.* Arteriosclerosis, 1983. **3**(6): p. 529-546.

129. Yermolenko, I.S., et al., *The Assembly of Nonadhesive Fibrinogen Matrices Depends on the alpha C Regions of the Fibrinogen Molecule.* Journal of Biological Chemistry, 2012. **287**(50): p. 41979-41990.

130. Podolnikova, N.P., et al., *Control of Integrin alpha(IIb)beta(3) Outside-In Signaling and Platelet Adhesion by Sensing the Physical Properties of Fibrin(ogen) Substrates.* Biochemistry, 2010. **49**(1): p. 68-77.

131. Binnig, G., C.F. Quate, and C. Gerber, *Atomic Force Microscope.* Phys.Rev.Lett., 1986. **56**(9): p. 930-933.

132. Zlatanova, J., S.M. Lindsay, and S.H. Leuba, *Single molecule force spectroscopy in biology using the atomic force microscope.* Progress in Biophysics and Molecular Biology, 2000. **74**: p. 37-61.

133. Butt, H.J., B. Cappella, and M. Kappl, *Force measurements with the atomic force microscope: Techniques, interpretation and applications.* Surface Science Reports, 2005. **59** p. 1-152.

134. Hinterdorfer, P. and Y.F. Dufrene, *Detection and localization of single molecular recognition events using atomic force microscopy.* Nature Methods, 2006. **3** p. 347-355.

135. Helenius, J., et al., *Single-cell force spectroscopy.* Journal of Cell Science, 2008. **121**(11): p. 1785-1791.

136. Liang, J. and J.M. Fernandez, *Mechanochemistry: One bond at a time.* ACS Nano, 2009. **3**: p. 1628-1645.

137. Fuhrmann, A. and R. Ros, *Single molecule force spectroscopy: a method for quantitative analysis of ligand-receptor interactions.* Nanomedicine, 2010. **5**: p. 657-666.

138. Benoit, M., et al., *Discrete interactions in cell adhesion measured by single-molecule force spectroscopy.* Nat.Cell Biol., 2000. **2**(6): p. 313-317.

139. Grandbois, M., et al., *Affinity imaging of red blood cells using an atomic force microscope.* J.Histochem.Cytochem., 2000. **48**(5): p. 719-724.

140. Taubenberger, A., et al., *Revealing early steps of alpha(2)beta(1) integrin-mediated adhesion to collagen type I by using single-cell force spectroscopy.* Molecular Biology of the Cell, 2007. **18**(5): p. 1634-1644.

141. Helenius, J., et al., *Single-cell force spectroscopy.* Journal of Cell Science, 2008. **121**(11): p. 1785-1791.

142. Mueller, T., et al., *Studying protein-mediated cell adhesion by single cell force spectroscopy.* European Journal of Cell Biology, 2008. **87**: p. 45-45.

143. Boettiger, D. and B. Wehrle-Haller, *Integrin and glycocalyx mediated contributions to cell adhesion identified by single cell force spectroscopy.* Journal of Physics-Condensed Matter, 2010. **22**(19).

144. Friedrichs, J., J. Helenius, and D.J. Muller, *Quantifying cellular adhesion to extracellular matrix components by single-cell force spectroscopy.* Nature Protocols, 2010. **5**(7): p. 1353-1361.

145. Dao, L., et al., *Revealing non-genetic adhesive variations in clonal populations by comparative single-cell force spectroscopy.* Experimental Cell Research, 2012. **318**(17): p. 2155-2167.

146. Elter, P., et al., *Low fibronectin concentration overcompensates for reduced initial fibroblasts adhesion to a nanoscale topography: Single-cell force spectroscopy.* Colloids and Surfaces B-Biointerfaces, 2012. **95**: p. 82-89.

147. Aliuos, P., et al., *Evaluation of single-cell force spectroscopy and fluorescence microscopy to determine cell interactions with femtosecond-laser microstructured*

titanium surfaces. Journal of Biomedical Materials Research Part A, 2013. **101A**(4): p. 981-990.

148. Madl, J., et al., *A combined optical and atomic force microscope for live cell investigations.* Ultramicroscopy, 2006. **106**(8-9): p. 645-651.

149. Gumpp, H., et al., *Ultrastable combined atomic force and total internal fluorescence microscope.* Review of Scientific Instruments, 2009. **80**(6).

150. Oreopoulos, J. and C.M. Yip, *Probing Membrane Order and Topography in Supported Lipid Bilayers by Combined Polarized Total Internal Reflection Fluorescence-Atomic Force Microscopy.* Biophysical Journal, 2009. **96**(5): p. 1970-1984.

151. Kufer, S.K., et al., *Optically monitoring the mechanical assembly of single molecules.* Nature Nanotechnology, 2009. **4**(1): p. 45-49.

152. Gradinaru, C.C., et al., *Simultaneous atomic-force and two-photon fluorescence imaging of biological specimens in vivo.* Ultramicroscopy, 2004. **99**(4): p. 235-245.

153. Noy, A. and T.R. Huser, *Combined force and photonic probe microscope with single, molecule sensitivity.* Review of Scientific Instruments, 2003. **74**(3): p. 1217-1221.

154. Fuhrmann, A., et al., *AFM stiffness nanotomography of normal, metaplastic and dysplastic human esophageal cells.* Physical Biology, 2011. **8**: p. 015007

155. Schulz, O., et al., *Tip induced fluorescence quenching for nanometer optical and topographical resolution.* Optical Nanoscopy, 2013. **2**: p. 1.

156. Hu, D.H., et al., *Correlated topographic and spectroscopic imaging by combined atomic force microscopy and optical microscopy.* Journal of Luminescence, 2004. **107**(1-4): p. 4-12.

157. Harke, B., et al., *A novel nanoscopic tool by combining AFM with STED microscopy.* Optical Nanoscopy 2012. **1**: p. 3.

158. Kumar, A. and G.M. Whitesides, *Features of gold having micrometer to centimeter dimensions can be formed through a combination of stamping with an elastomeric stamp and an alkanethiol "ink" followed by chemical etching.* Appl.Phys.Lett., 1993. **63**(14): p. 2002-2004.

159. Schulz, O., et al., *Simultaneous single molecule atomic force and fluorescence lifetime imaging.* PROC. of SPIE, 2010. **7571**: p. 757109

160. Rasband, W.S., *ImageJ*. 1997-2012, U. S. National Institutes of Health: Bethesda, Maryland, USA, http://imagej.nih.gov/ij/.

161. Delamarche, E., et al., *Patterned delivery of immunoglobulins to surfaces using microfluidic networks.* Science, 1997. **276**(5313): p. 779-781.

162. Duong, T.T., et al., *Size Dependent Free Solution DNA Electrophoresis in Structured Micro Fluidic Systems.* Microelectronic Engineering, 2003. **67-68C**: p. 905-912.

163. Nakano, A., et al., *Immunoglobulin G and Bovine Serum Albumin Streaming Dielectrophoresis in a Microfluidic Device.* Electrophoresis, 2011. **32**: p. 2314-2322.

164. Yakubenko, V.P., et al., *A molecular basis for integrin alpha(M)beta(2) ligand binding promiscuity.* Journal of Biological Chemistry, 2002. **277**(50): p. 48635-48642.

165. Lishko, V.K., V.P. Yakubenko, and T. Ugarova, *The interplay between integrins alpha(M)beta(2) and alpha(5)beta(1) during cell migration to fibronectin.* Experimental Cell Research, 2003. **283**: p. 116-126.

166. Lim, K., et al., *Visualization of integrin Mac-1 in vivo.* J Immunol Methods, 2015. **426**: p. 120-7.

167. Rosetti, R. and T. mayadas, *The many faces of Mac-1 in autoimmune disease.* Immunological Reviews, 2016. **269**: p. 175-193.

168. Flick, M.J., et al., *Leukocyte engagement of fibrin(ogen) via the integrin receptor alphaMbeta2/Mac-1 is critical for host inflammatory response in vivo.* J Clin Invest, 2004. **113**(11): p. 1596-606.

169. Pillay, J., et al., *Acute-phase concentrations of soluble fibrinogen inhibit neutrophil adhesion under flow conditions in vitro through interactions with ICAM-1 and MAC-1 (CD11b/CD18).* J Thromb Haemost, 2013. **11**(6): p. 1172-82.

170. Safiullin, R., et al., *Fibrinogen matrix deposited on the surface of biomaterials acts as a natural anti-adhesive coating.* Biomaterials, 2015. **67**: p. 151-9.

171. Helenius, J., et al., *Single-cell force spectroscopy.* J Cell Sci, 2008. **121**(11): p. 1785-91.

172. Friedrichs, J., J. Helenius, and D.J. Muller, *Quantifying cellular adhesion to extracellular matrix components by single-cell force spectroscopy.* Nat Protoc, 2010. **5**(7): p. 1353-61.

173. Lee, I. and R.E. Marchant, *Molecular interaction studies of hemostasis: fibrinogen ligand–human platelet receptor interactions.* Ultramicroscopy, 2003. **97**(1-4): p. 341-352.

174. Krieg, M., et al., *A bond for a lifetime: employing membrane nanotubes from living cells to determine receptor-ligand kinetics.* Angew Chem Int Ed Engl, 2008. **47**(50): p. 9775-7.

175. Friedrichs, J., et al., *A practical guide to quantify cell adhesion using single-cell force spectroscopy.* Methods, 2013. **60**(2): p. 169-78.

176. Sariisik, E., et al., *Decoding Cytoskeleton-Anchored and Non-Anchored Receptors from Single-Cell Adhesion Force Data.* Biophys J, 2015. **109**(7): p. 1330-3.

177. Baumgartner, W., et al., *Cadherin interaction probed by atomic force microscopy.* PNAS, 2000. **97**(8): p. 4005-4010.

178. Muller, D.J., et al., *Force probing surfaces of living cells to molecular resolution.* Nat Chem Biol, 2009. **5**(6): p. 383-90.

179. Hinterdorfer, P. and Y.F. Dufrene, *Detection and localization of single molecular recognition events using atomic force microscopy.* Nat Methods, 2006. **3**(5): p. 347-55.

180. Carvalho, F.A., et al., *Atomic force microscopy-based molecular recognition of a fibrinogen receptor on human erythrocytes.* ACSNano, 2010. **4**(8): p. 4609-4620.

181. Litvinov, R.I., et al., *Multi-step fibrinogen binding to the integrin (alpha)IIb(beta)3 detected using force spectroscopy.* Biophys J, 2005. **89**(4): p. 2824-34.

182. DUTTA, S., et al., *Probing αIIbβ3: Ligand Interactions by Dynamic Force Spectroscopy and Surface Plasmon Resonance.* Nano Life, 2013. **3**(01): p. 1340005.

183. Litvinov, R.I., et al., *Resolving two-dimensional kinetics of the integrin ≈í¬±IIb≈í,â§3-fibrinogen interactions using binding-unbinding correlation spectroscopy.* Journal of Biological Chemistry, 2012. **287**(42): p. 35275-35285.

184. Yang, H., et al., *Interaction between single molecules of Mac-1 and ICAM-1 in living cells: an atomic force microscopy study.* Experimental Cell Research, 2007. **313**: p. 3497-3504.

185. Taubenberger, A., et al., *Revealing early steps of α2β1 integrin-mediated adhesion to collagen type I by using single-cell force spectroscopy.* Molecular biology of the cell, 2007. **18**(5): p. 1634-1644.

186. Fu, C., et al., *Determining β2-integrin and intercellular adhesion molecule 1 binding kinetics in tumor cell adhesion to leukocytes and endothelial cells by a gas-driven micropipette assay.* Journal of Biological Chemistry, 2011. **286**(40): p. 34777-34787.

187. Liang, S., et al., *Two-dimensional kinetics of β(2)-integrin and ICAM-1 bindings between neutrophils and melanoma cells in a shear flow.* American journal of physiology. Cell physiology, 2008. **294**(3): p. C743-C753.

188. Li, N., et al., *Distinct binding affinities of Mac-1 and LFA-1 in neutrophil activation.* J Immunol, 2013. **190**(8): p. 4371-81.

189. Lomakina, E.B. and R.E. Waugh, *Micromechanical tests of adhesion dynamics between neutrophils and immobilized ICAM-1.* Biophysical Journal, 2004. **88**: p. 1223-1233.

190. Gergely, C., et al., *Unbinding process of adsorbed proteins under external stress studied by atomic force microscopy.* PNAS, 2000. **97**(20): p. 10802-10807.

191. Jackson, S.P., *The growing complexity of platelet aggregation.* Blood, 2007. **109**(12): p. 5087-5095.

192. Ruggeri, Z.M. and G.L. Mendolicchio, *Adhesion Mechanisms in Platelet Function.* Circulation Research, 2007. **100**(12): p. 1673-1685.

193. Furie , B. and B.C. Furie *Mechanisms of Thrombus Formation.* New England Journal of Medicine, 2008. **359**(9): p. 938-949.

194. Gawaz, M., H. Langer, and A.E. May, *Platelets in inflammation and atherogenesis.* The Journal of Clinical Investigation, 2005. **115**(12): p. 3378-3384.

195. Iannacone, M., et al., *Platelets mediate cytotoxic T lymphocyte-induced liver damage.* Nat Med, 2005. **11**(11): p. 1167-1169.

196. Jackson, S.P., *Arterial thrombosis[mdash]insidious, unpredictable and deadly.* Nat Med, 2011. **17**(11): p. 1423-1436.

197. Cooley, B.C., *In Vivo Fluorescence Imaging of Large-Vessel Thrombosis in Mice.* Arteriosclerosis, Thrombosis, and Vascular Biology, 2011. **31**(6): p. 1351-1356.

198. Kamocka, M.M., et al., *Two-photon intravital imaging of thrombus development.* Journal of Biomedical Optics, 2010. **15**(1): p. 016020-016020-7.

199. Edenburg, S.C., et al., *Platelet adhesion to fibrin(ogen), blood coagulation.* Fibrinolysis, 1993. **4**: p. 139-142.

200. Jen, C.J. and J.S. Lin, *Direct observation of platelet adhesion to fibrinogen and fibrin coated surfaces.* Am. J. Phys., 1991. **261**: p. H1457-H1463.

201. Corum, L.E., et al., *Using microcontact printing of fibrinogen to control surface-induced platelet adhesion and activation.* Langmuir, 2011. **27**(13): p. 8316-22.

202. Owaynat, H., et al., *Deposition of fibrinogen on the surface of in vitro thrombi prevents platelet adhesion.* Thromb Res, 2015. **136**(6): p. 1231-9.

203. Moreno-Arotzena, O., et al., *Characterization of Fibrin and Collagen Gels for Engineering Wound Healing Models.* Materials (Basel), 2015. **8**(4): p. 1636-1651.

204. Lam, W.A., et al., *Mechanics and contraction dynamics of single platelets and implications for clot stiffening.* Nat Mater, 2011. **10**(1): p. 61-6.

205. Nguyen, T.H., et al., *Rupture Forces among Human Blood Platelets at different Degrees of Activation.* Sci Rep, 2016. **6**: p. 25402.

206. Beaussart, A., et al., *Quantifying the forces guiding microbial cell adhesion using single-cell force spectroscopy.* Nat Protoc, 2014. **9**(5): p. 1049-55.

207. Bonnefoy, A., et al., *Efficiency of Platelet Adhesion to Fibrinogen Depends on both Cell Activation and Flow.* Biophysical Journal, 2000. **78**: p. 2834-2843.

208. Issekutz, A., D. Rowter, and T. Springer, *Role of ICAM-1 and ICAM-2 and alternate CD11/CD18 ligands in neutrophil transendothelial migration.* Journal of Leukocyte Biology, 1999. **65**: p. 117-126.

209. Radmacher, M., et al., *Measuring the viscoelastic properties of human platelets with the atomic force microscope.* Biophysical Journal, 1996. **70**: p. 556-567.

210. Sakariassen, K., et al., *Collagen type III induced ex vivo thrombogenisis in humans, role of platelets and leukocytes in deposition of fibrin.* Arteriosclerosis, 1990. **10**(2): p. 276-284.

211. Anderson, J.M., A. Rodriguez, and D.T. Chang, *Foreign body reaction to biomaterials.* Seminars in Immunology, 2008. **20**(2): p. 86-100.

212. Walton, E., *Giant-cell granuloma of the respiratory tract (Wegener's granulomatosis).* British Medical Journal, 1958. **2**(5091): p. 265.

213. Powell, A.E., et al., *Fusion between Intestinal epithelial cells and macrophages in a cancer context results in nuclear reprogramming.* Cancer Res, 2011. **71**(4): p. 1497-1505.

214. McINNES, A. and D.M. Rennick, *Interleukin 4 induces cultured monocytes/macrophages to form giant multinucleated cells.* The Journal of experimental medicine, 1988. **167**(2): p. 598-611.

215. McNally, A.K. and J.M. Anderson, *Interleukin-4 induces foreign body giant cells from human monocytes/macrophages. Differential lymphokine regulation of macrophage fusion leads to morphological variants of multinucleated giant cells.* The American journal of pathology, 1995. **147**(5): p. 1487.

216. Jenney, C.R., et al., *Human monocyte/macrophage adhesion, macrophage motility, and IL-4-induced foreign body giant cell formation on silane-modified surfaces in vitro.* Journal of biomedical materials research, 1998. **41**(2): p. 171-184.

217. Helming, L. and S. Gordon, *The molecular basis of macrophage fusion.* Immunobiology, 2008. **212**(9): p. 785-793.

218. Helming, L. and S. Gordon, *Molecular mediators of macrophage fusion.* Trends in Cell Biology, 2009. **19**(10): p. 514-522.

219. Riedl, J., et al., *Lifeact mice for studying F-actin dynamics.* Nature methods, 2010. **7**(3): p. 168-169.

220. Faust, J.J., et al., *Alpha-Fe2O3 elicits diameter-dependent effects during exposure to an in vitro model of the human placenta.* Cell Biology and Toxicology, 2014. **30**(1): p. 31-53.

221. Wolter, S., et al., *rapidSTORM: accurate, fast open-source software for localization microscopy.* Nat Meth, 2012. **9**(11): p. 1040-1041.

222. Jenney, C.R. and J.M. Anderson, *Alkylsilane-modified surfaces: Inhibition of human macrophage adhesion and foreign body giant cell formation.* Journal of biomedical materials research, 1999. **46**(1): p. 11-21.

223. Padmanabhan, J., et al., *Regulation of cell-cell fusion by nanotopography.* Scientific Reports, 2016. **6**.

224. Saltzman, W.M. and T.R. Kyriakides, *Cell interactions with polymers.* Principles of tissue engineering, 1997. **3**.

225. Podolnikova, N.P., et al., *The Role of Integrins αMβ2 (Mac-1, CD11b/CD18) and αDβ2 (CD11d/CD18) in Macrophage Fusion.* The American Journal of Pathology, 2016. **186**(8): p. 2105-2116.

226. DeFife, K.M., et al., *Spatial regulation and surface chemistry control of monocyte/macrophage adhesion and foreign body giant cell formation by photochemically micropatterned surfaces.* Journal of biomedical materials research, 1999. **45**(2): p. 148-154.

227. McDonald, G.R., et al., *Bioactive contaminants leach from disposable laboratory plasticware.* Science, 2008. **322**(5903): p. 917-917.

228. Lishko, V.K., et al., *Multiple binding sites in fibrinogen for integrin alphaMbeta2 (Mac-1).* J Biol Chem, 2004. **279**(43): p. 44897-906.

229. McNally, A.K. and J.M. Anderson, *β1 and β2 Integrins Mediate Adhesion during Macrophage Fusion and Multinucleated Foreign Body Giant Cell Formation.* The American Journal of Pathology, 2002. **160**(2): p. 621-630.

230. Milde, R., et al., *Multinucleated giant cells are specialized for complement-mediated phagocytosis and large target destruction.* Cell reports, 2015. **13**(9): p. 1937-1948.

231. Martinez, F.O., et al., *Genetic programs expressed in resting and IL-4 alternatively activated mouse and human macrophages: similarities and differences.* Blood, 2013. **121**(9): p. e57-e69.

232. Vignery, A., *Macrophage fusion: the making of osteoclasts and giant cells.* J Exp Med, 2005. **202**(3): p. 337-40.

233. Papadimitriou, J. and K.J. Kingston, *The locomotory behaviour of the multinu-cleate giant cells of foreign body reactions.* The Journal of pathology, 1977. **121**(1): p. 27-36.

234. Murch, A., et al., *Direct evidence that inflammatory multinucleate giant cells form by fusion.* The Journal of pathology, 1982. **137**(3): p. 177-180.

235. Papadimitriou, J. and R. Ashman, *Macrophages: current views on their differentiation, structure, and function.* Ultrastructural pathology, 1989. **13**(4): p. 343-372.

236. Aderem, A., *Phagocytosis and the inflammatory response.* Journal of Infectious Diseases, 2003. **187**(Supplement 2): p. S340-5.

237. Niedergang, F., *Phagocytosis.* Encyclopedia of Cell Biology, 2016. **2**: p. 751-757.

238. Chen, E.H., *Invasive podosomes and myoblast fusion.* Current topics in membranes, 2011. **68**: p. 235.

239. Sens, K.L., et al., *An invasive podosome-like structure promotes fusion pore formation during myoblast fusion.* J Cell Biol, 2010. **191**(5): p. 1013-1027.

240. Grashoff, C., et al., *Measuring mechanical tension across vinculin reveals regulation of focal adhesion dynamics.* Nature, 2010. **466**(7303): p. 263-6.

241. Yu, M., et al., *Increasing throughput of AFM-based single cell adhesion measurements through multisubstrate surfaces.* Beilstein J Nanotechnol, 2015. **6**: p. 157-66.

APPENDIX A

A THREE DIMENSIONAL MICROPATTERNED TUMOR MODEL FOR BREAST CANCER CELL MIGRATION STUDIES

Biomaterials 81 (2016) 72e83

Contents lists available at ScienceDirect

Biomaterials

journal homepage: www.elsevier.com/locate/biomaterials

A three dimensional micropatterned tumor model for breast cancer cell migration studies

Nitish Peela [a, 1], Feba S. Sam [a, 1], Wayne Christenson [b, c], Danh Truong [a], Adam W. Watson [d], Ghassan Mouneimne [d], Robert Ros [b, c, e], Mehdi Nikkhah [a, *]

[a] School of Biological and Health Systems Engineering (SBHSE), Arizona State University, Tempe, AZ 85287, USA
[b] Center for Biological Physics, Arizona State University, Tempe, AZ 85287, USA
[c] Department of Physics, Arizona State University, Tempe, AZ 85287, USA
[d] University of Arizona Cancer Center, Department of Cellular and Molecular Medicine, Tucson, AZ 85724, USA
[e] Biodesign Institute, Arizona State University, Tempe, AZ 85287, USA

article info

Article history:
Received 10 November 2015
Accepted 29 November 2015
Available online 2 December 2015

Keywords:
Gelatin methacrylate (GelMA)
Tumor model
MDA-MB-231
MCF7
MCF10A
Real-time cell tracking
Photolithography
Microengineering

abstract

Breast cancer cell invasion is a highly orchestrated process driven by a myriad of complex microenvironmental stimuli, making it difficult to isolate and assess the effects of biochemical or biophysical cues (i.e. tumor architecture, matrix stiffness) on disease progression. In this regard, physiologically relevant tumor models are becoming instrumental to perform studies of cancer cell invasion within well-controlled conditions. Herein, we explored the use of photocrosslinkable hydrogels and a novel, two-step photolithography technique to microengineer a 3D breast tumor model. The microfabrication process enabled precise localization of cell-encapsulated circular constructs adjacent to a low stiffness matrix. To validate the model, breast cancer cell lines (MDA-MB-231, MCF7) and non-tumorigenic mammary epithelial cells (MCF10A) were embedded separately within the tumor model, all of which maintained high viability throughout the experiments. MDA-MB-231 cells exhibited extensive migratory behavior and invaded the surrounding matrix, whereas MCF7 or MCF10A cells formed clusters that stayed confined within the circular tumor regions. Additionally, real-time cell tracking indicated that the speed and persistence of MDA-MB-231 cells were substantially higher within the surrounding matrix compared to the circular constructs. Z-stack imaging of F-actin/a-tubulin cytoskeletal organization revealed unique 3D protrusions in MDA-MB-231 cells and an abundance of 3D clusters formed by MCF7 and MCF10A cells. Our results indicate that gelatin methacrylate (GelMA) hydrogel, integrated with the two-step photolithography technique, has great promise in the development of 3D tumor models with well-defined architecture and tunable stiffness.

1. Introduction

Metastatic dissemination of cancer cells is a highly complex and multi-step biological process starting with the invasion of cancer cells through the extracellular (ECM) matrix of the stroma toward the blood vessels [1e5]. Cancer cell invasion through the tumor stroma is governed by diverse factors including biochemical signals and biophysical cues [2]. There are many in vivo animal models used to conduct biological studies on cancer invasion, but despite their significance, most of these models present an abundance of confounding variables, which create difficulties in attributing specific microenvironmental cues to cellular invasion [6]. In this regard, physiologically relevant in vitro tumor models, with precise control over microenvironmental cues, are crucial to better understand cancer cell invasion within a native-like breast tumor microenvironment.

In the past few years, there has been a tremendous initiative to develop in vitro models to study cancer cell behavior within three-dimensional (3D) microenvironments. For instance 3D surface topographies have been widely used to study cancer cell behavior in response to various geometrical features [5,7e10]. Despite their significance, these platforms have been limited in terms of tuning native-like parameters such as stiffness and matrix architecture. Alternatively, a wide variety of 3D hydrogel-based matrices such as

* Corresponding author.
E-mail address: mnikkhah@asu.edu (M. Nikkhah).
[1] These authors contributed equally to this work.

http://dx.doi.org/10.1016/j.biomaterials.2015.11.039
0142-9612/

Matrigel® [11], fibrin [12], collagen [13], and polyethylene glycol (PEG) [14] have shown great promise to recapitulate cancer cell invasion in a 3D matrix and assess cellular behavior in response to various biophysical and biochemical cues. Such 3D hydrogel-based matrices enable cells to retain accurate phenotypes and, consequently, exhibit physiological responses to microenvironmental stimuli in addition to displaying accurate cellecell and cellematrix interactions [15]. Although these models have resulted in outstanding biological findings, they lack specific patterned features that would enable precise control over cellular distribution, matrix architecture and stiffness to conduct fundamental studies on tumor biology.

The integration of microengineering technologies and advanced biomaterials (e.g. hydrogels) has offered great promise to develop well-defined microenvironments for fundamental biological studies. These technologies are appealing because they enable tight control over the cellular microenvironment [16]. Particularly, through the use of photocrosslinkable hydrogels and micropatterning techniques, it is possible to generate biologically relevant constructs for tissue engineering and cancer related studies. However, there are still very few studies on the use of photocrosslinkable hydrogels in the development of biologically relevant tumor models [17e20].

In this study, we explore the use of a novel, two-step photolithography technique and gelatin methacrylate (GelMA) hydrogel to develop a highly organized micropatterned breast tumor microenvironment model. GelMA has been demonstrated to be an excellent candidate for generating biologically relevant tissue constructs [21] since cells have readily adhered to, proliferated within, and migrated throughout the 3D matrix when encapsulated within the hydrogel [22e24]. More importantly, the use of GelMA enables the creation of arrays of specific cell-laden features with high precision and fidelity [25]. Previous studies using GelMA hydrogel have been largely focused on tissue engineering and regenerative medicine applications [22,23,26,27], with very few focused on cancer studies [17,28]. The proposed platform, presented herein, has unique advantages through the ability to independently decouple different cell-embedded regions within the tumor model and independently tune their stiffness. Furthermore, the microfabricated model enables precise visualization of cancer cell migration within a 3D matrix in response to microenvironmental cues. In order to validate the proposed microengineered tumor model, we primarily assessed the morphology and proliferation of highly invasive human breast cancer MDA-MB-231 cells, non-invasive, tumorigenic human breast cancer MCF7 cells, and non-tumorigenic mammary epithelial MCF10A cells. In addition, we analyzed migration patterns and cytoskeletal organization of the cells within different regions of the micropatterned breast tumor models.

2. Materials and methods

2.1. Synthesis of GelMA hydrogels

GelMA preparation was completed similar to prior studies [21,25]. First, a 10% (w/v) solution of type A porcine skin gelatin (SigmaeAldrich) was prepared in Dulbecco's phosphate buffered saline (DPBS; Gibco). This solution was then dissolved at 60 °C before proceeding to subsequent steps. Afterward, methacrylic anhydride (MA) was added drop-wise to the gelatin solution. Next, the mixture was stirred vigorously for three hours to ensure the completion of the reaction. In order to shift the equilibrium and stop the reaction, the mixture was diluted (5X) with warm (40 °C) DPBS. This crude prepolymer GelMA was dialyzed for one week in distilled water (replaced twice a day) using dialysis membranes (MWCO 12000-14000) at a constant temperature (40 °C) to filter out any salt byproducts created from the reaction between gelatin and MA. The desired degree of methacrylation was achieved by precisely controlling the proportion of MA to gelatin during synthesis (92 ± 2% methacrylation confirmed based on ^{1}H NMR). The gelatin methacrylate solution was lyophilized for one week to create a large quantity of dehydrated, porous macromer, which could be preserved for future experiments.

2.2. Cell culture

The invasive breast cancer MDA-MB-231 cell line, non-invasive tumorigenic breast cancer MCF7 cell line, and normal mammary MCF10A cell line were used in this study. All cell lines used during the course of the experiments expressed red fluorescence. Specifically, MDA-MB-231 cells expressing tdTomato were provided by the McCarty lab (Oregon Health & Science University), and MCF7/MCF10A cells were transduced with lentivirus to stably express cytosolic mCherry fluorescence. Cancer cells were maintained in 1X DMEM supplemented with 10% (w/v) fetal bovine serum (FBS), 1% (w/v) L-glutamine, and 1% (w/v) 1:1 penicillin:streptomycin. Normal mammary cells were maintained in DMEM:F12 supplemented with 1% (w/v) L-glutamine, epidermal growth factor (20 ng/mL), cholera toxin (100 ng/mL), insulin (10 mg/mL), hydrocortisone (0.5 mg/mL), and 5% (w/v) horse serum. All media and media supplements were provided by Life Technologies. Cells were kept at standard physiological conditions (humidified, 37 °C, 5% CO_2), were passaged weekly, and their media was changed every three days.

2.3. Microfabrication of the tumor model

In order to promote adherence of the GelMA hydrogel constructs, glass slides were functionalized with 3-(trimethoxysilyl) propyl methacrylate (TMSPMA, SigmaeAldrich) as described in previous protocols [22,23]. Subsequently, a 7 mL drop of 20% (w/v) PEG prepolymer solution with 0.5% (w/v) photoinitiator (PI) (2-hydroxy-1-(4-(hydroxyethoxy)phenyl)-2-methyl-1-propanone) was placed onto cut (area: <1 cm^2), sterilized glass slides. Next, an untreated coverslip was placed on top of the PEG prepolymer and was then exposed to ultraviolet (UV) light (360e480 nm, 800 mW) for 50s to form a layer of PEG coating on top of the TMSPMA-treated glass slides.

To microengineer the tumor model, GelMA macromer was dissolved in DPBS containing 0.5% (w/v) PI to create the prepolymer solution. Cells were encapsulated in the prepolymer solution through resuspension of pelleted cells (cell density: 6 x 10^6 cells per mL of GelMA). The tumor model was patterned by first pipetting a 15 mL droplet of cell-laden GelMA onto a spacer (depth: 100 mm). A PEG-coated glass slide was then inverted on top of the spacer thereby spreading the prepolymer solution to cover the area of the glass slide and fill in the 100 mm depth of the spacer (Fig. 1A,B). A photomask (designed with AutoCAD software and printed by CAD/Art Services Inc., Oregon) was then placed on the inverted PEG-coated glass slide and exposed to UV light for 12s (Fig. 1C). The photomask had a layout as described in Table 1 where an 11 x 11 array of transparent circles (radius: 500 mm) was surrounded by a black unpatterned area. After UV exposure, the patterned glass slide was washed with DPBS to remove the remaining uncrosslinked prepolymer, revealing an array of circular constructs. Next, the glass slides were stored in warmed DPBS until all constructs were microfabricated. Following that, a 13 mL drop of pristine GelMA (no cells) was placed onto the spacer and the patterned glass slide was inverted on top of it (Fig. 1DeE). The empty areas between circular constructs were filled by the pristine GelMA. This assembly was exposed to UV light for another 5s in order to crosslink the gel filled in between the circular constructs

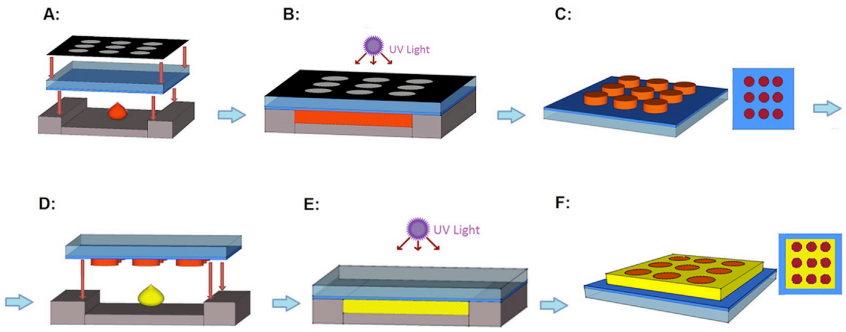

Fig. 1. (A) Schematic diagram depicting the development of the proposed tumor model. A drop of breast cancer cells encapsulated in photocrosslinkable GelMA prepolymer solution was pipetted onto a spacer and a glass slide/photomask was layered on top of it. (B) UV light was exposed to crosslink GelMA through the patterned photomask. (C) Uncrosslinked prepolymer solution was washed off the glass slide to reveal an array of high stiffness circular constructs. (D) A drop of pristine GelMA prepolymer solution was pipetted onto a spacer and the micropatterned circular constructs fabricated in (C) was placed on top of it, thereby spreading the hydrogel in between the constructs. (E) UV light was exposed to crosslink the hydrogel adjacent to the constructs, creating a surrounding matrix. (F) Representative schematic of the final microengineered tumor model with the high stiffness tumor constructs surrounded by low stiffness matrix.

Table 1
Geometrical features of the microengineered tumor model.[a]

Shape	Depth (mm)	Diameter (mm)	Spacing (mm)[b]	Surface ratio construct/surrounding
Circle	100	500	750	0.536

[a] Visualized in Fig. 2A.
[b] Spacing refers to the distance between the centers of adjacent tumor constructs.

(Fig. 1F). Upon completion of the experiment, the micropatterned tumor model was transferred from the DPBS baths to 24-well cell culture plates and media corresponding to each cell line was added. Cell culture media was exchanged every three days over the course of the experiments.

2.4. Stiffness measurements with Atomic Force Microscopy (AFM)

GelMA stiffness measurements were performed with a MFP-3D AFM (Asylum Research) placed on an inverted microscope (IX71, Olympus) [29e31]. A 40X objective with a NA of 0.65 (Olympus) was used to perform force measurements on the center of the circular GelMA constructs. Large tip AFM probes (LRCH-750, Team NanoTec) with a radius of ~810 nm were used (Fig. 2C). The thermal energy dissipation method [32] was used to determine the spring constant of the cantilevers (~0.15 N/m). Four force-indentation measurements were taken in a 90 mm^2 area at the center of 8 different circular GelMA constructs. Alternatively, forty force-indentation measurements in a 90 mm^2 area were taken on the non-patterned GelMA surface. Approach and retraction speed for all measurements was 2 mm/s. A trigger force of 10 nN was used for all force-indentation measurements. All measurements were done in 10X DPBS buffer solution. Young's Moduli from force indentation curves were determined using custom MATLAB routines. Force-indentation curves were analyzed using the power-law linearization method as described previously [33] based on the Briscoe indentation model for a blunted cone with a Poisson ratio of 0.5.

2.5. Cell viability assay

Cell viability was assessed on day 5 using a standard Live/Dead Assay Kit (Invitrogen™), which included calcein AM (CI) and ethidium homodimer (ETD). To prepare the solution, 0.5 ml of 4 mM CI and of 2 ml mM ETD in DMSO/H_2O 1:4 (v/v) were added to 1 mL DPBS. After 5 days of culture, the microenvironments were rinsed with warm DPBS and 150 ml of the Live/Dead solution was added to each well. The well plate was stored at physiological conditions (37 °C, humidified, 5% CO_2) for 30 min and subsequently imaged using an inverted fluorescence microscope (Zeiss Axio Observer Z1) with 10X magnification. Images were quantified by thresholding individual channels (red, green) and counting individual cells using the particle analyzer module of ImageJ (v. 1.48). All cells were transfected, expressing red fluorescence. Thus, percent viability was calculated by dividing the number of live cells (green) by the total number of cells (red).

2.6. Quantification of cell proliferation

Cell proliferation was quantified by counting cell nuclei on days 0, 1, 3 and 5 of culture. The cell-laden GelMA hydrogel constructs were rinsed with DPBS and fixed with a 4% paraformaldehyde (PFA) (w/v) solution in DPBS. After 30 min, the samples were washed three times (3X) with DPBS. A 0.1% (v/v) solution of 4′,6-diamidino-2-phenylindole (DAPI) (Life Technologies) in DPBS was prepared and added to each well. The samples were left in the DAPI solution for 15 min, and then washed 3X using DPBS. Next, the samples were fluorescently imaged, and the number of DAPI stained nuclei were counted using ImageJ (v. 1.48) software to determine proliferation and migration of each cell line at specific time points (Days 0, 1, 3 and 5). At least three samples were prepared for each condition within each experiment.

2.7. Live cell tracking

MDA-MB-231 cells embedded within the proposed model were imaged for five 12-h periods upon encapsulation (0e12 h, 24e36 h, 48e60 h, 72e84 h, and 96e108 h). Cellular tracking was performed through manual tracking of individual cells frame-by-frame over the course of each 12-h period. We tracked 13 cells per circular construct for a total of 4 constructs over the course of three

experiments (3 samples, 4 replicates, n ¼ 156 cells). After day 0, we analyzed up to 156 cells inside the circular constructs and up to 156 cells outside of the constructs. Using a custom cell tracking script (CellTracker; Budapest, Hungary; [34]) for Matlab (v. 2015b), we were able to store manually tracked cell paths and extract parameters such as directionality, persistence, and velocity at each time point. Additionally, representative cell tracks with respect to the origin were created using ImageJ (v. 1.48) Chemotaxis Cell Tracker Plug-In. We defined directionality as the angle created by the endeend distance of a cell's movement during a 12-h time period, persistence as the stepwise sum of distances traveled divided by the endeend distance, and velocity as stepwise distance divided by time.

2.8. Cytoskeletal organization and immunofluorescence staining

To assess F-actin and a-tubulin cytoskeletal organization, cell encapsulated hydrogel constructs were fixed with 4% (w/v) PFA solution in DPBS. The samples were rinsed 2X with DPBS-glycine for 10 min and washed with 0.05% (w/v) Tween-20 in DPBS for 10 min. The primary block, containing IF blocking solution (10% (w/v) goat serum, 0.2% (w/v) Triton X-100, and 0.1% (w/v) radioimmunoassay grade BSA) and 0.05% (w/v) Tween-20 in DPBS; was added to the samples for 1.5e2 h. Monoclonal mouse anti-a-tubulin (T9026, SigmaeAldrich) was diluted 1:500 (v/v) in IF buffer solution and centrifuged at 14k RPM for 10 min. The samples were stained with this solution overnight at 4 °C and washed 3X in IF buffer with 20-min intervals between washes. A 1:200 (v/v) dilution of anti-mouse Alexa-Fluor® 555 in IF buffer solution was centrifuged at 14k RPM to remove aggregates. The samples were then stained for 45 min and washed with IF buffer for 20 min. Subsequently, they were washed an additional 2X with 0.05% (w/v) Tween-20 in DPBS for 10 min. A 1:40 (v/v) dilution of Alexa Fluor-488 phalloidin (Life Technologies) and 1:1000 (v/v) dilution of DAPI in DPBS was added to the blocked samples overnight and incubated at 4 °C. The hydrogel constructs were then washed 3X with 0.05% (w/v) Tween-20 in DPBS. Upon F-actin staining, the cells were stained with DAPI to visualize the nuclei. The stained samples were inverted onto a glass coverslip with a droplet of ProLong® Diamond Antifade solution. The cell-encapsulated hydrogel constructs were imaged using a fluorescence microscope (Zeiss Axio Observer Z1) equipped with an Apotome.2 at 20X/40X magnification. Z-stacks and 2X2 tiles of the samples were obtained and 3D images were constructed using the Zen software. Circularity of the cells was determined by using top-view images of fluorescent F-actin staining. The images of individual constructs were fed into a custom script for the ImageJ software, which compared each individual clump or each individual cell to a perfect reference circle, outputting a percent circularity value.

2.9. Data collection and statistical analysis

Migration and proliferation data were analyzed over the course of three experiments (n ¼ 3) for each cell line. Each of the three experiments (samples) had three replicates, and the data for each of the nine replicates was collected within a 5 x 5 array of constructs, for a total of 225 individual circular constructs analyzed per cell line at each time point (Days 0, 1, 3, 5). Data for the live-dead analysis had the same method of data collection in terms of experiments, sample sizes, and replicates on days 1 and 5 of culture. Data for circularity was collected by measuring the circularity of the cells within the triplicate samples of one experiment for each of the three cell types.

A one-way analysis of variance (ANOVA) was conducted, which demonstrated statistically significant differences between each group when a ¼ 0.05. A Bonferroni's post-hoc test was subsequently completed in order to measure statistically significant differences between individual groups. All data were presented in mean ± standard deviation (SD). Statistical analysis/data presentation were performed in Graph Pad Prism (v. 6.0).

3. Results

3.1. Microfabrication and characterization of the tumor model

The microengineered tumor model was developed using 5% GelMA with high (92 ± 2%) degree of methacrylation due to its biocompatibility and reliability for photolithography applications [21,23]. The specific geometrical parameters of the microengineered tumor model are defined in Table 1. The thickness of the circular constructs was set to 100 mm due to its proven efficacy in the formation of patterned cellular constructs with high precision [23]. The spacing and diameter of the cell encapsulated circular constructs were optimized based on a series of preliminary experiments (data not presented). In particular, circular constructs of smaller diameters (250 mm, 100 mm) had lower pattern precision, forming rough edges and unclear boundaries around the circular constructs. Conversely, 500 mm constructs exhibited pristine boundaries and smooth edges. However, the spacing between circular constructs had no real effect on the precision of the photolithography process and can be adjusted in future studies depending on throughput needs. The parameters defined in this study allowed for excellent pattern fidelity and analysis on a high-throughput scale with an 11 x 11 array of tumor constructs per chip.

Upon optimization, separate aliquots of GelMA prepolymer solution were mixed with either 0.01% (w/v) rhodamine (red) or 0.01% (w/v) fluorescein (green) dye to visualize the localization of hydrogel constructs upon micropatterning (Fig. 2A). The developed two-step photolithography technique, as demonstrated in (Fig. 1), was used to form a high density array of circular constructs (red stained hydrogel) surrounded by a surrounding matrix (green stained hydrogel). In particular, the two-step process involved fabricating the circular constructs first (Fig. 1AeC), and, subsequently, filling in the surrounding regions (in between the constructs) by adding GelMA prepolymer (Fig. 1DeF). The circular constructs were, as such, crosslinked for a longer time period than the surrounding matrix. As the crosslinking time of the prepolymer solution has a direct positive correlation to the stiffness of the GelMA hydrogel [21], we expected that this method would create cell-embedded circular constructs with stiffness that is substantially higher than the surrounding matrix. To assess the capability of the proposed microfabrication technique in forming areas of differential stiffness on a single chip, the Young's moduli of the circular constructs and the surrounding matrix were measured by AFM (Fig. 2B, C). These measurements revealed a stiffness of 748 ± 90 Pa within the circular constructs which was over twice as stiff as the surrounding matrix measured at 313 ± 38 Pa (Fig. 2D). These data indicated the reliability of the proposed two-step photolithography technique to create a high-density array of circular constructs and a distinct surrounding matrix with tunable stiffness.

3.2. Cell viability

We evaluated viability of three distinct cell types, non-tumorigenic mammary epithelial MCF10A cells, non-invasive tumorigenic MCF7 cells, and highly invasive breast cancer MDA-MB-231 cells encapsulated within the microengineered tumor model on days 1 and 5 of culture. Representative images of the cell viability experiments (Supplementary Fig. S-1A) demonstrated

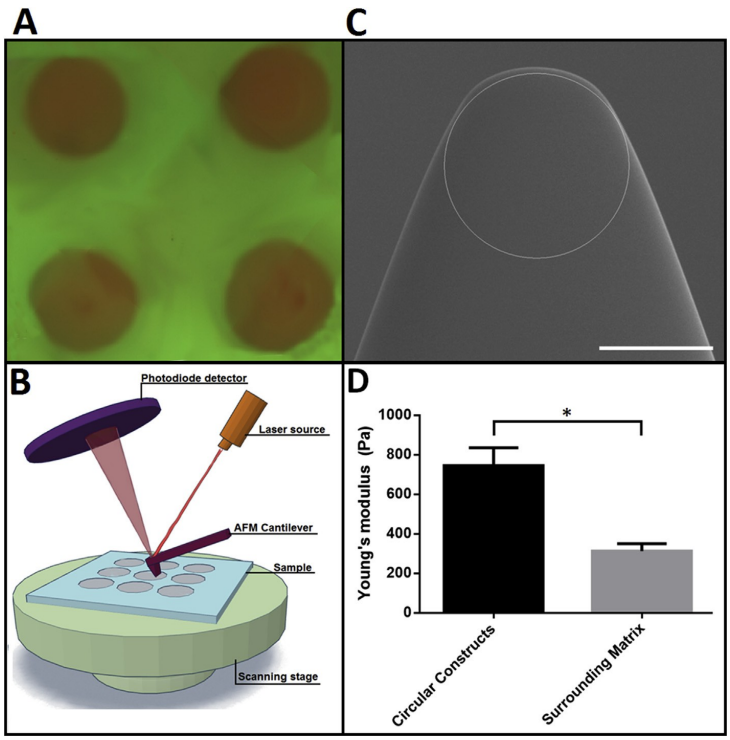

Fig. 2. (A) Representative fluorescence image of Rhodamine B stained circular constructs and Fluorescein stained surrounding matrix. (B) Schematic diagram of the AFM setup to perform local stiffness measurements. (C) SEM image of the AFM cantilever used to probe the hydrogel (radius of tip: 810 nm; scale bar represents 1 mm). (D) AFM measurements of the circular constructs and the surrounding matrix reveal a Young's modulus of 748 ± 90 and 313 ± 38 Pa respectively. Data is presented in mean ± SD; * ¼ $p < 0.05$.

excellent cell survival upon encapsulation and the microfabrication procedure. The percent of viable cells across all the three cell types had no statistically significant difference and was within 92 ± 3% after one day of encapsulation, which decreased to 83 ± 5% after 5 days of culture (Supplementary Fig. S-1B). Similarly, in previous studies, a wide array of cell types such as ovarian cancer cells, 3T3 fibroblast cells, cardiomyocytes, and HUVECs, encapsulated within GelMA hydrogel, exhibited high percent cell survival upon micropatterning [21,23,28,35]. Thus, our data confirmed that the specific parameters used to microengineer the tumor model (i.e. the two-step, 17 s UV exposure, and presence of PI within the prepolymer solution) did not have a substantial effect on overall cell viability.

3.3. Cell morphology, migration, and proliferation within the micropatterned constructs

To prevent cell from attaching onto the glass slide and promote cellular migration throughout the 3D hydrogel constructs, a layer of PEG was coated onto the glass slide due to its cell-repellant properties [23]. We performed preliminary control experiments where the circular constructs were patterned onto glass slides with and without PEG coating. When patterned on slides without PEG, nearly every single cell escaped from the micropatterned circular regions and migrated onto the glass slide (Supplementary Fig. S-2). These results indicated that, without PEG, the cells heavily adhered to and migrated along the glass slide. Conversely, adding PEG coating resulted in cell-repelling properties and facilitated the migration of the cells throughout the hydrogel layer.

Phase contrast images (Fig. 3) demonstrated that the three cell types (MCF10A, MCF7, MDA-MB-231) were homogeneously distributed throughout the hydrogel. Additionally, these cells had a round morphology on day 0 immediately after encapsulation within the micropatterned circular regions. However, between days 1 and 3 of culture, the cells began to exhibit characteristics specific to each cell type. In particular, MDA-MB-231 cells adopted a heterogeneous morphology, both round and elongated, with high cell density secondary to their high proliferative capacity. These cells started migrating toward the outer regions of the circular constructs as early as day 3 of culture, which continued at an increased rate by day 5 of culture (Arrows, Fig. 3A; Supplementary Fig. S-3). On the other hand, MCF7 cells formed clusters within and on the periphery of the circular constructs, exhibiting weak migratory characteristics and elongation toward the surrounding regions on the first day of culture (Arrows, Fig. 3B). These cells had no indication of an invasive phenotype by day 5 as they lost their elongated morphologies and began to form cellular clusters (Fig. 3B). Similarly, MCF10A cells formed cellular clusters upon day 1 of culture and demonstrated no significant migratory characteristics at any time point (Fig. 3C). These cells maintained a round morphology, while the size of the cellular clusters notably increased as a function of time.

Consistent with phase contrast images, fluorescence images of cells' nuclei demonstrated a significantly higher number of MDA-MB-231 cells within the circular constructs and the surrounding

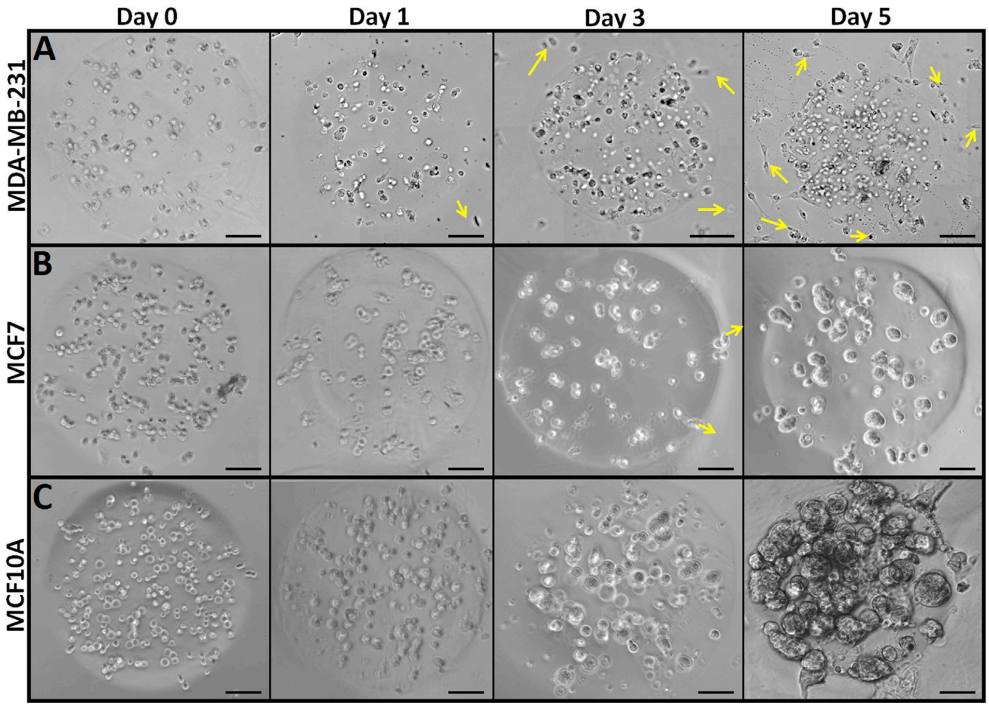

Fig. 3. Representative phase contrast images demonstrating changes in cellular morphology. (A) MDA-MB-231 cells spread rapidly creating a heterogeneous (spindle vs. round) morphology. Arrows point to cells that have invaded the surrounding stroma. (B) MCF7 cells exhibited a tendency to cluster, demonstrating only weak migration on days 1 and 3 of culture and small clusters by day 5. (C) MCF10A cells formed similar clusters by day 3 which grew bigger by day 5. Scale bars represent 100 mm.

matrix as compared to MCF7 and MCF10A cells. Cellular clustering was also evident in MCF7 and MCF10A cells (Fig. 4A). Quantitative analyses confirmed that the overall proliferation of MDA-MB-231 cells was significantly higher compared to MCF7 and MCF10A cells within the microengineered platform (Fig. 4B). A similar trend was observed with respect to the proliferation of cells within the high stiffness circular constructs (Fig. 4C). About 2.5 times more MDA-MB-231 cells disseminated from the circular areas toward the surrounding matrix by day 5 of culture as compared to MCF7 cells (12.9 ± 1.9% vs 5.2 ± 2.3%). Conversely, MCF10A cells exhibited nearly no invasive characteristics toward the outer regions of circular constructs (1.1 ± 0.2% by day 5) (Fig. 4D). However, there was still a statistically significant difference in the migration of MCF10A cells at each time point. This is due to the clumping tendency as some cells proliferated to form clusters on the boundaries of the circular constructs and the surrounding matrix (Supplementary Movies M6, M9). Differences in migratory characteristics of the cells were further highlighted in the real time experimentations. MDA-MB-231 cells elongated at the periphery of the constructs prior to contractile motion out into the surrounding matrix (Supplementary Movies M1–M3). They were observed to have a more rounded morphology and exhibited membrane blebs while migrating through the surrounding matrix (Supplementary Movie M4). It is also important to note that these cells demonstrated the ability to migrate between and back into constructs after initially invading the surrounding matrix (Supplementary Movie M5). Consequently, migration data presented consists of net migration values counting only the cells that have entered and remained in the surrounding matrix by day 5 of culture. Alternatively, MCF7 (Supplementary Movies M6–M8) and MCF10A (Supplementary Movies M9–M11) proliferated to form large cellular clusters. While proliferating, cellular clusters were often seen rotating within the 3D matrix, a phenomena described recently in glandular tissue created using laminin-rich gels [36].

Supplementary movies related to this article can be found online at http://dx.doi.org/10.1016/j.biomaterials.2015.11.039.

3.4. Live cell tracking

Due to the heterogeneous morphology of the MDA-MB-231 cells, we performed live cell tracking analyses to further investigate the migratory behavior induced by the architecture and biophysical properties of the tumor model. Fig. 5A, B and Supplementary Movies M2, M3 demonstrate representative cell tracks of MDA-MB-231 cells within the model for 12-h time periods during each day of culture. The cells disseminated from the circular constructs and invaded the surrounding matrix during all time periods. Interestingly, there was a substantial difference in the migratory phenotype of the cells tracked inside the circular constructs compared to those tracked within the surrounding matrix. We specifically analyzed angular directionality and plotted it as a normalized 360° rose plot (Fig. 5C). Cells inside the circular tumor region typically migrated in one common direction with respect to neighboring cells, while those in the surrounding matrix migrated with no particular (i.e. random) directionality.

Additionally, we analyzed the velocity and persistence of the

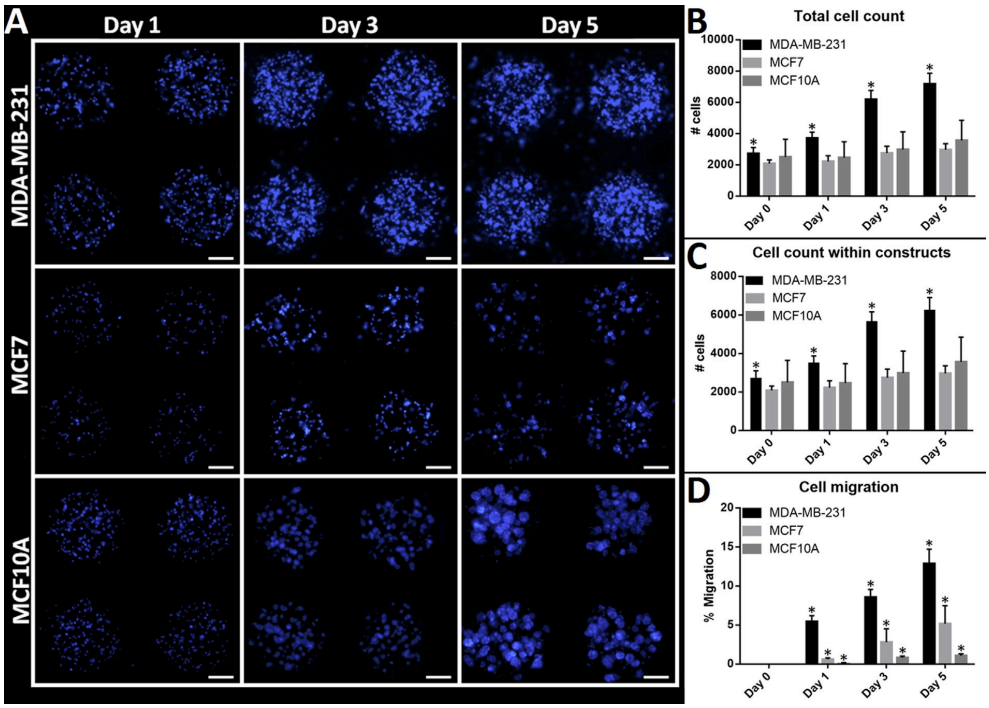

Fig. 4. Migration and proliferation of the cells within the tumor model. (A) Representative fluorescence images demonstrate DAPI stained cell nuclei. (B) Total cell proliferation, (C) cell proliferation within the tumor region, and (D) cellular invasion. Scale bars represent 200 mm. Data is presented in mean ± SD; * ¼ $p < 0.05$ compared to the previous time point.

cells inside and outside of the circular constructs. Generally, migration speed increased as a function of time, and the cells slowly matured to adopt an invasive phenotype and morphology (Fig. 6A). The velocity of cells in the surrounding matrix was significantly higher than that of cells within the circular region. Alternatively, cells both inside and outside of the constructs did not have substantial changes in persistence as a function of time (Fig. 6B). However, cells migrating through the surrounding matrix exhibited a significantly higher persistence than cells inside of the circular constructs at all time points.

3.5. Cytoskeletal organization

To further confirm our observations on cellular migration and gain insight into cell-matrix interactions/morphology, we performed 3D imaging of the actin and microtubule cytoskeletal organization of cells embedded throughout the tumor model. Preliminary images clearly demonstrated that the cells were embedded within the 3D hydrogel layer (100 mm height) of the high stiffness circular constructs (Supplementary Fig. S-4A) as well as the surrounding matrix (Supplementary Fig. S-4B).

Using 3D Z-stack immunofluorescence imaging of the actin cytoskeleton, we were able to visualize the 3D morphology of the cells. We observed several different cellular sub-structures including 3D elongated protrusions, flat protrusions and membrane blebs (Arrows, Fig. 7). In the representative images of the F-actin cytoskeleton, MDA-MB-231 cells displayed a wide range of invasive characteristics possessing a small number of flat protrusions and many elongated 3D protrusions. In addition, some cells exhibited membrane blebs as they invaded and migrated through the surrounding matrix (Fig. 7A, D). A few number of MCF7 cells showed flat protrusions on the periphery of the circular constructs, as demonstrated in the representative high magnification (40X) images (Fig. 7E). In MCF10A cells, the clustering tendency was significantly higher with no indications of protrusions. To further quantify cellular morphology, the circularity of the actin cytoskeleton was assessed for each of the three cell types (Fig. 7G) using the particle analyzer module of the Image J software. This analysis revealed that MDA-MB-231 cells presented a significantly less circular, and more heterogeneous, morphology when compared to MCF7 and MCF10A cells (Fig. 7G). Furthermore, images of the microtubule cytoskeleton (Fig. 8) revealed substantial microtubule expression in all three cell types, with clear visualization of mitotic spindles in proliferating cells (Arrows, Fig. 8). In MDA-MB-231 cells, both circular and elongated cells migrating through the 3D matrix exhibited either small or large subcellular protrusions (Fig. 8AeC). MCF7 and MCF10A cells demonstrated clear microtubule networks, which were more prominent in spread cells or large cellular clusters (Fig. 8DeI).

4. Discussion

It is now becoming more recognized that the integration of microfabrication techniques and advanced biomaterials (i.e. photocrosslinkable hydrogels) can provide a unique ability to develop highly organized cell-based constructs [18,27,37]. In this regard, GelMA hydrogel is an excellent candidate for cancer related studies due to its biocompatibility and ability to create organized cellular

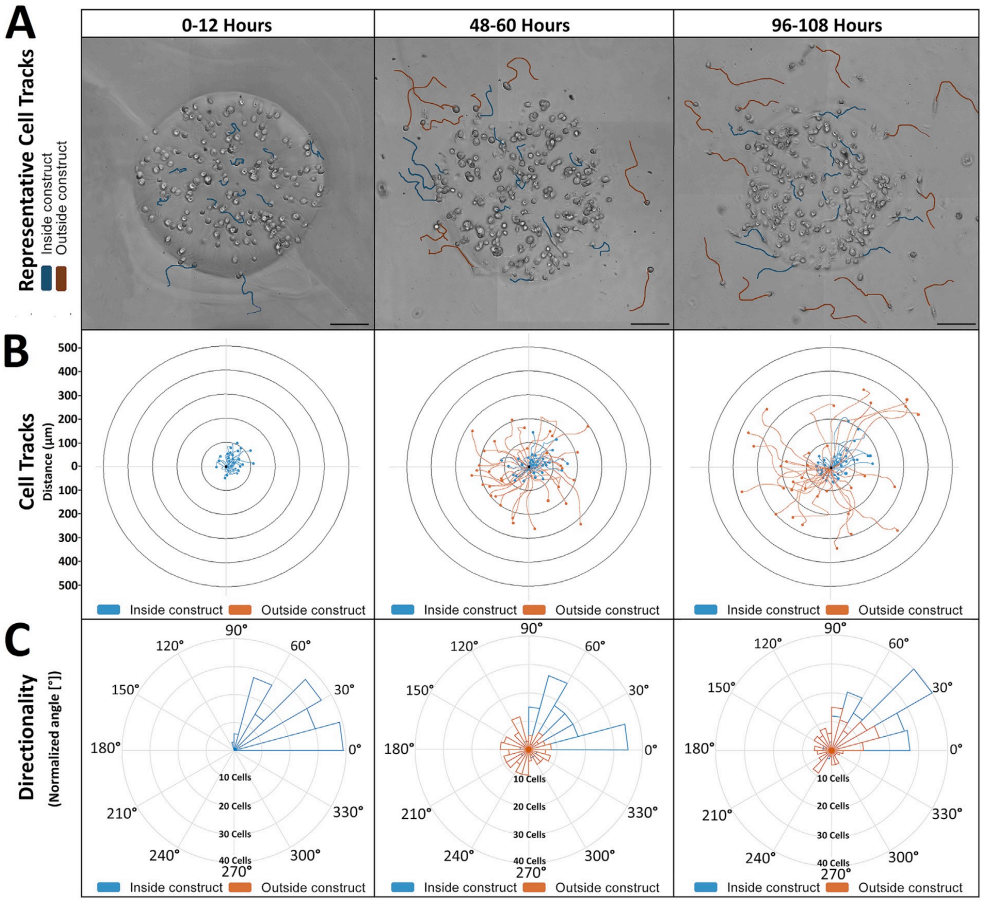

Fig. 5. (A) Representative cell tracks of MDA-MB-231 cells within the model. Blue lines indicate tracked cells that are initially within the circular construct at the start of the 12-h period, whereas orange tracks indicate cells that are initially outside the circular construct at the start of the 12-h period. (B) Reconstructed cell tracks normalized with respect to the origin, and (C) 360° rose plots measuring normalized angular directionality. Scale bars represent 100 mm. n ¼ 156 cells. (For interpretation of the references to color in this figure legend, the reader is referred to the web version of this article.)

constructs. However, the primary focus on the use of GelMA, thus far, has been centered on tissue engineering and regenerative medicine applications (e.g. formation of vascularized networks [23]). To our knowledge, there have not been specific studies utilizing GelMA to develop microengineered breast tumor models. Furthermore, there have been no significant attempts, using hydrogel-based matrices, to localize separate regions with tunable stiffness (i.e. circular constructs, surrounding region) within microengineered platforms.

In this work, we built upon our expertise in microfabrication technology by developing a novel, two-step photolithography technique to develop a 3D highly organized breast tumor microenvironment. GelMA has been demonstrated to be a biocompatible matrix for encapsulation with a vast array of cell types [21,23,28,35]. Consistent with previous studies, our work also confirmed that breast cancer and mammary epithelial cells had around 93% viability upon encapsulation, which decreased to ~82% by day 5 of culture, indicating that the two-step photolithography technique involving UV exposure and the presence of PI had minimal effect on overall cell survival. Furthermore, the crosslinking time of GelMA hydrogel (12s) resulted in a Young's modulus of about 750 Pa. This is consistent with previous studies where a crosslinking time of 60s yielded a Young's modulus of 3.5e4 kPa [21], indicating that the stiffness of the GelMA may be linearly dependent on the crosslinking time. It is important to note, however, that although the presence of UV exposure and PI did not influence the viability of previously studied cell types, including primary glioma cells and cardiomyocytes [17,35], the level of UV sensitivity may vary depending on cell type, including primary cancer cells or patient derived xenografts (PDX). In this regard, there are numerous studies exploring the use of visible light crosslinking to remedy the potential drawbacks of UV photocrosslinkable hydrogels [38,39]. The creation of a similar tumor model with a visible light crosslinking technique is a subject of our future studies.

An innovative aspect of our study was independently patterning 3D high stiffness circular constructs juxtaposed to a surrounding matrix of lower stiffness. Matrix stiffness is a crucial biophysical

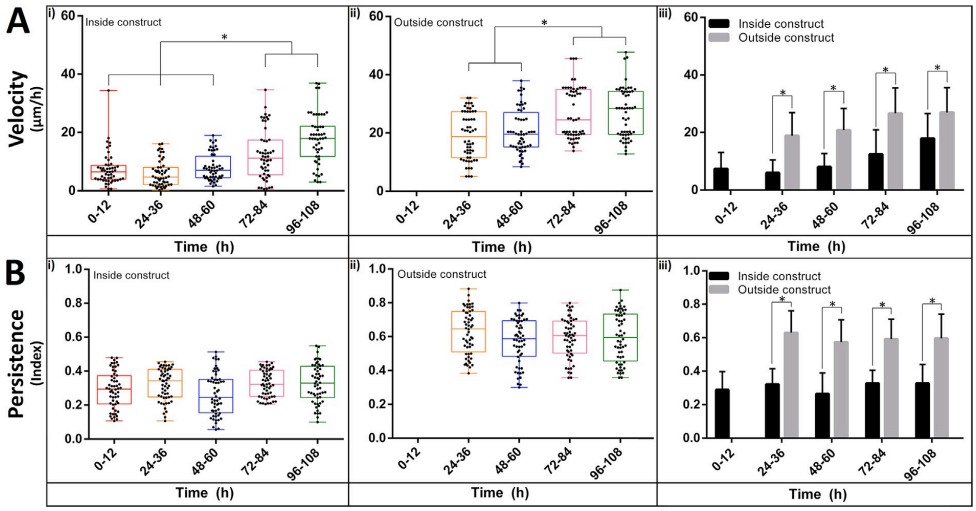

Fig. 6. ($A_{i/ii}$) Scatterplot of velocity of MDA-MB-231 cells over time inside of the circular constructs and outside of the constructs, and (A_{iii}) comparative bar graph of cell velocities in the surrounding matrix versus the circular tumor construct. ($B_{i/ii}$) Scatterplot of persistence indices of cells over time, and (B_{iii}) comparative bar graph of persistence. n ¼ 156 cells. Data is presented in mean ± SD; * ¼ $p < 0.05$.

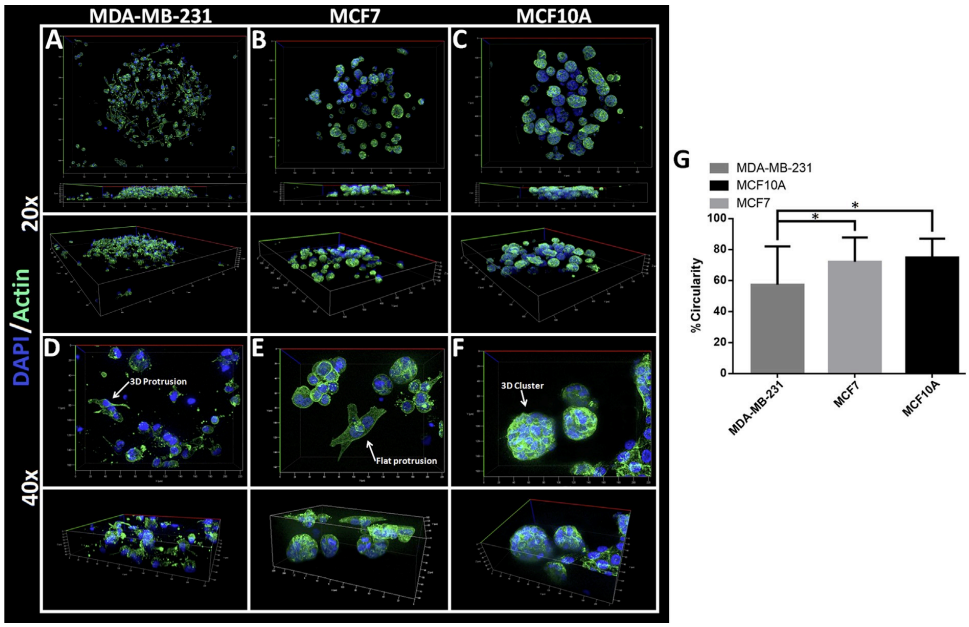

Fig. 7. F-actin (green) and DAPI (blue) stained cell-embedded tumor model on day 5 of culture. (AeC) Representative 20X image of MDA-MB-231, MCF7, and MCF10A cells respectively. (DeF) Representative 40X images highlighting specific cell-matrix interactions. (G) Circularity amongst the three cell types. MCF10A, MCF7, and MDA-MB-231 cells had circularities of 74.9 ± 12.1%, 72.1 ± 15.7%, and 57.3 ± 24.7% respectively. * ¼ $p < 0.05$. (For interpretation of the references to color in this figure legend, the reader is referred to the web version of this article.)

aspect of the tumor microenvironment and, consequently, has been heavily studied in collagen, polyacrylamide, and Matrigel© hydrogels [40,41]. However, several studies have focused on seeding cells on hydrogel sheets [41] with different stiffness rather than encapsulating them within 3D matrices, which may not accurately represent physiological cell behavior. In this regard, our model

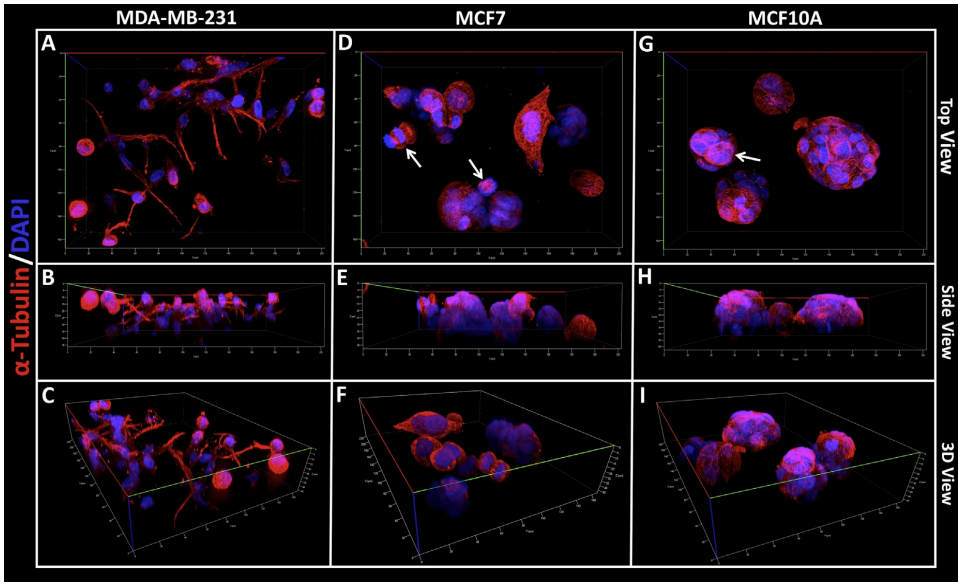

Fig. 8. α-tubulin (red) and DAPI (blue) stained cell-embedded tumor model on day 5 of culture. (A–C) Representative 40X Z-stack images of MDA-MB-231 cells, (D–F) MCF7 cells, and (G-I) MCF10A cells at three different angles (Top, Side, and 3D views). (For interpretation of the references to color in this figure legend, the reader is referred to the web version of this article.)

provides a distinct advantage, as we are able to encapsulate the cells in 3D, and independently modulate the stiffness of the matrix within distinguished regions of the microengineered tumor model. As such, we can assess the specific effects of matrix stiffness on breast carcinoma progression in vitro within the proposed 3D model.

Based on high-resolution live cell tracking analysis of the MDA-MB-231 cells, we observed significant differences in directionality, persistence, and velocity, which were influenced by whether the cells were inside or outside of the circular constructs on the initial time point. Fig. 5C indicated that cells had a specific directionality on all days of culture when they were migrating within the circular constructs. This result was in line with previous studies, which demonstrated that cells leave tracks and realign matrices when moving through 3D hydrogels, resulting in collective migration [42]. Thus, within our model, cells may have created tracks in the high stiffness circular constructs, which promoted migration in specific directions. Alternatively, the low stiffness surrounding matrix lacked structural support compared to the circular tumor region, so cells migrated with no particular angular directionality upon invasion.

Furthermore, the velocity of the cells moving through the surrounding matrix was substantially higher than those encapsulated within the tumor construct at all time points (Fig. 6A). This indicated that the stiffness of the 3D matrix may have played a role in migratory speeds. Other findings have also stated that cells exhibit an elongated, invasive phenotype within 3D hydrogels of lower stiffness [43,44]. Cellular persistence indices (i.e. the sum of step-wise distances divided by the endeend distance) indicated that cells exhibited low persistence and consequently changed their paths frequently while migrating within the circular constructs. Furthermore, the high cellular density within the circular tumor constructs increased the possibility of cell collisions, which may have inhibited cell velocity and caused cells to frequently shift their paths (i.e. reduced persistence). This observation is consistent with previous studies on contact inhibition of locomotion (CIL), which suggested that populations of invasive cells consistently alter their paths to avoid collisions with one another [45,46]. In future studies, we plan to perform further in-depth migration analysis by switching the stiffness to create low stiffness circular constructs with a high stiffness surrounding matrix. In addition, using the proposed model, we will be able to individually tune matrix stiffness and assess changes in cancer cell migration in response to a wide range of stiffness.

The proposed micropatterned tumor model also shed unique insight on cancer cell morphology. MDA-MB-231 cells adopted highly invasive characteristics with a mixture of round and spindle like morphologies. Specifically, the cells that migrated down on the glass slide formed flat protrusions, which was substantially different than the morphology exhibited by the cells embedded within the 3D gel (Fig. 7A, D; Arrows, Supplementary Fig. S-4B). This bimodal display of migratory morphology demonstrated that the mechanism for MDA-MB-231 cell migration was heavily influenced by substrate interactions (i.e. 2D vs 3D), in addition to matrix stiffness. Particularly, cells migrating through the hydrogel formed 3D protrusions and membrane blebs (Arrows, Supplementary Fig. S-4A; Supplementary Movie M4). These observations were consistent with the heterogeneous, 3D morphology observed in migrating cells cultured in Cell Derived Matrix (CDM) and Matrigel® [47,48]. Furthermore, due to the PEG coating on the glass slide of the proposed model, we observed that most of the cells were embedded within the 3D hydrogel matrix. In addition, MCF7 and MCF10A cells rapidly clustered as early as day 2 or 3, where the cluster grew larger by day 5. Interestingly, these cells adopted a different sheet-like morphology when proliferating on the periphery of the constructs. This was seen in phase contrast images (Fig. 4C, Supplementary Movie M-9) and was also illustrated by 40X actin images (Fig. 7F). Cell morphology in our model was consistent with prior studies that have shown increased spheroid formation in

high stiffness matrices [49]. In fact, numerous studies have been conducted which required the utilization of various biochemical signals, such as Cyclic AMP or co-culturing cancer cells with cancer associated fibroblasts (CAFs), in order to stimulate growth of morphologically accurate cellular clusters [50,51]. Thus, it is particularly interesting that when encapsulated within GelMA hydrogel, these cells readily clustered without the need for any biochemical stimuli. This further validates the ability of the proposed model to readily recreate in vivo-like morphologies.

All three cell types demonstrated well-expressed microtubules throughout the 3D matrix (Fig. 8). Migrating MDA-MB-231 cells demonstrated small and large subcellular protrusions (Fig. 8A–C), while MCF7 and MCF10A cells (Fig. 8D–I) exhibited microtubule networks in spread cells and cellular clusters. Microtubules are of particular significance as they are indicative of biophysical stresses at the cell-matrix interface, which have rarely been studied within 3D micropatterned hydrogels [52,53]. Additionally, various isotopes of microtubules are common targets of multiple drugs such as vinca alkaloids, taxanes, and nocodazole, which are common chemotherapeutics used today [54–56]. In fact, there are numerous studies investigating the specific impact of such therapeutics on microtubule disruption [8,57]. The ability of our model to assess potential changes in microtubule expression in a 3D matrix with well-defined architecture and tunable stiffness indicates that the proposed platform is a promising candidate to assess cell-matrix interactions in response to both biochemical and biophysical cues.

5. Conclusion

In this study, we created a tumor model using a novel, two-step photolithography technique and photocrosslinkable GelMA hydrogel. A unique aspect of our model was the compartmentalization of two distinct regions of the tumor microenvironment with differential stiffness. In particular, we developed high density array of cell embedded high stiffness circular constructs surrounded by a low stiffness matrix. We validated the model by encapsulating three cell types separately in order to investigate migratory behavior, cell viability, and cell morphology. High viability was observed regardless of the cell type. Interestingly, a bimodal display of morphology was displayed in MDA-MB-231 cells as, few cells migrated to the glass slide, elongating and assuming flat morphologies, while others exhibited 3D protrusions or membrane blebs when invading the surrounding hydrogel matrix. Due to the differential microarchitecture in our model with areas of distinct stiffness, cells migrating through the high stiffness circular constructs exhibited different invasive tendencies than those migrating through the surrounding matrix. In particular, cells in the surrounding areas migrated with high velocities and persistence when compared to those inside of the tumor constructs. We suspect that these behaviors were due to differences in matrix stiffness, as well as the high cell density within the patterned regions. In addition, 3D cellular clusters were observed in both MCF7 and MCF10A cells. These morphologically accurate structures formed without the addition of any biochemical stimuli, which demonstrates the versatility of GelMA in creating a biomimetic tumor microenvironment. The proposed platform could be potentially used for future studies of cancer cell behavior, high-throughput drug screening, and the development of personalized medicine.

Acknowledgments

The authors thank Bryant Doss for providing the Matlab routines for the analysis of the AFM indentation measurements, and Owen McCarty, Oregon Health & Science University for providing us tdTomato transfected MDA-MB-231 cells.

M.N. and R.R. acknowledge NSF award #1510700. R.R. acknowledges NIH/NCI grant U54CA143682 and NIH/NHLBI grant R01HL10753.

Appendix A. Supplementary data

Supplementary data related to this article can be found at http://dx.doi.org/10.1016/j.biomaterials.2015.11.039.

References

[1] S. Braun, B. Naume, Circulating and disseminated tumor cells, J. Clin. Oncol. Off. J. Am. Soc. Clin. Oncol. 23 (2005) 1623–1626.
[2] C. Foroni, M. Broggini, D. Generali, G. Damia, Epithelial-mesenchymal transition and breast cancer: role, molecular mechanisms and clinical impact, Cancer Treat. Rev. 38 (2012) 689–697.
[3] P. Friedl, K. Wolf, Tumour-cell invasion and migration: diversity and escape mechanisms, Nat. Rev. Cancer 3 (2003) 362–374.
[4] T.R. Geiger, D.S. Peeper, Metastasis mechanisms, Biochim. Biophys. Acta 1796 (2009) 293–308.
[5] P. Lu, V.M. Weaver, Z. Werb, The extracellular matrix: a dynamic niche in cancer progression, J. Cell Biol. 196 (2012) 395–406.
[6] T.V. Dyke, T. Jacks, Cancer modeling in the modern era: progress and challenges, Cell 108 (2002) 135–144.
[7] M. Nikkhah, J.S. Strobl, M. Agah, Attachment and response of human fibroblast and breast cancer cells to three dimensional silicon microstructures of different geometries, Biomed. Microdevices 11 (2009) 429–441.
[8] M. Nikkhah, J.S. Strobl, R. De Vita, M. Agah, The cytoskeletal organization of breast carcinoma and fibroblast cells inside three dimensional (3-D) isotropic silicon microstructures, Biomaterials 31 (2010) 4552–4561.
[9] M. Nikkhah, J.S. Strobl, E.M. Schmelz, P.C. Roberts, H. Zhou, M. Agah, MCF10A and MDA-MB-231 human breast basal epithelial cell co-culture in silicon micro-arrays, Biomaterials 32 (2011) 7625–7632.
[10] M. Nikkhah, F. Edalat, S. Manoucheri, A. Khademhosseini, Engineering microscale topographies to control the cell-substrate interface, Biomaterials 33 (2012) 5230–5246.
[11] H.K. Kleinman, G.R. Martin, Matrigel: basement membrane matrix with biological activity, Semin. Cancer Biol. 15 (2005) 378–386.
[12] J. Liu, Y. Tan, H. Zhang, Y. Zhang, P. Xu, J. Chen, et al., Soft fibrin gels promote selection and growth of tumorigenic cells, Nat. Mater. 11 (2012) 734–741.
[13] F. Grinnell, Fibroblast biology in three-dimensional collagen matrices, Trends Cell Biol. 13 (2003) 264–269.
[14] G.P. Raeber, M.P. Lutolf, J.A. Hubbell, Molecularly engineered PEG hydrogels: a novel model system for proteolytically mediated cell migration, Biophys. J. 89 (2005) 1374–1388.
[15] E. Cukierman, R. Pankov, D.R. Stevens, K.M. Yamada, Taking cell-matrix adhesions to the third dimension, Science 294 (2001) 1708–1712.
[16] T.H. Park, M.L. Shuler, Integration of cell culture and microfabrication technology, Biotechnol. Prog. 19 (2003) 243–253.
[17] S. Pedron, B.A. Harley, Impact of the biophysical features of a 3D gelatin microenvironment on glioblastoma malignancy, J. Biomed. Mater. Res. A 101 (2013) 3404–3415.
[18] L.E. Dickinson, C. Lutgebaucks, D.M. Lewis, S. Gerecht, Patterning microscale extracellular matrices to study endothelial and cancer cell interactions in vitro, Lab Chip 12 (2012) 4244–4248.
[19] J.M. Banks, B.A.C. Harley, R.C. Bailey, Tunable, photoreactive hydrogel system to probe synergies between mechanical and biomolecular cues on adipose-derived mesenchymal stem cell differentiation, ACS Biomater. Sci. Eng. 1 (2015) 718–725.
[20] A.T. Alsop, J.C. Pence, D.W. Weisgerber, B.A. Harley, R.C. Bailey, Photopatterning of vascular endothelial growth factor within collagen-glycosaminoglycan scaffolds can induce a spatially confined response in human umbilical vein endothelial cells, Acta Biomater. 10 (2014) 4715–4722.
[21] J.W. Nichol, S.T. Koshy, H. Bae, C.M. Hwang, S. Yamanlar, A. Khademhosseini, Cell-laden microengineered gelatin methacrylate hydrogels, Biomaterials 31 (2010) 5536–5544.
[22] H. Aubin, J.W. Nichol, C.B. Hutson, H. Bae, A.L. Sieminski, D.M. Cropek, et al., Directed 3D cell alignment and elongation in microengineered hydrogels, Biomaterials 31 (2010) 6941–6951.
[23] M. Nikkhah, N. Eshak, P. Zorlutuna, N. Annabi, M. Castello, K. Kim, et al., Directed endothelial cell morphogenesis in micropatterned gelatin methacrylate hydrogels, Biomaterials 33 (2012) 9009–9018.
[24] W. Schuurman, P.A. Levett, M.W. Pot, P.R. van Weeren, W.J. Dhert, D.W. Hutmacher, et al., Gelatin-methacrylamide hydrogels as potential biomaterials for fabrication of tissue-engineered cartilage constructs, Macromol. Biosci. 13 (2013) 551–561.
[25] A.I. Van Den Bulcke, B. Bogdanov, N.D. Rooze, E.H. Schact, M. Cornelissen, H. Berghmans, Structural and rheological properties of methacrylamide modified gelatin hydrogels, Biomacromolecules 1 (2000) 31–38.
[26] L.E. Bertassoni, M. Cecconi, V. Manoharan, M. Nikkhah, J. Hjortnaes, A.L. Cristino, et al., Hydrogel bioprinted microchannel networks for

vascularization of tissue engineering constructs, Lab Chip 14 (2014) 2202e2211.
[27] A. Dolatshahi-Pirouz, M. Nikkhah, A.K. Gaharwar, B. Hashmi, E. Guermani, H. Aliabadi, et al., A combinatorial cell-laden gel microarray for inducing osteogenic differentiation of human mesenchymal stem cells, Sci. Rep. 4 (2014) 3896.
[28] E. Kaemmerer, F.P. Melchels, B.M. Holzapfel, T. Meckel, D.W. Hutmacher, D. Loessner, Gelatine methacrylamide-based hydrogels: an alternative three-dimensional cancer cell culture system, Acta Biomater. 10 (2014) 2551e2562.
[29] O. Schulz, F. Koberling, D. Walters, M. Koenig, J. Viani, R. Ros, Simultaneous single molecule atomic force and fluorescence lifetime imaging, SPIE 7571 (2010) 757109e757110.
[30] A. Fuhrmann, J.R. Staunton, V. Nandakumar, N. Banyai, P. Davies, R. Ros, AFM stiffness nanotomography of normal, metaplastic and dysplastic human esophageal cells, Phys. Biol. 8 (2011) 10.
[31] D.B. Agus, J.F. Alexander, W. Arap, S. Ashili, J.E. Aslan, R.H. Austin, et al., A physical sciences network characterization of non-tumorigenic and metastatic cells, Sci. Rep. 3 (2013) 1449.
[32] H. Butt, M. Jaschke, Calculation of thermal noise in atomic force microscopy, Nanotechnology 6 (1995) 1e7.
[33] S. Guo, B.B. Akhremitcev, Packing density and structural heterogeneity of insulin amyloid fibrils measured by AFM nanoindentation, Biomacromolecules 7 (2006) 1630e1636.
[34] A. Kiss, P. Horvath, A. Rothballer, U. Kutay, G. Csucs, Nuclear motility in glioma cells reveals a cell-line dependent role of various cytoskeletal components, PLoS One 9 (2014) e93431.
[35] H. Saini, A. Navaei, A.V. Putten, M. Nikkhah, 3D cardiac microtissues encapsulated with the co-culture of cardiomyocytes and cardiac fibroblasts, Adv. Healthc. Mater. 4 (2015) 1961e1971.
[36] K. Tanner, H. Mori, R. Mroue, A. Bruni-Cardoso, M.J. Bissell, Coherent angular motion in the establishment of multicellular architecture of glandular tissues, Proc. Natl. Acad. Sci. 109 (2012) 1973e1978.
[37] L.C. Kimlin, G. Casagrande, V.M. Virador, In vitro three-dimensional (3D) models in cancer research: an update, Mol. Carcinog. 52 (2013) 167e182.
[38] T.I. Son, M. Sakuragi, S. Takahashi, S. Obuse, J. Kang, M. Fujishiro, et al., Visible light-induced crosslinkable gelatin, Acta Biomater. 6 (2010) 4005e4010.
[39] S.L. Fenn, R.A. Oldinski, Visible light crosslinking of methacrylated hyaluronan hydrogels for injectable tissue repair, J. Biomed. Mater. Res. B Appl. Biomater. (2015), http://dx.doi.org/10.1002/jbm.b.3347 [Epub ahead of print].
[40] M.H. Zaman, L.M. Trapani, A.L. Sieminski, D. Mackellar, H. Gong, R.D. Kamm, et al., Migration of tumor cells in 3D matrices is governed by matrix stiffness along with cell-matrix adhesion and proteolysis, Proc. Natl. Acad. Sci. U. S. A. 103 (2006) 10889e10894.
[41] C.M. Kraning-Rush, C.A. Reinhart-King, Controlling matrix stiffness and topography for the study of tumor cell migration, Cell Adh. Migr. 6 (2012) 274e279.
[42] P. Friedl, D. Gilmour, Collective cell migration in morphogenesis, regeneration and cancer, Nat. Rev. Mol. Cell Biol. 10 (2009) 445e457.
[43] M. Ehrbar, A. Sala, P. Lienemann, A. Ranga, K. Mosiewicz, A. Bittermann, et al., Elucidating the role of matrix stiffness in 3D cell migration and remodeling, Biophys. J. 100 (2011) 284e293.
[44] R.S. Stowers, S.C. Allen, L.J. Suggs, Dynamic phototuning of 3D hydrogel stiffness, Proc. Natl. Acad. Sci. 17 (2015) 1953e1958.
[45] R. Mayor, C. Carmona-Fontaine, Keeping in touch with contact inhibition of locomotion, Trends Cell Biol. 20 (2010) 319e328.
[46] R.A. Desai, S.B. Gopal, S. Chen, C.S. Chen, Contact inhibition of locomotion probabilities drive solitary versus collective cell migration, J. R. Soc. Interface 10 (2013) 20130717.
[47] R.J. Petrie, K.M. Yamada, At the leading edge of three-dimensional cell migration, J. Cell Sci. 125 (2012) 5917e5926.
[48] R. Poincloux, O. Collin, F. Lizarraga, M. Romao, M. Debray, M. Piel, et al., Contractility of the cell rear drives invasion of breast tumor cells in 3D matrigel, Proc. Natl. Acad. Sci. U. S. A. 108 (2011) 1943e1948.
[49] A. Lance, C. Yang, M. Swamyda, D. Dean, S. Deitch, K.J. Burg, et al., Increased extracellular matrix density decreases MCF10A breast cell acinus formation in 3D culture conditions, J. Tissue Eng. Regen. Med. (2013), http://dx.doi.org/10.1002/term.1675 [Epub ahead of print].
[50] P.I. Nedvetsky, S.H. Kwon, J. Debnath, K.E. Mostov, Cyclic AMP regulates formation of mammary epithelial acini in vitro, Mol. Biol. Cell 23 (2012) 2973e2981.
[51] S. Krause, M.V. Maffini, A.M. Soto, C. Sonnenschein, The microenvironment determines the breast cancer cells' phenotype: organization of MCF7 cells in 3D cultures, BMC Cancer 10 (2010) 263.
[52] S. Rhee, H. Jiang, C. Ho, F. Grinnell, Microtubule function in fibroblast spreading is modulated according to the tension state of cellematrix interactions, Proc. Natl. Acad. Sci. 104 (2007) 5425e5430.
[53] S.R. Peyton, C.M. Ghajar, C.B. Khatiwala, A.J. Putnam, The emergence of ECM mechanics and cytoskeletal tension as important regulators of cell function, Cell Biochem. Biophys. 47 (2007) 300e320.
[54] A. Rovini, A. Savry, D. Braguer, M. Carre, Microtubule-targeted agents: when mitochondria become essential to chemotherapy, Biochim. Biophys. Acta 1807 (2011) 679e688.
[55] M.A. Jordan, N. Wilson, Microtubules as a target for anticancer drugs, Nat. Rev. Cancer 4 (2004) 253e265.
[56] M.A. Jordan, C. Dumontet, Microtubule-binding agents: a dynamic field of cancer therapeutics, Nat. Rev. Drug Discov. 9 (2010) 790e803.
[57] D. Escuin, E.R. Kline, P. Giannakakou, Both microtubule-stabilizing and microtubule-destabilizing drugs inhibit hypoxia-inducible factor-1alpha accumulation and activity by disrupting microtubule function, Cancer Res. 65 (2005) 9021e9028.

APPENDIX B

GOLD NANOROD-INCORPORATED GELATIN-BASED CONDUCTIVE HYDROGELS FOR ENGINEERING CARDIAC TISSUE CONSTRUCTS

Full length article

Gold nanorod-incorporated gelatin-based conductive hydrogels for engineering cardiac tissue constructs

Ali Navaei [a], Harpinder Saini [a], Wayne Christenson [b,c], Ryan Tanner Sullivan [a], Robert Ros [b,c,d], Mehdi Nikkhah [a,⇑]

[a] School of Biological and Health Systems Engineering (SBHSE), Arizona State University, Tempe, AZ 85287, USA
[b] Department of Physics, Arizona State University, Tempe, AZ 85287, USA
[c] Center for Biological Physics, Arizona State University, Tempe, AZ 85287, USA
[d] Biodesign Institute, Arizona State University, Tempe, AZ 85287, USA

a r t i c l e i n f o

Article history:
Received 15 December 2015
Received in revised form 28 March 2016
Accepted 18 May 2016
Available online 20 May 2016

Keywords:
Gelatin methacrylate Conductive hydrogels Cardiac patches Synchronous beating Myocardial infarction
Calcium^{2+} puffs

a b s t r a c t

The development of advanced biomaterials is a crucial step to enhance the efficacy of tissue engineering strategies for treatment of myocardial infarction. Specific characteristics of biomaterials including elec- trical conductivity, mechanical robustness and structural integrity need to be further enhanced to pro- mote the functionalities of cardiac cells. In this work, we fabricated UV-crosslinkable gold nanorod (GNR)-incorporated gelatin methacrylate (GelMA) hybrid hydrogels with enhanced material and biolog- ical properties for cardiac tissue engineering. Embedded GNRs promoted electrical conductivity and mechanical stiffness of the hydrogel matrix. Cardiomyocytes seeded on GelMA-GNR hybrid hydrogels exhibited excellent cell retention, viability, and metabolic activity. The increased cell adhesion resulted in abundance of locally organized F-actin fibers, leading to the formation of an integrated tissue layer on the GNR-embedded hydrogels. Immunostained images of integrin b-1 confirmed improved cell- matrix interaction on the hybrid hydrogels. Notably, homogeneous distribution of cardiac specific mark-
ers (sarcomeric a-actinin and connexin 43), were observed on GelMA-GNR hydrogels as a function of GNRs concentration. Furthermore, the GelMA-GNR hybrids supported synchronous tissue-level beating of cardiomyocytes. Similar observations were also noted by, calcium transient assay that demonstrated the rhythmic contraction of the cardiomyocytes on GelMA-GNR hydrogels as compared to pure GelMA. Thus, the findings of this study clearly demonstrated that functional cardiac patches with superior elec- trical and mechanical properties can be developed using nanoengineered GelMA-GNR hybrid hydrogels.

Statement of Significance

In this work, we developed gold nanorod (GNR) incorporated gelatin-based hydrogels with suitable elec- trical conductivity and mechanical stiffness for engineering functional cardiac tissue constructs (e.g. car- diac patches). The synthesized conductive hybrid hydrogels properly accommodated cardiac cells and subsequently resulted in excellent cell retention, spreading, homogeneous distribution of cardiac specific markers, cell-cell coupling as well as robust synchronized (tissue-level) beating behavior.

1. Introduction

Myocardial infarction (MI) is a major cause of mortality amongst cardiovascular diseases in the United States accounting for approximately one death per minute [1]. Due to limited availability of donors and high complications associated with heart transplantation, cell-based therapies [2,3] and tissue engineering [4–6] have been considered as promising strategies for treatment of MI. Particularly, tissue engineering approaches have enabled the development of biomimetic cardiac patches [7–9], meshes [10,11] and cell sheets [12–14]. In this regard, hydrogel-based bio-materials have been proven to be suitable matrices for cardiac regeneration and repair [15–17]. To date, several synthetic and natural hydrogels, such as collagen [18], gelatin [19–21], alginate [22], Matrigel® [23], and poly(N-isopropylacrylamide) (PNIPAAM) [24] have been utilized to develop tissue substitutes to replace dysfunctional heart muscle. Although, these hydrogels have offered ECM-like microenvironment to support cardiac cell functions, the nanoscale architectural and electrical properties of the previously developed hydrogels are inferior to the characteristics of the native myocardium [17,25–27]. In particular, inadequate cell adhesion affinity along with electrically insulated structure of conventional hydrogels ultimately lead to poor cell-cell coupling between cardiomyocytes and thereby diminished functionalities of the engineered tissue [28,29].

Many recent studies have demonstrated that employing electrically conductive nanomaterials enables addressing the current shortcomings of conventional hydrogel-based scaffolds for cardiac tissue engineering [25,30,31]. In particular, carbon nanotubes (CNTs) have been amongst the prevalent conductive nanomaterials for engineering advanced biomaterials to support cardiac cell functions [32]. CNTs-embedded scaffolds [25,33] have demonstrated enhanced electrical properties facilitating the signal propagation and consequently improved cell-cell coupling. While incorporation of CNTs results in superior tissue level properties, controversial cytotoxicity issues have raised numerous concerns for their use in clinical practice [34–37]. In this regard, several strategies such as surface coating and/or functionalization [38] have been considered to reduce the cytotoxicity of CNTs. However, these alterations are expected to compromise the electrical properties of the nano-engineered scaffolds [39,40]. Additionally, the low solubility of carbon nanotubes may require complex fabrication procedures [38]. Therefore, utilizing electrically conductive nanomaterials with minimized cytotoxicity and less intensive fabrication procedures provides an ideal solution to develop cardiac tissue constructs with enhanced functionalities.

Gold nanostructures such as nanoparticles, nanorods, nano-wires, etc. are amongst the most promising nanomaterial candidates for biomedical applications [41–43]. High electrical conductivity, facile fabrication and modification processes [44], diverse nanoscale architecture [45], and minimized cytotoxicity [17,46–48] are the key advantages of gold nanomaterials. Several studies, exploiting gold nanostructures incorporated scaffolds, including alginate [26], poly(ε-caprolactone) [49,50], thiol-2-hydroxyethyl methacrylate (thiol-HEMA) [51], and decellularized omental matrix [52] have illustrated high potency of these nano-materials for cardiac tissue engineering. Despite outstanding findings, several aspects of the previously developed scaffolds, including cell adhesion, spreading and the formation of a uniform tissue layer still need to be improved to enhance the functionalities of the engineered cardiac tissues. In the pioneer work of Dvir et al. [26], alginate hydrogel incorporated with gold nanowires, was used to form cardiac tissue constructs. Despite the significant outcome and outstanding findings, alginate may not provide a suitable microenvironment for cell binding and attachment. Therefore, it is required to explore hydrogel-based matrices with superior cell adhesion characteristics along with enhanced electrical conductivity to support the functionalities of cardiac cells.

In this study, we developed Gold nanorod (GNR)-embedded gelatin methacrylate (GelMA) hybrid hydrogels with enhanced material and biological characteristics, for cardiac tissue engineering applications. GelMA is a photocrosslinkable hydrogel, comprised of dehydrated gelatin functionalized with methacrylate groups [53], suitable for a wide range of tissue engineering applications [54–56]. In particular, we fabricated GelMA-GNR hybrid hydrogels with variable GNR concentrations and performed extensive analyses to assess the material properties of the proposed hydrogel matrix. Furthermore, we conducted substantial biological studies to investigate cardiac cell retention, survival, cytoskeletal organization, expression of specific markers, as well as tissue-level beating and Ca^{2+} transient. The enhanced electrical properties of GelMA-GNR hybrid hydrogels and the nanoengineered architecture of the matrix resulted in improved cell-matrix interaction and cell-cell coupling, ultimately promoting the structural and functional properties of the engineered tissue.

2. Experimental methods

2.1. Materials

Gold (III) chloride trihydrate ($HAuCl_4$) (>99.9%), sodium borohydride ($NaBH_4$) (>99%),

hexadecyltrimethylammonium bromide (CTAB) (>99%), silver nitrate ($AgNO_3$) (>99%), and L-Ascorbic acid (>98%) were purchased from Sigma-Aldrich and used without fur- ther purification. Gelatin (Type A, 300 bloom from porcine skin), methacrylic anhydride (MA), 3-(trimethoxysilyl) propyl methacry- late (TMSPMA), and 2-hydroxy-1-(4-(hydroxyethoxy) phenyl)-2- methyl-1-propanone (the photoinitiatior) all were obtained from Sigma-Aldrich. Deionized water (DIW) (18 MX) was used for GNR fabrication processes.

2.2. Gold nanorod (GNR) synthesis

GNRs were synthesized using a previously established seed mediated growth method (Fig. S1) [57]. Briefly, first $HAuCl_4$ (0.5 mM) was dissolved in DIW (Distilled water) and mixed with a 2 mL aqueous solution of CTAB (0.2 M), which turned the color of the solution to deep yellow. Next, 240 µL of ice-cold $NaBH_4$ was added all at once to the solution under stirring and was kept agitated for 2 min. The color of the solution turned from deep yellow to brown-yellow immediately, indicating the formation of gold nanoparticles (seed solution). The seed solution contained gold nanoparticles (GNPs) with a mean diameter of less than 4 nm [57]. Afterwards, the growth solution was prepared by adding 1.12 mL $AgNO_3$ (4 mM in DIW) to 20 mL CTAB (0.2 M in DIW) followed by the addition of a 20 mL aqueous solution of $HAuCl_4$ (1 mM), which created a deep yellow solution. Subsequently, 280 µL ascorbic acid (13.88 mg in 1 mL DIW) was added gently to this solution, immediately making the solution colorless. The temperature was kept at 25 ºC during all the processes. Finally, a 48 µL aliquot of seed solution was poured into the growth solution at 30 ºC and the color of solution turned to brown-red over a period of half an hour, confirming the formation of GNRs. To obtain longer GNRs, the solution was kept overnight at 30 ºC. The solution contained GNRs with an average aspect ratio (length/width) of 3.15 (Table S1). Before further experimentation, the GNR colloid was centrifuged at 12,000 rpm for 10 min and washed 2 times with DIW to remove the excess CTAB.

2.3. Gelatin methacrylate synthesis

Gelatin methacrylate (GelMA) was synthesized according to previously established protocol [19]. In brief, type A gelatin (Sigma-Aldrich, USA) (10% w/v) was fully dissolved in Dulbecco's phosphate buffered saline (DPBS) at 50 ºC. Then, MA (8% v/v) was added drop-wise to the gelatin solution and stirred for 3 h at 50 ºC. To stop the methacrylation reaction, the solution was diluted 5 times by adding DPBS (50 ºC). The final solution was then poured into dialysis tubes (12–14 kDa molecular weight cutoff) and kept at 45 ºC in DIW under stirring for 7 days to eliminate the unreacted MA and salts. Dialyzed solution was passed through a 0.2 µm membrane filter and then freeze-dried for 7 days to obtain GelMA foam.

2.4. Preparation of GelMA-GNR hybrid hydrogels

First, photoinitiatior (0.5% w/v) was completely dissolved in DPBS, and then to this solution, lyophilized GelMA (5% w/v) with high degree of methacrylation (96.41 ± 1.54%) (data not shown), was added and kept at 80 oC until a clear solution was achieved. Second, certain amounts of centrifuged GNRs (0.5, 1 & 1.5 mg/mL) were mixed with GelMA prepolymer solution followed by water bath sonication for 1 h to obtain a homogeneous mixture. To prepare hybrid constructs (Fig. 1), 15 µL of the GelMA-GNR mixture was located between two 150 µm tall spacers and covered by glass slides coated with TMSPMA. The constructs were formed via photopolymerization by UV light (800 mW, 360–480 nm) for 6, 8, 25, and 35 s exposure time for 0, 0.5, 1, and 1.5 mg/mL GNR con-centrations respectively.

2.5. Characterization of GNRs and GelMA-GNR hybrid hydrogels

GNR micrographs were obtained by using transmission electron microscopy (TEM) (Philips CM200-FEG, USA) operating at an accelerating voltage of 200 kV. In addition, the energy dispersive X-ray spectroscopy (TEM-EDX, Philips CM200-FEG, USA) was utilized to the hydrogel constructs using NIH ImageJ software. To measure the mechanical stiffness (Young's modulus) of the hydrogel con- structs, 150 µm thick swollen hydrogels in DPBS were tested by an atomic force microscopy (AFM) (MFP-3D AFM, Asylum Research) with silicon nitride tips (MSNL, Bruker). Three samples were used for each GNR concentration and the contact model for a cone indenter was used [58,59]. For impedance analysis, hydrogel constructs were located between two indium tin oxide (ITO) coated glass slides (Sigma-Aldrich) with an AC bias sweeping (Agi- lent 4284A LCR meter) from 20 Hz to 1 MHz. Four samples were analyzed per each GNR concentration. To evaluate swelling behavior of pure and hybrid hydrogel constructs, 10 mm radius discshape (150 µm height) hydrogel constructs were prepared and immediately soaked in the DPBS and stored inside 37 ºC for 24 h. Constructs were blotted gently with KimWipe to remove the residual DPBS, and the weight values were subsequently recorded. The swollen hydrogels were immersed in liquid nitrogen, followed by lyophilization.

The porous micro-structure of hydrogel constructs was evaluated by means of scanning electron microscopy

(SEM) (XL30 ESEM FEG, USA). To prepare samples for SEM, fabricated hydrogels were located in DPBS inside an incubator (37 ºC) for 24 h. The swollen hydrogels were then submerged in liquid nitrogen followed by freeze-drying, and coating with Au/Pd (4 nm). However, the hydrogel constructs, which were used for localizing GNRs within GelMA hydrogel matrix, were coated with carbon followed by utilizing backscattered electron microscopy (SEM-BSE). Five SEM images were acquired to analyze the porosity and average pore size of each hybrid and pure hydrogels.

2.6. Cardiomyocytes isolation and culture

Neonatal rat ventricular cardiomyocytes were harvested from the ventricular region of 2 day old neonatal rats based on

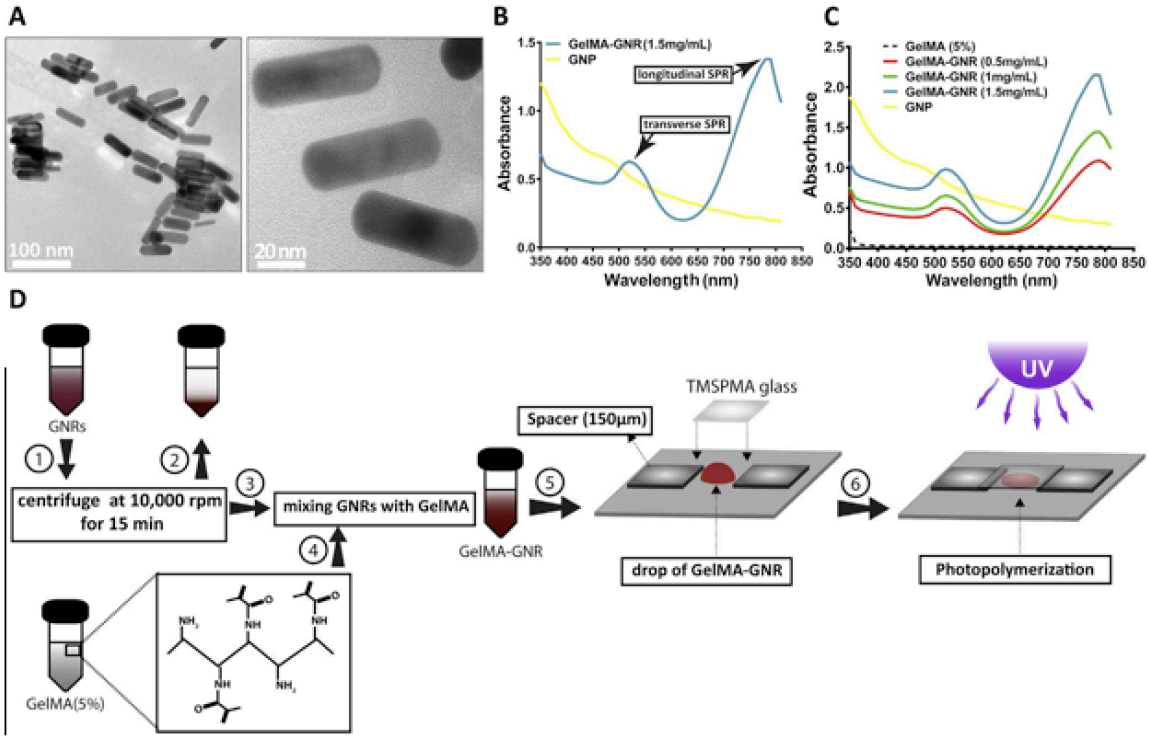

Fig. 1. Fabrication and characterization of GNRs and GelMA-GNR hybrid hydrogels. A) TEM micrographs of synthesized GNRs. B) UV–Vis absorbtion spectra of GNPs and GNRs, showing longitudinal and transverse surface plasmon resonance (SPR) peaks. C) UV–Vis absorbtion spectra of pure GelMA and GelMA-GNR hybrid prepolymer solutions with 0.5, 1, and 1.5 mg/mL GNRs concentrations. D) Schematic illustration of the fabrication procedure of GelMA-GNR hybrid hydrogel construct (numbers indicate the step sequence).

previously developed protocol [19] accepted by the Institution of Animal Care (IACUC) at Arizona State University. After isolation, the cardiomyocytes were separated from cardiac fibroblasts by pre-plating the isolated cell suspension for 1 h. Before seeding cardiomyocytes, the hydrogel constructs were washed 2 times, 10 min intervals, in 1% (v/v) penicillin-streptomycin (Gibco, USA) in DPBS and then washed 2 times in 10 min periods in the cardiac culture medium containing Dulbecco's modified eagle medium (DMEM) (Gibco, USA), fetal bovine serum (FBS) (10%) (Gibco, USA), L-Glutamine (1%) (Gibco, USA), and penicillin-streptomycin (100 units/mL) Harvested cardiomyocytes were seeded on top of disk-shape constructs (diameter × height, 10 mm × 150 µm; 7.5×10^5 cells/well) and were cultured in the cardiac specific culture media for 7 days under static condition.

2.7. Characterization of survival, retention, metabolic activity, and cytoskeleton organization

Cardiomyocytes viability was determined using standard Live/Dead assay kit (Life technologies, USA) based on manufacturer's instruction. Triplicate samples were used for each hydrogel construct and three individual areas were selected within each replicate (n = 9). Fluorescent images were acquired using a fluorescent microscope (Zeiss Observer Z1) and the subsequent quantifications were performed utilizing NIH ImageJ software. The

viability was quantified as number of live cells divided by total number of cells. Cell retention was measured by quantifying area fraction, using ImageJ software, one day upon seeding the cells. Five phase contrast images were taken within each sample (three samples for each hydrogel construct, (n = 15)). To examine metabolic activity of cells on the constructs, Alamar Blue assay kit (Invitrogen, USA) was used according to manufacturer's protocol at day 3, 5, and 7 of the culture. Three samples were specified for each hydrogel construct and results were normalized with respect to day 1.

To assess the cytoskeleton organization, hydrogel constructs were stained for F-actin fibers. Cells were fixed in paraformaldehyde (PF) and soaked in Triton X-100 for 45 min at room temperature to permeabilize the plasma membrane, and then blocked in 1% (v/v) bovine serum albumin (BSA) for 1 h. Finally, cardiomyocytes were stained (1:40 dilution in 1% BSA) with Alexa Fluor-488 phalloidin (Life technologies, USA) for 40 min, and counterstained with 40,6-diamidino-2-phenyl indole dihydrochloride (DAPI, 1:1000 dilution) for 18 min. Z-stack fluorescent images were taken by a fluorescent microscope equipped with ApoTome2 (Zeiss, Germany) and analyzed by ImageJ (FFT built-in plugin). Cells' nuclei alignment was quantified similar to previously established procedures [19,55]. Briefly, an ellipse (built-in plugin, Ima- geJ) was fitted to the nuclei (DAPI) and deviation angle from the main axis of ellipse with respect to the x-axis was determined. All alignment angles were normalized by subtracting from average angle of each image and presented in 10o increment spans.

2.8. Immunostaining for cardiomyocyte specific markers and cell-matrix interaction

Immunocytochemistry technique was used to visualize cardiac expressed proteins. Specific markers, including sarcomeric a-actinin, connexin 43 (Cx43) and troponin I, cardiomyocytes were fixed in 4% PF for 40 min, followed by treatment with 0.1% Triton X-100 for 45 min at room temperature to permeabilize the plasma membrane. Then, cells were blocked in 10% goat serum for 2 h at 4 ºC. Afterwards, cardiomyocytes were stained with primary anti- bodies (1:100 dilution in 10% goat serum for sarcomeric a-actinin and connexin 43, and 2 mg/mL in DPBS for troponin I) and placed in cold room (4 ºC) for 24 h. After primary staining (Abcam, USA), samples were washed three time in DPBS and stained with secondary antibodies (Life Technologies, USA) comprised of Alexa Fluor-594 (pseudo-colored with green) for sarcomeric a-actinin, Alexa Fluor-488 for troponin I, and Cx43 (pseudo-colored with red) at 1:200 dilution in 10% goat serum for 6 h. Eventually, cells were stained with DAPI (1:1000 dilution in DPBS) for 18 min to label the nucleus. For adhesion specific marker, integrin-b1, all staining steps were similar to cardiac specific markers except that the cells' membranes were not permeabilized and Alexa Fluor-594 secondary antibody was used to stain integrin-b1. High magnification (100×) images of sarcomeric a-actinin and Cx43 were obtained using confocal microscopy (Leica TCS SP5 AOBS Spectral Confocal System). Troponin I images were obtained using a fluorescent microscope equipped with ApoTome2.

2.9. Analysis of beating behavior of the cells

The spontaneous beating of cardiomyocytes was measured and monitored from day 1 to day 7 of the culture. For each data point, 3 videos (30 s long) were captured per sample (12 replicates for each group of hydrogel constructs). Representative beating signals were acquired using a custom written MATLAB code [25].

2.10. Intracellular Ca^{2+} transient assays

To assess intracellular Ca^{2+} transient within cultured neonatal cardiomyocytes on pure and hybrid hydrogels, calcium indicator assay kit (Life Technologies, USA) including Fluo-4 AM and Pluronic F127 (20% in DMSO) was utilized. All samples (pure and hybrids) on day 7 of the culture were washed one time with pre-warmed DPBS, followed by loading (10 mL/mL in DPBS) the calcium indicator solution (a mixture of 50 µg of Fluo-4 Am in 50 µL of Pluronic F127) for 45 min. Next, the indicator was discarded and the hydrogel constructs were soaked in pre- warmed Tyrode solution (Sigma- Aldrich, pH rv7.4) to allow de-esterification for 40 min. Afterwards, spontaneous increase in intracellular Ca^{2+} concentration were imaged using a fluorescent microscope (at 50 frame/s) at 488 nm wavelength. To analyze the change in Ca^{2+} concentration, the fluorescent dye intensity (F) during cells' contractions was normalized by dividing to the background intensity (F_0) and plotted over the time.

2.11. External electrical stimulation

The response of the cultured cardiomyocytes on top of pure and hybrid hydrogels to the external electrical stimulation were inves- tigated according to previously established protocol [60]. Primarily, a chamber was assembled using 2 carbon electrodes (5 mm) with 1 cm spacing attached to a plastic petri dish (6 mm diameter) by silicone adhesive (Fig. 10A). Platinum wires were connected to the carbon electrodes (at the opposite ends of each electrode) and all connections were sealed using silicone adhesive. The assembled chamber was sterilized before use by placing under UV light for 1 h. Pulsatile electrical signals produced by a pulse generator

(BK PRECISION 4052) were applied on the pure GelMA and hybrid GelMA-GNR hydrogels. Electrical pulses with 2 ms durations at three different frequencies (1, 2, and 3 Hz) were con- sidered for the experiment. The minimum required voltage to observe contraction of cardiomyocytes was defined as the excitation threshold.

2.12. Statistical analysis

All the data collected in this study were analyzed using one-way and two-way ANOVA analyses and reported as mean ± standard deviation (SD). To determine a statistically significant

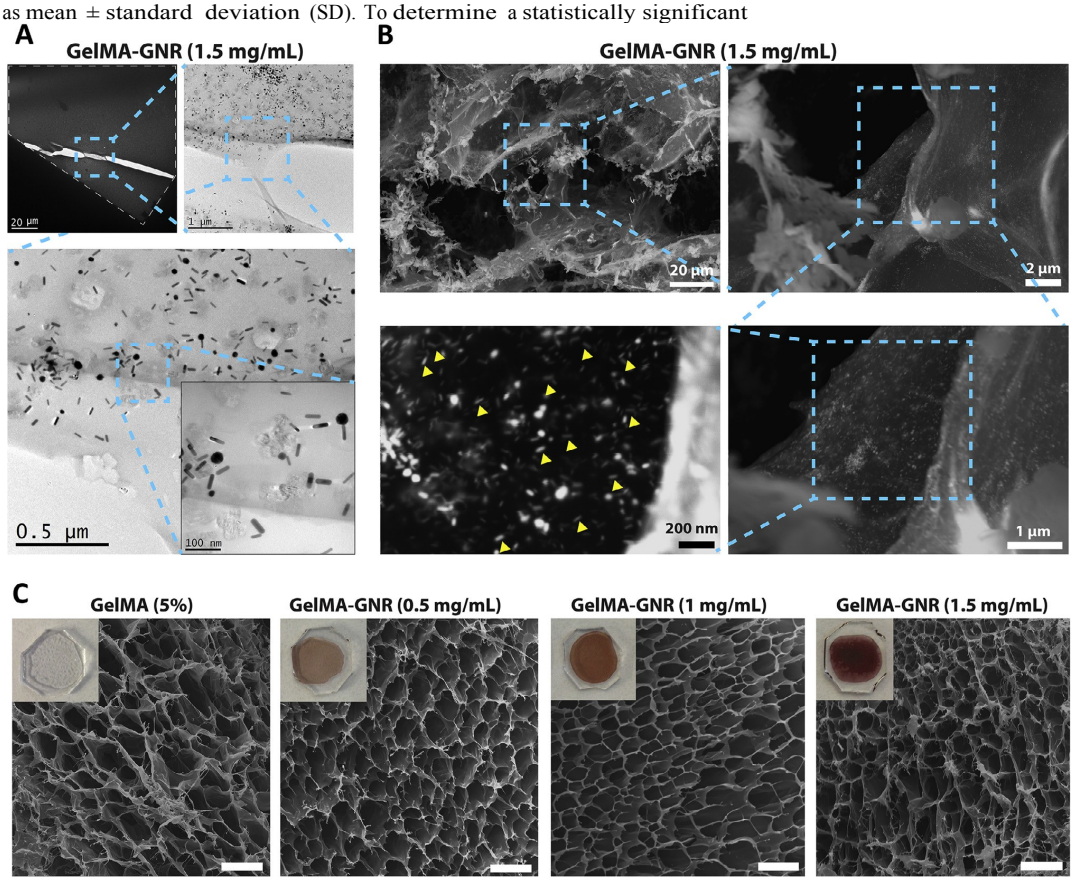

Fig. 2. Structural evaluation of pure and hybrid hydrogels. A) TEM micrographs showing GNRs embedded within a thin layer (white dashed line) of GelMA-GNR hybrid hydrogel (1.5 mg/mL) (black region is the TEM sample holder). B) Backscattered electron SEM images (SEM-BSE) of GelMA-GNR (1.5 mg/mL) hybrid hydrogels displaying the presence of GNRs (yellow arrow heads) within the GelMA matrix located on the pores. C) Secondary electron (SE-SEM) images illustrating cross-section of GelMA-GNR and pure GelMA hydrogels (insets are photographs of the related hydrogels). Scale bars represent 20 µm.

difference between groups, we used a Tukey's multiple comparison test with a p-value <0.05 considered to be significant. All the statistical analyses were performed by GraphPad Prism (v.6, GraphPad San Diego).

3. Results and discussion

3.1. Fabrication and characterization of GelMA-GNR hybrid hydrogels

The gold nanorods (GNRs) were synthesized via a seed-mediated growth technique [57] (Fig. S1). TEM micrographs (Fig. 1A) confirmed the rod-like shape of the GNRs. Fig. 1B shows the UV–Vis absorption spectrum with the longitudinal (rv810 nm) and transverse (rv530 nm) surface plasmon resonance (SPR) [43] wavelength peaks of the GNRs, demonstrating the successful fabrication of GNRs consistent with the previously published studies [57,61]. The average aspect ratio of the synthesized GNRs was calculated using TEM micrographs, approximately 3.15, as demonstrated in Supplementary Table S1. The GelMA-GNR prepolymer solution was sonicated to prepare a homogeneous hydrogel solution. All prepared prepolymer solutions (0.5, 1, and 1.5 mg/mL of GNRs) exhibited similar transverse and longitudinal wavelength peaks (Fig. 1C), confirming that the GNRs did not break into smaller sizes during the sonication process. The final GelMA-GNR hybrid hydrogel

constructs (150 µm thick) were formed through UV photopolymerization, as shown schematically in Fig. 1D.

The TEM images (Fig. 2A and Supplementary Fig. S2A) of a thin layer (1–5 µm) of the GelMA-GNR constructs showed that GNRs were successfully embedded within the hydrogel matrix (white dashed area). The energy dispersive X-ray spectroscopy (EDX) (Supplementary Fig. S2B) of the selected area (dashed line) further confirmed the presence of gold (Au) within the hydrogel layer. Additionally, backscattered electron (SEM-BSE) images (Fig. 2B) of GelMA-GNR hydrogel (1.5 mg/mL) demonstrated that GNRs located within the hydrogel matrix, specifically on the walls of pores. Furthermore, Fig. 2C shows similar micro-architecture within GelMA and GelMA-GNR hydrogel constructs. The SEM images demonstrated analogous micro-architecture of pure and hybrid hydrogels as well as no micro-agglomerations of GNRs within the hybrid hydrogel with 1.5 mg/mL GNR concentration. The SEM results clearly demonstrated that the incorporation of GNRs did not cause any considerable alteration within the GelMA micro-structure.

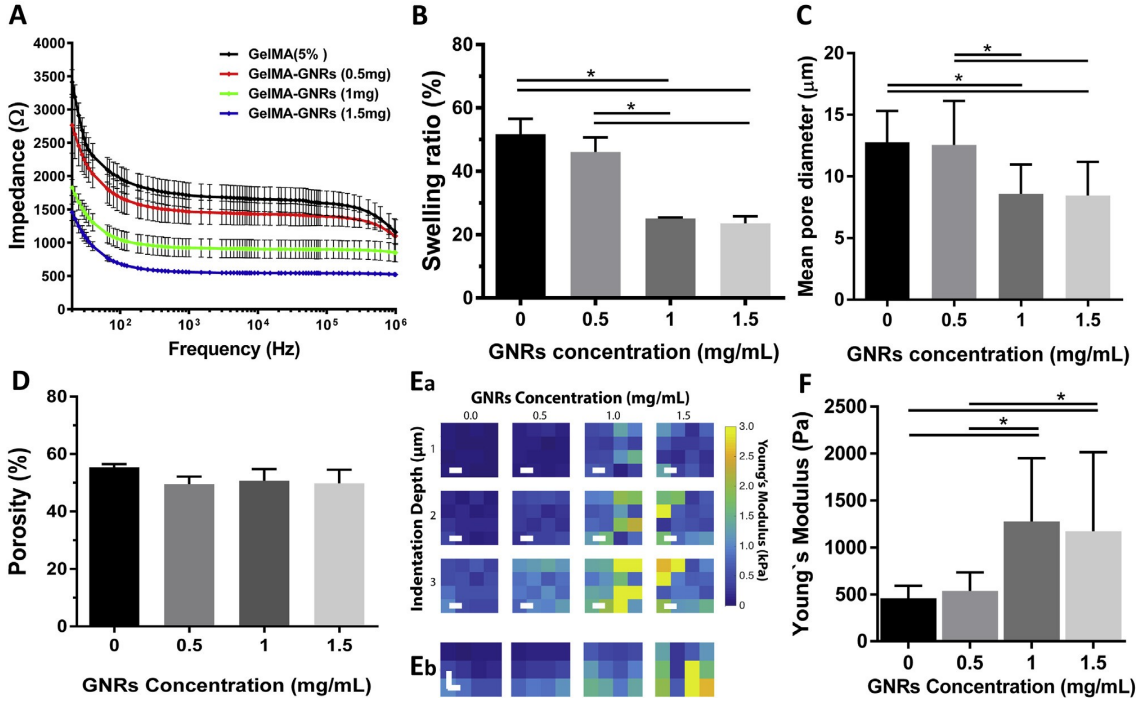

Fig. 3. Physical characteristics of pure and hybrid hydrogel constructs. A) Impedance of whole hydrogel construct (150 µm thick) decreased with the increase in concentration of GNRs. B) Swelling ratio percentage demonstrating lower swelling at high concentration of GNRs within hybrid hydrogels ($^{*}p < 0.05$); C) Mean pore diameter and D) porosity percentage of the hydrogel constructs (GelMA and GelMA-GNR), indicating the details of void structures calculated based on SEM images (n = 5; $^{*}p < 0.05$). Ea) Maps of Young's moduli for different indentation depths. The force indentation curves were fitted in 1 µm segments (0–1 µm, 1–2 µm, and 3–4 µm indentation depths). For each segment and curve the Young's modulus was determined. Eb) Cross section of depth dependent fit for different GNR concentrations. F) Average Young's moduli for different samples showing improved mechanical stiffness at high concentration of GNRs ($^{*}p < 0.05$). (Scale bars: vertical 1 µm; horizontal 20 µm).

Next, impedance analysis was performed to evaluate the electrical conductivity of the hybrid and pure hydrogel constructs. Fig. 3A indicates that GelMA-GNR hybrid hydrogels, with high concentrations of GNRs (1 and 1.5 mg/mL), exhibited relatively lower electrical impedance as compared to pure GelMA hydrogel at physiologically relevant frequencies [51]. The low electrical impedance of the hybrid hydrogels can be attributed to the resistive current passing through the bridging GNRs, suggesting that high concentration of GNRs improved the overall electrical conductivity of the hydrogel matrix. Such properties have been shown to facilitate signal propagation and coupling between cardiomyocytes [26,32].

Swelling and porosity are amongst other important properties of hydrogel-based scaffolds which directly influence nutrients and gas exchanges, specifically in case of cell encapsulation [55,62] and cell ingrowth within the constructs [63]. As illustrated in Fig. 3B, incorporation of high concentrations of GNRs (1 and 1.5 mg/mL) within the hydrogel matrices led to a statistically sig- nificant decrease in the swelling ratio, from 51 ± 4% for pure GelMA to 23 ± 2% for 1.5 mg/mL GelMA-GNR hybrid hydrogel. This decrease can be associated to the smaller average pore size (Fig. 3C) of the hybrid hydrogels (8 ± 2 µm for 1 and 1.5 mg/mL GNRs) as compared to the pure GelMA (12 ± 2 µm), ultimately leading to a decrease in the overall water content. Although incorporation of GNRs resulted in a decrease in pore size, nanoscale void structures were still available for nutrient and gas exchanges within the hydrogel constructs [63,64]. In addition, incorporation of GNRs did not notably influence the porosity percentage of the hydrogel constructs (Fig. 3D).

The Young's modulus, as a representative of mechanical stiffness of hydrogels,was measured using atomic force microscopy (AFM) based on nano-indentation to investigate the constructs' capability for enduring generated compressive forces by cardiomyocytes. The samples were indented in 4 × 4 grids up to a maximum depth of 4 μm and analyzed in 1 μm sections similar to previous studies [65]. Fig. 3Ea and Eb show the distribution of local Young's moduli of the hydrogels. The heterogeneity of stiffness increased as a function of GNR concentration. The average Young's moduli for indentation depths of 3–4 μm (Fig. 3F and Supplementary Fig. S3) confirmed a significant increase in elastic moduli of GelMA-GNR hybrid constructs up to 1.3 kPa with 1 mg/mL GNRs in comparison to 450 Pa for pure GelMA. The Young's modulus for pure GelMA construct (150 μm thickness, 6 s UV exposure), quantified herein, relatively correlated to similar studies for a 1 mm thick hydrogel with 60 s UV exposure [54,66]. The improved mechanical stiffness of hybrid hydrogels can be attributed to the increased structural integrity of the matrix caused by electrostatic interaction between positively charged GNRs [43,61] and the negatively charged amine groups [54] of GelMA backbone. Also, GNRs are envisioned to act as reinforcing fillers and thus inducing enhanced mechanical properties [67]. Despite the fact that incorporation of GNRs improved mechanical stiffness of pure GelMA hydrogel up to 1.3 kPa, this value was still considerably lower than the stiffness of the native human myocardium during contraction cycle [68]. However, cardiac patches [8,25,26] with similar Young's moduli have demonstrated the suitability of these scaffolds, in terms of mechanical robustness, to accommodate cultured cardiomyocytes contractile forces.

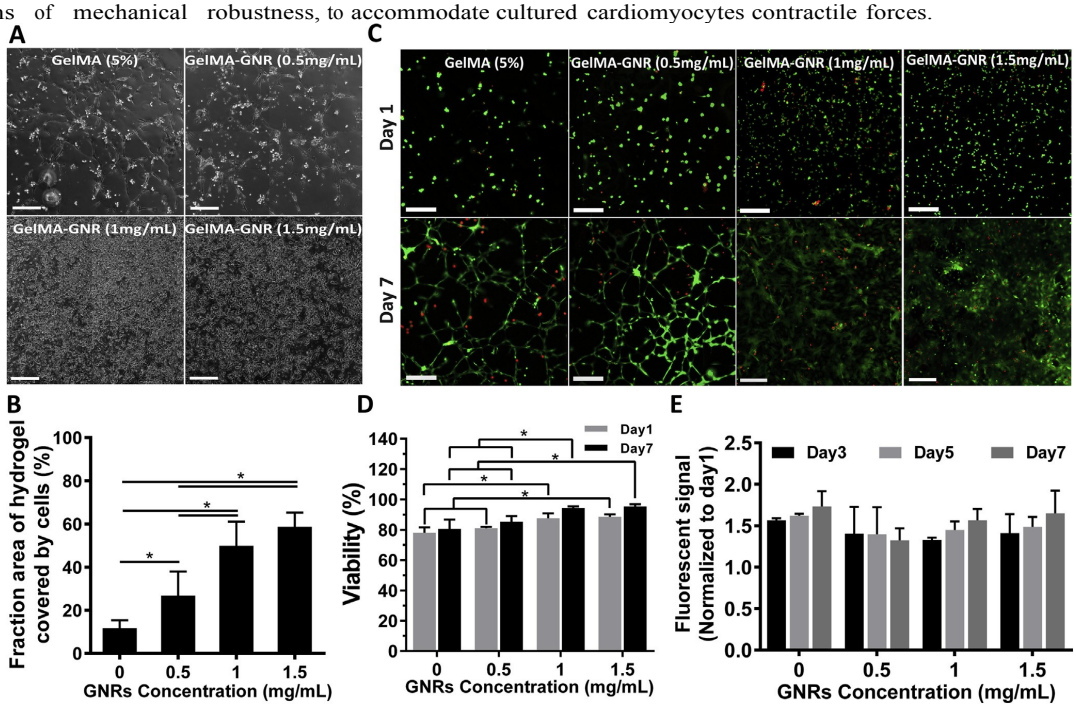

Fig. 4. Cardiomyocytes retention, survival, and metabolic activity. A) Phase-contrast images and B) fraction area of hydrogels covered by cardiomyocytes one day after cell seeding within all hybrid and pure hydrogels demonstrating more uniform and packed cell adhesion profile and significantly higher cell retention on GelMA-GNR as compared to pure GelMA ($^{*}p < 0.05$). C) Representative fluorescent images of live (green) and dead (red) cells and D) quantified cellular viability at day 1 and 7 of culture confirming high level of cell survival over the entire duration of culture ($^{*}p < 0.05$). E) Normalized Alamar Blue fluorescent signal depicting increased cellular metabolic activity at day 3, 5, and 7 of culture. All scale bars represent 250 μm. (For interpretation of the references to color in this figure legend, the reader is referred to the web version of this article.)

Previous studies have shown that due to the presence of MMP- sensitive moieties, GelMA hydrogel degrades in biological environ- ment mainly because of the action of collagenase enzyme [54]. Consistently, many studies in the literature have investigated the fate of other conductive nanomaterials (e.g. CNTs) embedded within hydrogel constructs in vivo [28]. The findings of these works have clearly confirmed that the CNTs remained within the close proximity of the cells and further facilitated cell-cell coupling [28,32]. Therefore, GelMA-GNR hybrid hydrogels are envisioned to degrade upon implantation. However extended in vivo study is required to assess the fate of GNRs upon degradation of the matrix. In vivo studies will be the subject of our future work.

3.2. Cardiomyocytes retention, survival, and metabolic activity

To evaluate the capability of the nanoengineered hydrogel constructs to support cell adhesion and spreading, the fraction area of the construct covered by seeded cardiomyocytes (day 1), was quantified as an indicator

for cell retention. The phase-contrast images on day 1 (Fig. 4A) demonstrated higher number, more packed and homogeneous distribution of adhered cardiomyocytes on GelMA-GNR hybrid hydrogels contrary to discrete and agglom- erated cell adhesion patterns on pure GelMA hydrogel. Further- more, a significant increase in cell retention (Fig. 4B) was observed as a function of GNR concentration; from 11 ± 3% for pure GelMA to 26 ± 11%, 49 ± 11%, and 58 ± 6% for 0.5, 1, and 1.5 mg/mL GelMA-GNR hybrid hydrogels respectively. This major dissimilar- ity between cell adhesion affinity of GelMA and GelMA-GNR hydrogels can be attributed to the increased stiffness and the pres- ence of GNRs providing cell anchoring points within the hydrogel constructs. To further confirm that the presence of GNRs was the main driver for higher cellular adhesion and retention, we pre- pared control hydrogel substrates using 20% GelMA with compara- ble stiffness to GelMA-GNR (1 and 1.5 mg/ml) hybrid constructs (Supplementary Fig. S4A and B). As expected, cellular retention was significantly lower on 20% GelMA hydrogel as compared to GelMA-GNR hybrid constructs with 1 and 1.5 mg/ml concentra- tions of GNRs (Supplementary Fig. S4C and D). These findings clearly demonstrate that GNRs embedded within GelMA hydrogel not only improved the stiffness of the constructs, but also pre- sented higher cell adhesion moieties thereby promoting overall cellular retention, specifically at the initial points of culture. Such properties make GelMA-GNR hybrid hydrogels as superior matri- ces due to suitable cellular adhesion cites [69,70], stiffness as well as electrical conductivity in comparison to previously reported gold-impregnated scaffolds for cardiac tissue engineering. For instance, Dvir et al. [26] incorporated gold nanowires within algi- nate hydrogel, which may not provide sufficient adhesion points to promote cell retention. In the study by You et al. [51], gold nanoparticles were embedded within thiol-HEMA/HEMA scaffolds. However, due to the cell-repellant nature of HEMA [55], the devel- oped constructs had to be treated with fibronectin [71] to increase cell adhesion prior to cell seeding.

Next, cell viability studies were performed at day 1 and 7 of the culture in order to provide a comprehensive (from seeding to the end culture period) investigation on cardiomyocytes survival

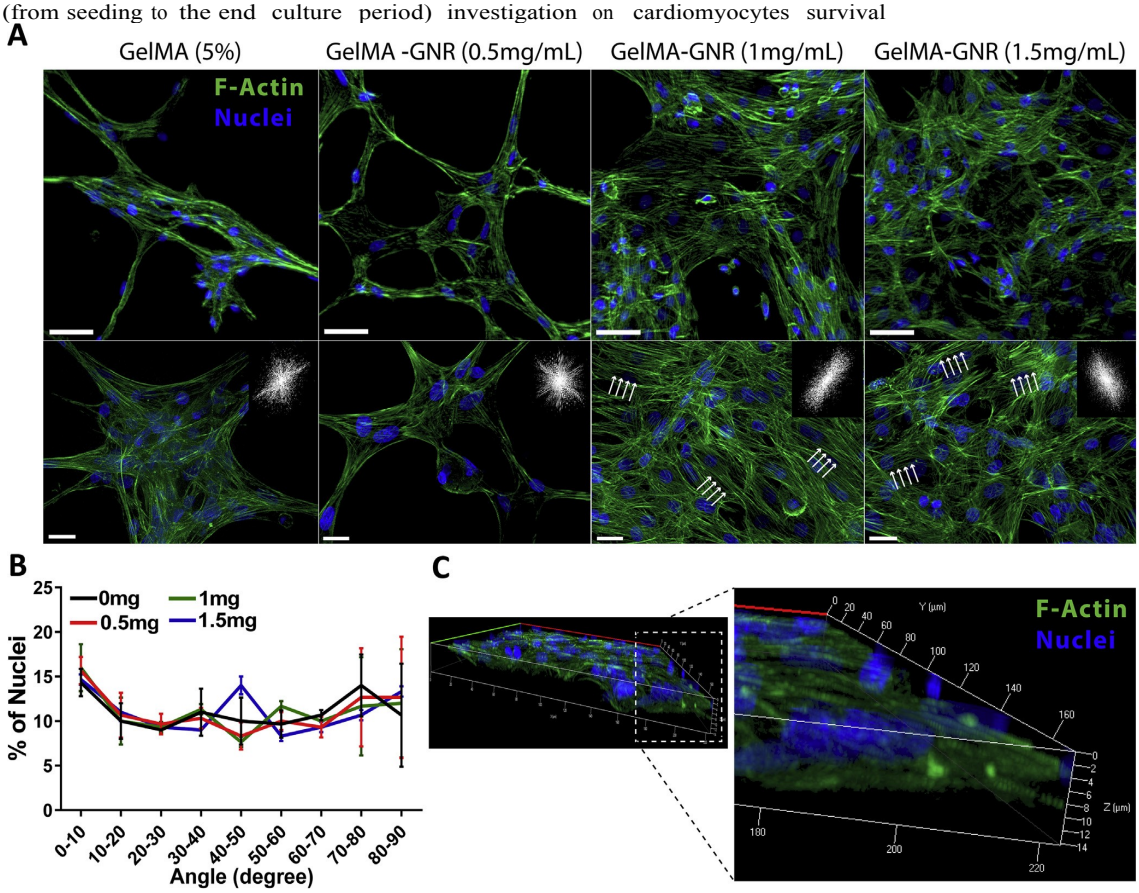

Fig. 5. F-actin cytoskeleton organization and nuclei alignment of cardiomyocytes. A) Z-stack (top-view) fluorescent images of F-actin stained (green) at day 7 of the culture for pure GelMA and all hybrid GelMA-GNR hydrogels illustrating highly organized, packed, and uniform distribution, as well as local alignment (with arrows) of fibers. DAPI (blue) represents stained nuclei. FFT images (top right insets) demonstrating local alignment of F-actin fibers on hybrid GelMA-GNR constructs, in contrast with randomly distributed filaments in pure GelMA hydrogel (top-row scale bars represent 50 μm; bottom-row scale bars represent 20 μm). B) Cardiomyocytes' nuclei alignment distribution from 0 to 90 degrees representing lack of significant alignment of cells' nuclei within all GelMA-GNR hybrid and pure GelMA hydrogels. C) A 3D Z-stack fluorescent image, showing the formation of highly packed and intact cardiac tissue layer on top of hybrid

hydrogels (1.5 mg/mL). (For interpretation of the references to color in this figure legend, the reader is referred to the web version of this article.)

seeded on the fabricated hybrid hydrogels (Fig. 4C and D). Fig. 4D illustrates that cardiomyocytes viability increased significantly from 78 ± 3% in pure GelMA hydrogel to 87 ± 3% in 1 mg/mL and 88 ± 1% in 1.5 mg/mL GelMA-GNR hybrid hydrogels at day 1. Sim- ilarly, viability values at day 7 within pure GelMA and hybrid hydrogels confirmed that the seeded cardiomyocytes maintained a considerably high level of survival. In addition, the statistically significant lower cellular viability within 20% GelMA control hydrogel (Supplementary Fig. S4E and F) as compared to hybrid GelMA-GNR constructs, further strengthens the argument that the presence of GNRs along with enhanced stiffness, enhanced cell retention and eventually led to higher viability of seeded cells.

We further determined the metabolic activity of the cultured cells using Alamar Blue assay at day 3, 5, and 7 of the culture (Fig. 4E) (normalized to day 1). Across all pure and GelMA-GNR hybrid hydrogels, no statistically significant cellular metabolic activity was observed. However, cultured cells exhibited a gradual increase in metabolic activity within each construct at day 5 and 7 as compared to day 3 of culture which can be due to presence of small population of cardiac fibroblasts during isolation of car- diomyocytes [25].

Overall, GelMA-GNR hybrid hydrogels supported cardiomy- ocytes culture and exhibited no major risk of cytotoxicity. Our find- ings are consistent with previous studies by Connor et al. [46] which demonstrated that CTAB-capped gold nanoparticle, washed 2 times with DI water before use, did not result in acute toxicity on the leukemia cells. Consistently, Shukla et al. [48] reported similar findings for exposing gold nanoparticles to the macrophages. In future studies, our group will further perform experiments to investigate the fate of GNRs using in vivo MI model.

3.3. Actin cytoskeleton organization and formation of cardiac tissue layer

In order to investigate the F-actin cytoskeleton organization of the cardiomyocytes and the formation of interconnected cell net- work (tissue layer), the cells were stained for F-actin fibers at day 7 of the culture. The expression of F-actin fibers enhanced on GelMA-GNR hydrogels with 1 and 1.5 mg/mL of GNR concentrations, in contrast to pure GelMA and hybrid hydrogel with 0.5 mg/mL of GNR concentration (Fig. 5A). The improved expres- sion of F-actin fibers can be directly correlated to the enhanced cell

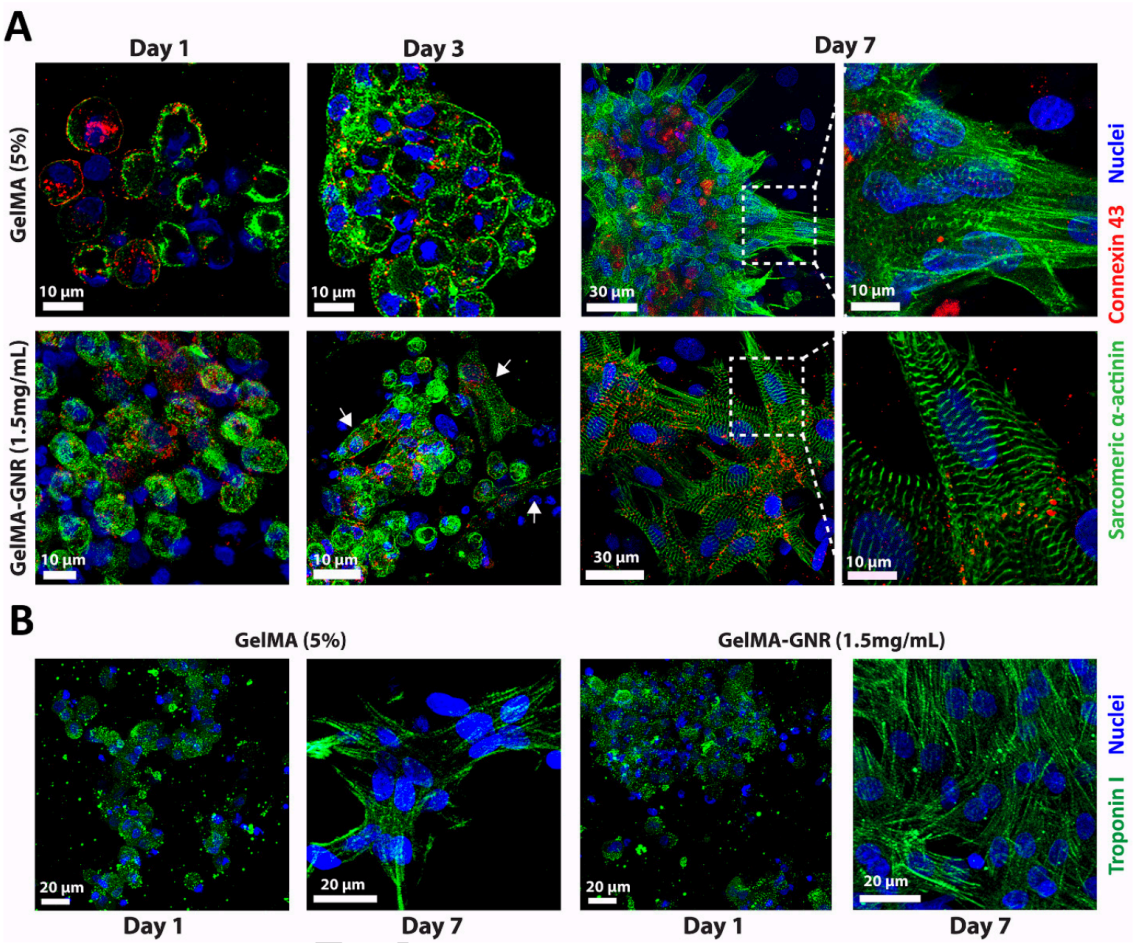

Fig. 6. Z-stack immunostained images of cardiac-specific markers. A) Representative immunostained images showing the expression of sarcomeric a-actinin (green) and Cx43 (red) on day 1, 3 (arrows showing sarcomeres formation), and 7 of the culture. B) Immunostained images of troponin I (green) on day 1 and 7 of culture for GelMA and 1.5 mg/mL GelMA-GNR hybrid hydrogels. (For interpretation of the references to color in this figure legend, the reader is referred to the web version of this article.)

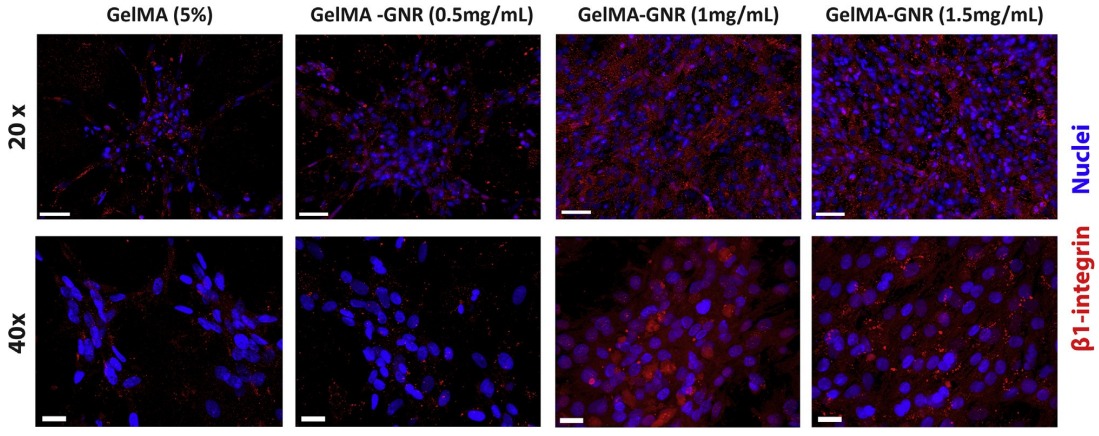

Fig. 7. Immunostained Z-tack images (20x and 40x) of integrin-b1 for pure GelMA and GelMA-GNR hybrid hydrogels (0.5, 1, and 1.5 mg/mL) on day 7, showing the presence and distribution of cell adhesion affinities. Scale bars represent 50 µm for 20x and 20 µm for 40x figure panel.

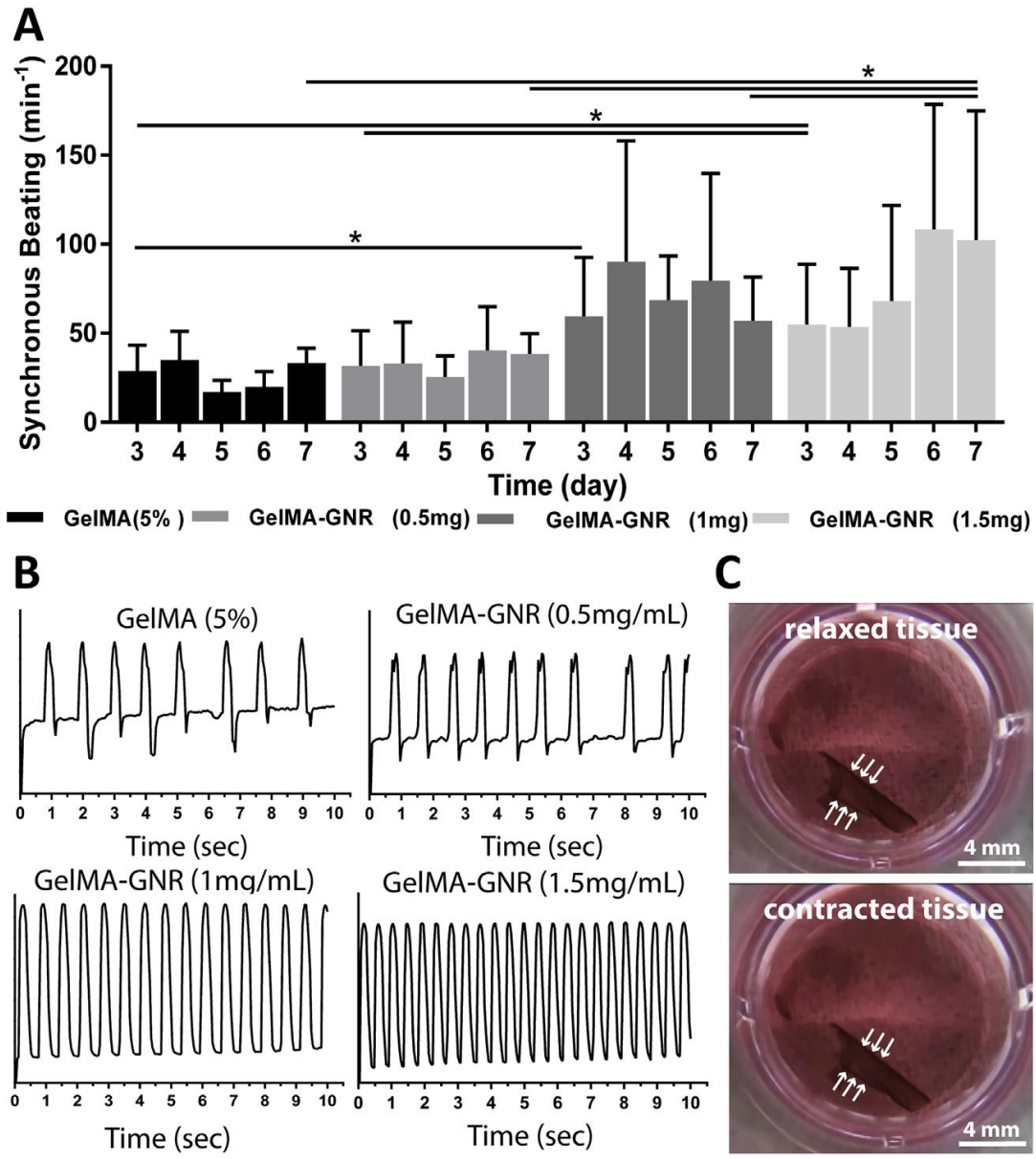

Fig. 8. Beating behavior of hydrogel constructs. A) Synchronous beating frequency (beats per minute (BPM)) of cardiomyocytes from day 3 to day 7 of culture depicting robust and stable beating behavior in GelMA-GNR hybrids. Significantly higher number of beating frequency were observed between highly GNR concentrated hybrids compared to 0.5 mg/mL GelMA-GNR and pure GelMA hydrogels ($^{*}p < 0.05$). B) Representative beating signal graphs represent more uniform contraction behavior within 1 and 1.5 mg/mL GelMA-GNR, in contrast to 0.5 mg/mL hybrid and pristine GelMA hydrogels. C) Photographs of a detached centimeter scale hybrid hydrogel tissue constructs (1.5 mg/mL GelMA-GNR) displaying contraction (white arrows) of the whole hydrogel construct by seeded cardiomyocytes.

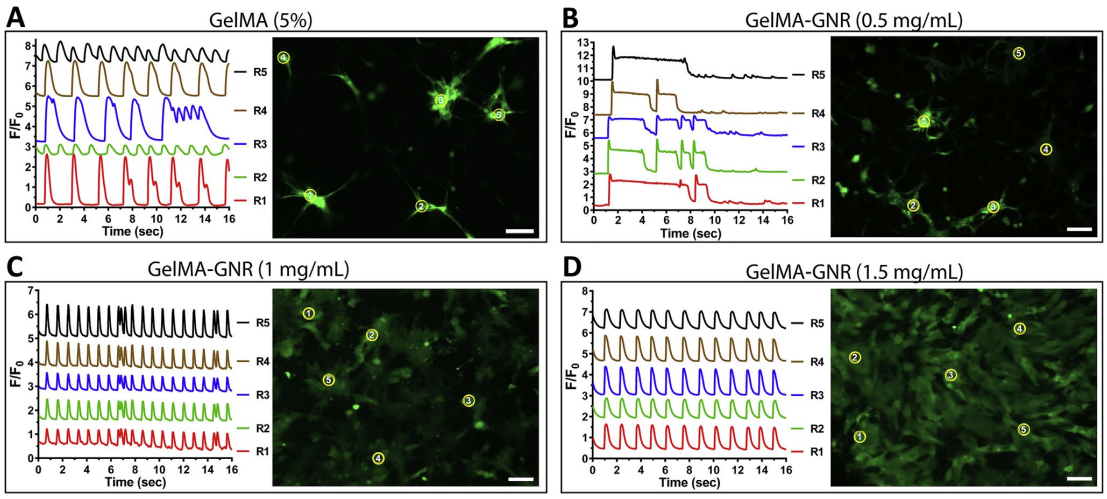

Fig. 9. Calcium transient and extracted related frequency signals of intracellular change in concentration of Ca^{2+} within cultured cardiomyocytes for A) pure GelMA (5%), B) GelMA-GNR (0.5 mg/mL), C) GelMA-GNR (1 mg/mL), and D) GelMA-GNR (1.5 mg/mL). R1 to R5 represent regions 1–5 and scale bars depict 100 μm.

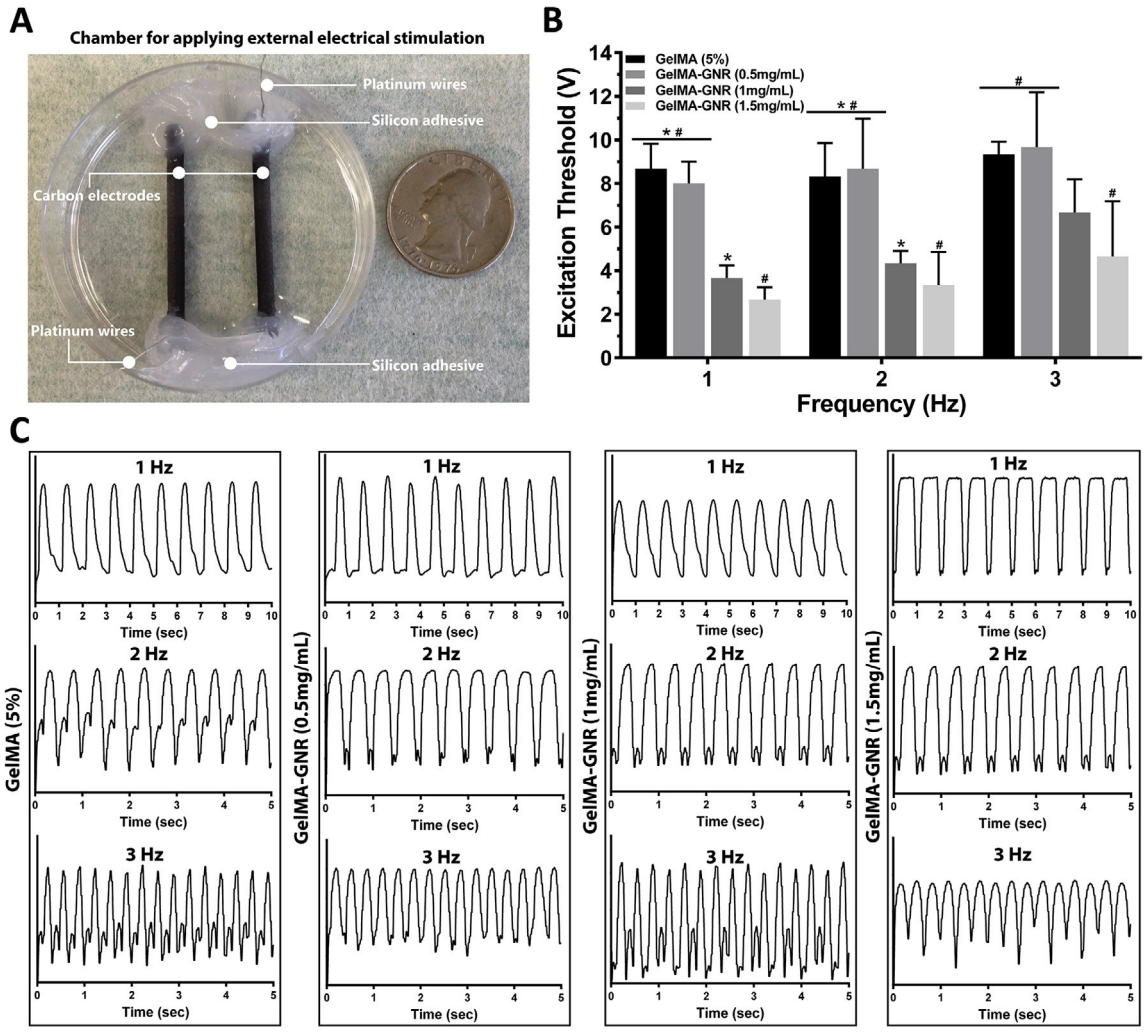

Fig. 10. A) Fabricated chamber for external electrical stimulation photograph. B) Excitation thresholds at different frequencies (1, 2, and 3 Hz) for pure and GNR-embedded hydrogels representing significantly lower ($^{*, \#}p < 0.05$) voltage for 1 and 1.5 mg/mL GelMA-GNR, in

contrast to 0.5 mg/mL hybrid and GelMA hydrogels. C) Beating frequency signals for all types of hydrogels at different applied frequencies.

retention (Fig. 4B) on hybrid hydrogels as also shown by phase contrast images (Fig. 4A). Furthermore at high concentration of GNRs, specifically at 1.0 mg/mL and 1.5 mg/mL, improved local alignment of F-actin fibers (Fig. 5A; white arrows) was observed. This can also be observed from Fast Fourier Transform (FFT) analysis of F-actin images which depicted enhanced local alignment of fibers within GelMA-GNR hybrid at high concentrations of GNRs as compared to pure GelMA hydrogel (Fig. 5A insets). Such induced local alignment at high concentration of GNRs is significant, since no global alignment (Fig. 5B) was observed due to absence of any micropatterned feature on the hydrogel constructs [19].

The elongated and highly packed cells within the hybrid GelMA-GNR hydrogels led to the formation of a uniform and inter- connected tissue layer. Particularly, the Z-stack fluorescent (Fig. 5C) and phase contrast images (Supplementary Fig. S5) con- firmed the formation of an intact tissue layer on top of hybrid hydrogel constructs over 7 days of the culture. Overall, the improved cellular spreading, induced by the bioactivity of gelatin structure and mediated cell adhesion by incorporation of GNRs, led to the formation of an integrated cardiac tissue layer.

3.4. Cardiac-specific markers and cell-matrix interaction

Cardiac-specific markers including sarcomeric a-actinin, Cx43, and troponin I were immunostained to assess the phenotype of the cultured cardiomyocytes over the culture period. While sar- comeric a-actinin and troponin I are the two specific proteins, involved in the actin-myosin contraction complex, Cx43 is a well-known gap junction protein responsible for synchronous con- traction of the cells [19,51,72,73]. As shown in Fig. 6 and Supplementary Fig. S6, at day 1 of culture, the cells mainly adopted a round morphology without intact formation of sarcomeres and tro- ponin I within all the hydrogel constructs. However, the immunos- tained images on day 3 displayed the formation of a few sarcomere structures specifically in case of GelMA-GNR hydrogels with 1 and 1.5 mg/mL GNRs (white arrows). Eventually on day 7, uniform and highly organized sarcomeric a-actinin structures were evident across hybrid hydrogels (e.g. 1.0 and 1.5 mg/mL) in contrast to pure GelMA constructs. Similar observations were made in troponin I immunostained images, demonstrating extended architecture as a marker of contractile machinery within hybrid hydrogels with high concentrations of GNRs. Thus, the assembled tissue on GelMA-GNR hybrids, with high concentration of impregnated GNRs, exhibited more organized myofilament assembly, consistent to previously reported studies [25,26,28,33]. Our immunostaining results for Cx43 gap junction proteins also demonstrated a similar trend. While on day 1, Cx43 expression was agglomerated and undispersed across all the groups, by day 7, a more homogenous distribution of Cx43 was observed, specifically on GelMA-GNR hybrid hydrogels (1 and 1.5 mg/mL). Therefore, GelMA-GNR hybrid hydrogels with high concentrations of GNRs demonstrated improved cell-cell coupling with mature contractile machinery as compared to pure GelMA hydrogel.

Further, to analyze the cell-matrix interaction on the synthe- sized hydrogel, samples were stained with Integrin-b1 which is a transmembrane protein and plays a significant role in mechan- otransduction [28]. Fig. 7 shows immunostained images of the cells at different magnifications (20x and 40x) on day 7 of the culture, confirming the abundance of integrin-b1 and consequently cell adhesion cites with higher concentrations of GNRs. The expression of integrin-b1 further confirmed our observations on improved cellular retention (Fig. 4B) and the abundance and organization of F-actin fibers (Fig. 5A) on hybrid constructs with higher concen- trations of GNRs (1 and 1.5 mg/mL).

Overall, seeded cardiomyocytes on GelMA-GNR hybrids, specif- ically with 1 and 1.5 mg/mL concentrations of GNRs, demonstrated improved tissue structure as compared to pure GelMA hydrogel. To further investigate the influence of conductive GelMA-GNR hydro- gels on tissue-level functionalities, we analyzed the spontaneous beating and intracellular Ca^{2+} transient of the cardiomyocytes as a function of time.

3.5. Beating behavior of cardiomyocytes

To assess tissue-level functionalities, beating behavior (repre- sented as an average number of synchronous beats per minute (BPM)) of cardiomyocytes seeded on hydrogel constructs was fur- ther analyzed through real-time video microcopy from day 1 to day 7 of the culture. Cardiomyocytes started beating in a sponta- neous and synchronous manner, as they created an interconnected cell network as a function of GNRs concentration on day 3. Fig. 8A displays average number of BPM for pure and hybrid hydrogel con- structs. As can be observed, hybrid tissue constructs with 1 and 1.5 mg/mL of GNRs exhibited a significantly higher beating fre- quency (BPM) as compared to pure GelMA hydrogel at day 3. By day 7, cardiomyocytes within 1.5 mg/mL GelMA-GNR hybrid hydrogels demonstrated notably increased beating frequency (102 ± 72 BPM), as compared to 1 mg/mL (56 ± 24 BPM), 0.5 mg/ mL (38 ± 11 BPM) GelMA-GNR hybrids, and pure GelMA (33 ± 9 BPM) hydrogel. Furthermore, representative beating signals (Fig. 8B) and real time movies (Supplementary movies M1, M2, M3, and M4) illustrated more synchronous, stable, and robust beating behavior within GelMA-GNR hybrids (1 and 1.5 mg/mL) in comparison to pure GelMA and hybrid hydrogel with 0.5 mg/ mL GNR concentration. Such beating behavior can be attributed to the enhanced electrophysiological characteristics

and improved cell-cell coupling of the formed tissues on nanoengineered hydro- gels. Additionally, to examine the capability of the formed cardiac tissue layer to contract the hydrogel construct, we detached 2 samples of hybrid hydrogels (1 and 1.5 mg/mL GelMA-GNR) at day 5 of culture from the TMSPMA glass slide and suspended the tissue in the culture media (Fig. 8C). Interestingly, we were able to success- fully create a suspended beating tissue sheet (centimeter scale) (Supplementary movies M5 and M6). These observations further confirmed that the formed cardiac tissue layers, on top of GelMA-GNR hydrogels, were highly functional to bend the 150 μm thick construct.

Although similar observations for highly stiff CNT-embedded GelMA hydrogels were reported by Shin et al. [25], cytotoxicity [34–37] and high UV absorption of CNTs [30] remain as major con- cerns for cardiac tissue engineering applications. Specifically, high UV absorbance of CNTs interferes with photoinitiatior excitation, and consequently influences hydrogel crosslinking process [25,30] and the subsequent formation of 3D tissue constructs (beyond 150 μm thickness). This is particularly crucial in case of 3D cellular encapsulation within hydrogel constructs, where the cells have to be exposed to extended duration of UV. On the other hand, GNRs with low UV absorption (Fig. 1B and C) and minimized cytotoxicity [46,47] enabled us to fabricate relatively thicker cardiac patches (e.g. 150 μm).

3.6. Intracellular Ca2+ transient

In order to investigate calcium signaling (puffs) within seeded cardiomyocytes, calcium ions transient (Ca^{2+}) analysis was per- formed. First, tissue constructs were loaded with the dye, followed by capturing videos from different region of 1 mm^2 of GelMA and GelMA-GNR hybrid hydrogels. Five different sites within each region were selected and the increase in concentration of Ca^{2+} ions was represented as fluorescent intensity of dye (F) divided by the background intensity (F_0). As represented in the Fig. 9 and Supplementary movie M7, intracellular Ca^{2+} puffs occurred at different frequencies across all 5 considered spots on pure GelMA and GelMA-GNR (0.5 mg/mL) hydrogels. However, cardiomyocytes cul- tured on GelMA-GNR hydrogels with 1 and 1.5 mg/mL of GNRs exhibited synchronized calcium spikes within all considered spots. Such calcium transient profile further confirmed enhanced cell-cell communication between cardiomyocytes cultured on electrically conductive hydrogels. Specifically, GNRs embedded in GelMA hydrogel at high concentration bridged the electrically insulated structure of the matrix and further played a role to facilitated sig- nal propagation between the cells.

3.7. Impact of external electrical stimulation

A custom made electrical stimulation set up, according to the previous protocol [60] (Fig. 10A), was utilized to evaluate the capa- bility of the hydrogel constructs for accommodation of external electrical stimuli. Excitation threshold, which is defined as the minimum required voltage to induce synchronous contractions of cardiomyocytes, was measured for three different frequencies (1, 2, and 3 Hz). Notably a lower excitation threshold (Fig. 10B) for 1 and 1.5 mg/mL GelMA-GNR hydrogels was observed as compared to 0 and 0.5 mg/mL GelMA-GNR hydrogel constructs at 1 and 2 Hz. In addition, at high frequency (3 Hz), only hybrid hydrogels with the highest amount of GNR concentration (1.5 mg/mL) exhib- ited significant difference in terms of excitation threshold. This decrease in excitation threshold can be attributed to the relatively lower impedance of GelMA-GNR hydrogels in comparison to pure GelMA hydrogel. Despite significant decrease in excitation thresh- old, all pure and hybrid hydrogels were enabled to generate similar beating pattern related to the applied frequencies (Fig. 10C and Supplementary movie M8–M11). Thus, it can be envisioned that GNRs incorporated within the tissue constructs could promote integration (electrically) with native myocardium as compared to pure GelMA hydrogel. Investigation of the integration of the nano- engineered constructs with the host myocardium in vivo, is the subject of our future studies.

4. Conclusion

In this study, we developed GNR-embedded GelMA hybrid hydrogels as an advanced biomaterial to develop functional cardiac tissue constructs for myocardial regeneration and repair. GNRs with the average aspect ratio of 3.15 (16 ± 2 nm width and 53 ± 4 nm length) were synthesized and homogeneously incorpo- rated with GelMA prepolymer solution, followed by UV crosslink- ing to fabricate hybrid GelMA-GNR hydrogel constructs (150 μm thick). The GelMA-GNR hybrids exhibited electrically and mechan- ically enhanced material characteristics as compared to pure GelMA hydrogel. Primarily, the GelMA-GNR hybrid hydrogels induced high cell retention and improved cytoskeleton organiza- tion. The highly mediated cell-matrix interactions, through integrin-b1, along with enhanced expression of cardiac specific markers (troponin I, sarcomeric a-actinin) resulted in the formation of interconnected cardiac tissue layers. Our further studies, confirmed that the stiffness of the matrix is not the only factor, and in fact GNRs are the major driver for higher cell adhesion and retention on the matrix. Due to the high affinity of the cells on the hybrid hydrogels, the formed tissues represented an orga- nized, packed, and uniform architecture while maintained a high level

of cellular viability and metabolic activity. Secondly, the con- ductive constructs facilitated cell-cell signaling and electrical sig- nal propagation, as confirmed through the expression of Cx43 gap junctions and synchronized calcium signaling amongst car- diomyocytes exposed to high concentration of GNRs (1.5 mg/mL). These enhancements eventually gave rise to higher functionalities of cardiac tissue constructs and specifically improved tissue con- tractility with lower excitation threshold. Notably, GelMA-GNR hybrids (1 and 1.5 mg/mL) illustrated more robust and syn- chronous beating behavior as compared to the pure GelMA hydro- gel. In conclusion, our findings confirmed that the nanoengineered GelMA-GNR hybrid hydrogels, with excellent characteristics, pro- vide a suitable matrices for specific applications in cardiac tissue engineering.

Acknowledgment

The monoclonal antibody, TI-4, developed by Stefano Schiaffino was purchased from the Developmental studies Hybridoma Bank, created by NICHD of the NIH and maintained at The University of Iowa, Department of Biology, Iowa City, IA 52242. We gratefully acknowledge the use of facilities with the LeRoy Eyring Center for Solid State Science at Arizona State University. We acknowl- edge N. Chamele for helping for impedance analyzing, and Bryant Doss for the development of the AFM analysis programs. This work was partially supported by National Institute of Health (NIH) grants HL107539 and U54CA143862 to Robert Ros.

Appendix A. Supplementary data

Supplementary data associated with this article can be found, in the online version, at http://dx.doi.org/10.1016/j.actbio.2016.05.027.

References

[1] D. Mozaffarian, E.J. Benjamin, A.S. Go, D.K. Arnett, M.J. Blaha, M. Cushman, S. de Ferranti, J.P. Despres, H.J. Fullerton, V.J. Howard, M.D. Huffman, S.E. Judd, B.M. Kissela, D.T. Lackland, J.H. Lichtman, L.D. Lisabeth, S.M. Liu, R.H. Mackey, D.B. Matchar, D.K. McGuire, E.R. Mohler, C.S. Moy, P. Muntner, M.E. Mussolino, K. Nasir, R.W. Neumar, G. Nichol, L. Palaniappan, D.K. Pandey, M.J. Reeves, C.J. Rodriguez, P.D. Sorlie, J. Stein, A. Towfighi, T.N. Turan, S.S. Virani, J.Z. Willey, D. Woo, R.W. Yeh, M.B. Turner, A.H.A.S. Comm, S.S. Subcomm, Heart disease and stroke statistics-2015 update a report from the American Heart Association, Circulation 131 (2015) E29–E322.
[2] D. Orlic, J. Kajstura, S. Chimenti, I. Jakoniuk, S.M. Anderson, B.S. Li, J. Pickel, R. McKay, B. Nadal-Ginard, D.M. Bodine, A. Leri, P. Anversa, Bone marrow cells regenerate infarcted myocardium, Nature 410 (2001) 701–705.
[3] A.R. Williams, K.E. Hatzistergos, B. Addicott, F. McCall, D. Carvalho, V. Suncion, A.R. Morales, J. Da Silva, M.A. Sussman, A.W. Heldman, J.M. Hare, Enhanced effect of combining human cardiac stem cells and bone marrow mesenchymal stem cells to reduce infarct size and to restore cardiac function after myocardial infarction, Circulation 127 (2013) 213–223.
[4] G.C. Engelmayr, M.Y. Cheng, C.J. Bettinger, J.T. Borenstein, R. Langer, L.E. Freed, Accordion-like honeycombs for tissue engineering of cardiac anisotropy, Nat. Mater. 7 (2008) 1003–1010.
[5] W.H. Zimmermann, I. Melnychenko, G. Wasmeier, M. Didie, H. Naito, U. Nixdorff, A. Hess, L. Budinsky, K. Brune, B. Michaelis, S. Dhein, A. Schwoerer, H. Ehmke, T. Eschenhagen, Engineered heart tissue grafts improve systolic and diastolic function in infarcted rat hearts, Nat. Med. 12 (2006) 452–458.
[6] J. Leor, S. Aboulafia-Etzion, A. Dar, L. Shapiro, I.M. Barbash, A. Battler, Y. Granot, S. Cohen, Bioengineered cardiac grafts – a new approach to repair the infarcted myocardium?, Circulation 102 (2000) 56–61
[7] N. Annabi, K. Tsang, S.M. Mithieux, M. Nikkhah, A. Ameri, A. Khademhosseini, A.S. Weiss, Highly elastic micropatterned hydrogel for engineering functional cardiac tissue, Adv. Funct. Mater. 23 (2013) 4950–4959.
[8] T. Dvir, A. Kedem, E. Ruvinov, O. Levy, I. Freeman, N. Landa, R. Holbova, M.S. Feinberg, S. Dror, Y. Etzion, J. Leor, S. Cohen, Prevascularization of cardiac patch on the omentum improves its therapeutic outcome, Proc. Natl. Acad. Sci. USA 106 (2009) 14990–14995.
[9] M. Kharaziha, M. Nikkhah, S.R. Shin, N. Annabi, N. Masoumi, A.K. Gaharwar, G. Camci-Unal, A. Khademhosseini, PGS: gelatin nanofibrous scaffolds with tunable mechanical and structural properties for engineering cardiac tissues, Biomaterials 34 (2013) 6355–6366.
[10] A. Teplenin, A. Krasheninnikova, N. Agladze, K. Sidoruk, O. Agapova, I. Agapov, V. Bogush, K. Agladze, Functional analysis of the engineered cardiac tissue grown on recombinant spidroin fiber meshes, PLoS One 10 (2015).
[11] M. Shin, O. Ishii, T. Sueda, J.P. Vacanti, Contractile cardiac grafts using a novel nanofibrous mesh, Biomaterials 25 (2004) 3717–3723.
[12] H. Masumoto, T. Ikuno, M. Takeda, H. Fukushima, A. Marui, S. Katayama, T. Shimizu, T. Ikeda, T. Okano, R. Sakata, J.K. Yamashita, Human iPS cell- engineered cardiac tissue sheets with cardiomyocytes and vascular cells for cardiac regeneration, Sci. Rep. UK 4 (2014).
[13] S. Masuda, T. Shimizu, M. Yamato, T. Okano, Cell sheet engineering for heart tissue repair, Adv. Drug Deliv. Rev. 60 (2008) 277–285.
[14] K. Matsuura, S. Masuda, Y. Haraguchi, N. Yasuda, T. Shimizu, N. Hagiwara, P.W. Zandstra, T. Okano, Creation of mouse embryonic stem cell-derived cardiac cell sheets, Biomaterials 32 (2011) 7355–7362.
[15] G. Camci-Unal, N. Annabi, M.R. Dokmeci, R. Liao, A. Khademhosseini, Hydrogels for cardiac tissue engineering, NPG Asia Mater. 6 (2014).
[16] A. Paul, A. Hasan, H. Al Kindi, A.K. Gaharwar, V.T.S. Rao, M. Nikkhah, S.R. Shin, D. Krafft, M.R. Dokmeci, D. Shum-Tim, A. Khademhosseini, Injectable graphene oxide/hydrogel-based angiogenic gene delivery system for vasculogenesis and cardiac repair, ACS Nano 8 (2014) 8050–8062.
[17] M. Kharaziha, A. Memic, D.A. Brafman, M. Nikkah, Nano-enabled approached for stem cell-based cardiac tissue engineering, Adv. Healthc. Mater. (2016), http://dx.doi.org/10.1002/adhm.201600088.
[18] S. Pedron, S. van Lierop, P. Horstman, R. Penterman, D.J. Broer, E. Peeters, Stimuli responsive delivery vehicles for cardiac microtissue transplantation, Adv. Funct. Mater. 21 (2011) 1624–1630.
[19] H. Saini, A. Navaei, A. Van Putten, M. Nikkhah, 3D cardiac microtissues encapsulated with the co-culture of cardiomyocytes and cardiac fibroblasts, Adv. Healthc. Mater. 4 (2015) 1961–1971.
[20] M.L. McCain, A. Agarwal, H.W. Nesmith, A.P. Nesmith, K.K. Parker, Micromolded gelatin hydrogels for extended culture of engineered cardiac tissues, Biomaterials 35 (2014) 5462–5471.
[21] R.K. Li, Z.Q. Jia, R.D. Weisel, D.A.G. Mickle, A. Choi, T.M. Yau, Survival and function of bioengineered cardiac grafts, Circulation 100 (1999) 63–69.
[22] S. Khalil, W. Sun, Bioprinting endothelial cells with alginate for 3D tissue constructs, J. Biomech. Eng. 131 (2009).
[23] M. Radisic, H. Park, H. Shing, T. Consi, F.J. Schoen, R. Langer, L.E. Freed, G. Vunjak-Novakovic, Functional assembly of engineered myocardium by electrical stimulation of cardiac myocytes cultured on scaffolds, Proc. Natl. Acad. Sci. USA 101 (2004) 18129–18134.
[24] A. Navaei, D. Truong, J. Heffernan, J. Cutts, D. Brafman, R.W. Sirianni, B. Vernon, M. Nikkhah, PNIPAAm-based biohybrid injectable hydrogel for cardiac tissue engineering, Acta Biomater. 32 (2016) 10–23.
[25] S.R. Shin, S.M. Jung, M. Zalabany, K. Kim, P. Zorlutuna, S.B. Kim, M. Nikkhah, M. Khabiry, M. Azize, J. Kong, K.T. Wan, T. Palacios, M.R. Dokmeci, H. Bae, X.W. Tang, A. Khademhosseini, Carbon-nanotube-embedded hydrogel sheets for engineering cardiac constructs and bioactuators, ACS Nano 7 (2013) 2369–2380.
[26] T. Dvir, B.P. Timko, M.D. Brigham, S.R. Naik, S.S. Karajanagi, O. Levy, H.W. Jin, K. K. Parker, R. Langer, D.S. Kohane, Nanowired three-dimensional cardiac patches, Nat. Nanotechnol. 6 (2011) 720–725.
[27] B.Z. Tian, J. Liu, T. Dvir, L.H. Jin, J.H. Tsui, Q. Qing, Z.G. Suo, R. Langer, D.S. Kohane, C.M. Lieber, Macroporous nanowire nanoelectronic scaffolds for synthetic tissues, Nat. Mater. 11 (2012) 986–994.

[28] J. Zhou, J. Chen, H.Y. Sun, X.Z. Qiu, Y.C. Mou, Z.Q. Liu, Y.W. Zhao, X. Li, Y. Han, C. M. Duan, R.Y. Tang, C.L. Wang, W. Zhong, J. Liu, Y. Luo, M. Xing, C.Y. Wang, Engineering the heart: evaluation of conductive nanomaterials for improving implant integration and cardiac function, Sci. Rep. 4 (2014).
[29] B. Liau, D.H. Zhang, N. Bursac, Functional cardiac tissue engineering, Regen. Med. 7 (2012) 187–206.
[30] S.R. Shin, H. Bae, J.M. Cha, J.Y. Mun, Y.C. Chen, H. Tekin, H. Shin, S. Farshchi, M. R. Dokmeci, S. Tang, A. Khademhosseini, Carbon nanotube reinforced hybrid microgels as scaffold materials for cell encapsulation, ACS Nano 6 (2012) 362–372.
[31] S. Pok, F. Vitale, S.L. Eichmann, O.M. Benavides, M. Pasquali, J.G. Jacot, Biocompatible carbon nanotube-chitosan scaffold matching the electrical conductivity of the heart, ACS Nano 8 (2014) 9822–9832.
[32] V. Martinelli, G. Cellot, F.M. Toma, C.S. Long, J.H. Caldwell, L. Zentilin, M. Giacca, A. Turco, M. Prato, L. Ballerini, L. Mestroni, Carbon nanotubes promote growth and spontaneous electrical activity in cultured cardiac myocytes, Nano Lett. 12 (2012) 1831–1838.
[33] M. Kharaziha, S.R. Shin, M. Nikkhah, S.N. Topkaya, N. Masoumi, N. Annabi, M.R. Dokmeci, A. Khademhosseini, Tough and flexible CNT-polymeric hybrid scaffolds for engineering cardiac constructs, Biomaterials 35 (2014) 7346–7354.
[34] C.P. Firme, P.R. Bandaru, Toxicity issues in the application of carbon nanotubes to biological systems, Nanomed. Nanotechnol. 6 (2010) 245–256.
[35] H. Dumortier, When carbon nanotubes encounter the immune system: desirable and undesirable effects, Adv. Drug Deliv. Rev. 65 (2013) 2120–2126.
[36] H.F. Cui, S.K. Vashist, K. Al-Rubeaan, J.H.T. Luong, F.S. Sheu, Interfacing carbon nanotubes with living mammalian cells and cytotoxicity issues, Chem. Res. Toxicol. 23 (2010) 1131–1147.
[37] S. Jain, S.R. Singh, S. Pillai, Toxicity issues related to biomedical applications of carbon nanotubes, J. Nanomed. Nanotechnol. 3 (2012) 140.
[38] S. Vardharajula, S.Z. Ali, P.M. Tiwari, E. Eroglu, K. Vig, V.A. Dennis, S.R. Singh, Functionalized carbon nanotubes: biomedical applications, Int. J. Nanomed. 7 (2012) 5361–5374.
[39] Y.Y. Huang, E.M. Terentjev, Dispersion of carbon nanotubes: mixing, sonication, stabilization, and composite properties, Polymers 4 (2012) 275–295.
[40] K. Liu, Y. Sun, X. Lin, R. Zhou, J. Wang, S. Fan, K. Jiang, Scratch-resistant, highly conductive, and high-strength carbon nanotube-based composite yarns, ACS Nano 4 (2010) 5827–5834.
[41] C.M. Cobley, J.Y. Chen, E.C. Cho, L.V. Wang, Y.N. Xia, Gold nanostructures: a class of multifunctional materials for biomedical applications, Chem. Soc. Rev. 40 (2011) 44–56.
[42] X.M. Jiang, L.M. Wang, J. Wang, C.Y. Chen, Gold nanomaterials: preparation, chemical modification, biomedical applications and potential risk assessment, Appl. Biochem. Biotechnol. 166 (2012) 1533–1551.
[43] X.H. Huang, S. Neretina, M.A. El-Sayed, Gold nanorods: from synthesis and properties to biological and biomedical applications, Adv. Mater. 21 (2009) 4880–4910.
[44] G. Frens, Controlled nucleation for the regulation of the particle size in monodisperse gold suspensions, Nat. Phys. Sci. 241 (1973) 20–22.
[45] L. Dykman, N. Khlebtsov, Gold nanoparticles in biomedical applications: recent advances and perspectives, Chem. Soc. Rev. 41 (2012) 2256–2282.
[46] E.E. Connor, J. Mwamuka, A. Gole, C.J. Murphy, M.D. Wyatt, Gold nanoparticles are taken up by human cells but do not cause acute cytotoxicity, Small 1 (2005) 325–327.
[47] N. Khlebtsov, L. Dykman, Biodistribution and toxicity of engineered gold nanoparticles: a review of in vitro and in vivo studies, Chem. Soc. Rev. 40 (2011) 1647–1671.
[48] R. Shukla, V. Bansal, M. Chaudhary, A. Basu, R.R. Bhonde, M. Sastry, Biocompatibility of gold nanoparticles and their endocytotic fate inside the cellular compartment: a microscopic overview, Langmuir 21 (2005) 10644–10654.
[49] S. Fleischer, M. Shevach, R. Feiner, T. Dvir, Coiled fiber scaffolds embedded with gold nanoparticles improve the performance of engineered cardiac tissues, Nanoscale 6 (2014) 9410–9414.
[50] M. Shevach, B.M. Maoz, R. Feiner, A. Shapira, T. Dvir, Nanoengineering gold particle composite fibers for cardiac tissue engineering, J. Mater. Chem. B 1 (2013) 5210–5217.
[51] J.O. You, M. Rafat, G.J.C. Ye, D.T. Auguste, Nanoengineering the heart: conductive scaffolds enhance connexin 43 expression, Nano Lett. 11 (2011) 3643–3648.
[52] M. Shevach, R. Zax, A. Abrahamov, S. Fleischer, A. Shapira, T. Dvir, Omentum ECM-based hydrogel as a platform for cardiac cell delivery, Biomed. Mater. 10 (2015).
[53] A.I. Van den Bulcke, B. Bogdanov, N. De Rooze, E.H. Schacht, M. Cornelissen, H. Berghmans, Structural and rheological properties of methacrylamide modified gelatin hydrogels, Biomacromolecules 1 (2000) 31–38.
[54] J.W. Nichol, S.T. Koshy, H. Bae, C.M. Hwang, S. Yamanlar, A. Khademhosseini, Cell-laden microengineered gelatin methacrylate hydrogels, Biomaterials 31 (2010) 5536–5544.
[55] M. Nikkhah, N. Eshak, P. Zorlutuna, N. Annabi, M. Castello, K. Kim, A. Dolatshahi-Pirouz, F. Edalat, H. Bae, Y.Z. Yang, A. Khademhosseini, Directed endothelial cell morphogenesis in micropatterned gelatin methacrylate hydrogels, Biomaterials 33 (2012) 9009–9018.
[56] L.E. Bertassoni, M. Cecconi, V. Manoharan, M. Nikkhah, J. Hjortnaes, A.L. Cristino, G. Barabaschi, D. Demarchi, M.R. Dokmeci, Y.Z. Yang, A. Khademhosseini, Hydrogel bioprinted microchannel networks for vascularization of tissue engineering constructs, Lab Chip 14 (2014) 2202–2211.
[57] B. Nikoobakht, M.A. El-Sayed, Preparation and growth mechanism of gold nanorods (NRs) using seed-mediated growth method, Chem. Mater. 15 (2003) 1957–1962.
[58] I.N. Sneddon, The relation between load and penetration in the axisymmetric boussinesq problem for a punch of arbitrary profile, Int. J. Eng. Sci. 3 (1965) 47–57.
[59] N. Peela, F.S. Sam, W. Christenson, D. Truong, A.W. Watson, G. Mouneimne, R. Ros, M. Nikkhah, A three dimensional micropatterned tumor model for breast cancer cell migration studies, Biomaterials 81 (2016) 72–83.
[60] N. Tandon, C. Cannizzaro, P.H.G. Chao, R. Maidhof, A. Marsano, H.T.H. Au, M. Radisic, G. Vunjak-Novakovic, Electrical stimulation systems for cardiac tissue engineering, Nat. Protoc. 4 (2009) 155–173.
[61] A. Gole, C.J. Murphy, Seed-mediated synthesis of gold nanorods: role of the size and nature of the seed, Chem. Mater. 16 (2004) 3633–3640.
[62] A. Dolatshahi-Pirouz, M. Nikkhah, A.K. Gaharwar, B. Hashmi, E. Guermani, H. Aliabadi, G. Camci-Unal, T. Ferrante, M. Foss, D.E. Ingber, A. Khademhosseini, A combinatorial cell-laden gel microarray for inducing osteogenic differentiation of human mesenchymal stem cells, Sci. Rep. 4 (2014).
[63] N. Annabi, J.W. Nichol, X. Zhong, C.D. Ji, S. Koshy, A. Khademhosseini, F. Dehghani, Controlling the porosity and microarchitecture of hydrogels for tissue engineering, Tissue Eng. B 16 (2010) 371–383.
[64] Y.H. Lee, J.H. Lee, I.G. An, C. Kim, D.S. Lee, Y.K. Lee, J.D. Nam, Electrospun dualporosity structure and biodegradation morphology of Montmorillonite reinforced PLLA nanocomposite scaffolds, Biomaterials 26 (2005) 3165–3172.
[65] A. Fuhrmann, J.R. Staunton, V. Nandakumar, N. Banyai, P.C.W. Davies, R. Ros, AFM stiffness nanotomography of normal, metaplastic and dysplastic human esophageal cells, Phys. Biol. 8 (2011).
[66] J.R. Xavier, T. Thakur, P. Desai, M.K. Jaiswal, N. Sears, E. Cosgriff-Hernandez, R. Kaunas, A.K. Gaharwar, Bioactive nanoengineered hydrogels for bone tissue engineering: a growth-factor-free approach, ACS Nano 9 (2015) 3109–3118.
[67] S.C. Tjong, Structural and mechanical properties of polymer nanocomposites, Mater. Sci. Eng. R 53 (2006) 73–197.
[68] A.I. Hassaballah, M.A. Hassan, A.N. Mardi, M. Hamdi, An inverse finite element method for determining the tissue compressibility of human left ventricular wall during the cardiac cycle, PLoS One 8 (2013).
[69] H.-B. Wang, M. Dembo, Y.-L. Wang, Substrate flexibility regulates growth and apoptosis of normal but not transformed cells, Am. J. Physiol. Cell Physiol. 279 (2000). C1345-C50.
[70] H. Aubin, J.W. Nichol, C.B. Hutson, H. Bae, A.L. Sieminski, D.M. Cropek, P. Akhyari, A. Khademhosseini, Directed 3D cell alignment and elongation in microengineered hydrogels, Biomaterials 31 (2010) 6941–6951.
[71] D.F. Mosher, L.T. Furcht, Fibronectin – review of its structure and possible functions, J. Invest. Dermatol. 77 (1981) 175–180.
[72] P.A. Guerrero, R.B. Schuessler, L.M. Davis, E.C. Beyer, C.M. Johnson, K.A. Yamada, J.E. Saffitz, Slow ventricular conduction in mice heterozygous for a connexin43 null mutation, J. Clin. Invest. 99 (1997) 1991–1998.
[73] M. Oyamada, H. Kimura, Y. Oyamada, A. Miyamoto, H. Ohshika, M. Mori, The expression, phosphorylation, and localization of connexin-43 and gapjunctional intercellular communication during the establishment of a synchronized contraction of cultured neonatal rat cardiac myocytes, Exp. Cell Res. 212 (1994) 351–358.

APPENDIX C

MATLAB CODE FOR SINGLE CELL FORCE SPECTROSCOPY SINGLE MOLECULE ANALYIS

```
function [data]=getfit(ibw)

% This function imports .ibw files made in Igor, and pulls all the
% important data for single molecule analysis from single
% cell force spectroscopy curves. It calls 4 other functions,
%'ForceCurve',
% 'correct_virtual_deflection', 'getpoints', and 'getfitregions.'
% This ends up creating a structure for each force curve consisting of
% the fields:
% 'FC','iAs','iBs','rigidities','distances','forces','jumppoints', and
% 'basepoints'
%
% 'ForceCurve' is a function written by Bryant Doss that pulls all the
% important information from the wave notes of the .ibw file.
% This function will work on all force curve files in a single folder,
% but there must only be force curve files in the folder.
% It's best to do 5 or so force curves at a time.
%
% 'rigidities' is the slope leading up to a rupture. 'forces' is the
% rupture force. 'distances' is the distance from the beginning of the
% retraction curve to the beginning of the rupture. 'basepoints' is the
% beginning of the rupture, and 'jumppoints' is the end of the rupture.
% 'iAs' and 'iBs' are the reference points for the portion of data used
% to determine the slope before the rupture.
FC=ForceCurve(ibw)
close all
figure(1)
plot(FC.ret(:,1),FC.ret(:,2))
choice=menu('OK or skip this curve?','OK','skip');
if choice==1

    outcurve = correct_virtual_deflection (FC)

    [basepoints,jumppoints,distances,forces]=getpoints(outcurve)

    [rigidities,iAs,iBs]=getfitregions(outcurve,basepoints,jumppoints)

data.FC=outcurve;
data.iAs=iAs;
data.iBs=iBs;
data.rigidities=rigidities;
data.distances=distances;
data.forces=forces;
data.jumppoints=jumppoints;
data.basepoints=basepoints;
else
data.FC=FC;
data.iAs=[];
data.iBs=[];
data.rigidities=[];
data.distances=[];
data.forces=[];
data.jumppoints=[];
data.basepoints=[];
end
```

```
function [newoutcurve] = correct_virtual_deflection (incurve, point)
%     if nargin < 2
%         % Manually choose point
%         point = manual(incurve);
%     end

    outcurve = incurve;

    % Uncomment to correct the extension
%     npoints = get_index(incurve,point);
%     outcurve = incurve;
%     fit = polyfit(incurve.zsens_defl_ext(1:npoints,1), ...
%           incurve.zsens_defl_ext(1:npoints,2), 1);
%
%     slope = fit(1);
%
%     outcurve.zsens_defl_ext(:,2) = incurve.zsens_defl_ext(:,2) - ...
%           incurve.zsens_defl_ext(:,1) * slope;
%
%     outcurve.ext(:,1) = outcurve.zsens_defl_ext(:,1) - ...
%           outcurve.zsens_defl_ext(:,2);
%
%     outcurve.ext(:,2) = outcurve.zsens_defl_ext(:,2) * outcurve.k;

    % Uncomment to correct the retraction using point-and-click
    close;

   % Open a menu to determine a baseline to correct the curve off of.
    plot(incurve.ret(:,1),incurve.ret(:,2),'-','color','blue');
    set(gcf,'Position',[500,500,900,500]);
    xlabel('Distance [m]')
    ylabel('Force [N]')
    title('Click to start then end baseline')
    [point1,~]=ginput(1);
    [point2,~]=ginput(1);
    close;
    ret_diffs = abs(incurve.ret(:,1) - point1);
    reti = find(ret_diffs == min(ret_diffs));
    npoints1 = reti(1);
    ret_diffs = abs(incurve.ret(:,1) - point2);
    reti = find(ret_diffs == min(ret_diffs));
    npoints2 = reti(1);

    % Here down corrects the curve based on the slope of the baseline

    pit = polyfit(incurve.zsens_defl_ret(npoints1:npoints2,1), ...
        incurve.zsens_defl_ret(npoints1:npoints2,2), 1);

    slope = pit(1);

    outcurve.zsens_defl_ret(:,2) = incurve.zsens_defl_ret(:,2) -...
        incurve.zsens_defl_ret(:,1) * slope;

    outcurve.ret(:,1) = outcurve.zsens_defl_ret(:,1) - ...
        outcurve.zsens_defl_ret(:,2);
```

```
    outcurve.ret(:,2) = outcurve.zsens_defl_ret(:,2) * outcurve.k;
    % Optional: plot corrected curve
    plot(outcurve.ret(:,1),outcurve.ret(:,2));


% Shifting the curve so that the y-intercept of the baseline is the
% beginning of the new retraction force curve, and the baseline
% represents 0 force.

    lit = fit(incurve.ret(npoints1:npoints2,1), ...
        incurve.ret(npoints1:npoints2,2),'poly1')

    litcoeffs = coeffvalues(lit);
    slope = litcoeffs(1);
    intercept = litcoeffs(2);
    BL(:,1) = incurve.ret(:,1);
    BL(:,2) = incurve.ret(:,1).*slope + intercept;

    i = find(incurve.ret(:,2) <= BL(:,2),1,'last');

    newoutcurve.ret(:,1)=incurve.ret(:,1);
    newoutcurve.ret(:,2)=incurve.ret(:,2)-BL(:,2);
    newoutcurve.ret(:,1) = newoutcurve.ret(:,1) - newoutcurve.ret(i,1);
    newoutcurve.ret(:,2) = newoutcurve.ret(:,2) - newoutcurve.ret(i,2);

    plot(newoutcurve.ret(:,1),newoutcurve.ret(:,2));

end
```

```
function [basepoints,jumppoints,distances,forces]=getpoints(outcurve)
close all;

% This function opens up a menu to allow you to manually select
% the basepoints and jumppoints of rupture events. You need to make
sure
% that you do this step correctly and in order. That means selecting
% 'Beginning' and 'End' consecutively. There should always be an 'End'
% for each 'Beginning.' Do this step carefully.

 % First convert corrected curve to pN and nm.
    outcurve.ret(:,1)=outcurve.ret(:,1).*1e9;
    outcurve.ret(:,2)=outcurve.ret(:,2).*1e12;

    % Set up your variable arrays.
    forces = [];
    jumppoints = [];
    basepoints = [];
    distances = [];

% Plot the corrected force curve.
hold on;
plot(outcurve.ret(:,1),outcurve.ret(:,2),'color','b');
set(gcf,'Position',[15 50 1500 800])
i=1;

    while (i)


        % Open menu to begin electing rupture events.
        choice=menu('Select Beginning and End of
Ruptures','Beginning',...
            'End','All Done');

        % Use MATLABs tools like zoom and the frame grabber to
carefully
        % select rupture beginnings and ends.
        if choice==1
            title('Click the Beginning')
            [x,y]=ginput(1);
            % get closest datapoint to clicked point
            distancesb=sqrt((outcurve.ret(:,1)-x).^2+...
                (outcurve.ret(:,2)-y).^2);

            [cdistanceb,idistanceb]=min(distancesb);

            basepoint = [outcurve.ret(idistanceb,1),...
                outcurve.ret(idistanceb,2)];

            basepoints = [basepoints; basepoint];
            hold on

            plot(basepoint(:,1),basepoint(:,2),'kx','MarkerSize',10,...
                'LineWidth',2, 'Color', 'red')
        end
```

```
        if choice==2
            title('Click the End')
            [x,y]=ginput(1);
            % get closest datapoint to clicked point
            distancesa=sqrt((outcurve.ret(:,1)-x).^2+...
                (outcurve.ret(:,2)-y).^2);

            [cdistancea,idistancea]=min(distancesa);

            jumppoint = [outcurve.ret(idistancea,1),...
                outcurve.ret(idistancea,2)];

            jumppoints = [jumppoints; jumppoint];

            hold on

            plot(jumppoint(:,1),jumppoint(:,2),'kx','MarkerSize',...
                10,'LineWidth',2, 'Color', 'black')


        end

        if choice==3

            i = 0;

        end

    end

    % This loop calculates the distance for each rupture event and
    % force of each rupture event.

    for j =1:length(basepoints)

           distances = [distances; abs(basepoints(j,1))];
           forces = [forces; jumppoints(j,2)-basepoints(j,2)];

    end

% Here is a plot to show your progress
     hold on
     plot(jumppoints(:,1),jumppoints(:,2),'kx','MarkerSize',10,...
         'LineWidth',2)

     plot(basepoints(:,1),basepoints(:,2),'kx','MarkerSize',10,...
         'LineWidth',2, 'Color', 'red')

end
```

```
function
[rigidities,iAs,iBs]=getfitregions(outcurve,basepoints,jumppoints)
close all;

% This function is to determine the region of the curve to fit with
% a linear fit prior to the rupture event. It calls a menu, and lets
% you select the data to be fit. Whatever you do, DO NOT click so
% that you select data that occurs after or to the left of the rupture.
% If you do that it will crash the program.

iAs=[];
iBs=[];
rigidities=[];
outcurve.ret(:,1)=outcurve.ret(:,1).*1e9;
outcurve.ret(:,2)=outcurve.ret(:,2).*1e12;
%window size parms
width=1000 %width of half window in tens of nanometers
height=200 %height of half window in pN



for i=1:length(basepoints)

hold on;
plot(outcurve.ret(:,1),outcurve.ret(:,2),'color','b');
plot(basepoints(i,1),basepoints(i,2),'kx','MarkerEdgeColor','r',...
    'MarkerSize',15,'LineStyle','none')

plot(jumppoints(i,1),jumppoints(i,2),'kx','MarkerEdgeColor','k',...
    'MarkerSize',15,'LineStyle','none')

xlim([basepoints(i,1)-width basepoints(i,1)+width])
ylim([basepoints(i,2)-height basepoints(i,2)+height])

% set(gcf,'Position',[15 50 1900 800])
% choice=menu('OK or skip','OK','skip');
% if choice==1
    title('Click to the right of the red x ')
    [x,y]=ginput(1);
    % get closest datapoint to clicked point
    distancesb=sqrt((outcurve.ret(:,1)-x).^2+(outcurve.ret(:,2)-y).^2);
    [cdistanceb,idistanceb]=min(distancesb);

    % get closest point to the basepoint
    distancesa=sqrt((outcurve.ret(:,1)-basepoints(i,1)).^2+...
        (outcurve.ret(:,2)-basepoints(i,2)).^2);

    [cdistancea,idistancea]=min(distancesa);

    iAs=[iAs; idistancea];
    iBs=[iBs; idistanceb];

    % fit the curve region
    [rigidity]=mypolyfit(outcurve,idistancea,idistanceb);
```

```
    rigidities=[rigidities; rigidity];

% else
%     rigidities=[rigidities; nan];
%     iAs=[iAs; nan];
%     iBs=[iBs; nan];
%
% end

end
```